



**Some pages of this thesis may have been removed for copyright restrictions.**

If you have discovered material in Aston Research Explorer which is unlawful e.g. breaches copyright, (either yours or that of a third party) or any other law, including but not limited to those relating to patent, trademark, confidentiality, data protection, obscenity, defamation, libel, then please read our [Takedown policy](#) and contact the service immediately (openaccess@aston.ac.uk)

# **Polyoxometalates as solid acid catalysts for sustainable chemistry**

Lucia Frattini

Doctor of Philosophy

Aston University

European Bioenergy Research Institute  
(EBRI)

September 2017

©Lucia Frattini, 2017

Lucia Frattini asserts her moral right to be identified as the author of this thesis  
This copy of the thesis has been supplied on condition that anyone who consults it  
is understood to recognise that its copyright belongs to its author and that no  
quotation from the thesis and no information derived from it may be published  
without appropriate permission or acknowledgement.

Aston University  
EBRI (European Bioenergy Research Institute)

**Polyoxometalates as solid acid catalysts  
for sustainable chemistry**

Lucia Frattini  
Doctor of Philosophy

September 2017

Polyoxometalates, also known as heteropolyacids (HPA), are solid acids widely utilised in heterogeneous catalysis. The physicochemical properties of HPAs facilitate surface-type or bulk-type reactions, dependent on substrate polarity. For the latter, the gas-phase dehydration of ethanol was investigated representing an environmentally friendly solution to produce bio-ethylene, a key compound to the chemical industry; while for the former, the solventless liquid-phase isomerisation of  $\alpha$ -pinene was studied due to the widespread applications of its derivatives. Supported HPAs, exhibiting the Keggin structure, were prepared on commercial low surface area fumed silica and mesoporous high surface area SBA-15 via wet impregnation technique to elucidate structure-activity behaviours in both catalytic systems relative to their bulk equivalents. In addition, different types of HPAs, phosphotungstic acid (HPW), silicotungstic acid (HSiW) and phosphomolybdic acid (HPMo), were studied to observe the role of acid strength on product distribution.

The successful synthesis of supported HPAs was confirmed by multiple characterisation techniques, revealing an inverse relationship between loading and dispersion which is further promoted through the use of mesoporous SBA-15 as the support, whereas non-porous fumed silica induced agglomeration which in turn increases the degree of crystalline water present in the HPAs. n-Propylamine TPD evaluated acid strength decreases in the order of HPW>HSiW>HPMo, which is independent of support. Support choice did not influence selectivity in either reaction, but did impact greatly on catalytic activity, imparting significant reaction rate and turnover frequency enhancement. For surface-type reaction, SBA-15 showed to be the optimal support due to greater active sites accessibility, whereas in the case of the bulk-type reaction, the fumed silica based materials, with larger 3D HPAs structures, even at low loadings, showed superior performance. Product distributions were affected through the choice of HPA, with higher selectivity towards camphene, for  $\alpha$ -pinene isomerisation, and ethylene, for ethanol dehydration, observed over the HPW catalysts.

**Key words:** Heteropolyacids, crystalline water, ethanol dehydration,  $\alpha$ -pinene isomerisation, SBA-15

## Dedication

To Nano

*“My face is mine, my hands are mine, my mouth is mine, but I am not. I am yours.”*

## Acknowledgments

To start I would like to express my deep gratitude to Dr Marta Granollers Mesa and Dr Christopher Parlett, my research supervisors, for their excellent assistance and valuable critiques during the writing of this research. Their time and willingness to help have been very much appreciated.

I would like to express my great thankfulness to Professor Adam Lee and Professor Karen Wilson, for giving me the opportunity to carry out this research and for their patient guidance and useful advices during this three years.

I must recognise the School of Engineering and Applied Science at Aston University for providing the funding of this project, and the European Bioenergy Research Institute (EBRI) for the facilities.

I would like to extent my thanks to Dr Mark Isaacs for the acquisition of valuable STEM images and XPS analysis, Dr Violaine Mendez, Dr James Hunns and Miss Rima Trofimovaite for XRF analysis. I am particularly grateful for the assistance and friendship given by Dr Lachlan Ciddor and Dr James Bennett during the first year of my PhD for their help setting up the flow-reactor. I am extremely appreciative to the Surface, Materials and Catalysis Group members for their valuable support. Individually, I would like to thank Miss Brunella Barbero, Dr Amin Osatiashtiani and the EBRI volleyball team for being great colleagues and good friends.

My deep gratitude goes to my family and friends for their unfailing love and continuous encouragement throughout the year of my studies. Without them this work would not have been possible.

Last but no means least, special recognitions are made to the admirable patience, love and friendship of Mr Mariano Tapia Reche for being there in the good and hard times.

# List of contents

## ***Chapter 1 Introduction***

1.1	Heterogeneous catalysis for Sustainable Chemistry	21
1.1.1	Green and sustainable chemistry	21
1.1.2	Principles of catalysis	23
1.1.3	Heterogeneous acid catalysts	24
1.1.4	Catalyst deactivation	25
1.2	Silica-based supports	27
1.2.1	The role of support in catalysis	27
1.2.2	Generic properties	28
1.2.3	Ordered mesoporous silica	29
1.3	Heteropolyacids	31
1.3.1	Structure of solid HPA	32
1.3.2	Types of reaction: surface and bulk	33
1.3.3	Generic properties	34
1.3.4	Applications	36
1.4	$\alpha$ -Pinene isomerisation	37
1.4.1	Introduction	37
1.4.2	Sustainable chemicals from Turpentine	37
1.4.3	$\alpha$ -Pinene market and derivatives	38
1.4.4	Isomerisation reaction	41
1.5	Bioethanol dehydration	45
1.5.1	Introduction	45
1.5.2	Ethanol vs Bioethanol	45
1.5.3	Ethanol Dehydration	48
1.6	Thesis aims	54
1.7	References	54

## ***Chapter 2 Experimental***

2.1	Catalyst synthesis	67
2.1.1	Synthesis of SBA-15	67
2.1.2	Synthesis of supported heteropolyacids	68
2.2	Catalyst characterisation	68

2.2.1	X-ray Fluorescence (XRF)	68
2.2.2	C, H, N and S elemental analysis (CHNS)	69
2.2.3	Powder X-ray diffraction (XRD)	69
2.2.4	Nitrogen porosimetry	72
2.2.5	Scanning transmission electron microscopy (STEM) and energy dispersive X-ray analysis (EDX)	75
2.2.6	Thermogravimetric analysis (TGA)	77
2.2.7	Propylamine chemisorption and temperature programmed desorption (TPD)	78
2.2.8	Diffusive reflection infrared Fourier transform spectroscopy (DRIFTS)	79
2.2.9	NH <sub>3</sub> titration and temperature programmed desorption (TPD)	80
2.2.10	X-ray photoelectron spectroscopy (XPS)	81
2.2.11	Raman spectroscopy	83
2.3	Catalytic tests	84
2.3.1	Batch reaction – $\alpha$ -Pinene isomerisation	84
2.3.2	Continuous flow reaction – Ethanol dehydration	86
2.4	List of chemicals	89
2.5	References	90

### ***Chapter 3 Structural characterisation of supported HPA***

3.1	Introduction	93
3.2	Results and discussion	93
3.2.1	Phosphotungstic acid based materials	93
3.2.1.1	X-ray Fluorescence (XRF)	93
3.2.1.2	Powder X-ray diffraction (XRD)	94
3.2.1.3	Nitrogen porosimetry	98
3.2.1.4	Scanning transmission electron microscopy (STEM)	103
3.2.1.5	Thermogravimetric analysis (TGA)	104
3.2.1.6	n-Propylamine chemisorption and temperature programmed desorption (TPD)	109
3.2.1.7	NH <sub>3</sub> titration and Temperature programmed desorption (TPD)	111
3.2.1.8	Diffusive reflection infrared Fourier transform spectroscopy (DRIFTS)	114
3.2.1.9	Raman spectroscopy	117

3.2.1.10	X-ray photoelectron spectroscopy (XPS)	120
3.2.2	Silicotungstic and phosphomolybdic acid based materials	122
3.2.2.1	X-ray Fluorescence (XRF)	122
3.2.2.2	Powder X-ray diffraction (XRD)	123
3.2.2.3	Nitrogen porosimetry	125
3.2.2.4	Thermogravimetric analysis (TGA)	127
3.2.2.5	n-Propylamine chemisorption and temperature programmed desorption (TPD)	129
3.2.2.6	Diffusive reflection infrared Fourier transform spectroscopy (DRIFTS)	131
3.2.2.7	Raman spectroscopy	132
3.2.2.8	XPS – X-ray photoelectron spectroscopy	133
3.3	Conclusions	135
3.4	References	136

#### ***Chapter 4 Alpha pinene isomerisation***

4.1	Introduction	141
4.2	Results and discussion	142
4.2.1	Reaction profiles on supported HPW: support architecture effect	143
4.2.2	Reaction profiles on supported HPW: temperature effect	147
4.2.3	Selectivity dependence on acid strength	150
4.2.4	Mechanism study	153
4.3	Conclusion	156
4.4	Reference	158

#### ***Chapter 5 Ethanol dehydration***

5.1	Introduction	161
5.2	Results and discussion	162
5.2.1	Reaction profiles on unsupported HPA	163
5.2.1.1	Unsupported HPW	163
5.2.1.2	Unsupported HSiW and HPMo	166
5.2.2	Reaction profiles on supported HPAs	170
5.2.2.1	Supported HPW: the influence of support architecture	170
5.2.2.2	Supported HPW: recycling the catalyst	176
5.2.2.3	Supported HPW: the influence of temperature	182
5.2.2.4	Supported HSiW and HPMo	191

5.3	Conclusions	193
5.4	References	194

### ***Chapter 6 Conclusions***

6.1	Conclusions	198
6.1.1	Effect of type of support	198
6.1.2	Effect of HPA type	199
6.1.3	Costs analysis	200
6.2	References	202

### ***Appendix***

Appendix A	204
Appendix B	208

## List of Abbreviations

- BET** - Brunauer, Emmett and Teller Adsorption Theory
- BJH** - Barrett, Joyner and Halenda Pore Size Distribution Method
- CHNS** - Carbon, Hydrogen, Nitrogen, Sulfur elemental analysis
- DEE** - Diethyl ether
- DRIFTS** - Diffuse reflection infrared Fourier transform spectroscopy
- EDX** - Energy dispersive X-ray analysis
- HPA** - Heteropolyacid
- HPMo** - Phosphomolybdic acid
- HPW** - Phosphotungstic acid
- HSiW** - Silicotungstic acid
- K.U.** - Keggin Unit
- rpm** – Revolution per minutes
- STD** - Internal standard
- STEM** - Scanning transmission electron microscope
- TGA** - Thermogravimetric analysis
- TOF** - Turnover frequency
- TPD** - Temperature programmed desorption
- XPS** - X-ray photoelectron spectroscopy
- XRD** - Powder X-ray diffraction
- XRF** - X-ray fluorescence

# List of Equations, Figures, Schemes and Tables

## Chapter 1 Introduction

<b>Figure 1.1</b> – The 12 principles of green chemistry.	22
<b>Figure 1.2</b> – Major types of deactivation in heterogeneous catalysis.	26
<b>Figure 1.3</b> – Silica structure with relative hydroxyl groups, in its anhydrous and hydrous form.	29
<b>Figure 1.4</b> – Schematic stepwise synthesis of mesoporous materials.	30
<b>Figure 1.5</b> – Phosphotungstic acid Keggin structure.	32
<b>Figure 1.6</b> – Hierarchical structure of phosphotungstic acid in the solid state.	33
<b>Figure 1.7</b> – Types of catalysis for heteropolyacids, where the K.U. are depicted in grey, with an arbitrary number of hydrogens (white) and water molecules (blue), where R stands for reagent and P, product.	34
<b>Table 1.1</b> – PKa values for various heteropolyacids and other mineral acids in acetic acid solutions	35
<b>Figure 1.8</b> – Tertiary structure of hydrated phosphotungstic acid.	35
<b>Scheme 1.1</b> – Valuable compounds obtained from $\alpha$ -pinene	40
<b>Figure 1.9</b> – $\alpha$ -Pinene isomerisation reaction mechanism.	42
<b>Figure 1.10</b> – Global bioethanol production by country/region and year.	46
<b>Table 1.2</b> – Substrate for bioethanol production and their production potentials	47

## Chapter 2 Experimental

<b>Equation 2.1</b> – Calculation of the theoretical loading.	67
<b>Figure 2.1</b> – Illustrative representation of X-ray fluorescence.	68
<b>Equation 2.2</b> – Moseley's law,	69
<b>Figure 2.2</b> – Schematic of X-ray interference with atomic lattice (top); relation between lattice spacing (d) and correlation between $\lambda$ and $\theta$ (bottom).	70
<b>Equation 2.3</b> – Bragg's law.	70
<b>Equation 2.4</b> – d-spacing calculation, where a = lattice parameter and h,k,l are Miller indices.	71
<b>Equation 2.5</b> – Scherrer equation.	71
<b>Figure 2.3</b> – Schematic of the relationship between the hexagonal SBA-15 structure, d (100) = layer spacing and a = pore spacing.	72
<b>Equation 2.6</b> – Inter layer spacing calculation.	72

<b>Figure 2.4</b> – (left) IUPAC nomenclature for the six type of isotherms; relative pressure is defined as $P/P_0$ ; the volume adsorbed ( $\text{cm}^3 \text{g}^{-1}$ ); (right) IUPAC nomenclature for the 4 types of hysteresis loop.	74
<b>Equation 2.7</b> – BET equation.	75
<b>Equation 2.8</b> – Kelvin equation.	75
<b>Figure 2.5</b> – Schematic STEM microscope configuration.	77
<b>Figure 2.6</b> – Photo showing Mettler Toledo TGA/DSC 2 Star System.	78
<b>Figure 2.7</b> – n-Propylamine proposed mechanism over protonic acid sites.	79
<b>Equation 2.9</b> – Kubelka-Munk equation.	80
<b>Figure 2.8</b> – Photo showing DRIFT configuration (right) and the praying mantis environmental cell (left).	80
<b>Figure 2.9</b> – Photo showing consecutive performed injections, revealing the breakthrough zone and the plateau zone.	81
<b>Figure 2.10</b> – Photoemission and Auger process.	83
<b>Equation 2.10</b> – Kinetic energy evaluation via XPS.	83
<b>Figure 2.11</b> – The Raman effect.	84
<b>Figure 2.12</b> – photo showing the a Radleys Starfish reactor.	85
<b>Equation 2.11</b> – Conversion and products selectivity.	85
<b>Figure 2.13</b> – Typical chromatogram for $\alpha$ -pinene isomerisation.	86
<b>Figure 2.14</b> – Continuous flow reactor – photo (top); scheme (bottom).	87
<b>Figure 2.15</b> – Typical chromatograms for ethanol dehydration reaction.	88

### ***Chapter 3 Structural characterisation of supported HPA***

<b>Figure 3.1</b> – Representation of the most common HPAs architectures.	93
<b>Table 3.1</b> – XRF elemental analysis of HPW supported on fumed $\text{SiO}_2$ and SBA-15 and corresponding unsupported material.	94
<b>Figure 3.2</b> – (a) Low angle powder XRD pattern of parent SBA-15 and (b) low angle powder XRD of HPW functionalised SBA-15.	95
<b>Table 3.2</b> – Unit cell parameter and corresponding pore spacings for HPW/SBA-15 samples.	95
<b>Figure 3.3</b> – (a) Powder XRD patterns for fumed silica and HPW/fumed silica, and (b) SBA-15 and HPW/SBA-15 with pure HPW shown for reference.	96
<b>Table 3.3</b> – Particle size dependence on W loading for fumed silica and SBA-15 series.	97
<b>Figure 3.4</b> – In-situ XRD pattern of the unsupported HPW collected from 25 to 600 °C ( $10 \text{ }^\circ\text{C min}^{-1}$ ) under $\text{N}_2$ flow ( $10 \text{ mL min}^{-1}$ ).	98

<b>Figure 3.5</b> – Effect of temperature on particle sizes from in-situ study.	98
<b>Figure 3.6</b> – Isotherms of adsorption and desorption for both supports, fumed silica (a) and SBA-15 (b).	99
<b>Figure 3.7</b> – Isotherms of adsorption and desorption for supported materials at different W wt% HPW/fumed silica offset by 50 cm <sup>3</sup> g <sup>-1</sup> (a), and HPW/SBA-15 offset by 150 cm <sup>3</sup> g <sup>-1</sup> (b).	100
<b>Figure 3.8</b> – Surface area values of HPW/fumed silica and HPW/SBA-15 (N <sub>2</sub> BET) (a); micropore surface area (on first and second y-axis) HPW/Fumed silica and HPW/SBA-15 (N <sub>2</sub> t-plot) (b).	101
<b>Figure 3.9</b> –BJH pores size distributions of HPW/SBA-15 (a); and pore diameter and pore volume of HPW/SBA-15 as function of W loading (b).	102
<b>Equation 3.1</b> – where SA <sub>support</sub> is the BET measured surface area per gram of support, NA is the Avogadro number, and "ω <sub>HPW</sub> " is the mass fraction.	102
<b>Figure 3.10</b> – Surface coverage dependence of silica supported HPW.	103
<b>Figure 3.11</b> – STEM dark-field images of (a) 2.2 wt% HPW/fumed silica, (b) 15.5 wt% HPW/fumed silica, (c) 59.6 wt% HPW/fumed silica; (c and d) 3.2 wt% HPW/SBA-15, (e) 55.7 wt% HPW/SBA-15. Insets show corresponding EDX atomic ratio lines profiles.	104
<b>Scheme 3.1</b> – Proposed thermo-decomposition process of phosphotungstic acid under N <sub>2</sub> flow [18].	104
<b>Figure 3.12</b> – Thermal analysis expressed as % mass loss as function of temperature on HPW/fumed silica series (a) and HPW/SBA-15 (b).	105
<b>Figure 3.13</b> – Physisorbed water (a) and crystalline water (b) mass loss for unsupported HPW and supported HPW on fumed silica and SBA-15.	106
<b>Figure 3.14</b> – Differential thermal analysis of supported HPW as a function of loading, HPW/fumed silica (a) and HPW/SBA-15 (b).	107
<b>Figure 3.15</b> – n-propylamine TPD relative intensities of m/z normalised per g of sample for supported HPW on fumed silica (a) and on SBA-15 (b).	108
<b>Table 3.4</b> – n-Propylamine measured acid sites densities of supported HPW.	109
<b>Figure 3.16</b> – Fitting example of mass normalised 41 m/z MS channel from n-propylamine TPD-MS for 15.5 wt% W on fumed silica (a), and 16.9 wt% W on SBA-15 (b).	110
<b>Figure 3.17</b> – Relative acid loading for strong, medium and weak sites based on the relative peak area % (obtained from profile deconvolution) and the total acid loading as function of W wt% on both supports, fumed silica (a) and SBA-15 (b).	111
<b>Figure 3.18</b> – Stacked NH <sub>3</sub> TPD data of HPW/fumed silica (a) and HPW/SBA-15 (b). Inset, TPD profile obtained for unsupported HPW.	112

<b>Table 3.5</b> – NH <sub>3</sub> -TPD measures acid site densities of supported HPW.	112
<b>Figure 3.19</b> – Fitting example of mass normalised 17 m/z MS channel from ammonia titration and TPD for 6.2 wt% W on fumed silica (a), and 9.0 wt% W on SBA-15 (b).	113
<b>Figure 3.20</b> – Relative acid loading for strong, medium and weak sites based on the relative peak area % (obtained from profile deconvolution) and the total acid loading as function of W wt% on both supports, fumed silica (a) and SBA-15 (b).	114
<b>Figure 3.21</b> – DRIFT spectra of SBA-15 and fumed silica, and assignment of silanol group function to vibrational signal (a); isolated OH K-M intensities as function of bulk W loading for HPW supported on fumed silica and SBA-15 [36] (b).	115
<b>Figure 3.22</b> – Stacked DRIFT spectra of supported HPW on fumed silica (a), and SBA-15 (b) as function of W bulk wt%, pure HPW and supports are reported for comparison.	116
<b>Figure 3.23</b> – DRIFTs spectra of unsupported HPW collected from 120 to 600 °C (a); and dependence of Kubelka-Munk intensities on temperature indicating thermal stability of HPW units (b).	117
<b>Figure 3.24</b> – Raman spectra of mesoporous SBA-15 (a) and commercial WO <sub>3</sub> (b).	118
<b>Figure 3.25</b> – Stacked Raman spectra of HPW/Fumed silica (a); and HPW/SBA-15 (b). Labelled peaks (▼) are referred to unsupported HPW features.	119
<b>Figure 3.26</b> – Stacked Raman spectra with dotted line indicating relative peak position, for HPW on fumed silica (a) and SBA-15 (b).	120
<b>Figure 3.27</b> – Background subtracted W 4f XP spectra of HPW/fumed silica series (a); and ratio of integrated signal of interfacial to bulk W 4f species across the loading on SBA-15, and correlation between surface and bulk W wt% loadings(b).	121
<b>Figure 3.28</b> – Background subtracted W 4f XP spectra of HPW/SBA-15 series (a); and ratio of integrated signal of interfacial to bulk W 4f species across the loading on SBA-15, and correlation between surface and bulk W wt% loadings (b).	122
<b>Table 3.6</b> – XRF elemental analysis data of synthesised materials.	123
<b>Figure 3.29</b> – Low angle powder XRD pattern of HPMo/SBA-15 (a) and HSiW/SBA-15 (b).	123
<b>Table 3.7</b> – Unit cell parameter and corresponding pore spacings for supported HPMo and HSiW on SBA-15.	124
<b>Figure 3.30</b> – Wide angle XRD patterns for (a) HPMo/SBA-15, and (b) HSiW/SBA-15 as function of metal loading. Unsupported HPAs are added as reference.	125
<b>Table 3.8</b> – Particle size dependence of Mo and W loading on SBA-15.	125
<b>Figure 3.31</b> – Stacked isotherms of nitrogen adsorption and desorption for	

SBA-15 supported HPAs at different metal wt%; HPMo/SBA-15 (offset of 100 cm <sup>3</sup> g <sup>-1</sup> ) (a) and HSiW/SBA-15 (offset of 150 cm <sup>3</sup> g <sup>-1</sup> ) (b).	126
<b>Table 3.9</b> – Textural properties of HPMo and HSiW on SBA-15 across the metal loading, wt%.	127
<b>Figure 3.32</b> – BJH pore size distribution for HPMo/SBA-15 series (a), and HSiW/SBA-15 series (b).	127
<b>Figure 3.33</b> – Thermal analysis expressed as % mass loss as function of temperature on HPMo/SBA-15 series (a) and HSiW/SBA-15 (b).	128
<b>Figure 3.34</b> – Thermogravimetric analysis of SBA-15 supported materials, HPMo (a) and HSiW (b).	129
<b>Figure 3.35</b> – n-Propylamine TPD relative intensities of m/z normalised per g of sample for SBA-15 supported HPA over the metal wt% series; HPMo/SBA-15 (a) and HSiW/SBA-15 (b).	130
<b>Table 3.10</b> – n-Propylamine measured acid sites densities of SBA-15 supported HPMo and HSiW.	130
<b>Figure 3.36</b> – Fitting example of 41 m/z MS channel normalised for the g of solid sample, collected during n-propylamine chemisorption and TPD analysis, and obtained via Casa XPS software on and HPMo/SBA-15, bulk Mo 8.7 wt% (a), and HSiW/SBA-15, bulk W 9.9 wt% (b).	131
<b>Figure 3.37</b> – Stacked DRIFT spectra of HPMo/SBA-15 series (a), and HSiW/SBA-15 series (b), as function of metal loading wt%, pure HPAs and support are reported for comparison.	132
<b>Figure 3.38</b> – Stacked Raman spectra of HPMo/SBA-15 (a); and HSiW/SBA-15 (b).	133
<b>Figure 3.39</b> – Background subtracted Mo 3d XP spectra of HPMo/SBA-15 series (a); and ratio of integrated signal of interfacial to bulk Mo 3d species across the loading on SBA-15, and correlation between superficial and bulk Mo wt% (b).	134
<b>Figure 3.40</b> – Background subtracted W 4f XP spectra of HSiW/SBA-15 series (a); and ratio of integrated signal of interfacial to bulk W 4f species across the loading on SBA-15, and correlation between superficial and bulk W wt% (b).	135

#### ***Chapter 4 Alpha pinene isomerisation***

<b>Scheme 4.1</b> – Principal products of $\alpha$ -pinene isomerisation.	142
<b>Equation 4.1</b> – Equation used to calculate ethanol conversion % and products selectivity.	142

<b>Figure 4.1</b> – Influence of stirring rate on the $\alpha$ -pinene normalised initial rate over 3.2 wt% of HPW/SBA-15. Reaction conditions: 126 mmol of $\alpha$ -pinene, 0.2 cm <sup>3</sup> of tetradecane (as an internal standard), 60 °C, 0.1 g of catalyst.	143
<b>Figure 4.2</b> – $\alpha$ -Pinene isomerisation reaction profile for 9.0 wt% of bulk W on SBA-15. Reaction conditions: 126 mmol of $\alpha$ -pinene, 0.2 cm <sup>3</sup> of tetradecane (STD), 60 °C, 0.1 g of catalyst, 700 rpm of stirring rate	144
<b>Figure 4.3</b> – Effect of bulk W loading and silica supports on $\alpha$ -pinene isomerisation activity (a) and turnover frequencies (b). Reaction conditions: 126 mmol of $\alpha$ -pinene, 0.2 cm <sup>3</sup> of tetradecane (STD), 60 °C, 0.1 g of catalyst, 700 rpm of stirring rate.	145
<b>Scheme 4.2</b> – Dependence of $\alpha$ -pinene isomerisation reactivity on structure and loading of HPW supported on high surface area, mesoporous SBA-15 (left) and non-porous fumed silica (right).	146
<b>Figure 4.4</b> – Products selectivity ratio as function of W wt% supported on SBA-15. Reaction conditions: 126 mmol of $\alpha$ -pinene, 0.2 cm <sup>3</sup> of tetradecane (STD), 0.1 g of catalyst, at 60 °C, stirring rate 700 rpm (a). Dependence of monocyclic / polycyclic ratio to bulk W loading and silica supports (b).	147
<b>Figure 4.5</b> – Effect of bulk W loading and silica supports on $\alpha$ -pinene isomerisation activity (a) and turnover frequencies (b). Reaction conditions: 126 mmol of $\alpha$ -pinene, 0.2 cm <sup>3</sup> of tetradecane (STD), 30 °C, 0.1 g of catalyst, 700 rpm of stirring rate.	148
<b>Figure 4.6</b> – Dependence of monocyclic to polycyclic ratio to bulk W loading and silica supports.	149
<b>Figure 4.7</b> – $\alpha$ -Pinene isomerisation reaction profiles as function of time (min) depending on the heteropolyacid involved at 9 wt% of heteroatom supported on SBA-15 (a); and relative TOF (b). Reaction conditions: 126 mmol of $\alpha$ -pinene, 0.2 cm <sup>3</sup> of tetradecane (STD), 0.1 g of catalyst, at 60 °C, stirring rate 700 rpm.	151
<b>Figure 4.8</b> – Correlation between selectivity towards the two products families (monocyclics / polycyclic) and acid strength measured via n-propylamine chemisorption and TPD of common 9 wt% W (or Mo) loading on SBA-15.	152
<b>Scheme 4.3</b> – Acid catalysed routes to polycyclic versus monocyclic products from $\alpha$ -pinene.	153
<b>Table 4.1</b> – Conversion and yields obtained after 6 h of reaction employing 0.1 g of catalyst (16 wt% W/SBA-15), 126 mmol of reagent, 0.2 cm <sup>3</sup> of tetradecane (STD), at 60 °C, stirring rate 700 rpm.	154
<b>Scheme 4.4</b> – Proposed mechanism of the $\alpha$ -pinene isomerisation reaction.	156

## Chapter 5 Ethanol dehydration

- Equation 5.1** – Products formed by the direct dehydration of ethanol, with relative formation enthalpies at 25 °C [2]. 161
- Equation 5.2** – Equation used to calculate ethanol conversion % and products selectivity. 162
- Equation 5.3** – Space time yield equation where molPt are the moles of ethylene or diethyl ether formed per unit of time, MW is the molecular weight of the compound of interest, and Vcatalyst is the volume of the fixed bed reactor. 162
- Figure 5.1** – Influence of the mass catalyst on ethanol dehydration at 150 °C. Values were averaged after 90 min on stream. 163
- Figure 5.2** – Ethanol dehydration reaction profiles carried out with unsupported HPW at different temperatures: 150 °C (a) and 275 °C (b). 164
- Figure 5.3** – Influence of catalyst mass to volume ratio on ethanol conversion as function of temperature (a), and influence of temperature on ethylene selectivity (b). 165
- Figure 5.4** – Arrhenius Ea for ethanol dehydration reaction carried out on unsupported HPW. 166
- Figure 5.5** – Ethanol dehydration reaction profile carried out with unsupported HSiW (a) and unsupported HPMo (b). 167
- Figure 5.6** – Ethanol conversion and ethylene selectivity depending on the heteropolyacid used. 168
- Figure 5.7** – Ethylene selectivity dependence on the proton density and acid strength, determined via n-propylamine TPD of unsupported heteropolyacid, HPW (●), HSiW (▲) and HPMo (◆). 169
- Figure 5.8** – Ethanol dehydration dependence on reaction temperature employing unsupported HSiW (a) and HPMo (b). 170
- Figure 5.9** – Ethanol conversion and ethylene space time yields as function of time at 225 °C, employing HPW/Fumed silica (a, c), and HPW/SBA-15 (b, d). 171
- Figure 5.10** – Influence of bulk W loading on the conversion of ethanol for the two series, HPW/SBA-15 and HPW/Fumed silica. 172
- Figure 5.11** – Influence of bulk W loading on the selectivity towards diethyl ether (DEE) and ethylene for the two series, HPW/SBA-15 and HPW/Fumed silica. 173
- Figure 5.12** – Dependence of ethanol dehydration activity on bulk W loading and silica support. 174
- Figure 5.13** – Turnover frequencies for ethanol dehydration as function of bulk W loading for HPW/SBA-15 and HPW/Fumed silica. 175

<b>Figure 5.14</b> – Correlation between ethanol dehydration TOFs and water mass loss measured for unsupported and supported HPW on fumed silica and SBA-15.	176
<b>Figure 5.15</b> – Reaction profiles for fresh and recycled 38.2 wt% of bulk W loaded on SBA-15: ethanol conversion (a), diethyl ether (b) and ethylene (c) space time yield, and comparison of conversion and ethylene selectivity after each run (d).	177
<b>Figure 5.16</b> – Reaction profiles for fresh and recycled 38.2 wt% of bulk W loaded on SBA-15, employing a 2.9 M solution of water in ethanol as feed: ethanol conversion (a), and ethylene (b) and diethyl ether (c) space time yield, and comparison of conversion and ethylene selectivity after each run (d).	179
<b>Figure 5.17</b> – Reaction profiles for fresh and recycled 38.2 wt% of bulk W loaded on SBA-15, employing a 6.2 M solution of water in ethanol as feed: ethanol conversion (a), and ethylene (b) and diethyl ether (c) space time yield, and comparison of conversion and ethylene selectivity after each run (d).	180
<b>Figure 5.18</b> – Comparison between conversion (a) and ethylene selectivity (b) after each run for anhydrous ethanol (0 mol L <sup>-1</sup> ), 2.9 and 6.2 mol L <sup>-1</sup> of hydrous ethanol.	181
<b>Figure 5.19</b> – Influence of water content on the retainment of catalyst activity after three consecutive cycles.	182
<b>Figure 5.20</b> – Influence of temperature on selectivity toward ethylene and diethyl ether, for 38.2 wt% of bulk W loaded on SBA-15.	183
<b>Figure 5.21</b> – Influence of temperature on ethanol conversion for 38.2 wt% of bulk W loaded on SBA-15.	184
<b>Figure 5.22</b> – Temperature influence on ethylene and DEE space time yields employing 50 mg 38.2 wt% HPW/SBA-15 as function of time: diethyl ether space time yield (a) and ethylene space time yield (b).	185
<b>Figure 5.23</b> – Influence of temperature on ethanol activity (a), and catalyst deactivation rate (b).	186
<b>Figure 5.24</b> – CHNS elemental analysis (a) and TPO (b) obtained on spent catalyst (38.2 wt% HPW/SBA-15) at different reaction temperatures.	187
<b>Figure 5.25</b> – XRD pattern of fresh and spent catalyst at different reaction temperatures (a); HPW and WO <sub>3</sub> phase % calculated for each catalyst.	188
<b>Figure 5.26</b> – Ethanol dehydration carried out with water as co-feed, using 38.2 wt% of HPW/SBA-15 as catalyst; ethanol conversion (a), and space time yields of ethylene and DEE (b).	189
<b>Figure 5.27</b> – Catalyst deactivation rate employing a solution 6.2 M of water in ethanol (10% vol/vol).	190
<b>Figure 5.28</b> – Arrhenius E <sub>a</sub> for ethanol dehydration reaction over W loading 9.0 wt% on SBA-15.	191

**Figure 5.29** – Ethanol dehydration kinetic parameters attained at 225 °C, employing SBA-15 supported HPAs as function of time: conversion (a) and ethylene space time yield (b). 192

**Figure 5.30** – Ethylene selectivity and TOFs dependence on acid strength of SBA-15 supported heteropolyacid, 38.2 wt% HPW/SBA-15 (●), 30.9 wt% HSiW/SBA-15 (▲) and 32.3 wt% HPMo/SBA-15 (◆). 193

## **Chapter 6 Conclusions**

**Figure 6.1** – Dependence of Keggin units dispersion and/or agglomeration on loading and support architecture for HPW/SBA-15 series (left) and HPW/fumed silica series (right). 198

**Figure 6.2** – Turnover frequencies measured for (a)  $\alpha$ -pinene isomerisation reaction as a function of bulk W loadings and (b) ethanol dehydration reaction as a function of water mass loss, for both supported series. 199

**Figure 6.3** – Selectivity and turnover frequencies attained for SBA-15 supported HPAs in  $\alpha$ -pinene isomerisation reaction common 9 wt% of W (or Mo) (a); and (b) ethanol dehydration reaction for 38 wt% of W, 31 wt% of W, and 32 wt% of Mo, of SBA-15 supported HPW, HSiW and HPMo respectively. 200

**Table 6.1** – Costs evaluation for 1 kg of silica support. 201

**Table 6.2** – Costs evaluation for 1 kg of supported HPW catalysts based on the amount of product formation. 202

## **Appendix A**

**Figure 1** – Reaction profiles of  $\alpha$ -pinene isomerisation as function of time employing bulk W 3.2 wt% on SBA-15. 204

**Figure 2** – Reaction profiles of  $\alpha$ -pinene isomerisation as function of time and bulk W loadings over fumed silica (a), and SBA-15 (b). 204

**Figure 3** – Reaction profiles of  $\alpha$ -pinene isomerisation as function of time and bulk W loadings over fumed silica (a), and SBA-15 (a). 205

**Figure 4** – Reaction profiles of products yields of  $\alpha$ -pinene isomerisation as function of time for supported HPMo and HSiW on SBA-15 with 9 wt% of bulk metal loading. HPMo/SBA-15 (a), HSiW/SBA-15 (b). 206

**Figure 5** – Reaction profiles of  $\alpha$ -pinene isomerisation products as function of time employing 9.0 wt% of bulk W on SBA-15;  $\gamma$ -Terpinene (a), Limonene (b), Terpinolene (c),  $\beta$ -Pinene (d),  $\alpha$ -Terpinene (e), Camphene and p-Cymene (f). 206

<b>Figure 6</b> – Reaction profiles of $\beta$ -pinene isomerisation as function of time for supported HPAs on SBA-15 with 9 wt% of heteroatom.	207
<b>Scheme 1</b> – Reaction mechanism from isomerisation of $\alpha$ -pinene to the main products limonene and camphene.	207

### ***Appendix B***

<b>Figure 1</b> – Ethanol conversion as function of time at different temperatures range, using 50 (a), 100 (b) and 150 (c) of unsupported HPW.	208
<b>Figure 2</b> – Diethyl ether space time yield as function of time at different temperatures, using as catalyst 50 (a), 100 (b) and 150 (c) of unsupported HPW.	209
<b>Figure 3</b> – Ethylene space time yield as function of time at temperatures ranged 150-275 °C, using as catalyst 50 (a), 100 (b) and 150 (c) of unsupported HPW.	210
<b>Figure 4</b> – Ethanol dehydration reaction values obtained employing unsupported HSiW as function of time: conversion (a), diethyl ether space time yield (b) and ethylene space time yield (c).	211
<b>Figure 5</b> – Ethanol dehydration reaction values obtained employing unsupported HSiW as function of time: conversion (a), diethyl ether space time yield (b) and ethylene space time yield (c).	212
<b>Figure 6</b> – Diethyl ether space time yield as function of time at 225 °C, employing HPW/SBA-15(a), and HPW/Fumed silica.	213
<b>Figure 7</b> – Diethyl ether space time yield attained at 225 °C, employing SBA-15 supported HPAs as function of time.	213

# ***Chapter 1***

## ***Introduction***

## 1.1 Heterogeneous catalysis for Sustainable Chemistry

Over the past three decades, environmental protection and economical growth have been the driving forces for a great variety of research fields. In the chemical sector, an enormous number of studies have been addressed to replace waste-inefficient harmful/toxic historic processes, at both laboratory and industrial scale. In this scenario, catalysis and catalytic technologies play vital roles. Catalysts are used to increase reaction rate and product yields, thus are highly valuable in the chemical industry; today, 90% of all chemical processes employ catalysis in their production. In 2013, catalysts global market was valued US \$19.2 billion, and is expected to reach US \$24.1 billion by 2018, at a growing rate of 3.9%, estimated between 2012 and 2018 [1]. Catalysis is employed in multitude of different industrial sectors, such as petrochemical, chemical synthesis, polymers and environmental, with the latter rapidly growing worldwide, reaching more and more importance in years to come [1].

### 1.1.1 Green and sustainable chemistry

With growing concerns in relation to climate change, in conjunction with an increasing global population and associated demand for consumer goods, the fundamental requirements for modern chemicals is to be sustainable, i.e. to have green credentials including being biomass derived and produced/isolated via environmental acceptable processes.

The *Green Chemistry* concept was introduced in the early 90s, in order to produce safer chemicals and industrial processes, and was part of a US Pollution Prevention Act [2]. Through the years, notable agencies such as the Organisation for Economic Cooperation and Development (OECD) and the International Union of Pure and Applied Chemistry (IUPAC), both government-based and independent bodies, have collaborated in order to establish a new branch of greener chemicals, synthetic pathways and reaction conditions.

In 1998, Professor P. T. Anastas coined the 12 Principles of green chemistry, [3, 4], providing guidelines for the basis of chemical synthesis with reduced environmental impact, as shown in **Figure 1.1**. Starting from the first principle, waste prevention, catalysis is placed at the 9<sup>th</sup> position. Whilst the principle suggests using catalytic instead of stoichiometric reagents, employing catalysts that are able to increase the selectivity, reduce volumes, waste and reaction time, catalysis fits in also in the others, such as waste prevention, atom economy, reduction of derivatives and so on.

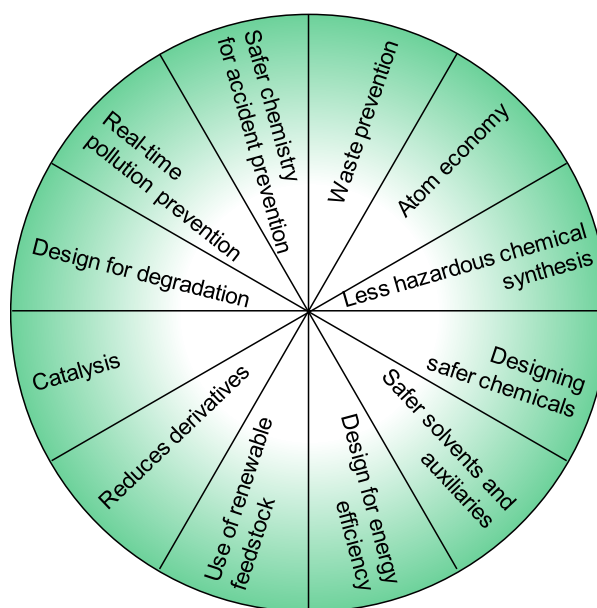


**Figure 1.1** – The 12 principles of green chemistry.

In 2000, IUPAC defined the term Green Chemistry as [5]:

*“the invention, design, and application of chemical products and processes to reduce or eliminate the use and generation of hazardous substances”.*

The term Sustainable Chemistry is based on the later definition of Brundtland Commission upon sustainable development as [6]:

*“development that meets the needs of the present generation without compromising the ability of future generation to meet their own needs”.*

Today the definition of sustainable has evolved from a synonym for green to a far more complicated definition including social, economic and ecological domains [7, 8]. Sustainability through chemistry has become a concept based on green chemistry and has expanded to a fast, flexible and eco-friendly vision, interlinked to pursuit the progress [9]. To reach this objective, industrial chemistry must find new radical approaches to fulfil these requirements:

- enhance the quality of products during their entire life cycle;
- resized and integrated processes (smaller volumes, multi-step reactions, catalytic reaction, efficient separation & storage);
- designing inherently safer processes;
- minimizing and substituting the quantity of hazardous material.

Sustainable chemistry includes several challenges, which cover more than one discipline; new legislations and government policies have been developed to fulfil social

needs of health and safety, whereas industries aimed to adapt and respect the new regulations and safety parameters.

The role of catalysis for sustainable energy requires improvement to three urgent catalytic transformations: from heavy fossil residues to fuels, from biomass to fuels and chemical building blocks, and photo/electro chemical conversion of CO<sub>2</sub> and water [10].

### 1.1.2 Principles of catalysis

The International Union of Pure and Applied Chemistry (IUPAC) defines in the second edition of the Gold Book, Compendium of Chemical Terminology a catalyst as [11]:

*“A substance that increases the rate of a reaction without modifying the overall standard Gibbs energy change in the reaction; the process is called catalysis”.*

In other words, a catalyst provides an alternative reaction path of the overall reaction mechanism, which possesses a lower activation energy barrier of the transition state. A catalyst influences only the kinetic rate at which the equilibrium is reached and not its thermodynamic constant [12].

Based on the number of phases involved in the system, catalysis can be divided in two sub-divisions: homogeneous and heterogeneous catalysis. Homogeneous catalysis occurs when catalyst and reagent are in the same unique phase, mainly liquid. Extensively investigated, homogeneous catalytic compounds, such as transition metal complexes, are potentially highly selective in a wide range of reactions with tunable properties, electronically and sterically, by varying the type of metal and/or ligands. Catalyst separation, via distillation or chemical extraction, and further product purification are the central problems of this category, complicating catalyst recyclability and increasing overall process cost and reducing environmentally sustainable [13-16]. Several old industrial plants are still operating with homogeneous catalytic systems in the liquid phase, as the Friedel-Craft aromatic substitution using aluminium chloride AlCl<sub>3</sub>, or the Monsanto Process for the production of acetic acid (AA) where transition metal Rh salts, in combination with I<sup>-</sup>, convert CO and methanol. Homogeneous catalysed gas-phase reactions take place mostly in the stratosphere when photo-degraded chlorofluorocarbons (CFC) catalyse the conversion of ozone to oxygen.

Heterogeneous catalysis takes place between two or more phases, such as solid catalysts and liquid/gas reagents. Solid catalysts are easily separated from the reaction mixture, via filtration, centrifugation or decantation, reducing both economic and environmental impact. Catalyst design is crucial and requires the combination of different properties necessary for the industrial application, such as activity, selectivity, lifetime,

deactivation and toxicity [17]. The chemistry behind heterogeneous catalytic processes is still not fully understood and surface-sensitive and operando *in situ* time resolved analytical instrumentations are fundamental to shed insight into surface catalytic phenomena. Temperature, pressure, catalyst architecture, reagent concentration and agitation of reactant mixture have a great impact on the chemical potential of heterogeneous reactions, enhancing or weakening system efficiency [18]. Examples of important heterogeneous reactions are ammonia synthesis using  $N_2$  and  $H_2$  over iron oxides and alumina (Haber-Bosch Process [19]), olefin polymerisation using  $TiCl_3$  on  $MgCl_2$  (Zigler-Natta type catalysts [20]), hydrodesulfurization (HDS) of petroleum via Mo-Co on alumina catalyst and lots of other paramount catalytic processes.

Within heterogeneous catalysts, it is possible to identify several categories depending on their properties and the types of reactions in which they are employed; this include acid, base, redox, cascade/multicomponent etc. Acid/base catalysis are founded on Brønsted and Lewis concepts, and are widely applied in both laboratory and industrial scale. Reactions included in this category are isomerisation, dehydration, alkylation, etherification, cracking, condensation, hydration, oligomerization and esterification. Cascade type reactions are generally used for fine chemicals and are systems whereby products from the first reaction (1), formed over one active sites, desorb to react over another active site, forming product (2). The catalytic system can be comprised of one single material or multiple different catalytic components, and being a sequence of reactions with no physical separation between the production of product (1) and (2), allowing for the reduction of waste, solvents and reagents volumes, is referred to as one-pot reactions. This type of approach is extensively used in industrial processes, as, for example, in the paper, cosmetic and polymer industry.

### 1.1.3 Heterogeneous acid catalysts

Solid acids can be classified based on the physical properties with examples including zeolites and zeotypes, mesoporous materials, mixed oxides, heteropolyacids and organic-inorganic materials [21].

- *Zeolites* are crystalline aluminosilicate compounds, with a well-defined structure and pores ranging from 0.3 to 1.4 nm. The typical crystalline zeolite is formed of corner-sharing  $SiO_4$  and  $AlO_4$  with different Si:Al ratios; when Si or Al are substituted with other transition elements, as Ga, Fe, Ge, Ti, V, Cr, Mn and Co, they are referred as zeotypes. The substitution of the  $Si^{4+}$  with the  $Al^{3+}$  (or other trivalent ions) generates Brønsted acidity in these materials, leaving a negatively charged oxygen that is charge-balanced either by protons or by a counter ion, such as  $Na^+$ ,  $K^+$ ,  $Ca^{2+}$ ,  $Mg^{2+}$  or  $NH_4^+$ . Upon thermal

treatment, dehydroxylation occurs, leaving Lewis acid sites on the surface. Although the number of possible zeolites and zeotypes is tremendously high, only a few are actually applied at industrial scale, as ZSM-5 (silicalite), FAU (faujasite), MOR (mordenite), BETA (beta) and LTA (Linde type A, or zeolite A) [22].

- *Mesoporous molecular sieves* were first introduced to expand the potential of zeolites, to process petroleum derivatives with larger molecular size. These materials have pores (channels) sized between 2 and 50 nm, can be amorphous or crystalline in nature, and generally, possess weaker acidity than zeolites. Mesoporous aluminosilicates, mesoporous silicas including SBA-15 and MCM-41, are part of this wide category. Improved properties to enhance catalytic performances can be achieved by post-synthesis treatments (i.e. impregnation and grafting) [21, 22].

- *Mixed oxides* are oxides that possess more than one cationic species or a single cation with different oxidation states. These materials have a great variety of possible structures, pores sizes, and functional groups, and can be either crystalline or amorphous. Important examples widely studied are perovskites and perovskite-like compounds ( $\text{CaTiO}_3$ ), garnets and derivatives ( $\text{X}^{2+}_3\text{Y}^{3+}_2(\text{SiO}_4)_3$ ), magnetite with  $\text{Fe}^{3+}$  and  $\text{Fe}^{2+}$ , and also sulfated and phosphated zirconia extensively applied in acid catalysed reactions [23].

- *Heteropolyacids* are another important class of mixed oxides, used as acid catalysts, formed of polyoxometallate anions. Their properties and application are discussed herein in the following paragraphs.

- *Organic-inorganic composites* are ordered inorganic structures functionalised with organic groups by grafting or co-precipitation. Periodic mesoporous organosilicas (PMOs) are part of this category, with alkyl-sulfonic groups one example that can be incorporated or surface bonded to the silica matrix. The organic functional groups can be classed as either reactive, and participate in the reaction cycle, or passive, enhancing catalysts resistance to thermal and chemical degradation.

#### 1.1.4 Catalyst deactivation

Catalyst deactivation is an important concern when designing heterogeneous catalysts. Causes of deactivation are basically due to thermal, chemical and mechanical reasons, and lead to a decrease in catalytic activity and/or selectivity, during the reaction time. Harsh reaction conditions, reactant (or product) composition, or the catalyst instability are the major factors. The mechanisms whereby catalyst deactivation occurs can be classified into different types: poisoning, fouling, thermal degradation, volatilisation of

active phase and vapour/liquid-solid reactions (leaching), and attrition/crushing [24], as reported in **Figure 1.2**.



**Figure 1.2** – Major types of deactivation in heterogeneous catalysis [25].

- Catalyst poisoning is due to strong chemisorption of reactants, products and impurities on active sites. As a result, reactive sites are blocked and, sometimes, also the neighbouring sites exhibit a different electronic state on the surface. Evaluation of the chemisorption energy of certain compounds on the catalyst surface gives a brief indication of whether or not a compound is a potential poison. In the case that chemisorption is weak, reactivation of the catalyst is possible. Common poisoning agents are: toxic heavy metals and ions (As, Pb, Hg, Zn, Cu and Fe) because they are able to interact with free orbitals and may form alloys; multiple bonded molecules as unsaturated hydrocarbons, (NO<sub>x</sub> and CO), being able to adsorb through multiple bonds. For instance, CO adsorbs strongly on Ni and Co, whereas catalysts containing alkali metals adsorb easily CO<sub>2</sub> and SO<sub>x</sub> compounds; amines and ammonia are well-known poisons for acidic catalysts. Poisoning can be selective or non-selective on the active site; as a common rule, the deactivation process is non-selective if the loss of activity is proportional to the concentration of the poison [24].

- Catalyst fouling occurs with deposition of carbonaceous species on the surface of the catalyst, leading to pore blockage. These species can be identified as carbon or coke; the latter is derived from condensation (which may lead to polymerisation) of hydrocarbons; while the former is formed by the disproportionation of CO [24]. Olefin and aromatics are considered possible coke precursors because, under certain conditions, they can react on catalyst acid sites leading to chain and cycloaddition reactions resulting in the formation of heavy hydrocarbons and polynuclear aromatics [26].

- Crystallite growth of the active phase (sintering), support collapse, and phase change (a catalytically active phase transforms to a non-catalytically active one) are all effects of catalyst thermal deactivation. Sintering is the process whereby either the crystallites or the atoms (in extreme cases vapours) migrate on the support surface and eventually collide and coalesce, to form bigger agglomerates. The process is reversible under specific conditions,  $O_2$  or  $Cl_2$ , leading to redispersion [24]. The use of textural and physical promoters can inhibit the sintering process.

- Volatilisation of active components leads also to catalyst deactivation and occurs when gaseous reagents react with the catalyst to form volatile compounds. Common types of products formed by this process are metal carbonyls, oxides and halides, e.g. Ru volatilises in the presence of  $O_2$  at high temperatures to  $RuO_3$ ,  $Ni(CO)_4$  can be formed between (0-300 °C) in CO rich environments, while  $PtCl_4$  is formed with chlorine traces in the feed [24]. Some compounds can also be lost because the reaction temperature is close to their sublimation point, as in the case of  $P_2O_5$ ,  $MoO_3$ , and  $Bi_2O_3$ .

- Finally, catalysts can undergo mechanical failure due to the crushing of pellets or granules of the catalyst during the loading into the reactor, producing fine powders, attrition between catalytic pellets and granules which lead to a size reduction and breakage and erosion of the catalyst due to high fluid velocity.

The understanding of deactivation mechanisms, by employing in-situ surface techniques, operando studies and computation modelling, can provide powerful insight into the design of new heterogeneous catalyst and optimising of a catalytic process.

## 1.2 Silica-based supports

### 1.2.1 The role of support in catalysis

Depending on the chemical reaction and the economical requirements of the industrial process, it is possible to distinguish three different structural types of solid catalyst: *bulk catalysts*, *supported catalysts*, and *coated catalysts*. In catalysis, bulk materials are carrier-free entirely catalytic solids; supported catalysts are materials in which the active phase is widely dispersed on a highly porous material (either inert or catalytically active). Coated catalysts, on the other hand, are formed by a thin layer of the active phase, generally 100  $\mu m$ , which covers the surface of a non-porous support [27].

Supported catalysts are widely used at both industrial and laboratory scale. The active phase can be either supported on a pre-shaped carrier or co-precipitated during the support synthesis. The most common preparation methods are impregnation, ion-exchange, adsorption and deposition/precipitation. Impregnation is a very well-

established technique, whereby a certain volume of liquid (aqueous or organic), containing the active phase or its precursor, wet the support surface and is subsequently removed by drying. *Wet impregnation* (WI) and *incipient wet impregnation* (IWI) are two sub-categories of this methodology, where the former occurs with an excess of solvent, whereas in the latter, the volume of solvent used is enough to fill support pores [17]. The procedure is based on the fact that the oxide support surfaces possess hydroxyl groups which are able to anchor the active phase by hydrogen bond interaction or dehydroxylation reactions forming a covalent bond with water production [28].

The type of support is usually chosen to fulfil economical and technical requirements; generally, must be preferably both highly thermostable, with considerable mechanical strength, and chemically suitable in the reaction mixture. Silica,  $\gamma$ -alumina and activated carbon are the most frequently used supports due to the low bulk density, thermal stability and overall production costs [27]. Other common supports are zeolites, ceria, zirconia, titania, magnesia, clays and hydrotalcite, which are also important due to their chemical nature, acidity/basicity, physical properties and texture. Additionally, interactions between support and active phase are also a critical point to be considered (too strong or too weak) because of their possible influence on the catalyst activity [29]. In the case of heteropolyacids (HPA), it is reported that when supported their acidity decreases in the following order depending on the type of support:  $\text{SiO}_2 > \alpha\text{-Al}_2\text{O}_3 >$  carbon [30]. In addition, when supported on a basic solid material such as MgO, HPA decomposition occurs due to the acid-base reaction between support and active phase [31, 32].

Silica supports are widely chosen because of displays great properties as support, such as excellent both chemical and thermal stability, size ranged porosity, thus tunable accessibility, and the ease of organic groups to robustly anchor onto the surface to provide catalytic centres.

### 1.2.2 Generic properties

Silica is a simple binary oxide commonly used in catalysis that can be arranged in a variety of structures. The silicate tetrahedra,  $\text{SiO}_4^{4-}$ , is the anionic elementary compound, which, if connected with other tetrahedra, results to the net chemical formula of  $\text{SiO}_2$ , where each O atom bridges two Si atoms with covalent bonds. At room temperature, hydrated silicas exhibit silanol groups on the surface,  $\equiv\text{Si-OH}$ , which are distinguished in isolated, germinal and vicinal hydroxyl groups (Figure 1.3). Under specific conditions of pressure and temperature, the silanols condense to form water and siloxane links (Si-O-Si); the total removal of hydroxyl groups occurs at 800 °C. Although silica's surface

exhibits negligible Brønsted acidity, it is able to generate H-bond interactions, making it a great candidate as a support.

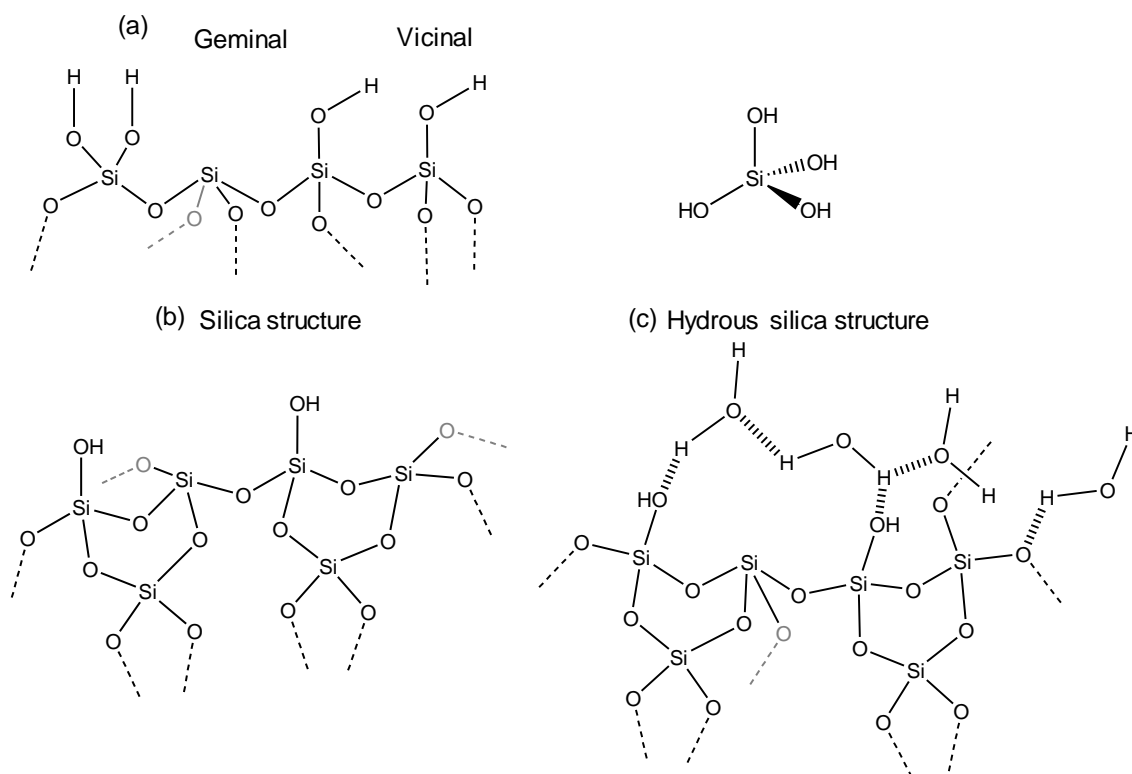


**Figure 1.3** – Silica structure with relative hydroxyl groups, in its anhydrous and hydrated form.

### 1.2.3 Ordered mesoporous silica

Over the last few decades, the capability of controlling the architecture of materials (as surface area, defined porosity and texture) has received significant attention due to the wide range of possible applications, such as in catalysis, photonics, drug delivery, sensors, adsorption/separation and nanotechnology [33].

Mesoporous silicates, with pore sizes ranging from 2 to 50 nm, have an important role in the family of porous materials. Controlled mesoporosity is introduced by using supramolecular templates, or structure-directing agents (SDA), which, during the condensation of the silica precursor, help the formation of the mesostructured network. Templates can be divided in *soft templates*, as surfactants and polymers, or *hard templates*, such as carbonates, carbon and metal oxides; after the synthesis, they can be easily removed via dissolution at certain pH, solvent extraction, or burned-off. The resulting material exhibit a structure that replicates the SDA assembly, with a narrow pore size distribution, high surface area, and tunable pore sizes depending on pH, temperature and template type. The first reported ordered mesoporous material was

published in 1971 [34], but it was not until 1992 that this new class of materials opened up a whole field of research, and a cationic surfactant was used for the synthesis of MCM-41, which stands for Mobil Composition of Matter No.41 [35-37].

Since then, a tremendous number of mesoporous materials have been synthesised by varying the reaction conditions. In the SBA-family, for which the synthetic pathway uses non-ionic templates at strong acid conditions, SBA-15 is the most popular mesoporous material used as support for a huge variety of catalytic applications. SBA-15 is highly ordered, with two-dimensional hexagonal mesostructure (space group  $P6mm$ ), synthesised in acid media (pH  $\sim 1$ ) using a triblock copolymer, as non-ionic structure driving agent [38]. Working at pH  $> 2$ , neither the silica-gel nor the precipitation of precursor occurs, whereas at neutral pH  $\sim 7$ , only disordered and amorphous silica is obtained. Non-ionic surfactants are preferable because of their lower toxicity, biodegradability and wide range of assembly geometries [33], an example of this category are the amphiphilic triblock copolymers, which allows for thick silica walls making the material more thermostable.

Block copolymers are formed by two distinct parts: one hydrophilic and the other hydrophobic and their ratio modifies the micelles array, effecting pore shape and architecture [39]. A larger hydrophilic moiety results in spherical micelles, as the hydrophobic region would be fully encapsulated; in the opposite case, disc-shaped micelles would aggregate forming rods whereby the core is hydrophobic and the corona hydrophilic. P123 is commonly used in the synthesis of SBA-15, and its formula is  $(PEO)_{20}-(PPO)_{70}-(PEO)_{20}$ , where PEO is poly(ethylene oxide) and PPO is poly(propylene oxide). In the aqueous solution of water-soluble surfactant, the hydrophobic PPO dwell in the micelle core, while the hydrophilic PEO lies in the corona, as depicted in **Figure 1.4**.

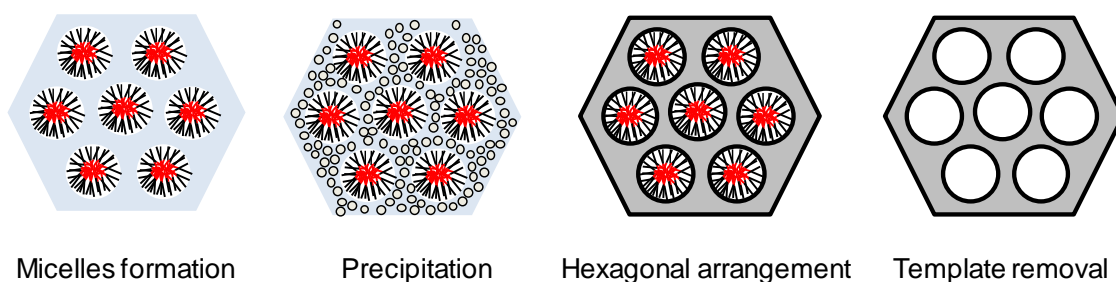
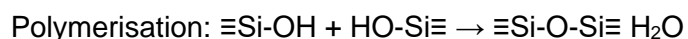


**Figure 1.4** – Schematic stepwise synthesis of mesoporous materials.

During the reaction the inorganic precursor, generally tetraethyl orthosilicate, TEOS, hydrolyses releasing ethanol to further polymerise:





The hydrolysis rate changes depending on the nature of the silica precursor, slowing down or accelerating the synthesis. The optimal reaction temperature is chosen based on the critical micellar temperature (CMT) and cloud point (CP) [40]. The former refers to the lowest temperature at which surfactants form micelles, and the latter indicates at what temperature starts the phase-separation and the micellar solution becomes cloudy. Through the years, several studies have been made to understand the kinetics of the process and the mechanism of the silica mesostructure formation [36, 41-45]. Flodström et al. [46, 47] investigated on the mechanism that occurs when an amphiphilic structure agent, P123, is used for the synthesis of SBA-15. A self-assembly mechanism is proposed, whereby the kinetics of silica polymerisation matches the kinetics of micelles aggregation. Silica hydrolysis followed by polymerisation generate attractive forces between micelles, which eventually coalesce forming cylindrical aggregates defining the silica 2D hexagonal pattern [46].

After the precipitation, hydrothermal treatment, usually between 80–150 °C, facilitates the reorganisation, growth and crystallisation of the mesostructure; in this range, higher temperatures induce micelle expansion resulting in a larger pore diameter of the final material. For temperatures >150 °C, destruction of the micelles array and surfactant decomposition is observed. Calcination is the most common method to remove the SDA using a slow ramp rate to avoid damaging the mesoporous network architecture.

### 1.3 Heteropolyacids

In the great variety of mixed oxides, the most commonly studied are double oxides, such as perovskite-like structures ( $\text{ABO}_3$ , as  $\text{CaTiO}_3$ ), and heteropolyacids (HPA), called also polyoxometalates. HPAs offer an environmentally friendly solution for a wide range of reactions both in homogeneous and in heterogeneous catalysis [48-55]. Their structure is the result of aqueous condensation of more than two oxoanions of high valent transition metals (M) as  $\text{W}^{6+}$ ,  $\text{Mo}^{6+}$ ,  $\text{V}^{5+}$  and  $\text{Nb}^{5+}$  called *addenda atoms*, in addition to a *heteroatom* (X), or central atom, which coordinates with O, ranging between 4 and 12 depending on the coordination number. Several structures are possible by varying the number of atoms involved; the foremost studied is the Keggin structure where one heteroatom occupies a central position in the form of a tetrahedron,  $\text{XO}_4$ , while surrounded by 12  $\text{MO}_6$ . These species are arranged in 4 triplets,  $\text{M}_3\text{O}_{13}$ , where each triplet shares an oxygen atom with the central atom [56], having as general formula  $\text{H}_n(\text{XM}_{12}\text{O}_{40})^{n-1}$ , as reported in **Figure 1.5**. Heteropolyacids salts are obtained when cations replace at least one of the  $\text{H}^+$  balancing the charge of the polyanion. Due to the

tunable structural properties, chemical factors and oxidizing ability, HPAs and their salts are widely used as solid catalysts, in their bulk form or supported, for acid catalysis or catalytic oxidation. Herein, the acid properties and catalysis will be extensively discussed.



**Figure 1.5** – Phosphotungstic acid Keggin structure.

### 1.3.1 Structure of solid HPA

The structure of HPA was first studied in the early 70s. As largely accepted, HPAs possess three substructures called *primary*, *secondary* and *tertiary* structures (**Figure 1.6**). The heteropolyanion alone defines the *primary* structure without counter cation or protons; the charge balanced single unit cell identifies the *secondary* structure as for example a typical Keggin unit, while agglomeration of multiple units into a solid architecture represent the *tertiary* structure. Bulk HPAs exhibit very low surface area, about  $10 \text{ m}^2 \text{ g}^{-1}$  and no porosity. However, when HPA salts are formed by large cations with low valency as  $\text{Cs}^+$ ,  $\text{K}^+$  and  $\text{NH}_4^+$ , higher values of surface area,  $50\text{-}100 \text{ m}^2 \text{ g}^{-1}$ , are observed. The micro- and mesoporosity of these materials result from *intercrystalline* voids and not *intracrystalline* porosity, as proved by Okuhara et al. [53] via porosimetry and TEM analysis. Understanding the hierarchical structure of HPAs and their salts is crucial to understand their applicability in catalysis.

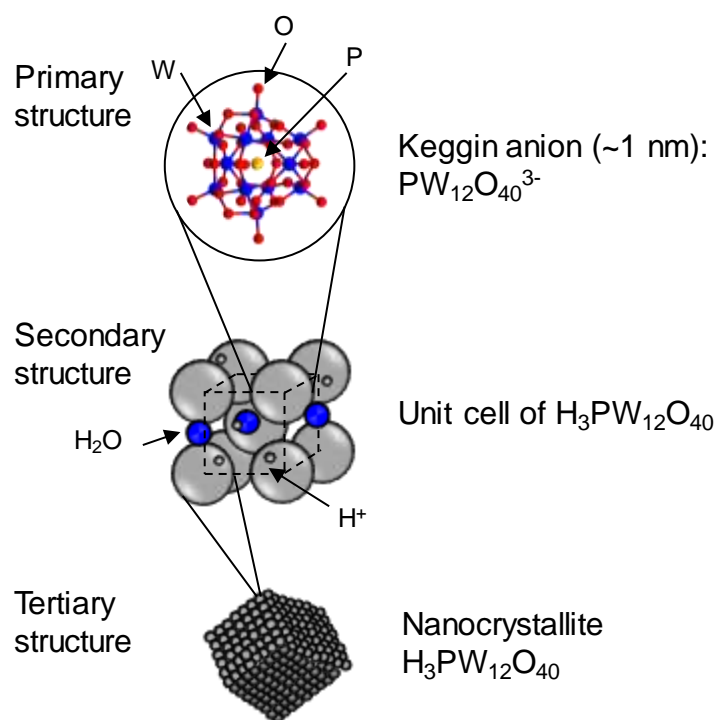


**Figure 1.6** – Hierarchical structure of phosphotungstic acid in the solid state [56].

### 1.3.2 Types of reaction: surface and bulk

Misono et al. [56] defined the catalytic activity of HPA driven by two different types of reaction, as reported in **Figure 1.7**, where reagent (R) and products (P) interact either at the surface or penetrate into the 3D bulk. The former represents the common reaction process in a heterogeneous system, where the catalysis occurs on the external surface of the solid, and the reactant is a nonpolar molecule that only reacts with the external acid protons. Reaction rates are governed by catalyst surface area and proton accessibility to the apolar substrate. The latter bulk catalytic mechanism occurs within the tertiary structure, in which the reactant diffuses, resulting in expanded interpolyanion distance, and occurs when the reactants are polar. Once formed, the products diffuse back to the external surface and into the reactant phase (gas or liquid). Furthermore, this bulk-type catalytic mechanism can be divided into two sub-categories: *pseudoliquid* and redox catalysis. *Pseudoliquid* catalysis is observed for acid catalysed reactions, with protons from the bulk being active species. The denomination of *pseudoliquid* arises from the fact that polar molecules, such as water, alcohols and small amines are capable of diffusing into the bulk HPA structure, creating a concentrated reaction solution where conversion takes place [57]. Redox processes are found for oxidation reactions, in which protons and electrons diffused rapidly within the bulk.

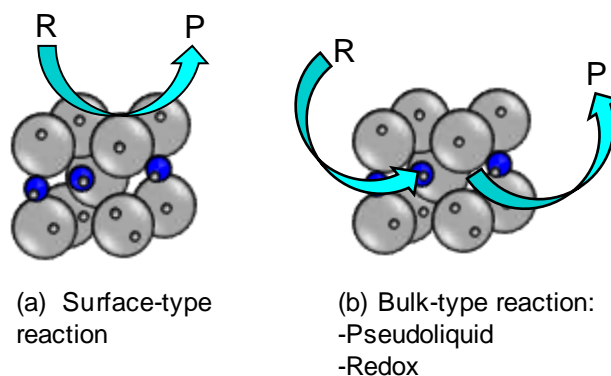


**Figure 1.7** – Types of catalysis for heteropolyacids, where the K.U. are depicted in grey, with an arbitrary number of hydrogens (white) and water molecules (blue), where R stands for reagent and P product.

### 1.3.3 Generic properties

Heteropolyacids are strong Brønsted solid acids, reported to be stronger than common inorganic acids such as HCl, H<sub>2</sub>SO<sub>4</sub>, HBr and HClO<sub>4</sub>, as shown in **Table 1.1** [58].

**Table 1.1** – pKa values for various heteropolyacids and other mineral acids in acetic acid solutions [59, 60]

Acid	pKa
H <sub>3</sub> PW <sub>12</sub> O <sub>40</sub>	4.7
H <sub>4</sub> SiW <sub>12</sub> O <sub>40</sub>	4.7
H <sub>3</sub> PMo <sub>12</sub> O <sub>40</sub>	4.8
CF <sub>3</sub> SO <sub>3</sub> H	5.0
HClO <sub>4</sub>	4.9
HBr	5.6
H <sub>2</sub> SO <sub>4</sub>	7.0
HCl	8.4

Phosphotungstic acid (HPW), with the formula H<sub>3</sub>PW<sub>12</sub>O<sub>40</sub>, is one example of a Keggin type heteropolyacid, which possess three acidic protons; similar Keggin HPAs are H<sub>4</sub>SiW<sub>12</sub>O<sub>40</sub>, H<sub>3</sub>PMo<sub>12</sub>O<sub>40</sub>, H<sub>4</sub>SiMo<sub>12</sub>O<sub>40</sub>. In aqueous media, the acid is fully dissociated, whilst in other solvents, such as acetone, acetonitrile, ethanol are more stable and pKas are measurable [58-60]. The strong acidity of HPAs arises from their ability to delocalise the negative charge (-3) of the heteropolyanion, over 40 oxygen atoms. The Keggin structure is considered the most stable of all possible HPAs structures. The nature of the addenda- and central-atom play a crucial role determining the acid strength and the redox properties; as general rule for solid HPAs is that W-based materials are stronger

acids than Mo-based ones, as elucidated from ammonia adsorption calorimetry [58, 61]. Changing the central atom also leads to differences into solid acidity, with acidity increasing with the increase of central atom oxidation state, following the order:  $P^{5+} > Si^{4+} \sim Ge^{4+} > B^{3+} > Co^{2+}$  [58, 62, 63]. The acid strength of supported HPAs changes with support and follows the order:  $SiO_2 > Al_2O_3 > \text{carbon}$ , which suggests that the greater interaction with the support results in reduced retainment of the bulk acid strength. Understanding proton mobility, their location, and thus their interaction with the polyanion is challenging and different techniques have been applied to gain a greater understanding, examples include IR [64], LCAO-Mo calculation [65], DFT quantum chemical calculation [66], SEDOR NMR [67],  $^{31}P$ ,  $^1H$  and  $^{17}O$  magic-angle spinning NMR [52, 68, 69]. **Figure 1.8** shows a simplified *tertiary* structure of four Keggin units, wherein H atoms are displayed either as free protons or the hydronium ion  $H_3O^+$ . In the former, protons can coordinate to bridging oxygens, known as  $O_b$ , also referred to as *core* ( $O_c$ ) and *edge* ( $O_e$ ), depending on the link being either is M-O-X or M-O-M respectively, or to terminal oxygen atoms,  $O_t$  in the case of M=O. In the latter,  $H^+$  exist as protonated water monomers  $H_3O^+$  and/or dimers  $H_5O_2^+$  situated between the polyanions and functioning as a bridge between two or more *primary* structures.

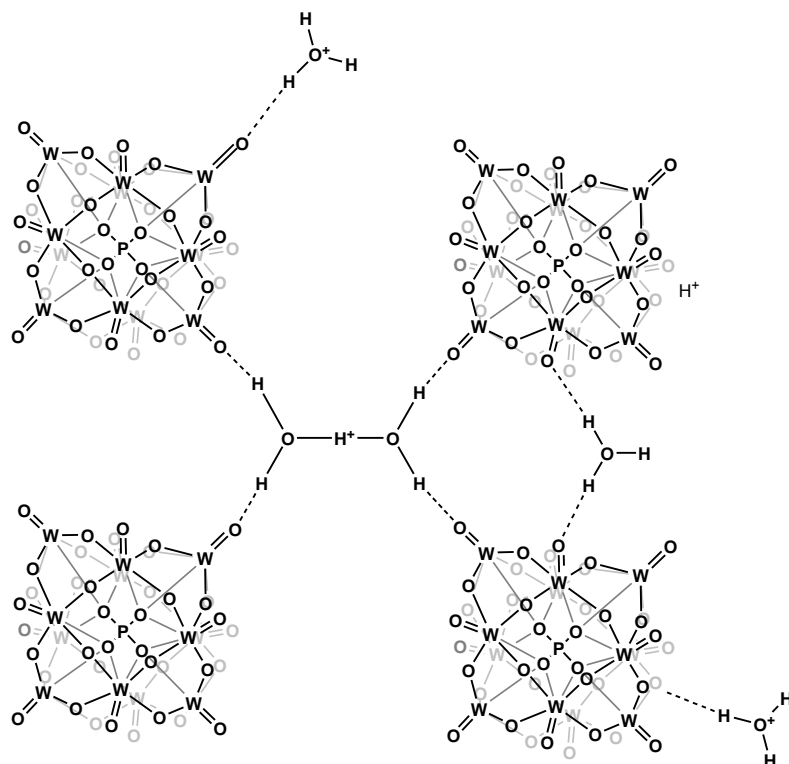


**Figure 1.8** – Tertiary structure of hydrated phosphotungstic acid.

Uchida et al.[70] studied the influence of the HPW hydration on the surface, and the species present,  $H_3O^+$  or  $H_5O_2^+$  by MAS-NMR analysis, and observed that the formation of aqueous dimers are prevalent when the number of water molecules per polyanion is

greater than 4. Water molecules cover significant importance in proton mobility, facilitating the migration of  $H^+$  between neighbouring HPW clusters.

The thermal stability of HPA varies dramatically depending on the type of HPA, some are highly stable and can carry out reaction at high temperatures in the vapour-phase, while others decompose easily under mild conditions and are not suited for catalytic purposes [71]. Kozhevnikov et al. [49] reported that thermal stability can be improved with the formulation of oxide composites of HPAs with zirconia or niobia, although this is at the detriment of acid strength. Such procedures calcine the oxides composite at temperatures higher than HPAs decomposition ( $> 350\text{ }^\circ\text{C}$ ), aiming to form HPAs fragments linked to niobia or zirconia, which eventually exhibit both Brønsted and Lewis acidity.

### 1.3.4 Applications

Heteropolyacids and their derivatives, at both laboratory and industrial scale, have been shown to be capable to catalyse a vast array of reactions [52, 53, 71-74], with examples of some of the more common applications including; paraffin and aromatics alkylation, Friedel Crafts or acylation of benzoyl chloride with *p*-xylene [75], trans alkylation of phenols to prepare antioxidant compounds [76-78], esterification reactions for biodiesel production [79-83], alcohol oxidation [84], and isomerisation reaction of terpenes [85-88]. In addition, the catalytic dehydration of alcohols has also been investigated for  $C_1$ - $C_6$  alcohols, in both liquid and gas phase. Liquid phase oxidation reactions have also been carried out with supported heteropolyacids, in their HPW form or modified with metal ions [89]. Epoxidation of cyclic alkenes, over HPW and HSiW on MCM-41, with  $H_2O_2$  in *t*-butanol at  $80\text{ }^\circ\text{C}$  [90], and the oxidation of benzenethiol to the sulphonic acid, employing HPW and  $H_2O_2$  are also known [91, 92]. Water-tolerant HPA systems have been developed to facilitate their application in aqueous reaction media, through the introduction of  $Cs^+$  as counter cation replacing  $H^+$ . Water-tolerant HPAs have been applied in sugar dehydration, of glucose and fructose, to obtain high-value compounds such as 5-hydroxymethylfurfural (HMF) [93]. Combination of noble metals and heteropolyacids have been investigated as bifunctional catalysts, two examples are the commercialised Pd-HPA system used for the two-steps hydration-oxidation reactions from ethylene to acetic acid [94], and Pt- $Cs_{2.5}$ HPW for the isomerisation reactions of *n*-butane whereby the noble metal prevent catalysts deactivation. The proposed reaction mechanism includes a (i) dehydrogenation on metal sites of butane to butene, (ii) an acid-catalysed isomerisation of butenes to iso-butylene and (iii) hydrogenation on the metal sites [95]. Glycerol oxidative-dehydration to acrylic acid is catalysed by vanadium

substituted CsHPW and CsHPMo, which works also as a bifunctional catalyst, with the first step being the alcohol dehydration over the acid site to acrolein and the second step the oxidation of acrolein to acrylic acid [96].

HPAs have been utilised as photocatalysts in both the homogeneous [97, 98] and heterogeneous catalytic splitting of water, the reduction of metal salts for the preparation of nanoclusters, and the degradation of organic compounds for water waste treatment [99, 100]. HPAs have also been employed as an additive in fuel cells to enhance proton conductivity and therefore the overall cell performances, through either immobilisation at the electrodes or incorporation in the ion exchange membrane [101].

## **1.4 $\alpha$ -Pinene isomerisation**

### **1.4.1 Introduction**

The isomerisation of  $\alpha$ -pinene is an important chemical reaction for the green synthesis of limonene, camphene and other key compounds in the perfumery, pharmaceutical, alimentary and fine chemicals industry. In nature, pinene is found in the volatile fraction of resins of pine trees or other plants part of the *Coniferae* family. The non-volatile resin component, called rosin, is also used for several applications. Industrially, pinenes,  $\alpha$ - and  $\beta$ -, are the major components of crude turpentine, extracted from wood, and by product of the forestry and manufacturing industry. Turpentine is a potential bio-source of green chemicals, capable of fulfilling the ideal principles of a sustainable biorefinery resulting in the environmentally and economically viable production of fine chemicals.

### **1.4.2 Sustainable chemicals from Turpentine**

Turpentine is a mixture of oleoresins obtained from trees, predominantly terpene-based compounds, isomers of  $C_{10}H_{16}$ , and its production reaches 350000 ton/annum [102]. The flammable composition can be used pure, as an industrial solvent, or as a source of chemicals for organic synthesis, production of drugs, pesticides, insecticides, and fuel additives [103, 104]. To obtain turpentine, wood residues, wood chips and logs, must be transformed into a pulp via mechanical or chemical processes.

- The mechanical pulping separates the wood fibres through the collapse of the structure by mechanical grinding. The two-common process are known as: the stone ground wood process (SGW) also called pressurised ground wood process (PGW), where wood and water pass through a rotating grinder stone made of silicon carbide or aluminium oxide grits; and the refiner mechanical pulping (RMP), where the pulp is produced from wood passing between grooved discs. Additionally, processes soften the

wood before the mechanical grinding using steam or chemical treatments, known as thermomechanical (TMP) and chemi-thermo mechanical pulping process (CTMP). High-quality turpentine is obtained as a by-product during the wood softening process, through steam distillation [105].

- In contrast, chemical pulping processes cook the wood residues in an aqueous solution of chemicals which separate the fibres and extract the cellulose. The pulping chemicals can be acidic, alkaline and neutral. The Kraft process is the most widely used and accounts for the 80% of the US pulp manufacturing [106]; additionally, acid sulfite and neutral sulphite semi-chemical processes are also used. In the Kraft process, the pulping chemicals are sodium hydroxide and sodium sulfide, also called white liquor. During the process, volatiles compounds are formed and condensed, with the collected mixture being the sulphate turpentine and the remaining pulp further purified and processed [107]. Turpentine is obtained from desulfurisation of crude sulfate turpentine (CST), the major by-product of the Kraft process and contains from 1 to 6 wt% of sulphur [108]. Unpurified CST has been evaluated as a potential motor fuel, but corrosion and contamination prevented its application. Desulfurisation of CST can be achieved using heterogeneous catalysis, for example supported  $\text{CoO}/\text{MoO}_3$  and  $\text{NiO}/\text{MoO}_3$  on  $\text{Al}_2\text{O}_3$  materials [108, 109].

Comparison of the two methods to obtain turpentine, mechanical and chemical, reveals that the Kraft process (chemical) is more efficient, producing up to 16 kg of turpentine per ton of pulp, while the thermomechanical reaches only 0.3 kg/ton [110]. Energy and waste calculation revealed that the chemical treatment generates enormous volumes of toxic waste compared to the mechanical, suggesting that the former better fulfils the environmental requirements of green and sustainable engineering. The market value of crude sulphate turpentine was valued in 2015 at USD 213.87 million and is supposed to reach USD 279.5 million by 2022, with an annual growth rate of 4.10% [111]

#### **1.4.3 $\alpha$ -Pinene market and derivatives**

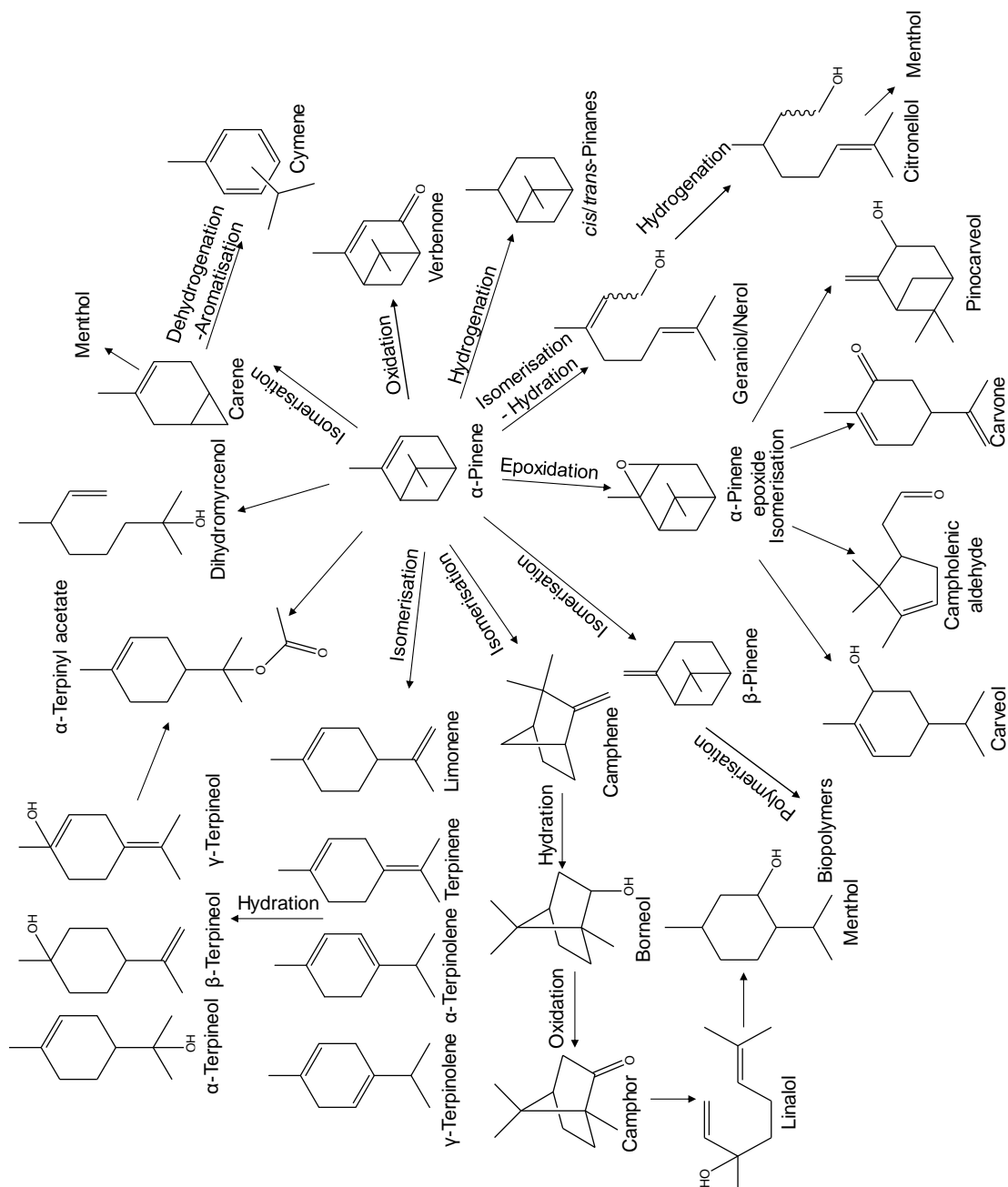
$\alpha$ -Pinene, a valuable compound, is a colourless water insoluble compound with a boiling point of 155 °C, and characteristic aroma reminiscent of woody pines, citrus and spicy. Pinenes,  $\alpha$ - and  $\beta$ -, are hydrocarbons derived from isoprene, and are part of the terpenes family, which is a vast class of organic compounds produced naturally from plant and some insects. At an industrial scale, terpenes and terpenoids (functionalised terpenes), are obtained via distillation of turpentine [112].

In 2010, the estimated  $\alpha$ -pinene world consumption was 230000 lb per annum [113] and tremendous number of catalytic chemical processes have been developed for the

production of pinene derivatives through hydrogenation, oxidation, isomerization/rearrangement, hydration, hydroformylation, condensation, cyclization and ring contraction. Pinene derivatives are used for a wide range of different applications, such as bioaromas, biopolymers and biofuels; moreover, they are described as good therapeutic agents, antibacterial, acaricidal and anti-inflammatory [114-116]. Among these applications, recent studies reported also antispasmodic, anticancer, antimutagenic properties [117]. The great variety of chemicals obtained from  $\alpha$ -pinene transformations is depicted in **Scheme 1.1**.

The epoxidation of  $\alpha$ -pinene to obtain  $\alpha$ -pinene epoxide (POX), has been investigated employing supported titanium oxide on silica based materials as heterogeneous catalyst. Different supports and bifunctional catalysts, including trivalent ions as  $\text{Fe}^{3+}$  or  $\text{Al}^{3+}$ , have been also investigated by several groups, improving the selectivity towards POX [80]. Hydrogen peroxide and tert-butyl hydroperoxide (TBHP) have been used as epoxide agents, which are beneficial and form non-toxic recyclable compounds at the end of the reaction. Further isomerisation of POX leads to a variety of compounds, including d-verbene, campholenic aldehyde, pinocarvenol, trans-carvenol, p-cymene which are widely used in the fragrance industry and are highly valuable fine chemicals [118, 119]. The Lewis and/or Brønsted character of the heterogeneous catalyst plays a crucial role when considering selectivity towards one of these compounds. Campholenic aldehyde is the most desired compound because it is a key intermediate in the synthesis of santalol, a sandalwood-like fragrance [119, 120].

Hydration of  $\alpha$ -pinene leads to the  $\alpha$ -terpineol, which possesses the typical lilac odour and is used as a fragrance in soaps and cosmetics. It can be obtained from either pinene or turpentine, using aqueous inorganic acids or Brønsted solid acids, such as HPAs, either bulk or supported. The reaction leads to a mixture of pinene's hydrated derivatives, as terpineol and terpineols oligomers, or pinene isomers like limonene and terpinenes. Further acetoxylation of terpineol can be carried out using organic acetic acid to obtain  $\alpha$ -terpinyl acetate (woody and bergamot aroma) and dihydromyrcenol (citrus and floral type aroma), both valuable compounds in the fragrance and alimentary industry.



**Scheme 1.1** – Valuable compounds obtained from  $\alpha$ -pinene [80].

Pinenes are also used for the synthesis of homo and co-biopolymers. Although both  $\alpha$ - and  $\beta$ - pinene can be polymerised, the  $\beta$ -structure is preferable due to the highly reactive *exo*-methylene double bond. Lu et al. [121] obtained the poly( $\beta$ -pinene) employing a Shift-based Ni catalyst by cationic polymerisation and methyl aluminoxane (MAO) as initiator at 40 °C. The optimisation of the synthesis to more environmentally friendly condition made the low-weight terpene derived polymers more industrially interesting to produce epoxy resins and polyols [122]. Another interesting monoterpene obtained from  $\alpha$ -pinene isomerisation, and used for bio-polymer production, is limonene. The functionalisation of limonene as a thiolene is a powerful technique to convert a C=C bond into a HS-R group, which is more active in polymerisation reactions and easily initiated either thermally or via UV, under air and in water. Epoxidation of limonene can also be used for the synthesis of polycarbonates and polyurethanes, both widely used for electronical, automotive and aircraft components, medical and niche applications, i.e. including drinking bottles, food containers, but also screens/glasses/lenses that require higher impact-resistance than glass. Limonene is also the precursor of p-cymene, which can be oxidised to produce terephthalic acid, the monomer of the polyalkylene terephthalate, more commonly known as PET. In the last few decades, a wide range of copolymers has been synthesised using several polymerisation techniques, employing terpenes and terpenoids for biodegradable, non-toxic and biocompatible materials [122, 123]. Limonene is also used for the menthol synthesis, which whilst it can be extracted from mint its market demands exceed production solely from extraction and thus alternative routes are required.

Camphene is a bicyclic monoterpene, derived from  $\alpha$ -pinene isomerisation, with approximately 10 tons per annum used as a fragrance additive and 12 tons per annum as solvent in the automotive industry [102]. Camphene is also used for the synthesis of camphor which is widely used for the synthesis of fine chemicals, such as insect repellents, celluloid (made from the mixture of nitrocellulose and camphor), plastics, and explosives [102].

#### 1.4.4 Isomerisation reaction

The isomerisation reaction is the most feasible and useful  $\alpha$ -pinene transformation, which leads to two different classes of valuable compounds, called monocyclic and polycyclic monoterpenes, whereby limonene and camphene are the major compounds respectively. **Figure 1.9** reports the major products obtained during the isomerisation, discerning between polycyclic compounds: camphene,  $\beta$ -pinene, tricycene and

fenchene, and monocyclic compounds: limonene, terpinolene,  $\alpha$ - and  $\gamma$ -terpinene and p-cymene.

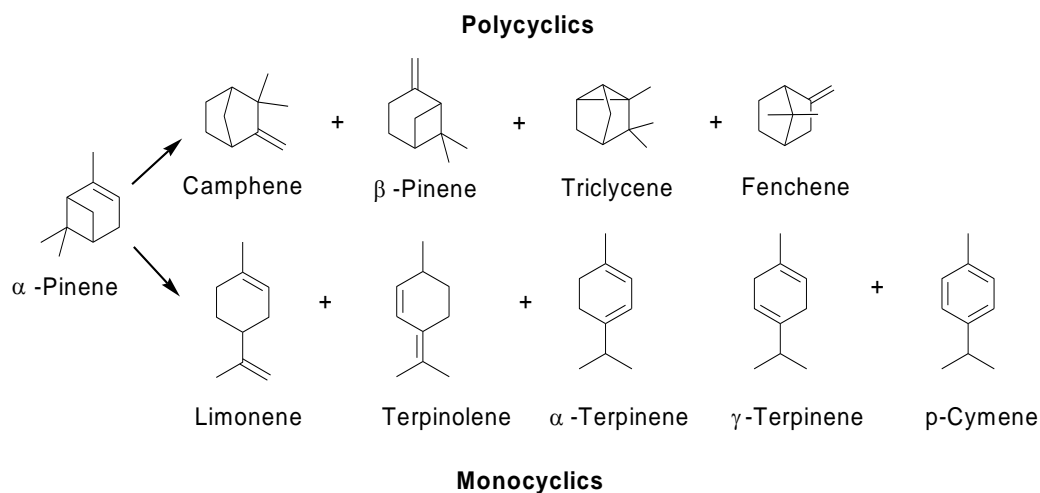


**Figure 1.9** –  $\alpha$ -Pinene isomerisation reaction mechanism.

The liquid phase  $\alpha$ -pinene isomerisation reaction, employing a heterogeneous catalyst, was first investigated by Gurvich et al. in 1915 [124]. From that time, a paramount number of catalysts and different reaction conditions have been investigated to govern the reaction mechanism and terpene rearrangements.

In 1972, Stanislaus and Yeddanapalli [125] studied the vapour phase catalytic isomerisation of  $\alpha$ -pinene using alumina-based materials as solid acid catalysts. They were the first to prove that acid strength has a strong influence on product distribution, concluding that isomerisation of the bi- and tricyclic compounds (camphene family) occurred only over strong acid sites. Ohnishi et al. [126] observed comparable results and studied the possible correlation between acidity and catalytic activity/selectivity of  $\text{NiSO}_4$ ,  $\text{SiO}_2\text{-Al}_2\text{O}_3$ , and  $\text{ZnS}$  (calcined at different temperatures) as heterogeneous catalysts, with both Brønsted and Lewis acidic properties. They concluded that the isomerisation reaction does not occur in the presence of Lewis acids in an aprotic solvent, but starts with the irreversible protonation of both  $\alpha$ - and  $\beta$ -pinenes, investigated separately, over Brønsted acid sites, which is the beginning of the isomerisation pathway. The industrial conversion of  $\alpha$ -pinene occurs under mild conditions, employing acidified  $\text{TiO}_2$  treated with an acid solution of sulfuric acid, at  $150\text{ }^\circ\text{C}$ , which reaches 30% conversion and revealed a zero order of reaction [127]. Severino et al [128, 129] tried to improve the catalytic performances of acidic titania by varying the amount of sulfuric acid and studying the effect of catalyst activation temperature on conversion and selectivity. Results revealed that catalyst activity followed a volcano-like trend as a function of the amount of acid, observing a maximum at 5%, whilst higher catalyst activation temperatures led to higher camphene selectivity at the expense of conversions. The

increased selectivity was attributed to increase of accessibility to catalyst pore structure. Findik et al. [130] studied the activity of 100 g of wood turpentine (containing 85% of  $\alpha$ -pinene) with different heterogeneous solid acid catalysts (2.5 g) such as halloysite treated with acetic acid, HCl activated clay, activated  $\text{TiO}_2$  on  $\text{SiO}_2$  with NaOH and HCl, activated carbon and clinoptilolite (natural zeolites). Their results showed that turpentine conversion to camphene is increased with reaction temperature, reaching the maximum at 155 °C, with clinoptilolite being the most active catalyst; whereas activated carbon and titanium-based catalysts treated with NaOH were inactive. To shed further insight on the greater performances of clinoptilolite catalysts, Allahverdiev et al. [131, 132] carried out the solventless isomerisation of  $\alpha$ -pinene in autoclave (in  $\text{N}_2$  atmosphere) with pressures ranging, 1-20 bar, employing 2 g of catalysts, activated at 520 °C prior analysis. It was found that reaction perform increases with pressure over the range 1-10 bar, above this value rates were independent on pressure; reaction kinetics was described as first order against  $\alpha$ -pinene consumption, with activation energy being 80.9  $\text{kJ mol}^{-1}$ . It was proposed that upon  $\alpha$ -pinene transformation, camphene slowly isomerises to tricyclene, and eventually reaches equilibrium concentration; in contrast limonene rapidly isomerises to other monocyclic products, via double bond migration.

The catalytic activity of zeolites towards  $\alpha$ -pinene isomerisation was investigated by Lopez et al. [133] employing dealuminated mordenites (MOR), faujasite (FAU) and an amorphous 13% alumina aluminosilicate, at 120 °C in a batch reactor. Mordenite proved to be the most promising catalyst, giving a maximum of 54% selectivity to camphene calculated based on the sum of camphene and limonene yields (68%). Undefined by-products are also observed over microporous zeolites, with the degree of their formation proportional to pore diameters. Furthermore,  $\alpha$ -pinene isomerisation rate was normalised to the number of  $\text{Al}^{3+}$  per unit cell ( $\text{Al}^{3+}$  density) in order to compare activities obtained for different zeolites structures. A volcano-like curve was observed displaying a maximum of activity for about 1 and 6  $\text{Al}^{3+}$  per unit cell, as calculated in the MOR and FAU structures, respectively. Mesoporous silicas for the isomerisation of  $\alpha$ -pinene were firstly investigated by Yamamoto et al. [134] employing 50 mg of FMS-16 modified with Al. Pretreatment temperature dependence on catalytic activity was investigated showing a maximum at 400 °C, for which 77.8% conversion and 41% of selectivity towards camphene were obtained. Additionally, although the number of Lewis acid sites increased with the calcination temperature, camphene selectivity was reported being unchanged, suggesting that Lewis acid sites did not participate in the reaction. The role of Brønsted and Lewis acid sites is extremely controversial and still under debate. In 2002, Besun et al. [135] investigated in detail the effects of surface area, pore size

distribution and ratio Brønsted /Lewis on  $\alpha$ -pinene isomerisation employing acid-activated montmorillonite (clay). As a result, they concluded that pure strong Brønsted acid catalysts with high pore volumes and mesopore diameters ( $> 2$  nm), with low dealumination degrees, are good catalysts for the production of camphene. Interestingly, for materials that showed both types of acidity, via pyridine chemisorption and IR analysis, the ones with the highest ratio L/B exhibit higher selectivity towards camphene, and that increasing the Brønsted acidity of a catalyst results in a great degree of the secondary reaction of limonene. Ecomier et al. [136, 137] studied the isomerisation reaction at 60 °C employing 100 mg of sulfated zirconia as Brønsted and Lewis acid catalysts. They observed that increasing the amount of sulfur the selectivity ratio camphene: limonene decreases. Furthermore, the group also hypothesized that at low S wt%, weak Brønsted acid sites are formed, which favour camphene, while high S loadings promote limonene production due to the presence of stronger Brønsted acid sites. Hammett indicators were used as a method to discern strong/weak acid sites and no further study was made on the role of Lewis acid sites on selectivity nor upon the ratio Brønsted: Lewis sites. Further studies on sulfated zirconia did not consider the Brønsted: Lewis ratio but obtained similar results to previous literature [138]. In 2003, Masini et al. [139] first employed SiO<sub>2</sub> supported phosphotungstic acid (HPW) as heterogeneous acid catalyst for the isomerisation of  $\alpha$ -pinene, investigating the effect of calcination temperature (300-500 °C) on catalytic performances. In the study, they observed that decreasing the calcination temperature, conversion is higher and reached its highest value of 40%. Further studies [140, 141] of HPW on different supports, TiO<sub>2</sub>, ZrO<sub>2</sub>, and SiO<sub>2</sub> proved that SiO<sub>2</sub> is a better support for HPW because showed greater performances for  $\alpha$ -pinene activity. Newman et al. [86, 87] studied the activity of HPW commercial silica with pores sized 10 nm at different wt%, investigating the effect of HPW dispersion on catalytic activity. They suggested that an optimum catalyst activity is observed for the sub-monolayer coverage when HPW form tetramers that trap crystalline water. Conversion reached 45% for the ~30 wt% of HPW on silica, with almost a 1 to 1 selectivity towards camphene and limonene. Cs-doped HPW [82], different HPAs supported on natural zeolites and MCMs materials [142-144] have been employed to improve catalyst activity, lowering the ratio catalyst: substrate and investigating the effects of the ratio Brønsted: Lewis acid sites on the isomerisation pathways. Pd-Zn/Al SBA-15 catalysts were employed by Golets et al. [145] for the selective production of p-cymene from  $\alpha$ -pinene, by isomerisation and dehydrogenation of the substrate.

## 1.5 Bioethanol dehydration

### 1.5.1 Introduction

The largest use of ethanol is as a fuel or fuel additive in automotive engines. In Brazil, gasoline is blended with at least 25% of anhydrous ethanol, with 90% of new cars able to use as fuel the azeotropic mixture of ethanol and water [146]. As a blended agent, ethanol increases the oxygen content of the gasoline allowing a more complete combustion and oxidation with reduced amounts of CO, CH<sub>x</sub> and aromatic compounds. Ethanol has higher octane number than gasoline and when blended has the ability to enhance the octane number of the mixture. Disadvantages of bioethanol as a fuel is that it possesses only 66% of the energy density of gasoline reducing car efficiency at starts. More recent application of bioethanol, apart being a widely used solvent in the manufacturing industry (in cosmetics, pharmaceuticals, detergent and coatings), is as a feedstock for the synthesis of important building blocks in the organic chemistry, including ethylene, ethers, ethyl-amines and ethyl acrylate. Important bulk chemicals derived from ethanol are acetic acid formed via oxidation over silver catalysts [147], ethyl acetate via oxidation using PdO/SiO<sub>2</sub> [148] and acetone employing Cu/ZnO/Al<sub>2</sub>O<sub>3</sub> [149]. Butadiene can also be produced from ethanol either via one step reaction at 400-450 °C using silica gel impregnated with tantalum oxide (Lebedev process [150]) or via two steps reaction, producing acetaldehyde from ethanol dehydrogenation followed by aldol condensation with a second molecule of ethanol and dehydration. Ethanol can also be used in the synthesis of longer chain alcohols, as butanol, albeit with relatively low yields and harsh reaction conditions [151].

### 1.5.2 Ethanol vs Bioethanol

Although synthetic ethanol (from crude oil) and bioethanol are the same compound that behaves identically under reaction conditions, they differ in their isotopic compositions in the amount of <sup>14</sup>C. This is an important feature since new tax credits are intended for blends of bioethanol and gasoline. Although synthetic ethanol is currently half the cost of ethanol derived from sugar cane, environmental concerns and the increase of petrol costs has led to several companies expanding their synthetic ethanol plants to also process bioethanol [152].

Synthetic ethanol is readily produced from natural gas, coal and petrol fractions. Annual production of synthetic ethanol reaches 2 million tons, which is mainly produced in Saudi Arabia, Africa, the United States of America, Europe and Japan. The production of

ethanol from petroleum ethylene is a one-step process, where direct hydration of ethylene with steam employing phosphoric acid supported on silica as catalyst occurs in a fixed bed reactor. The reaction is reversible and exothermic. The reaction is carried out at 220 °C to limit by-product formation, while 60-70 atm pressure is used to drive alcohol formation, at the expense of increased operating costs. The final mixture of water, ethanol and other impurities are separated in a series of distillation columns, where finally the azeotropic mixture of ethanol and water, 95% and 5% respectively, is obtained.

Bioethanol as an energy source is not a new idea, and its applicability has been investigated since the 1990's [153]. Unfortunately, due to higher production costs compared to petrol it has been mostly ignored for almost two decades [1]. In today's market, bioethanol is gaining greater attention, as a green and sustainable biofuel and bio-reactant, locally produced from renewable raw materials. The bar chart in **Figure 1.10** illustrates the world bioethanol production, expressed in billions of gallons between 2007 and 2015, highlighting the contribution of each country or region per year. In 2015, the United States was the world largest producer of bioethanol, by producing 14 billion of gallons alone mainly from corn, followed by Brazil with 7 billion of gallons obtained from sugar cane; together, the USA and Brazil, produce almost 85% of the world's bioethanol.

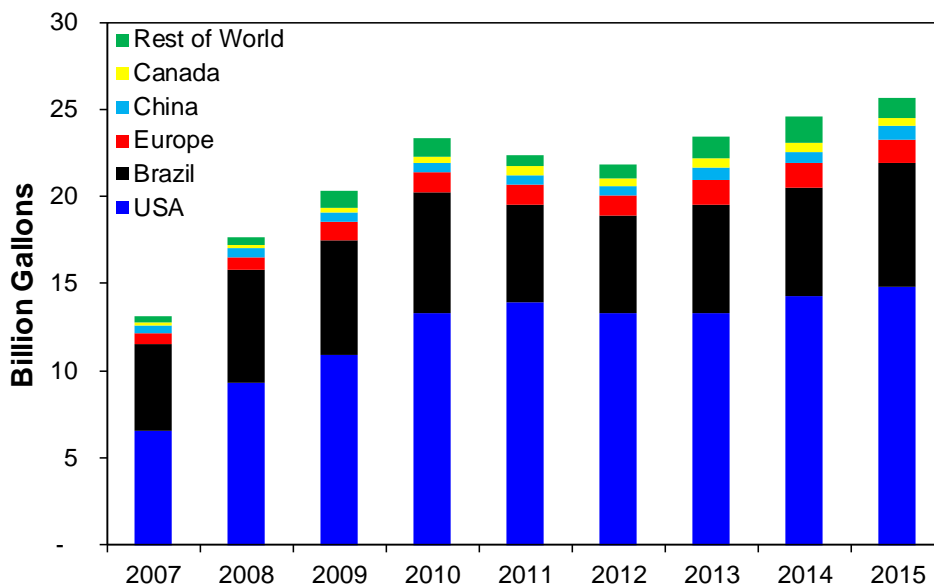


**Figure 1.10** – Global bioethanol production by country/region and year [154].

Bioethanol is obtained from fermentation of sugars derived from biological feedstocks classified as sucrose-containing feedstocks (e.g. sugar cane and sugar beet), starchy materials (e.g. wheat and corn), and lignocellulosic biomass (e.g. wood and straw). The

type of feedstock and complexity of the production process strongly influence the overall ethanol yields, whilst the availability of raw materials and their possible competition with food crops is also of concern. The selection of biological feedstock depends on the local and agroecological conditions of the considered country/region. For instance, the USA and Europe have based their bioethanol production on starch rich substrates as they are more economically viable, while in Brazil sugar cane is the most utilised feedstock. **Table 1.2** reports the ethanol production potentials depending on the type of substrate [155]. Values are directly correlated to the amount of fermentable sugars, which, for example, is higher in corn and rice compared to sugar cane and sugar beet. It is worth mentioning that although sugar-based materials have lower production potentials compared to starchy materials, their productivity for cultivated hectare is higher resulting in higher ethanol annual yields [156]. Lignocellulosic materials seem to be a more suitable substrate for the production of bioethanol as they are not dependent on the climate changes, easily available in tropical and temperate countries, their production is not related to food production, avoiding an entirely biofuels-dedicated crop situation, and their processing can be integrated to existing industrial plants [157].

**Table 1.2** – Substrate for bioethanol production and their production potentials

Feedstock	Bioethanol production potential / L ton <sup>-1</sup>
Sugar cane	70
Sugar beet	110
Sweet potato	125
Potato	110
Cassava	180
Maize	360
Rice	430
Barley	250
Wheat	340
Bagasse and other cellulose biomass	280

Lignocellulosic biomass, as corn stover, wheat and rice straw, is converted to bioethanol via either thermochemical or biochemical routes. The thermochemical production starts with biomass gasification, which converts raw materials into syngas, H<sub>2</sub> and CO. The syngas is then transformed in a mixture of alcohols either catalytically or by bacteria. Unfortunately, due to the high costs of the processes and low yields obtained (50%), the thermochemical production of ethanol is economically unviable. In contrast, the biochemical process involves (1) extraction of simple fermentable sugars from biomass, (2) fermentation of sugars and (3) final separation from water at low temperatures [158]. The first step to obtain fermentable sugars is crucial and allows the biomass breakdown.

Two operations are generally involved: pretreatment and hydrolysis [159]. The pretreatment increases the yields obtainable from hydrolysis by 80%, through softening the hardest cellulosic structures, but the step needs to be both economically viable whilst also avoiding degradation of carbohydrates and formation of side-products[160]. Hydrolysis commonly proceeds via acidic or enzymatic conditions. Once the mixture of fermentable sugars is obtained, containing glucose, xylose, mannose, galactose and arabinose, carefully selected microorganisms can convert those sugars into ethanol and carbon dioxide. In theory, 1 kg of sugars produces 0.51 kg of ethanol and 0.49 kg of CO<sub>2</sub>, however, in practice part of the sugars are actually consumed by the microorganisms for their own growth [160]. Starchy compounds undergo the same types of treatments, albeit with milder process conditions due to starch being easier to convert into sugars [161].

Lignocellulosic biomass, as raw material, is a promising path for the production of bioethanol. Possible technologies in this area are extensively investigated at industrial scale, and their application in the medium/long term would improve worldwide sustainability.

### **1.5.3 Ethanol Dehydration**

In 1950, technologies to obtain ethylene from ethanol by dehydration were readily available in the United States and in Europe. However, the development of processes based on steam cracking of hydrocarbons from natural gas and petroleum fractions allowed a large-scale cost-effective ethylene production. In the current time, with the decrease of bio-ethanol production costs and growing environmental concerns, a biomass-based route is gaining more attention and is expected to replace at least partially fossil fuel based production in the near future. Further advantages to produce ethylene from bioethanol are: (i) post-process ethylene purification steps are significantly reduced/eliminated due to the high purity of bioethylene, reducing operation costs, investment, and offering fast returns; (ii) raw materials are locally available and not limited by resource distribution; (iii) technology feasible and readily available with no need for commissioning of complex equipment or plant construction [162].

Ethylene is one of the main components in the chemical industry, from which almost 75% of all chemical products are produced, such as plastics, fertilisers, polymers, toys, car components and a wide range of everyday use products. It is the monomer for polyethylene (PE), which is used in low-density (LDPE), linear low density (LLDPE), and high density (HDPE) structures, poly(ethylene terephthalate) (PET); it is precursor of ethylbenzene and styrene, ethylene oxide, glycol ethers, ethylene mono and dichloride,

bromide [163]. In 2012, ethylene production reaches 100 million tons per year and continues to grow.

Current technologies operating to produce bioethylene are Braskem (Brasil), Chematur (Sweden), the Hummingbird process of British Petroleum (BP), and the Atol process, born as a joint collaboration between Axens, Total and IFPEN. The ethanol to ethylene Brazilian plant Braskem has the capacity to produce 200 000 tons per year from sugar cane. In 2010, the company also started producing green polyethylene, which was the first biopolymer to be produced at industrial scale [164]. The Chematur process capacity ranges between 5000 and 200000 tons of bioethylene per year, employing Syndol catalyst, which is an  $\text{Al}_2\text{O}_3\text{-MgO/SiO}_2$  based catalyst, in a four adiabatic reactors [165]. The Hummingbird process, announced in 2013 by BP, is capable of producing between 50000 and 300000 tons of bioethylene per year, employing heteropolyacid based catalysts, between 160–270 °C at 1–45 bar with unreacted ethanol recirculated into the reactor [166]. The Atol process produces similar amounts of bioethylene per year, working, however, under harsh conditions, between 400-500 °C [166].

Although these processes seem capable of producing a great amount of bioethylene, it is shaded compared to the annual capacity of a steam cracker, as the Formosa Petrochemical Corporation (Taiwan) which produces 2935000 tons of ethylene per year [162].

Dehydration of bioethanol starts with the protonation of the hydroxyl group of the alcohol, which leaves a water molecule; this result in the loss of a proton from the methyl group, to complete the catalytic cycle and thus regenerate the acidic catalyst, and subsequent hydrocarbon rearrangement to ethylene [162]. To improve the green credentials of the process, catalysts, reaction conditions, and reactor designs have been investigated. Herein, the different types of catalysts will be reviewed, and classed within four main categories, to summarise the achievements of scientific research of the last 60 years, these being phosphoric acid systems, oxide catalysts, molecular sieves catalysts and heteropolyacids.

- *Phosphoric acid derived catalytic materials* were the first employed (in 1930) for the industrial dehydration of ethanol. Easily produced by loading the phosphate group on clay or coke [167-169], but suffering easy deactivation and requiring long regeneration times have result in these materials no longer being used.

- *Mixed oxides* are another class of catalysts used for the dehydration of ethanol, which are mainly alumina-based catalysts. In 1967, de Boer et al. [170] published a study on the dehydration of ethanol on  $\eta$  and  $\gamma\text{-Al}_2\text{O}_3$  suggesting that the former exhibited higher reaction rates because possesses higher Al density per  $\text{m}^2$  of the outer surface

compared to the latter. It was also reported that ethylene production obeyed the Langmuir-Hinshelwood mechanism, while diethyl ether formation occurred following the Rideal-Eley mechanism. Roca et al [171] studied the reaction employing Si-Al catalytic system finding that the two reactions towards ethylene and diethyl ether are parallel reactions. In 1980, Halcon/Scientific Design Company developed the Syndol catalyst for dehydration reaction operating at 650 °C in an adiabatic reactor, obtaining 97% of ethylene selectivity and 97-99% ethanol conversion [172]. The catalysts, which was active for 8-12 months, is a multi-oxide catalyst based on  $\text{Al}_2\text{O}_3\text{-MgO/SiO}_2$  [168]. The extreme reaction temperatures brought researchers to investigate more thoroughly the Syndol-based catalytic systems, especially in trying to dope  $\text{Al}_2\text{O}_3$  with mixed oxides. Ezzo et al [173, 174] investigated on the catalytic dehydration of ethanol employing  $\gamma\text{-Al}_2\text{O}_3\text{-Cr}_2\text{O}_3$  catalysts, discovering that the use of  $\text{Cr}_2\text{O}_3$  helps to reduce the reaction temperature to 300 °C. El-Katatny et al. [175] synthesised dispersed  $\alpha\text{-Fe}_2\text{O}_3$  species (0-10 wt%) on  $\gamma\text{-Al}_2\text{O}_3$  catalytic materials to use at low temperatures, between 140 and 250 °C. Results revealed that the major improvement was observed only with high  $\text{FeO}_x$  loading, 10 wt%, obtaining higher ethylene selectivity compared to raw  $\gamma\text{-Al}_2\text{O}_3$ . Doheim et al. [176] developed an  $\text{Al}_2\text{O}_3$  catalyst adding  $\text{MnO}_2$  and  $\text{Na}_2\text{O}$  to the structure, achieving high ethanol conversion at 350-450 °C and relatively low space time velocity. Chen et al.[177] improved the reaction setup by using a micro-channelled reactor, over the range of 380-440 °C, equipped with 10 wt%  $\text{TiO}_2$  on  $\gamma\text{-Al}_2\text{O}_3$  catalyst. Ethanol conversion achieved 99.96%, and an ethylene yielded of  $26 \text{ g g}_{\text{cat}}^{-1} \text{ h}^{-1}$ . Platelet  $\gamma\text{-Al}_2\text{O}_3$  was recently tested by Lee et al. [178], proving that there is no difference in products distribution based on catalyst shape. It is also concluded that on  $\gamma\text{-Al}_2\text{O}_3$ , the ethoxide species is the key intermediate rather than the molecular ethanol, suggesting also that the formation of diethyl ether increases with ethanol pressure.

The activated alumina based catalysts, although their good thermal stability, need high reaction temperatures and low space time velocities to have appreciable activity, increasing the overall energy consumptions and costs.

- *Molecular sieves catalysts* are another class of catalysts suitable for dehydration reactions. As described previously, molecular sieve materials have defined and ordered structures, with different physical and chemical properties, both tunable depending on the reagents used and synthesis procedure. A great variety of molecular shape-selective materials have been investigated, with ZSM-5 types and SAPO (Si-Al-phosphate) being the most studied.

ZSM-5 molecular sieved catalysts are widely used in the petrochemical industry, being excellent shape-selective acid catalysts with a pore structure (0.56 x 0.55 nm) suitable for the transformation of light hydrocarbons. At first, these materials were utilised without

any modification, reaching high conversion and high selectivity. Anderson et al. [179] described in 1980 the wide range of catalytic reactions carried out with these type of materials, including alcohol dehydration. ZSM-5 materials are good catalysts for the dehydration of ethanol, and active at relatively low temperatures, between 200-300 °C; unfortunately, their acidity leads to the formation of coke and carbonaceous species, which deposit on the surface, reducing the efficiency of the catalyst on stream during the reaction time. Moser et al. [180] studied the dehydration of dilute bioethanol (20% vol/vol), obtained from the fermentation process, prior to distillation, employing ZSM-5 and by varying the ratio Si: Al. Operating at high temperatures, 500 °C, the group found that higher selectivity towards ethylene was observed when the zeolite is silicon rich (high Si:Al). Modification of ZSM-5 is mainly focused on the prevention of coking, to increase life-time of the catalysts, and allow for operation at mild temperatures. It is reported that impregnating ZSM-5 with H<sub>3</sub>PO<sub>4</sub> helps to reduce catalyst deactivation from coking, and retaining ethylene selectivity; however, in order to improve the catalytic conversion, higher temperatures are required (>300 °C) [169, 181-184]. Alkali compounds [185] have been also used to reduce acid strength and reduce catalyst deactivation. Zn and Mn on ZSM-5 [186] were also investigated as possible dehydration catalysts, showing no diethyl ether formation at 400 °C, revealing, however, low stability with time on stream. Cu and NaCu-ZSM-5 have been also investigated by Bun et al. [187], but side reactions, effected ethylene selectivity. Ni modified zeolites have been also investigated [188] and was shown to be a good co-catalyst to limit the production of heavy compounds. La-P modified ZSM-5 is the most promising catalyst, which operates at low temperature (240 °C) and is highly selective [189]. The most favourable composition is 0.5% La and 2% P, prepared by impregnation of the commercial catalyst with H<sub>3</sub>PO<sub>4</sub> and La(NO<sub>3</sub>) solutions, dried and then calcined. Stability of over 70 hours was reported, although further investigations into stability at different operating conditions and evaluation on production cost are required to be applied on an industrial scale. Investigations on the activity of other zeolites, H-MOR, H-BEA, H-Y, H-USY, H-FER and H-MFI, have been also carried out. Phung et al. [190, 191] found that coke is produced more on H-MOR and H-BEA, and that H-MOR is the most active converting ethanol. H-FER and H-USY exhibit the highest selectivity towards ethylene at 300 °C. SAPO type materials are a family of silico-alumino-phosphate materials (SAPO-n, where n indicates a specific structure type), developed by the Union Carbide Corporation (UCC) in New York, USA, 1984 [192]. SAPOs, name that derives from (Si<sub>x</sub>Al<sub>y</sub>P<sub>z</sub>)O<sub>2</sub>, possess a crystalline microporous structure, with properties in between of zeolites and of aluminophosphates. Arias et al. [193] studied the activity of SAPO-5 and SAPO-11 comparing these with the alumino-phosphate counterparts, AlPO<sub>4</sub>-5 and AlPO<sub>4</sub>-11,

focusing on the effects of structural pore architecture and Brønsted-Lewis character on products distribution. The group found that SAPO-n catalysts were more active and have higher yields towards ethylene at 320 °C compared to AlPO-n materials. SAPO-5 showed 90% ethylene yield whereas SAPO-11 only 60%, which is correlated to the higher Brønsted acid density measured on the former. They concluded that no structural properties were observed to influence ethylene yields since pores of SAPO-5 are broader than the ones of SAPO-11. Zhang et al. [181] reported the metal modified SAPO-34, Ni-SAPO-34, is more selective than the undoped material, enhancing ethylene selectivity from 85% to 92% when the reaction is carried out at 350 °C. Chen et al. [194] reported Zn<sup>2+</sup> and Mn<sup>2+</sup> modified SAPO-11 and SAPO-34, revealing that M<sup>2+</sup> catalysts are more active in dehydrating ethanol compared to their relative undoped materials, with Mn being more active than Zn. The group suggested that the introduction of M<sup>2+</sup> led to the formation of a greater number of weak acid sites, which help the catalytic system in addition to the strong sites, while too strong acidity leads to ethylene polymerisation.

Compared to alumina-based catalysts, modified molecular sieved are very active catalysts that work efficiently at low temperatures. Unfortunately these suffer from deactivation, through coking, and high production costs which have prevent their application for the industrial production of ethylene from ethanol dehydration [168].

- *Heteropolyacids* are very versatile materials, which can be used for ethanol dehydration to ethylene. They benefit for being active at lower temperature than other classes of catalytic systems, but suffer decreased ethanol conversion. Saito et al. [195] was one of the first study to employ heteropolyacids for the dehydration of ethanol, investigating on the transient behaviour based on pseudo-liquid catalysis model. They observed that even after the ethanol feed had stopped, formation of ethylene persisted for a considerable time, whilst diethyl ether production decreased with time, suggesting that ethylene formation proceeds via a unimolecular decomposition of adsorbed ethanol, whilst ether formation occurs between an activated molecule and physisorbed ethanol molecules. In 1989, Okuhara et al. [68] employed Cs modified HPW as the catalyst for ethanol dehydration, finding that Cs-based materials have lower absorption capacities compared to their acid forms and higher partial pressures of ethanol are required to observe a pseudoliquid catalytic system. Haber et al. [196] studied the catalytic behaviour of supported HPW on Y-type zeolite and silica via simple wet impregnation carrying out the reaction at between 125 and 370 °C. They found that, at 300 °C, low loading of HPW on HY are much more active than their counterparts on silica, due to the absence of pseudo liquid phase arising from higher dispersion, indicating that the degree of HPW agglomeration is critical when silica is employed as support. The effect of HPW

loading was investigated by Bokade et al. [197], using montmorillonite as the support at 250 °C. Additionally, the effect of diluted ethanol (80% m/m in water) was investigated on the reaction activity, as a more environmentally friendly feedstock. The 30 wt% of HPW was found the most active catalyst converting 74% of ethanol with 92% of selectivity at 250 °C, with Na doped HPW and HPMo also investigated although no catalytic improvements were apparent. The use of different HPAs as acid catalysts for the dehydration of ethanol was investigated by Varisli et al. [198]. They studied the activity of unsupported HPW, HSiW and HPMo, and discovered that both acid strength and thermostability are responsible for the higher performances of HPW, achieving 77% of ethylene selectivity, against 58% and 20% for HSiW and HPMo, respectively at 250 °C. In 2011, Gurgul et al. [199] studied the activity of Ag modified HPW catalyst,  $\text{Ag}_3\text{PW}_{12}\text{O}_{40}$ , for the dehydration of ethanol using air as carrier gas. The influence of air humidity on the catalytic activity of APW was also investigated, and it was found that, at 220 °C with 2% of humidity, 70% of ethanol was converted achieving 99.8% of ethylene selectivity. However, SEM imaging and XPS analysis of the spent catalytic material revealed surface composition changes, with the formation of silver nano-structures. Increasing humidity to 9% led to full ethanol conversion but lower ethylene selectivity; although at these conditions the AgPW was stable. Ciftci et al. [200] studied the catalytic activity of HPW incorporated in MCM-41, comparing material prepared using a one-pot hydrothermal procedure against HPW impregnated of MCM-41. At 250 °C, the two catalysts showed different catalytic activity with the impregnated material being the most active and the most selective, 65% ethanol conversion and 70% ethylene selectivity, compared to the incorporated HPW, which achieved 30% conversion and 30% ethylene selectivity. In terms of catalyst stability, however, the incorporated HPW did not deactivate and no coke formation was observed up to 300 °C. Varisli et al. [201] studied the catalytic activity of HSiW supported on calcined and uncalcined MCM-41, proving that calcined MCM-41 led to higher performances, with 80% ethanol conversion at 225 °C, than the uncalcined one, with only 30%; although no information regarding catalyst stability and life span was reported. In 2015, Holclajtner-Antunovic et al. [202] synthesised Ag-modified and unmodified HPW supported on SBA-15 and  $\text{TiO}_2$  with 30 wt% loading. The  $\text{TiO}_2$  supported catalyst showed poorer activities compared to the SBA-15 counterparts with AgPW/SBA-15 giving almost full conversion (98%) at 250 °C and 99% ethylene selectivity. Unfortunately, rapid deactivation led to a loss of 50% activity and selectivity after only 5 hours on stream at 300 °C. Popa et al. [203] studied Cs modified HPMo ( $\text{CsH}_2\text{PMo}_{12}\text{O}_{40}$ ) supported on SBA-15 at different loadings, and observed that even at the low temperature of 150 °C acetaldehyde was formed as a by-product, with it reaching 20% selectivity at 300 °C. Popa et al. [204] found high amount

of by-products for Ni-PMo on SBA-15, which they attributed to Ni incorporation leading to similar activation energies for both ethylene (dehydration path) and acetaldehyde (dehydrogenation path) formation.

In conclusion, a great number of catalytic materials and reaction conditions have been investigated for ethanol dehydration. The production process of bioethylene is feasible and could easily be integrated to other industrial processes, making it more economically advantageous. The worldwide demand for ethylene is enormous and whilst bioethanol to bioethylene is currently not at the stage to replace the fossil fuel based synthetic pathway further development, including catalysts design and refinement, will be critical if bio-derived ethylene is to become the major production route.

## 1.6 Thesis aims

To investigate HPA catalytic systems for surface-type reactions, the solventless liquid phase  $\alpha$ -pinene isomerisation, and bulk-type reactions, the gas-phase dehydration of ethanol, to identify structure function relationships.

To design heterogeneous supported catalysts based on the HPA family employing two different silica-based supports with different architecture and pore structure, being commercial non-porous fumed silica and the lab synthesised highly ordered mesoporous SBA-15, and to investigate the role of support on the physicochemical properties of the deposited HPAs.

To study the reaction mechanism of  $\alpha$ -pinene and ethanol dehydration over pure Brønsted acid HPA catalysts, and elucidate the underlying factors that result in deactivation of HPAs.

## 1.7 References

- [1] TransparencyMarketResearch, Catalyst Market – Global Industry Size, Share, Growth, Trends and Forecast 2012 – 2018, 2013.
- [2] S.M. Johnson, *Colum. J. Envtl. L.* 17 (1992) 153.
- [3] P.T. Anastas, M.M. Kirchhoff, *Accounts of Chemical Research* 35 (2002) 686-694.

- [4] P.T. Anastas, J.C. Warner, *Green Chemistry: Theory and Practice*, Oxford University Press, 1998.
- [5] P. Tundo, P. Anastas, D.S. Black, J. Breen, T.J. Collins, S. Memoli, J. Miyamoto, M. Poliakoff, W. Tumas, *Pure and Applied Chemistry* 72 (2000) 1207-1228.
- [6] O. Hutzinger, *Environmental Science and Pollution Research* 6 (1999) 123-123.
- [7] G. Brundtland, M. Khalid, S. Agnelli, S. Al-Athel, B. Chidzero, L. Fadika, V. Hauff, I. Lang, M. Shijun, M. Morino de Botero, M. Singh, S. Okita, A. Others, *Our Common Future ('Brundtland report')*, Oxford University Press, USA, 1987.
- [8] M. Burmeister, F. Rauch, I. Eilks, *Chemistry Education Research and Practice* 13 (2012) 59-68.
- [9] T. Bieringer, S. Buchholz, N. Kockmann, *Chemical Engineering & Technology* 36 (2013) 900-910.
- [10] A.T. Bell, B.C. Gates, D. Ray, M.R. Thompson, *Basic Research Needs: Catalysis for Energy*, 2008, p. Medium: ED; Size: PDFN.
- [11] A.D. McNaught, A.D. McNaught, *Compendium of chemical terminology*, Blackwell Science Oxford, 1997.
- [12] P. Atkins, J. De Paula, *Elements of physical chemistry*, Oxford University Press, USA, 2013.
- [13] J. Falbe, H. Bahrmann, *Journal of Chemical Education* 61 (1984) 961.
- [14] J.H. Clark, D.J. Macquarrie, *Chemical Society reviews* 25 (1996) 303-310.
- [15] B.M. Trost, *Angewandte Chemie International Edition in English* 34 (1995) 259-281.
- [16] R.A. Sheldon, *Chemical Society reviews* 41 (2012) 1437-1451.
- [17] M. Campanati, G. Fornasari, A. Vaccari, *Catalysis Today* 77 (2003) 299-314.
- [18] K. Wilson, A.F. Lee, *Heterogeneous catalysts for clean technology*, Wiley-VCH, 2013.
- [19] T. Travis, *Chemistry and Industry* (1993) 581-585.
- [20] H. Sinn, W. Kaminsky, *Advances in Organometallic Chemistry* 18 (1980) 99-149.
- [21] A. Corma, *Current Opinion in Solid State and Materials Science* 2 (1997) 63-75.
- [22] G. Centi, S. Perathoner, *Sustainable Industrial Chemistry*, Wiley-VCH Verlag GmbH & Co. KGaA, 2009, pp. 73-198.

- [23] T. Okuhara, *Chemical Reviews* 102 (2002) 3641-3665.
- [24] C.H. Bartholomew, *Applied Catalysis A: General* 212 (2001) 17-60.
- [25] J.A. Moulijn, A.E. van Diepen, F. Kapteijn, *Applied Catalysis A: General* 212 (2001) 3-16.
- [26] O. Deutschmann, H. Knözinger, K. Kochloefl, T. Turek, *Ullmann's Encyclopedia of Industrial Chemistry*, Wiley-VCH Verlag GmbH & Co. KGaA, 2009.
- [27] G. Ertl, H. Knözinger, F. Schüth, J. Weitkamp, *Handbook of heterogeneous catalysis*, Wiley-VCH, 2008.
- [28] P.L.J. Gunter, J.W. Niemantsverdriet, F.H. Ribeiro, G.A. Somorjai, *Catalysis Reviews* 39 (1997) 77-168.
- [29] J.E. Herrera, J.H. Kwak, J.Z. Hu, Y. Wang, C.H.F. Peden, *Top Catal* 49 (2008) 259.
- [30] S. Choi, Y. Wang, Z. Nie, J. Liu, C.H.F. Peden, *Catalysis Today* 55 (2000) 117-124.
- [31] T. Matsuda, A. Igarashi, Y. Ogino, *Journal of The Japan Petroleum Institute* 23 (1980) 30-34.
- [32] I.V. Kozhevnikov, *Applied Catalysis A: General* 256 (2003) 3-18.
- [33] Y. Wan, D. Zhao, *Chemical reviews* 107 (2007) 2821-2860.
- [34] C. Vincent, *Process for producing low-bulk density silica*, Google Patents, 1971.
- [35] J.S. Beck, W.S. Borghard, C.T. Kresge, M.E. Leonowicz, W.J. Roth, J.C. Vartuli, *Synthetic porous crystalline material its synthesis and use*, Google Patents, 1993.
- [36] C. Kresge, M. Leonowicz, W. Roth, J. Vartuli, J. Beck, *nature* 359 (1992) 710-712.
- [37] J. Beck, J. Vartuli, W.J. Roth, M. Leonowicz, C. Kresge, K. Schmitt, C. Chu, D.H. Olson, E. Sheppard, S. McCullen, *Journal of the American Chemical Society* 114 (1992) 10834-10843.
- [38] D. Zhao, J. Feng, Q. Huo, N. Melosh, G.H. Fredrickson, B.F. Chmelka, G.D. Stucky, *Science* 279 (1998) 548-552.
- [39] Y. Wan, Y. Shi, D. Zhao, *Chemical communications* (2007) 897-926.
- [40] G.B. Dutt, *The Journal of Physical Chemistry B* 109 (2005) 4923-4928.

- [41] A. Monnier, Sch, xfc, F. th, Q. Huo, D. Kumar, D. Margolese, R.S. Maxwell, G.D. Stucky, M. Krishnamurty, P. Petroff, A. Firouzi, M. Janicke, B.F. Chmelka, *Science* 261 (1993) 1299-1303.
- [42] J. Frasc, B. Lebeau, M. Soulard, J. Patarin, R. Zana, *Langmuir* 16 (2000) 9049-9057.
- [43] J. Patarin, B. Lebeau, R. Zana, *Current Opinion in Colloid & Interface Science* 7 (2002) 107-115.
- [44] G.J.D.A. Soler-Illia, C. Sanchez, B. Lebeau, J. Patarin, *Chemical reviews* 102 (2002) 4093-4138.
- [45] O. Regev, *Langmuir* 12 (1996) 4940-4944.
- [46] K. Flodström, H. Wennerström, V. Alfredsson, *Langmuir* 20 (2004) 680-688.
- [47] K. Flodström, C.V. Teixeira, H. Amenitsch, V. Alfredsson, M. Lindén, *Langmuir* 20 (2004) 4885-4891.
- [48] M.J. Janik, R.J. Davis, M. Neurock, *The Journal of Physical Chemistry B* 108 (2004) 12292-12300.
- [49] I.V. Kozhevnikov, *Journal of Molecular Catalysis A: Chemical* 262 (2007) 86-92.
- [50] I.V. Kozhevnikov, *Chemical Reviews* 98 (1998) 171-198.
- [51] I.V. Kozhevnikov, *Catalysis Reviews* 37 (1995) 311-352.
- [52] T. Okuhara, N. Mizuno, M. Misono, *Applied Catalysis A: General* 222 (2001) 63-77.
- [53] T. Okuhara, N. Mizuno, M. Misono, in: W.O.H. D.D. Eley, G. Bruce (Eds.), *Advances in Catalysis*, Academic Press, 1996, pp. 113-252.
- [54] N. Mizuno, M. Misono, *Chemical Reviews* 98 (1998) 199-217.
- [55] N. Mizuno, K. Kamata, K. Yamaguchi, *Top Catal* 53 (2010) 876-893.
- [56] M. Misono, *Chemical communications* (2001) 1141-1152.
- [57] S. Shikata, T. Okuhara, M. Misono, *J. Mol. Catal. A: Chem* 100 (1995) 49-59.
- [58] M.N. Timofeeva, *Applied Catalysis A: General* 256 (2003) 19-35.
- [59] M.N. Timofeeva, M.M. Matrosova, G.M. Maksimov, V.A. Likholobov, *Kinetics and Catalysis* 42 (2001) 785-790.
- [60] M.N. Timofeeva, G.M. Maksimov, V.A. Likholobov, *Kinetics and Catalysis* 42 (2001) 30-34.

- [61] G.M. Maksimov, M.N. Timofeeva, V.A. Likholobov, *Russian Chemical Bulletin* 50 (2001) 1529-1532.
- [62] C.W. Hu, M. Hashimoto, T. Okuhara, M. Misono, *Journal of Catalysis* 143 (1993) 437-448.
- [63] T. Okuhara, C. Hu, M. Hashimoto, M. Misono, *Bulletin of the Chemical Society of Japan* 67 (1994) 1186-1188.
- [64] K.Y. Lee, N. Mizuno, T. Okuhara, M. Misono, *Bulletin of the Chemical Society of Japan* 62 (1989) 1731-1739.
- [65] H. Taketa, S. Katsuki, K. Eguchi, T. Seiyama, N. Yamazoe, *The Journal of Physical Chemistry* 90 (1986) 2959-2962.
- [66] B.B. Bardin, S.V. Bordawekar, M. Neurock, R.J. Davis, *The Journal of Physical Chemistry B* 102 (1998) 10817-10825.
- [67] T. Ueda, T. Tatsumi, T. Eguchi, N. Nakamura, *The Journal of Physical Chemistry B* 105 (2001) 5391-5396.
- [68] T. Okuhara, T. Arai, T. Ichiki, K.Y. Lee, M. Misono, *Journal of Molecular Catalysis* 55 (1989) 293-301.
- [69] T. Okuhara, H. Watanabe, T. Nishimura, K. Inumaru, M. Misono, *Chemistry of Materials* 12 (2000) 2230-2238.
- [70] S. Uchida, K. Inumaru, M. Misono, *The Journal of Physical Chemistry B* 104 (2000) 8108-8115.
- [71] N. Mizuno, M. Misono, *Chemical Reviews* 98 (1998) 199-217.
- [72] M. Heravi, S. Sadjadi, *Journal of the Iranian Chemical Society* 6 (2009) 1-54.
- [73] Y. Ren, B. Yue, M. Gu, H. He, *Materials* 3 (2010) 764-785.
- [74] N.M.a.M. Misono, (1997).
- [75] Y. Izumi, R. Hasebe, K. Urabe, *Journal of Catalysis* 84 (1983) 402-409.
- [76] G. Kamalakar, K. Komura, Y. Kubota, Y. Sugi, *Journal of Chemical Technology & Biotechnology* 81 (2006) 981-988.
- [77] P. Kamala, A. Pandurangan, *Catalysis Communications* 9 (2008) 2231-2235.
- [78] G. Kamalakar, K. Komura, Y. Sugi, *Applied Catalysis A: General* 310 (2006) 155-163.
- [79] A. Engin, H. Haluk, K. Gurkan, *Green Chemistry* 5 (2003) 460-466.
- [80] A. Corma, S. Iborra, A. Velty, *Chemical Reviews* 107 (2007) 2411-2502.

- [81] L. Pesaresi, D.R. Brown, A.F. Lee, J.M. Montero, H. Williams, K. Wilson, *Applied Catalysis A: General* 360 (2009) 50-58.
- [82] K. Narasimharao, D. Brown, A. Lee, A. Newman, P. Siril, S. Tavener, K. Wilson, *Journal of Catalysis* 248 (2007) 226-234.
- [83] X.-X. Han, K.-K. Chen, W. Yan, C.-T. Hung, L.-L. Liu, P.-H. Wu, K.-C. Lin, S.-B. Liu, *Fuel* 165 (2016) 115-122.
- [84] C. Rocchiccioli-Deltcheff, A. Aouissi, S. Launay, M. Fournier, *Journal of Molecular Catalysis A: Chemical* 114 (1996) 331-342.
- [85] L. Frattini, M.A. Isaacs, C.M.A. Parlett, K. Wilson, G. Kyriakou, A.F. Lee, *Applied Catalysis B: Environmental* 200 (2017) 10-18.
- [86] A.D. Newman, A.F. Lee, K. Wilson, N.A. Young, *Catalysis Letters* 102 (2005) 45-50.
- [87] A.D. Newman, D.R. Brown, P. Siril, A.F. Lee, K. Wilson, *Physical chemistry chemical physics : PCCP* 8 (2006) 2893-2902.
- [88] E.V. Gusevskaya, *ChemCatChem* 6 (2014) 1506-1515.
- [89] S. Albonetti, L. Dal Pozzo, F. Trifirò, *Eurasian Chemico-Technological Journal* 3 (2017) 221-229.
- [90] D. Carriazo, C. Domingo, C. Martin, V. Rives, *Journal of Solid State Chemistry* 181 (2008) 2046-2057.
- [91] G. Centi, F. Cavani, F. Trifirò, *Selective oxidation by heterogeneous catalysis*, Springer Science & Business Media, 2012.
- [92] A. Kumar, P. Singh, S. Kumar, R. Chandra, S. Mozumdar, *Journal of Molecular Catalysis A: Chemical* 276 (2007) 95-101.
- [93] G. Lv, L. Deng, B. Lu, J. Li, X. Hou, Y. Yang, *Journal of Cleaner Production* 142 (2017) 2244-2251.
- [94] K.i. Sano, H. Uchida, S. Wakabayashi, *Catalysis Surveys from Asia* 3 (1999) 55-60.
- [95] K. Na, T. Okuhara, M. Misono, *Journal of Catalysis* 170 (1997) 96-107.
- [96] X. Li, Y. Zhang, *ACS Catalysis* 6 (2016) 2785-2791.
- [97] E. Papaconstantinou, *Chemical Society reviews* 18 (1989) 1-31.
- [98] D. Sattari, C.L. Hill, *Journal of the American Chemical Society* 115 (1993) 4649-4657.

- [99] G. Marci, E.I. García-López, L. Palmisano, *European Journal of Inorganic Chemistry* 2014 (2014) 21-35.
- [100] E.I. García-López, G. Marci, F.R. Pomilla, A. Kirpsza, A. Micek-Ilnicka, L. Palmisano, *Applied Catalysis B: Environmental* 189 (2016) 252-265.
- [101] M. Kourasi, R.G.A. Wills, A.A. Shah, F.C. Walsh, *Electrochimica Acta* 127 (2014) 454-466.
- [102] M. Golets, S. Ajaikumar, J.-P. Mikkola, *Chemical Reviews* 115 (2015) 3141-3169.
- [103] P. Knuuttila, P. Kukkonen, U. Hotanen, Method and apparatus for preparing fuel components from crude tall oil, Google Patents, 2015.
- [104] C. Kaplan, M.H. Alma, A. Tutuş, M. Çetinkaya, F. Karaosmanoğlu, *Petroleum Science and Technology* 23 (2005) 1333-1339.
- [105] R. Rachwalik, M. Hunger, B. Sulikowski, *Applied Catalysis A: General* 427 (2012) 98-105.
- [106] L. Szabó, A. Soria, J. Forsström, J.T. Keränen, E. Hytönen, *Environmental Science & Policy* 12 (2009) 257-269.
- [107] A.V. Someshwar, J.E. Pinkerton, *Air Pollution* (1992).
- [108] P. Knuuttila, J. Nousiainen, A. Rissanen, Process and apparatus for producing hydrocarbons from feed-stocks comprising tall oil and terpene-compounds, Google Patents, 2016.
- [109] F.o. Casbas, D. Duprez, J. Ollivier, *Applied Catalysis* 50 (1989) 87-97.
- [110] M. Lindmark, Biotransformation of turpentine constituents: oxygenation and esterification, Doctoral Thesis, Sweden: Sweden University, 2003.
- [111] ResearchandMarket, (2016).
- [112] K.A.C. Vespermann, B.N. Paulino, M.C.S. Barcelos, M.G. Pessôa, G.M. Pastore, G. Molina, *Applied Microbiology and Biotechnology* 101 (2017) 1805-1817.
- [113] G.A. Burdock, Fenaroli's handbook of flavor ingredients, CRC press, 2016.
- [114] W.A. Bernardes, R. Lucarini, M.G. Tozatti, L.G. Bocalon Flauzino, M.G. Souza, I.C. Turatti, M.L. Andrade e Silva, C.H. Martins, A.A.d. Silva Filho, W.R. Cunha, *Zeitschrift für Naturforschung C* 65 (2010) 588-593.
- [115] C.-F. Kuo, J.-D. Su, C.-H. Chiu, C.-C. Peng, C.-H. Chang, T.-Y. Sung, S.-H. Huang, W.-C. Lee, C.-C. Chyau, *Journal of agricultural and food chemistry* 59 (2011) 3674-3685.

- [116] M. Martinez-Velazquez, R. Rosario-Cruz, G. Castillo-Herrera, J. Flores-Fernandez, A. Alvarez, E. Lugo-Cervantes, *Journal of Medical Entomology* 48 (2011) 822-827.
- [117] J.S. Raut, S.M. Karuppaiyl, *Industrial Crops and Products* 62 (2014) 250-264.
- [118] S. Santoyo, S. Cavero, L. Jaime, E. Ibanez, F. Senorans, G. Reglero, *Journal of food protection* 68 (2005) 790-795.
- [119] W.F. Hölderich, J. Röseler, G. Heitmann, A.T. Liebens, *Catalysis Today* 37 (1997) 353-366.
- [120] P.J. Kunkeler, J.C. van Der Waal, J. Bremmer, B.J. Zuurdeeg, R.S. Downing, H. Van Bekkum, *Catalysis letters* 53 (1998) 135-138.
- [121] P. Yu, A.-L. Li, H. Liang, J. Lu, *Journal of Polymer Science Part A: Polymer Chemistry* 45 (2007) 3739-3746.
- [122] P.A. Wilbon, F. Chu, C. Tang, *Macromolecular rapid communications* 34 (2013) 8-37.
- [123] M. Winnacker, B. Rieger, *ChemSusChem* 8 (2015) 2455-2471.
- [124] L. Gurvich, *Russian Chemical Society* 47 (1915) 827-830.
- [125] A. Stanislaus, L.M. Yeddanapalli, *Canadian Journal of Chemistry* 50 (1972) 61-74.
- [126] O. Ryuichiro, T. Kozo, M. Shinsuke, N. Tadao, *Bulletin of the Chemical Society of Japan* 47 (1974) 571-574.
- [127] R. Albert, S. Traynor, R. Webb, *Naval Stores* (1989).
- [128] A. Severino, A. Esculcas, J. Rocha, J. Vital, L.S. Lobo, *Applied Catalysis A: General* 142 (1996) 255-278.
- [129] A. Severino, J. Vital, L.S. Lobo, *Studies in Surface Science and Catalysis*, Elsevier, 1993, pp. 685-692.
- [130] S. Findik, G. Gündüz, *J Amer Oil Chem Soc* 74 (1997) 1145-1151.
- [131] A.I. Allahverdiev, S. Irandoust, D. Yu. Murzin, *Journal of Catalysis* 185 (1999) 352-362.
- [132] A.I. Allahverdiev, S. Irandoust, B. Andersson, D.Y. Murzin, *Applied Catalysis A: General* 198 (2000) 197-206.
- [133] C.M. López, F. J. Machado, K. Rodríguez, B. Méndez, M. Hasegawa, S. Pekerar, *Applied Catalysis A: General* 173 (1998) 75-85.

- [134] T. Yamamoto, T. Tanaka, T. Funabiki, S. Yoshida, *The Journal of Physical Chemistry B* 102 (1998) 5830-5839.
- [135] N. Beşün, F. Özkan, G. Gündüz, *Applied Catalysis A: General* 224 (2002) 285-297.
- [136] M.A. Ecomier, K. Wilson, A.F. Lee, *Journal of Catalysis* 215 (2003) 57-65.
- [137] M.A. Ecomier, A.F. Lee, K. Wilson, *Microporous and Mesoporous Materials* 80 (2005) 301-310.
- [138] N.P. Comelli, Esther; Ponzi, Marta, *J Amer Oil Chem Soc* 82 (2005) 531-535.
- [139] O. Masini, L. Grzona, N. Comelli, E. Ponzi, M. Ponzi, *Journal of the Chilean Chemical Society* 48 (2003) 101-104.
- [140] N.A. Comelli, L.M. Grzona, O. Masini, E.N. Ponzi, M.I. Ponzi, *Journal of the Chilean Chemical Society* 49 (2004) 245-250.
- [141] L. Grzona, O. Masini, N. Comelli, E. Ponzi, M. Ponzi, *Reaction Kinetics and Catalysis Letters* 84 (2005) 199-204.
- [142] G. Nie, J.-J. Zou, R. Feng, X. Zhang, L. Wang, *Catalysis Today* 234 (2014) 271-277.
- [143] X. Ma, D. Zhou, X. Chu, D. Li, J. Wang, W. Song, Q. Xia, *Microporous and Mesoporous Materials* 237 (2017) 180-188.
- [144] J.J. Zou, N. Chang, X. Zhang, L. Wang, *ChemCatChem* 4 (2012) 1289-1297.
- [145] M. Golets, S. Ajaikumar, M. Mohln, J. Wärnä, S. Rakesh, J.P. Mikkola, *Journal of Catalysis* 307 (2013) 305-315.
- [146] M. Vohra, J. Manwar, R. Manmode, S. Padgilwar, S. Patil, *Journal of environmental chemical engineering* 2 (2014) 573-584.
- [147] M. Eckert, G. Fleischmann, R. Jira, H.M. Bolt, K. Golka, *Ullmann's Encyclopedia of Industrial Chemistry*, Wiley-VCH Verlag GmbH & Co. KGaA, 2000.
- [148] P.C. Zonetti, J. Celnik, S. Letichevsky, A.B. Gaspar, L.G. Appel, *Journal of Molecular Catalysis A: Chemical* 334 (2011) 29-34.
- [149] C.P. Rodrigues, P.C. Zonetti, C.G. Silva, A.B. Gaspar, L.G. Appel, *Applied Catalysis A: General* 458 (2013) 111-118.
- [150] Z. Wang, *Comprehensive Organic Name Reactions and Reagents*, John Wiley & Sons, Inc., 2010.
- [151] S. Fu, Z. Shao, Y. Wang, Q. Liu, *Journal of the American Chemical Society* (2017).

- [152] BetaAnalytic, Synthetic Ethanol: Global Trends and Supply.
- [153] H.B. Aditiya, T.M.I. Mahlia, W.T. Chong, H. Nur, A.H. Sebayang, *Renewable and Sustainable Energy Reviews* 66 (2016) 631-653.
- [154] R.F. Association, *Global Ethanol Production by Country/Region and Year*, 2016.
- [155] M. Balat, H. Balat, C. Öz, *Progress in Energy and Combustion Science* 34 (2008) 551-573.
- [156] Ó.J. Sánchez, C.A. Cardona, *Bioresource Technology* 99 (2008) 5270-5295.
- [157] S.I. Mussatto, G. Dragone, P.M.R. Guimarães, J.P.A. Silva, L.M. Carneiro, I.C. Roberto, A. Vicente, L. Domingues, J.A. Teixeira, *Biotechnology Advances* 28 (2010) 817-830.
- [158] C. Brunschwig, W. Moussavou, J. Blin, *Progress in Energy and Combustion Science* 38 (2012) 283-301.
- [159] C.N. Hamelinck, G.v. Hooijdonk, A.P.C. Faaij, *Biomass and Bioenergy* 28 (2005) 384-410.
- [160] M. Balat, H. Balat, *Applied Energy* 86 (2009) 2273-2282.
- [161] M. Balat, *Energy Conversion and Management* 52 (2011) 858-875.
- [162] D. Fan, D.-J. Dai, H.-S. Wu, *Materials* 6 (2012) 101-115.
- [163] H. Zimmermann, R. Walzl, *Ullmann's Encyclopedia of Industrial Chemistry*, Wiley-VCH Verlag GmbH & Co. KGaA, 2000.
- [164] Braskem, Beverage industry bets on Green Plastic, 2017. Retrieved from <https://www.braskem.com.br/braskem-news-detail/beverage-industry-bets-on-green-plastic>
- [165] C. Engineering, *Ethylene to Ethanol*, 2015.
- [166] A. Mohsenzadeh, A. Zamani, M.J. Taherzadeh, *ChemBioEng Reviews* 4 (2017) 75-91.
- [167] J.M. Winterbottom, in: C. Kemball, D.A. Dowden (Eds.), *Catalysis: Volume 4*, The Royal Society of Chemistry, 1981, pp. 141-174.
- [168] M. Zhang, Y. Yu, *Industrial & Engineering Chemistry Research* 52 (2013) 9505-9514.
- [169] D. Zhang, R. Wang, X. Yang, *Catalysis Letters* 124 (2008) 384-391.
- [170] J.H. de Boer, R.B. Fahim, B.G. Linsen, W.J. Visseren, W.F.N.M. de Vleeschauwer, *Journal of Catalysis* 7 (1967) 163-172.

- [171] F.F. Roca, L. De Mourgues, Y. Trambouze, *Journal of Catalysis* 14 (1969) 107-113.
- [172] J.J. McKetta Jr, *Encyclopedia of chemical processing and design*, CRC press, 1997.
- [173] E. Ezzo, G. El-Shobaky, M. Selim, *Surface Technology* 10 (1980) 47-54.
- [174] E. Ezzo, N. Yousef, H. Mazhar, *Surface Technology* 14 (1981) 65-72.
- [175] E.A. El-Katatny, S.A. Halawy, M.A. Mohamed, M.I. Zaki, *Applied Catalysis A: General* 199 (2000) 83-92.
- [176] M.M. Doheim, A.S. Ahmed, H.A. El-Boohy, G.A. El-Shobaky, *Journal of Radioanalytical and Nuclear Chemistry* 254 (2002) 583-588.
- [177] G. Chen, S. Li, F. Jiao, Q. Yuan, *Catalysis Today* 125 (2007) 111-119.
- [178] J. Lee, J. Szanyi, J.H. Kwak, *Molecular Catalysis* 434 (2017) 39-48.
- [179] J.R. Anderson, T. Mole, V. Christov, *Journal of Catalysis* 61 (1980) 477-484.
- [180] W.R. Moser, R.W. Thompson, C.-C. Chiang, H. Tong, *Journal of Catalysis* 117 (1989) 19-32.
- [181] X. Zhang, R. Wang, X. Yang, F. Zhang, *Microporous and Mesoporous Materials* 116 (2008) 210-215.
- [182] K. Ramesh, L.M. Hui, Y.-F. Han, A. Borgna, *Catalysis Communications* 10 (2009) 567-571.
- [183] K. Ramesh, C. Jie, Y.-F. Han, A. Borgna, *Industrial & engineering chemistry research* 49 (2010) 4080-4090.
- [184] Q. Sheng, K. Ling, Z. Li, L. Zhao, *Fuel Processing Technology* 110 (2013) 73-78.
- [185] A.G. Gayubo, A. Alonso, B. Valle, A.T. Aguayo, J. Bilbao, *AIChE Journal* 58 (2012) 526-537.
- [186] R. Le Van Mao, P. Levesque, G. McLaughlin, L.H. Dao, *Applied Catalysis* 34 (1987) 163-179.
- [187] S. Bun, S. Nishiyama, S. Tsuruya, M. Masai, *Applied catalysis* 59 (1990) 13-29.
- [188] I. Rossetti, M. Compagnoni, E. Finocchio, G. Ramis, A. Di Michele, Y. Millot, S. Dzwigaj, *Applied Catalysis B: Environmental* 210 (2017) 407-420.
- [189] Y. Hu, N. Zhan, C. Dou, H. Huang, Y. Han, D. Yu, Y. Hu, *Biotechnology Journal* 5 (2010) 1186-1191.

- [190] T.K. Phung, G. Busca, *Chemical Engineering Journal* 272 (2015) 92-101.
- [191] T.K. Phung, L. Proietti Hernández, A. Lagazzo, G. Busca, *Applied Catalysis A: General* 493 (2015) 77-89.
- [192] B.M. Lok, C.A. Messina, R.L. Patton, R.T. Gajek, T.R. Cannan, E.M. Flanigen, *Journal of the American Chemical Society* 106 (1984) 6092-6093.
- [193] D. Arias, A. Colmenares, M.L. Cubeiro, J. Goldwasser, C.M. López, F.J. Machado, V. Sazo, M.R. de Agudelo, *Catalysis letters* 45 (1997) 51-58.
- [194] Y. Chen, Y. Wu, L. Tao, B. Dai, M. Yang, Z. Chen, X. Zhu, *Journal of Industrial and Engineering Chemistry* 16 (2010) 717-722.
- [195] Y. Saito, H. Niiyama, *Journal of Catalysis* 106 (1987) 329-336.
- [196] J. Haber, K. Pamin, L. Matachowski, D. Mucha, *Applied Catalysis A: General* 256 (2003) 141-152.
- [197] V.V. Bokade, G.D. Yadav, *Applied Clay Science* 53 (2011) 263-271.
- [198] D. Varisli, T. Dogu, G. Dogu, *Chemical Engineering Science* 62 (2007) 5349-5352.
- [199] J. Gurgul, M. Zimowska, D. Mucha, R.P. Socha, L. Matachowski, *Journal of Molecular Catalysis A: Chemical* 351 (2011) 1-10.
- [200] A. Ciftci, D. Varisli, K. Cem Tokay, N. Asli Sezgi, T. Dogu, *Chemical Engineering Journal* 207-208 (2012) 85-93.
- [201] D. Varisli, T. Dogu, G. Dogu, *Industrial & Engineering Chemistry Research* 47 (2008) 4071-4076.
- [202] I. Holclajtner-Antunović, D. Bajuk-Bogdanović, A. Popa, V. Sasca, B. Nedić Vasiljević, A. Rakić, S. Uskoković-Marković, *Materials Chemistry and Physics* 160 (2015) 359-368.
- [203] A. Popa, V. Sasca, O. Verdes, I. Holclajtner-Antunović, *Reaction Kinetics, Mechanisms and Catalysis* 115 (2015) 355-375.
- [204] A. Popa, V. Sasca, *Reaction Kinetics, Mechanisms and Catalysis* (2017) 1-16.

## ***Chapter 2***

### ***Experimental***

## 2.1 Catalyst synthesis

### 2.1.1 Synthesis of SBA-15

Well-ordered hexagonal (space group  $P6mm$ ) mesoporous silica (SBA-15) was synthesised following the amphiphilic triblock copolymer procedure proposed by Zhao et al. [1]. Hence in order to form the emulsion, 10 g of Pluronic 123 was dissolved in H<sub>2</sub>O (75.5 cm<sup>3</sup>) at 40 °C, and stirred until complete dissolution. An aqueous solution 2 M of HCl (291.5 cm<sup>3</sup>) is added to facilitate the precipitation. The desired amount of silica precursor, tetraethyl orthosilicate (15.5 cm<sup>3</sup>), was added and left under vigorous stirring for 20 h at 40 °C. The precipitate was aged for 24 h at 80 °C, and finally the solid was filtrated and washed with distilled water and ethanol (total volume 1000 cm<sup>3</sup>) until complete neutralisation of the pH. Soft template removal was carried out by calcination, under air, for 6 h at 500 °C (1 °C/min).

### 2.1.2 Synthesis of supported heteropolyacids

A series of heteropolyacids, phosphotungstic acid (HPW), silicotungstic acid (HSiW) and phosphomolibdic acid (HPMo), supported on SBA-15 and fumed silica were prepared via wet impregnation [2], using different W or Mo wt% loadings (ranged 2-60 wt%). To perform the wet impregnation, the required amount of HPA (obtained using **Equation 2.1** [3]) was dissolved in 30 cm<sup>3</sup> of methanol in a round bottom flask, containing either support and stirred for 12 h at room temperature. The solvent was evaporated at room temperature, and the remaining solid ground and stored in air, without additional thermal treatment. Adsorbed water is extremely important to retain chemical and physical properties of HPAs, as protonic acidity and cluster aggregation.

$$\text{Theoretical loading\%} = 100\% \times \frac{W_{\text{HPA}}}{(W_{\text{HPA}} + W_{\text{Support}})}$$

**Equation 2.1** – Calculation of the theoretical loading.

where  $W_{\text{HPA}}$  is the mass of HPA corrected for the amount of crystalline water measured by thermogravimetric analysis and  $W_{\text{Support}}$  is the mass of support used.

## 2.2 Catalyst characterisation

### 2.2.1 X-ray Fluorescence (XRF)

Bulk elemental analysis was carried out via X-ray fluorescence on a Bruker S8 Tiger instrument, with the mass percentage of each element determined by SPECTRA software.

Fluorescence occurs when a core electron is hit by high-energy X-ray causing its ejection as a photoelectron. Destabilisation of the K-shell, due to the resulting core hole, results in atomic relaxation with an electron from a high energy orbital dropping into the core hole [4], the *demoted electron*. This is accompanied by an energy loss through *secondary X-ray* photoemission at a unique wavelength characteristic of each atom. Emission lines in the XRF spectra typically identify K-L and L-M, transitions according to IUPAC nomenclature as shown in **Figure 2.1**.

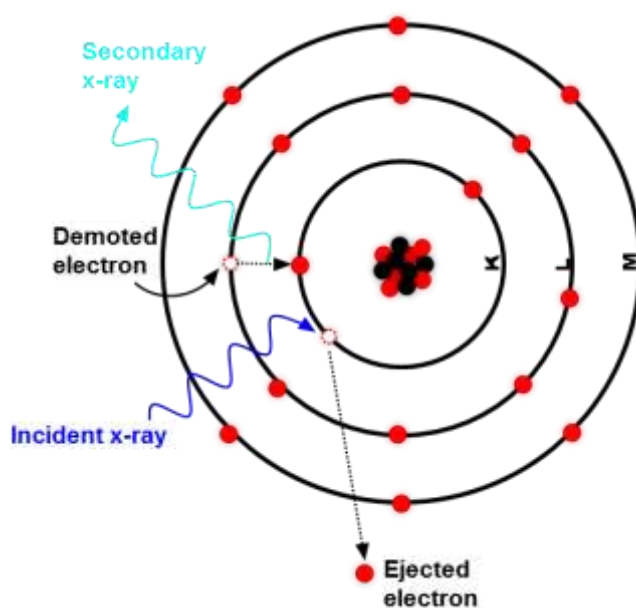


**Figure 2.1** – Illustrative representation of X-ray fluorescence.

**Equation 2.2** describes the energy of the fluorescent photon associated with electron relaxation, termed Moseley's law:

$$E = \frac{m_e q_e^2 q_z^2 (Z-1)^2}{8h^2 \epsilon_0^2} \cdot \left( \frac{1}{n_f^2} - \frac{1}{n_i^2} \right)$$

**Equation 2.2** – Moseley's law,

where,  $m_e$  is the electron mass,  $q_e$  is the electron charge,  $q_z$  represents the nuclear charge,  $Z$  atomic number,  $h$  is Planck's constant,  $\epsilon_0$  is the vacuum permittivity and  $n_f$  and  $n_i$  are the quantum numbers of the final and initial electron states respectively.

### 2.2.2 Carbon, Hydrogen, Nitrogen and Sulphur elemental analysis (CHNS)

Bulk carbon content of spent catalysts was determined on a Thermo-Scientific Flash 2000 CHNS/O analyser, equipped with Scientific MAS 200R autosampler, using He as carrier gas.

For CHNS elemental determination, sample flash combustion process takes place in a quartz tube reactor heated at  $\sim 1000$  °C, converting carbon to carbon dioxide, hydrogen to water, nitrogen to nitrogen gas or oxide and sulfur to sulfur dioxide, other products formed during the combustion are removed via adsorbents. The resultant gases are passed over high purity copper to remove any trace of oxygen and to convert the sample into the elemental gases (i.e. nitrogen oxide into nitrogen gas). GC separation and thermal conductivity detection (TCD) detection are used for the quantification of the elements.

### 2.2.3 Powder X-ray diffraction (XRD)

Powder XRD patterns were recorded on a Bruker D8 Advance Diffractometer equipped with a LynxEye high-speed strip detector. Cu K $\alpha$  (1.54 Å, 8.04 KeV) radiation was produced, monochromated using a nickel filter and calibrated to the diffraction pattern of quartz. Low angle data collection occurred between  $2\theta = 0.45$ - $8^\circ$  (step size  $0.01^\circ$  and scan speed of  $0.014^\circ \text{ s}^{-1}$ ) and wide angle collection between  $2\theta = 10$ - $80^\circ$  (step size  $0.02^\circ$  and scan speed of  $0.02^\circ \text{ s}^{-1}$ ). Powder samples were placed in a spinner, ensuring the surface was flat, without any further treatment.

In situ measurements were performed under N<sub>2</sub> flow, heating the sample to the desired temperature (ramp rate  $10$  °C  $\text{min}^{-1}$ ), and collecting the diffraction pattern after 60 min at each temperature. In-situ measurements were performed using an Anton-Paar XRK-900 cell fitted with beryllium windows and gas flow was controlled using Bronkhorst EL-flow select mass flow controllers (error of  $\pm 0.1$  ml  $\text{min}^{-1}$ ) and an Eurotherm 2604 advanced controller. The X-ray source was aligned using the parallel beam geometry for

in-situ measurements, using a Göbel mirror and 0.2 mm slit, resulting in a spot size of 0.3 mm.

Solid matter is described as amorphous, for which there is a random arrangement of atoms, or crystalline where atoms are arranged in a two or three-dimensional ordered repetition of same unit cells. In crystalline solids, the interaction between X-rays and the powder sample, results in a specific X-ray diffraction pattern, characteristic of the unique atomic arrangement. Laboratory X-ray photons are typically produced from a copper anode, which in turn is excited by high-energy electrons generated from a tungsten filament. Cu  $K\alpha$  X-ray photons are directed at the finely packed powder sample, in which crystalline or ordered phases are homogeneously distributed. As shown in

**Figure 2.2**, the elastic scattering of the incident radiation, in all directions, will generate constructive, if in-phase, and destructive, if not in-phase, interference. These interference diffraction patterns are indicative of the phase and structural order within solids [4-6].

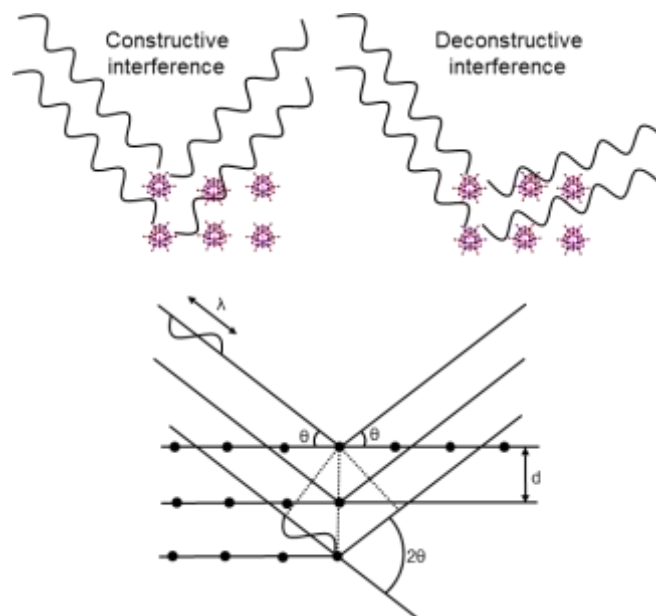


**Figure 2.2** – Schematic of X-ray interference with atomic lattice (top); relation between lattice spacing ( $d$ ) and correlation between  $\lambda$  and  $\theta$  (bottom).

According to the Bragg's Law (Equation 2.3), constructive interference occurs for specific values of  $\theta$  when the distance between scatters is equal to the X-ray wavelength multiplied by an integer value [7]:

$$n\lambda = 2d \sin (\theta)$$

**Equation 2.3** – Bragg’s law.

where,  $n$  is an integer number (1, 2, 3 ...), referred to the number of reflections,  $\lambda$  is the wavelength of the incident wave,  $d$  is lattice distance, and  $\theta$  is the diffraction angle.

Lattice planes of crystallites are denoted by the Miller indices (h, k, l), which indicate the set of all planes with same symmetry, that intercept the unit cell. The indices are inversely proportional to the lattice vectors. When the unit cell is described as a cubic system, the lattice vectors are equals ( $a = b = c$ ), and the planes spacing can be also calculated as:

$$d = \frac{a}{\sqrt{h^2 + k^2 + l^2}}$$

**Equation 2.4** – d spacing calculation, where  $a$  = lattice parameter and h,k,l are Miller indices.

For laboratory X-ray sources, crystalline materials and ordered porous solids generate diffraction peaks only when the length scale of periodicity exceeds around 2 nm; additionally, a decrease of particle size leads to an increase of peak width. Thus, large crystallites with numerous lattice planes create well-defined and more intense peaks due to multiple constructive diffractions; whereas, in small crystals this effect does not occur leading to less intense peaks [6]. The Scherrer Equation describes the relation between particle size and peak FWHM [8]:

$$PS_{av} = \frac{k\lambda}{\left(\sqrt{(B^2 + S^2)} \cos\theta\right)}$$

**Equation 2.5** – Scherrer equation.

where  $S$  is the systematic broadening caused by the diffractometer;  $B$  is the FWHM of the diffraction peak;  $k$  is a constant (0.9); and  $PS_{av}$  is the averaged particle size (Å).

As deduced from Bragg’s law (**Equation 2.3**), the position of the diffraction peaks is inversely proportional to sample’s periodicity. Thus, crystalline materials display diffraction peaks at high values of  $2\theta$ , within 10-80° (wide angle analysis), whereas macromolecules and highly ordered porous materials, as SBA-15 and MCM-14, which exert a long-range order due to the pore network, exhibit peaks between 0-10° (low angle

analysis). **Figure 2.3** displays how to derive structural properties of mesoporous materials from XRD analysis.

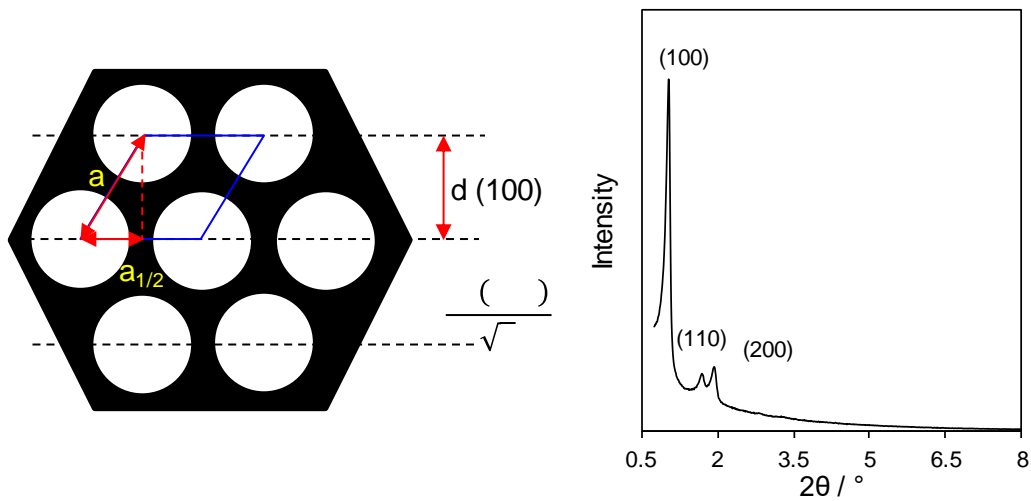


**Figure 2.3** – Schematic of the relationship between the hexagonal SBA-15 structure,  $d(100)$  = layer spacing and  $a$  = pore spacing.

When Miller indices and Bragg's law are combined, as in **Equation 2.6**, the space between layers,  $d(100)$ , is measured, and  $a$  can be finally deduced by geometrical relationship. Additionally, pore spacing can be hence combined with porosimetry analysis to calculate wall thickness of the ordered mesoporous structure by simply subtraction with pore diameter.

$$a = \frac{\lambda \sqrt{h^2 + k^2 + l^2}}{2 \sin \theta}$$

**Equation 2.6** – Inter layer spacing calculation.

where  $a$  = lattice parameter;  $\lambda$  is wavelength of Cu K $\alpha$  radiation;  $h, k, l$  are Miller indices; and  $\theta$  is the diffraction angle.

#### 2.2.4 Nitrogen porosimetry

Nitrogen porosimetry was conducted on a Quantachrome Nova 4200e porosimeter, employing, for data analysis, Novawin v11.0 software. Samples were degassed at 120°C for 4 h prior to N<sub>2</sub> adsorption at -196 °C. BET surface areas calculated over the range  $P/P_0 = 0.05-0.2$ , in which a linear correlation was observed [9]. Mesopore size distributions were obtained on the desorption isotherm, and calculated using the BJH model [10].

Adsorption, of atoms or molecules on surface of materials, occurs by two methods, physisorption or chemisorption. N<sub>2</sub> adsorption at low temperature is classified in the former and is widely used to characterise textural properties of solid materials. Physisorption occurs due to weak van der Waals forces (dipole-dipole interaction) that occur between the adsorbate, in this case nitrogen, and adsorbent, the surface of the solid.

At constant temperature and pressure, adsorption leads to a decrease in system entropy, thus, if the process is to be spontaneous (negative Gibbs free energy), then adsorption enthalpies must always be negative (exothermic) [11, 12]. The enthalpy of physisorption is usually <20 kJ mol<sup>-1</sup>, insufficient for bond breaking, with the energy produced dissipated as thermal motion [12]. N<sub>2</sub> adsorption is performed at its condensation temperature, -196 °C, at which temperature adsorption is dominated by London forces (sub-category of the van der Waals) through induced dipoles. These dispersion forces are responsible for attractive adsorbate-adsorbate and adsorbate-surface interactions. According to the dynamic equilibrium of the system, the rate of adsorption equal the rate of desorption, and the volume of N<sub>2</sub> adsorbed is recorded as a function of pressure at constant temperature to produce an adsorption isotherm [13].

The isotherm shape depends on the nature of the adsorbent; IUPAC classification [14] define six different types as shown in **Figure 2.4-left**. Microporous materials (such as activated carbon, zeolites and some porous oxides) display a reversible type I isotherm, where adsorbent and adsorbate strongly interact within the micropores. Type II isotherm is observed for non-porous and macroporous materials, in which *point a* represents the monolayer completion and the beginning of multilayer adsorption. Type III occurs when interactions between adsorbate molecules are stronger than those with the adsorbent, characteristic of non-porous material. Type IV isotherm possess, as type II, a *rounded knee* shape (*point a*), which indicates monolayer formation prior to multilayer formation; this isotherm also exhibits a hysteresis loop associated with capillary condensation occurring within the mesopores. Type V isotherms also show hysteresis, which is common for materials that have mesoporosity; however, for type V a greater interaction occurs between adsorbate molecules than adsorbate-adsorbent. Finally, type VI isotherms display a stepwise multilayer sorption, which is due to a uniform non-porous surface.

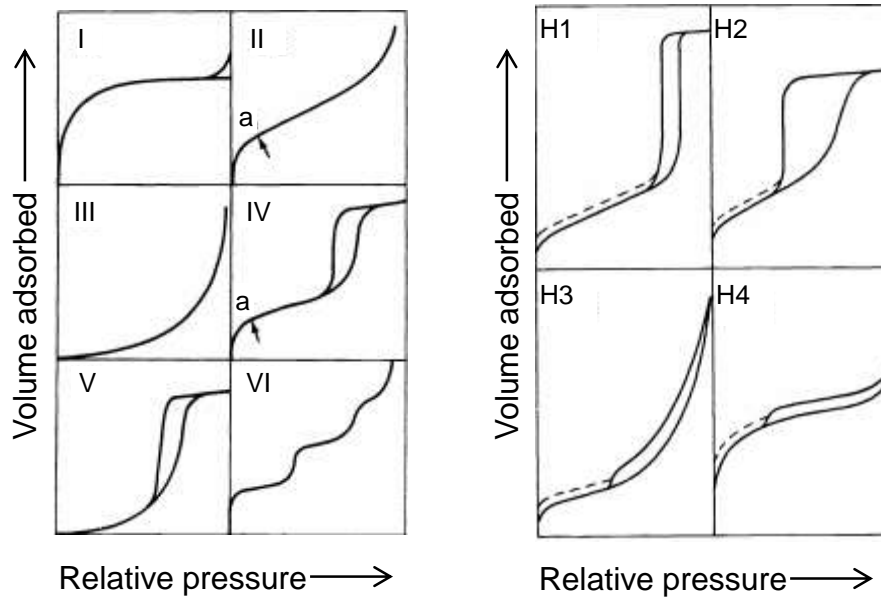


**Figure 2.4** – (left) IUPAC nomenclature for the six type of isotherms; relative pressure is defined as  $P/P_0$ ; the volume adsorbed ( $\text{cm}^3 \text{g}^{-1}$ ); (right) IUPAC nomenclature for the 4 types of hysteresis loop. [15]

As described above, mesoporous structures exhibit, generally, either type IV or type V isotherms, where capillary condensation leads to the formation of a hysteresis loop. Depending on the pore structure, a variety of shapes have been characterised and are here reported in **Figure 2.4-right** [14]. H1 and H2 are often attributed to uniform well-shaped pores and ink-bottle pores respectively, while slit-shaped pores produce H3 and H4 (with type I character).

The surface area measurement employs the Brunauer-Emmet-Teller (BET) [9] calculation (**Equation 2.7**) and is widely used to characterise textural properties of solids.

$$\frac{P}{V_a(P_0-P)} = \frac{1}{V_m C} + \frac{C-1}{V_m C} \left( \frac{P}{P_0} \right)$$

$$V_m = \frac{1}{(\text{Gradient} + \text{Intercept})}$$

$$C = \left( \frac{\text{Gradient}}{\text{Intercept}} \right) + 1$$

$$sa = \frac{V_m \sigma N_a}{mv}$$

**Equation 2.7** – BET equation.

where  $P$  is pressure;  $P_0$  is the saturation pressure;  $V_a$  refers to the volume absorbed and  $V_m$  to the monolayer volume;  $C$  is the multilayer adsorption parameter;  $sa$  is the surface area,  $\sigma$  is the  $N_2$  cross-sectional area ( $0.162 \text{ nm}^2$ ), assuming hexagonal close packing;  $N_a$ , the Avogadro number;  $m$ , sample mass, and, finally,  $v$ , the gas molar volume.

Pore size distributions were calculated using the BJH method (from the researchers Berret, Joyner and Halenda) [10], which is the most widely used for mesoporous materials. It employs an extension of the Kelvin model (**Equation 2.8**) to describe pore filling, assumes cylindrically shaped pores, and a hemispherical meniscus with zero contact angle.

$$\ln\left(\frac{P}{P_0}\right) = -\left(\frac{2\gamma v \cos\theta}{RT r_m}\right)$$

**Equation 2.8** – Kelvin equation.

where  $P/P_0$  refers to the relative pressure in equilibrium with condensed gas meniscus;  $\gamma$  is the liquid surface tension;  $v$  is the condensed adsorbate molar volume;  $\cos\theta$ , the adsorbate surface contact angle (0 for  $N_2$  thus  $\cos\theta = 1$ );  $R$ , the gas constant;  $T$  the temperature, and, finally,  $r_m$ , the mean radius of condensed gas meniscus.

### 2.2.5 Scanning transmission electron microscopy (STEM) and energy dispersive X-ray analysis (EDX)

Scanning TEM (STEM) images were recorded on an aberration-corrected JEOL 2100F FEG STEM operating at 200 keV and equipped with a spherical aberration probe corrector (CEOS GmbH) and a Bruker XFlash 5030 EDX. The powder samples were dry deposited onto 300-mesh carbon coated copper grids. Micrographs were analysed using ImageJ 1.41 software.

A scanning transmission electron microscope (STEM) is a type of transmission electron microscope (TEM) in which the electron beam is scanned over the sample in a raster (moving from side to side and from top to bottom), similarly to scanning electron microscope (SEM). In the STEM configuration (see **Figure 2.5**), a high-energy electron beam is firstly focused to form a small probe via a series of condenser lenses to provide

an atomic-scale spot and enhance the resolution. The probe is further reduced and fired onto the sample via a combination of objective lenses and an aberration system. The scan coils allow the beam to be moved rastering the sample, which, makes the STEM a suitable technique for analytical purposes, employing Z contrast dark-field imaging (called high-angle annular dark-field HAADF), energy dispersive X-ray (EDX) and electron energy loss spectroscopy (EELS). When the probe strikes onto the sample, the elastically transmitted electrons exhibit different angles with the respect of the optical axis [16, 17]. Bright field detector, perpendicular to the transmitted beam, collects information about the electrons that leave the sample with a relatively low angle compared to the incident beam convergence angle. HAADF is an annular detector that collects the electrons transmitted at higher scattering angles. Signals are proportional to sample density and thickness but also to the atomic number of the sample, hence the heavier the atom, the higher the intensity of the scattering, and the brighter the image will be [18]. The combination of HAADF and the raster scan technique, allow the exact identification of the atoms in the specimen. When the electrons transmitted are non-elastically scattered, the amount of energy loss can be measured (EELS) giving information about the chemical bonding, valence and conduction bands electronic properties and so. EDX measurements use the X-rays emitted from the sample hit by the probe, which excites core holes in atoms within the sample. Relaxation of higher energy electrons into these core holes is accompanied by X-ray fluorescence with an energy characteristic of the element and hence provides information about the atomic composition of the sample [19].

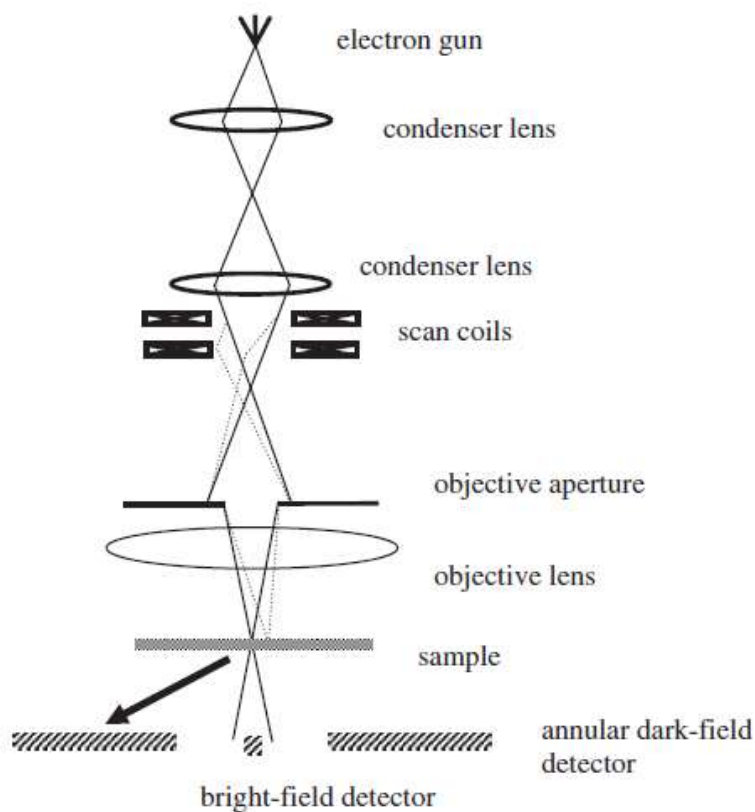


**Figure 2.5** – Schematic STEM microscope configuration [20].

### 2.2.6 Thermogravimetric analysis (TGA)

Thermogravimetric analysis (TGA) was performed on a Mettler Toledo TGA/DSC 2 Star System calibrated with  $\text{Al}_2\text{O}_3$ , using Mettler Star1 analysis software for data analysis (**Figure 2.6**). Samples (5-10 mg) were placed into an alumina crucible (70  $\mu\text{L}$ ) and heated between 40 and 800°C employing a ramp rate of 10°C  $\text{min}^{-1}$ , under  $\text{N}_2$  (~60 mL  $\text{min}^{-1}$ ). The sample's mass was recorded as function of temperature, and analysed after subtraction of the corresponding mass loss of an empty crucible.

TGA is an important technique, which monitors mass changes under applied heat, and reveals the thermal stability of components within a sample. For instance, TGA analysis of HPA samples was employed to determine water desorption, which occurs in two discrete steps (as reported in **Chapter 3**), and heteropolyanion decomposition. Analysis of the support also revealed possible synthetic residues.



**Figure 2.6** – Picture showing Mettler Toledo TGA/DSC 2 Star System.

### **2.2.7 Propylamine chemisorption and temperature programmed desorption (TPD)**

N-propylamine (Sigma Aldrich,  $\geq 99\%$ ) chemisorption, followed by temperature programmed desorption (TPD) allowed acid strength analysis of solid samples. 10 mg of materials were impregnated with  $0.5 \text{ cm}^3$  of n-propylamine and dried under *vacuum*, prior analysis, at  $40^\circ\text{C}$ . Samples (5-10 mg) were placed into an alumina crucible ( $70\mu\text{L}$ ), and TPD was performed on a Mettler Toledo TGA/DSC 2 Star System between 40 and  $800^\circ\text{C}$ , using a ramp rate of  $10^\circ\text{C min}^{-1}$  employed with a Pfeiffer Vacuum, ThermoStar MS spectrophotometer detector (**Figure 2.6**).

Solid acidity was determined studying the desorption temperature (indicated by mass loss) of reactively-formed propene, formed at the catalyst acid sites (followed by MS). The reaction to ammonia and propene is an elimination similar to the Hofmann reaction, which produces alkenes from quaternary ammonium salts via anti-Saytsev elimination [21]. In our case, the alkyl amine reacts with the acid sites of the sample in a concentrated elimination, and extraction of the most available proton of the alkyl chain hence forming the alkene [22-24]. n-Propylamine was chosen over other amine, as ethylamine or butylamine, because it is less subject to secondary reactions; while the iso-amine was rejected due to the lower temperature of reaction to alkene and ammonia.

In **Figure 2.7** is reported the proposed mechanism that occurs over the surface of catalysts:

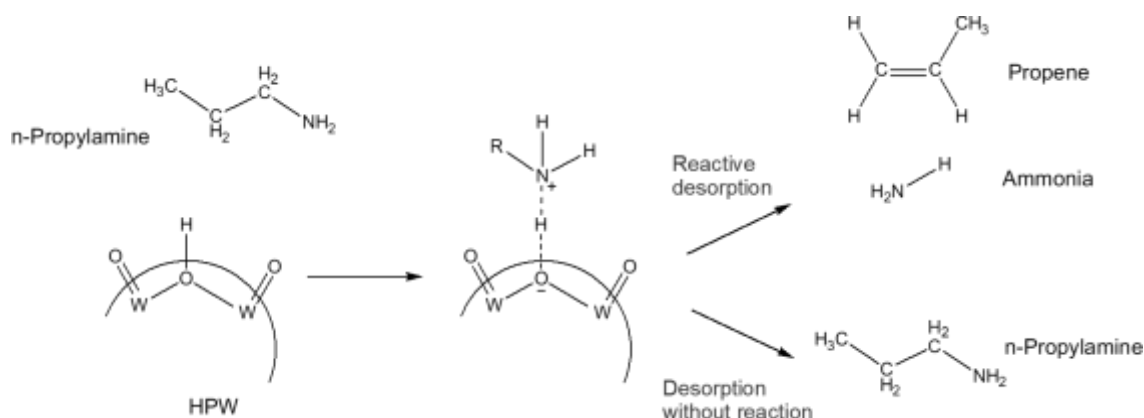


**Figure 2.7** – n-Propylamine proposed mechanism over protonic acid sites [22].

### 2.2.8 Diffusive reflection infrared Fourier transform spectroscopy (DRIFTS)

DRIFT spectra were collected on samples diluted in KBr (5 wt%) powder and stored at 70 °C under vacuum before analysis. Spectra were recorded at 120 °C on a Thermo Scientific Nicolet iS50 FT-IR spectrometer equipped with a praying mantis environmental cell (**Figure 2.8**). Data collection was employed with Omnic software and spectra plotted in Kubelka-Munk form as function of wavenumber. In situ measurements were performed on samples diluted in KBr (10 wt%) powder and stored at 120 °C prior analysis. Spectra were collected under N<sub>2</sub> heating the sample at the desired temperature (ramp rate 10 °C min<sup>-1</sup>), between 120 and 600 °C, after 30 min at each temperature.

Infrared (IR) spectroscopy is a non-destructive technique which studies “vibrational transitions” associated with changes in dipole moment during exposure of molecules to infrared light [7]. IR radiation has lower energies than visible light, i.e. longer wavelength and lower frequencies. The infrared region (from 100 μm to 1 μm of the electromagnetic spectrum) is divided into three sub-regions named on their energy values compared with the visible range: Near-IR (close to the visible range), Far-IR and Mid-IR. Depending on the functional groups and sample surface roughness, incident radiation can be transmitted or reflected with energy adsorptions characteristic of the molecular species present whose vibrational modes are excited [12].

Samples were first diluted with an inert IR transparent material, potassium bromide, to prevent complete adsorption of incident photons. Analysis was performed in reflections mode (DRIFTS) employing the Kubelka-Munk formalism to reflection spectra [25]:

$$f(R_{\infty}) = \frac{(1-R_{\infty})^2}{2R_{\infty}} = \frac{k}{s}$$

**Equation 2.9** – Kubelka-Munk equation.

where  $R_{\infty}$  is the absolute reflectance of the layer,  $s$  is the scattering coefficient and  $k$  is the molar absorption coefficient.

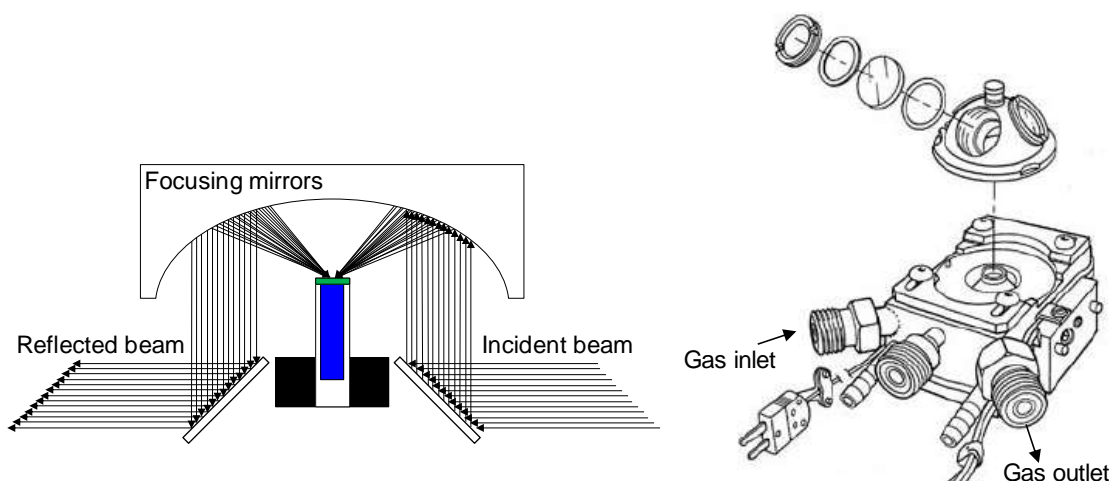


**Figure 2.8** – Scheme showing DRIFT configuration (right) and the praying mantis environmental cell (left).

### 2.2.9 $\text{NH}_3$ titration and temperature programmed desorption (TPD)

Surface acidity was also studied via ammonia chemisorption using a Quantachrome ChemBET3000 system with a MKS Minilab MS detector. Samples (25–50 mg) were placed in a quartz U-shaped chemisorption cell and outgassed at  $150^\circ\text{C}$  under flowing He ( $150 \text{ cm}^3 \text{ min}^{-1}$ ) for 4 h prior to titration. Manual injections ( $0.05 \text{ cm}^3$ ) of 10 vol%  $\text{NH}_3$  in He were carried out at  $100^\circ\text{C}$ , and the  $\text{NH}_3$  signal (17 m/z) monitored in real-time. Consecutive injections were performed until complete saturation of acid sites (indicated by first breakthrough and then a plateau in the signal of non-adsorbed ammonia, see **Figure 2.9**) occurred. Temperature programmed desorption (TPD) was subsequently performed on ammonia saturated samples between  $100$  and  $800^\circ\text{C}$  employing a ramp rate of  $10^\circ\text{C min}^{-1}$  under flowing He ( $150 \text{ cm}^3 \text{ min}^{-1}$ ).

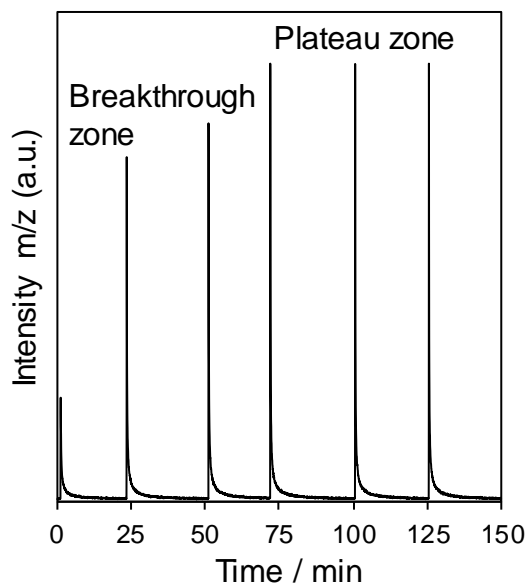


**Figure 2.9** – Photo showing consecutive performed injections, revealing the breakthrough zone and the plateau zone.

As already described for  $N_2$  porosimetry, atoms and molecules can adsorb on the surface of solid compound via physical or chemical adsorption [12].  $NH_3$  adsorption over solid acids occurs via the latter. In chemisorption, strong interactions exist between adsorbate species and specific sites on the surface, which in the case of a catalyst usually correlate with the active sites. The enthalpy of adsorption due to chemical bond formation varies greatly depending on the adsorbate and surface involved;  $NH_3$  chemisorbed on Fe for instance exhibits a  $\Delta H_{ads}$  around  $200 \text{ kJ mol}^{-1}$  [12]. Chemisorption can be molecular (non-dissociative) or dissociative depending on the nature of the components, temperature and pressure.

The technique is used to calculate the amount (mmol) of ammonia chemisorbed per g of sample, assuming a 1:1 stoichiometry between ammonia and acid sites, thus, enables the determination of the acid site density of samples. TPD can be also performed to determine the adsorption energy of  $NH_3$  from measurement of its desorption temperature during sample heating.

### 2.2.10 X-ray photoelectron spectroscopy (XPS)

XPS analysis was carried out on a Kratos Axis HSi photoelectron spectrometer equipped with a charge neutralizer and magnetic focusing lenses, employing monochromatic Al  $K\alpha$  radiation (1486.6 eV). Spectral fitting was performed using CasaXPS version 2.3.14,

with W 4f spectra and Mo 3d spectra fitted with a common Doniach-Sunjic lineshape and FHMW. Errors were estimated by varying a Shirley background across reasonable limits.

XPS analysis gives useful information on elemental composition, electronic and chemical state of solid sample, oxidation state, and electronegativity of any ligands. It is a surface-sensitive technique due to the short mean free path of excited photoelectrons, which in laboratory instruments are typically only detectable from the top 1-3 nm of a surface [11]. Electron analysers detect the intensity of emitted photoelectrons with kinetic energies spanning 0-1500 eV, which yields the surface composition of the material [26]. Measurements are normally made under ultra-high vacuum (UHV) due to the short mean free path of the photoelectrons which must be detected, with spectra usually reported according to the binding energy of photoelectrons. Photo-excitation occurs as previously described, with incident X-ray photons exciting core electrons, which are ejected as photoelectrons with kinetic energies characteristic of each element (**Figure 2.10**). Atomic relaxation results in X-ray fluorescence, and the emission of secondary photoelectrons via the Auger process, in which some energy from a demoting electron is transferred to a valence electron which is ejected from the atom with a specific kinetic energy. Auger energies are independent of the X-ray radiation source inducing them and hence can be used to discriminate elements whose photoelectron energies from direct core-hole excitation overlap [26].

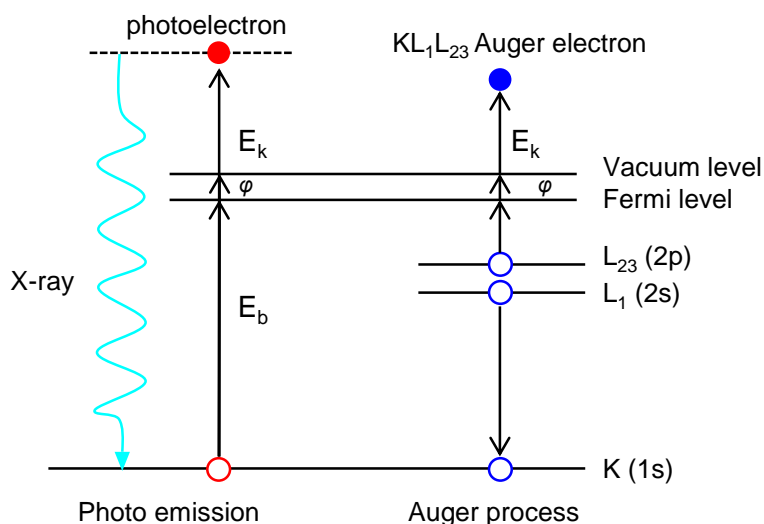


**Figure 2.10** – Photoemission and Auger process.

The binding energy of an emitted photoelectron is related to its kinetic energy by Rutherford's law (**Equation 2.10**).

$$E_k = h\nu - E_b - \phi$$

**Equation 2.10** – Kinetic energy evaluation via XPS.

where  $E_k$  is the kinetic energy of the photoelectron,  $h$  is Planck's constant,  $\nu$  is the frequency of the exciting radiation,  $E_b$  is the binding energy of the photoelectron, and  $\phi$  represents the work function of the spectrometer, and is related to the instrument.

This technique allows the discrimination of photoelectrons arising from quantum states. The cumulative angular momentum of electrons ( $j$ ) is described by the relation  $j = l + s$ ; where  $s$  is the spin angular momentum ( $s$ ) and  $l$ , the orbital angular momentum, 0, 1, 2, 3... labelled respectively as s, p, d, f... . Thus, for each  $l \geq 1$ , being  $s$  either  $+1/2$  or  $-1/2$ ,  $j$  will possess a couple of sub-levels, which will generate two photoemission peaks.

Quantum theory calls this effect the spin-orbit splitting, with the energy separation (due to angular momentum coupling) and relative intensity of spin-orbit split components determined by the atomic orbitals from which the photoelectron arises.

### 2.2.11 Raman spectroscopy

Raman spectra were obtained on a InVia Raman Microscope Renishaw fitted with 532 and 633 nm lasers, and Wire 3.4 software. Data were collected ranging between 100–1200  $\text{cm}^{-1}$ , employing a 532 nm source and x20 lens magnification; samples were exposed for 10 sec to the beam source, recoding 50 accumulations at 50 % laser power.

Raman spectroscopy originates from the interaction of light with matter; however, it focuses on molecular vibrations associated with *inelastically* scattered photons generated by an intense laser radiation [7]. According to quantum theory, molecules exhibit discrete rotational and vibrational energy levels. When hit by a photon, the energy of a compound transits to an excited virtual state. The descending process, to a lower real state, occurs via photoemission. The emitted photons which exhibit different frequencies than the  $\nu_0$ , lead to Stokes and anti-Stokes emissions, as depicted in **Figure 2.11** [4, 12]. The Stokes emission possesses longer wavelength (lower energy) than the incident radiation, while it is greater than  $\nu_0$  for the anti-Stokes.

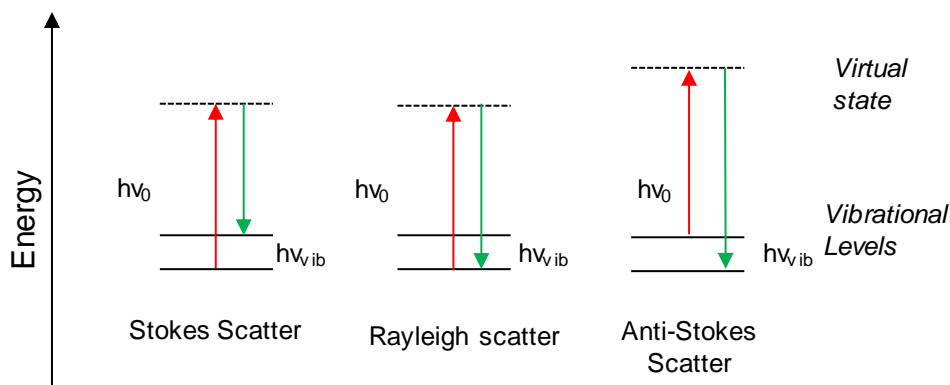


**Figure 2.11** – The Raman effect.

## 2.3 Catalytic tests

Catalytic tests were performed employing synthesised solid catalysts, to study the effect of support architecture and acidic strength (by changing the type of HPA) first, on the alpha-pinene isomerisation, a batch type reaction; and second, on ethanol dehydration a flow type reaction.

### 2.3.1 Batch reaction – $\alpha$ -Pinene isomerisation

The catalytic conversion of  $\alpha$ -pinene was carried out in a Radleys Starfish glass reactor (25 mL), mixing the solution with a magnetic stirrer, under air at 60 °C (**Figure 2.12**). The reaction mixture was prepared mixing 0.2 cm<sup>3</sup> of internal standard tetradecane to 126 mmol of  $\alpha$ -pinene in a round-bottom flask. The homogeneous mixture was stirred at 700 rpm and heated, thus 100 mg of catalyst were added. Aliquots (0.25 mL) were sampled periodically during 6 h of reaction, filtered, diluted in DCM and analysed by using a Bruker Scion 456-GC with an 8400 autosampler, fitted with a CP-5 column (30 m  $\times$  0.32 mm  $\times$  0.25  $\mu$ m) and flame ionisation detector.

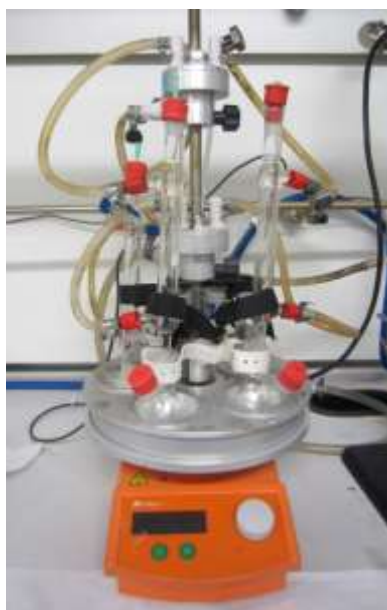


**Figure 2.12** – Pictutre showing the Radleys Starfish reactor.

Response factor values determined from multipoint calibration curves allowed the calculation of product yield. An exemplary chromatogram is reported in **Figure 2.13**. Conversion and selectivity were determined employing **Equation 2.11**; activities were obtained from the linear portion of reaction profiles. Experiments were repeated twice for reproducibility and values are quoted  $\pm 2$ .

$$\text{Conversion / \%} = \left( \frac{[\text{mol}_{t=0} - \text{mol}_t]}{\text{mol}_t} \right) \times 100$$

$$\text{Product selectivity / \%} = \left( \frac{\text{mol}_i}{\sum \text{mol}_{\text{products}}} \right) \times 100$$

**Equation 2.11** – Conversion and product selectivity.

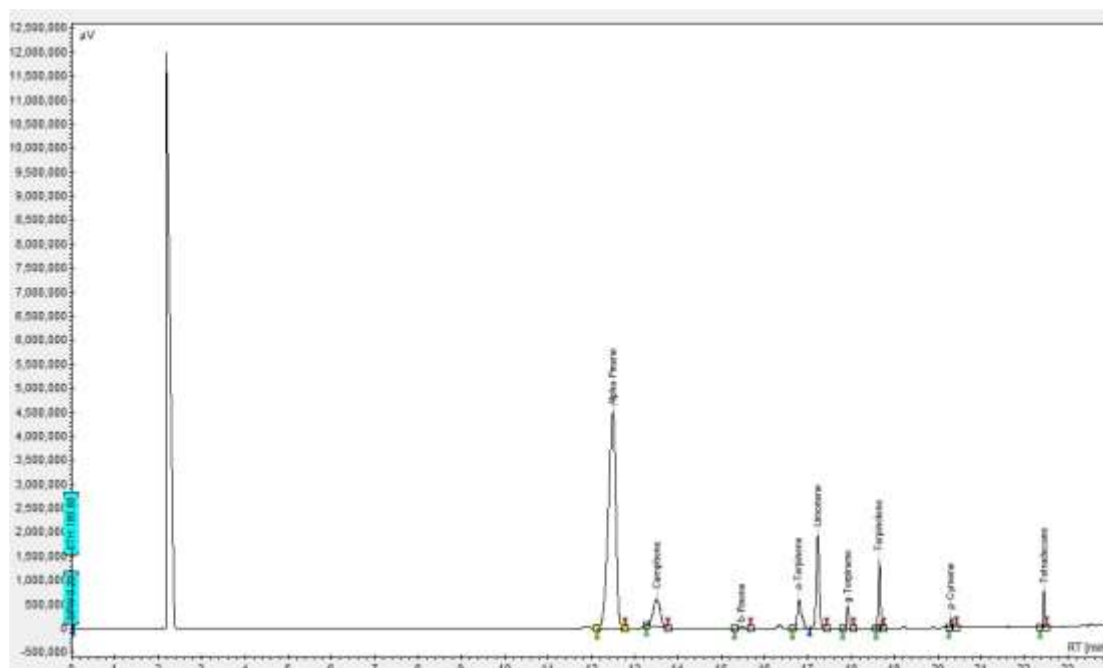


**Figure 2.13** – Typical chromatogram for  $\alpha$ -pinene isomerisation.

### 2.3.2 Continuous flow reaction – Ethanol dehydration

Gas phase reactions were undertaken using a glass tube continuous plug-flow reactor (10 mm of inner diameter, 420 mm of total length), packed with 5 cm<sup>3</sup> of fixed catalytic bed, and reaction occurred at atmospheric pressure (

**Figure 2.14**). All the lines were heated at 100 °C in order to prevent condensation of liquid compounds along the system. The quartz reactor was heated using a Carbolite VST 12/200 Split Tube furnace. On-line GC analysis for product detection were performed using a Shimadzu GC-2014 fitted with HP-PLOT Q column (30mm×0.53mm×40 $\mu$ m), flame ionisation detector (FID) and thermal conductivity detector (TCD) and equipped with Vici Valco Instrument E36-220 gas-sampling valve 100°C. Data analysis was performed with LabSolutions software. Multipoint calibration curves were employed to calculate response factor of liquid and gas compounds, using liquid solutions and well-defined gas mixtures (see *List of chemicals*) respectively.

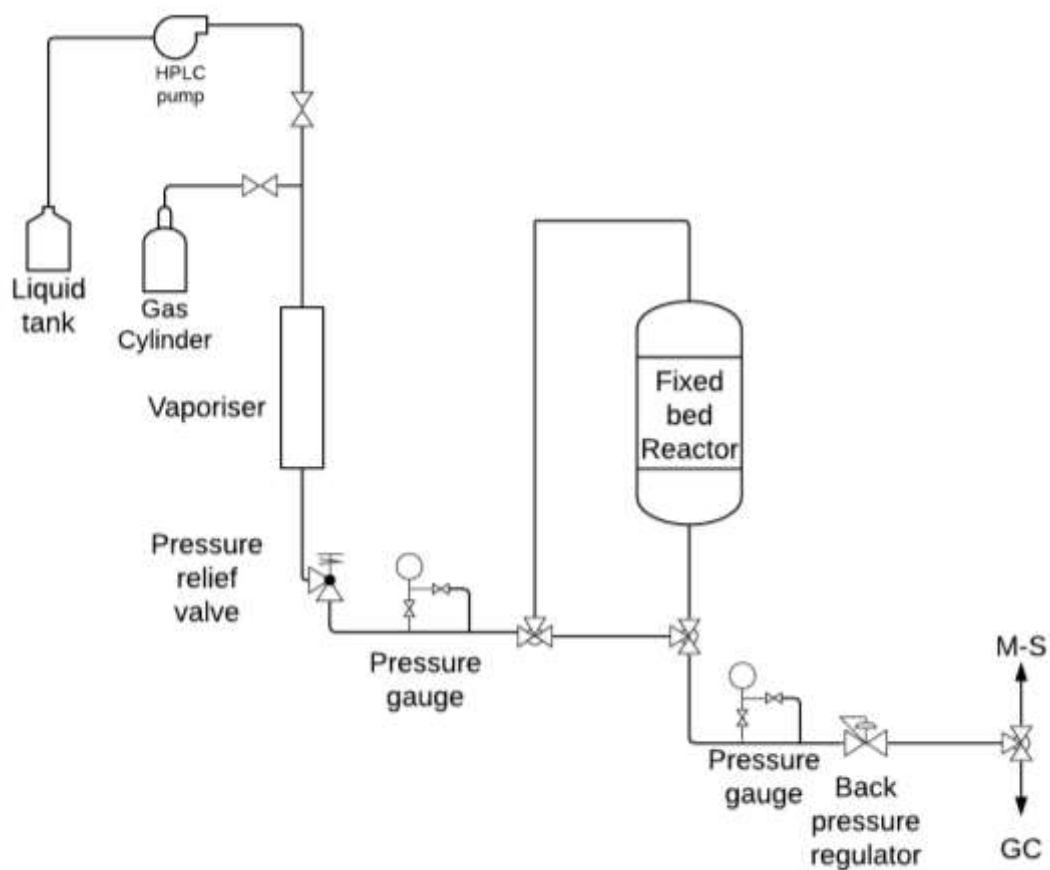
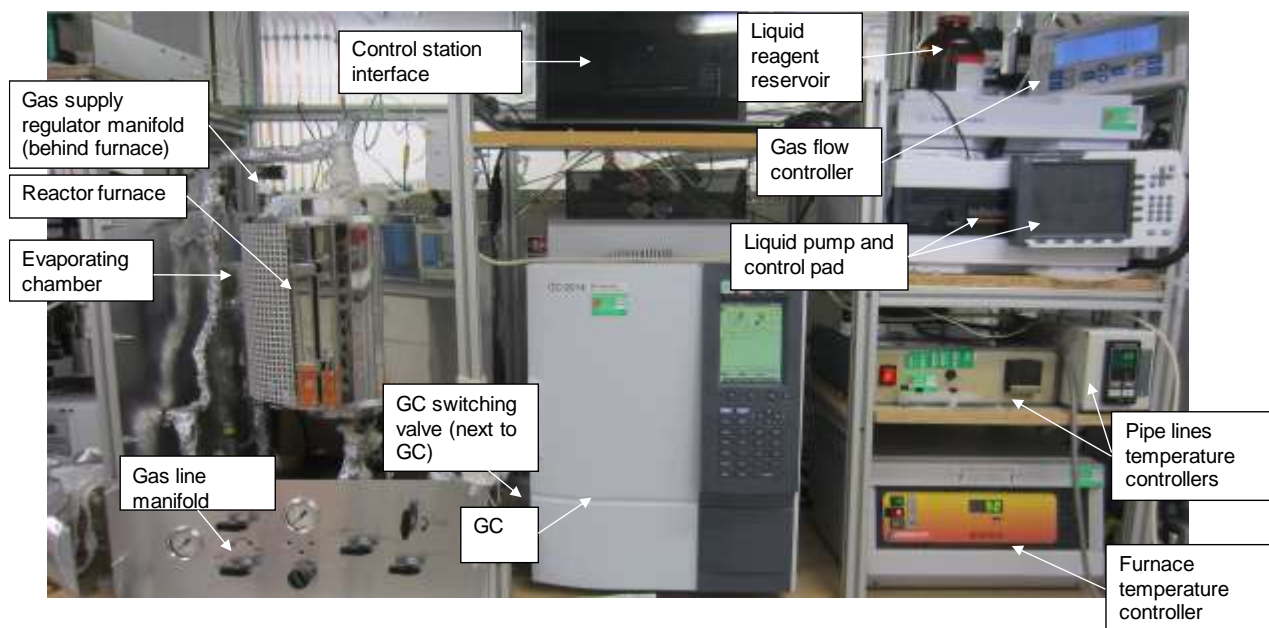


**Figure 2.14** – Continuous flow reactor – photo (top); scheme (bottom).

As shown in

**Figure 2.14**-bottom, liquid feed was added to the N<sub>2</sub> stream using a 1200 capillary Iso Pump Infinity Agilent, to avoid back-pressure of gas. At the evaporator unit, a ½” stainless steel tube filled with quartz chips, the total stream was homogenously mixed and in gaseous phase. By-pass line and reactor line, were switched alternatively as required. Reaction conditions were as follows:

### Ethanol dehydration

Nitrogen 50 cm<sup>3</sup>min<sup>-1</sup>, Ethanol 0.2 mLmin<sup>-1</sup> liquid (0.0034 mol min<sup>-1</sup>). Stainless steel pipes heated at 100 °C and reactor temperature ranging between 150-350°C.



**Figure 2.15** – Typical chromatogram for ethanol dehydration reaction.

## 2.4 List of chemicals

- Pluronic 123 (poly(ethylene glycol)-*block*-poly(propylene glycol)-*block*-poly(ethylene glycol)), Sigma Aldrich,  $M_n \sim 5,800$ .
- Hydrochloric acid (HCl), VWR Chemicals, 37%.
- Tetraethyl orthosilicate (TEOS), Sigma-Aldrich,  $\geq 99.999\%$ .
- Ethanol, VWR Chemicals, ACS reagent.
- Silica, fumed, Sigma Aldrich, powder.
- Phosphotungstic acid (HPW), Sigma Aldrich,  $\geq 99.9\%$ .
- Silicotungstic acid, (HSiW), Sigma Aldrich,  $\geq 99.9\%$ .
- Phosphomolybdic acid (HPMo), Sigma Aldrich,  $\geq 99.9\%$ .
- Methanol, VWR Chemicals, ACS reagent.
- $\alpha$ -Pinene, Sigma Aldrich, 99.9%.
- Tetradecane, Sigma Aldrich,  $\geq 99\%$ .
- Dichloromethane (DCM), Thermo Fisher Scientific, Laboratory reagent grade.
- $\beta$ -Pinene, Sigma Aldrich,  $\geq 98\%$ .
- $\gamma$ -Terpinene, Sigma Aldrich, 97%.
- Terpinolene, Fluka analytical, purum,  $\geq 97\%$ .
- Camphene, Sigma Aldrich, 95%.
- $\alpha$ -Terpinene, Sigma Aldrich, 85%.
- Absolute, Ethanol, Thermo Fisher Scientific,  $\geq 99.9\%$ .
- 1-Butene gas, Varian Analytical Ins, 1.2% (mol/mol).
- Ethylene gas, Air Product Inc., 1% (vol/vol).
- CO<sub>2</sub>, Air Product Inc., 10% (vol/vol).
- Diethyl ether, Fluka analytical,  $\geq 99.0\%$  (GC).
- Potassium bromide (KBr), Spectrograde for IR spectroscopy, Thermo Fisher Scientific

## 2.5 References

- [1] D. Zhao, J. Feng, Q. Huo, N. Melosh, G.H. Fredrickson, B.F. Chmelka, G.D. Stucky, *Science* 279 (1998) 548-552.
- [2] A.D. Newman, A.F. Lee, K. Wilson, N.A. Young, *Catalysis Letters* 102 (2005) 45-50.
- [3] V. Brahmkhatri, A. Patel, *Applied Catalysis A: General* 403 (2011) 161-172.
- [4] J.M. Hollas, *Modern Spectroscopy*, Wiley, 2004.
- [5] A.W. Hull, *Journal of the American Chemical Society* 41 (1919) 1168-1175.
- [6] C. Hammond, *The basics of crystallography and diffraction*, Oxford University Press Oxford, 2009.
- [7] J.W. Niemantsverdriet, *Spectroscopy in catalysis*, John Wiley & Sons, 2007.
- [8] P. Scherrer, *Nachr. Ges. Wiss. Göttingen* 2 (1918) 96-100.
- [9] S. Brunauer, P.H. Emmett, E. Teller, *Journal of the American Chemical Society* 60 (1938) 309-319.
- [10] E.P. Barrett, L.G. Joyner, P.P. Halenda, *Journal of the American Chemical Society* 73 (1951) 373-380.
- [11] G.A. Somorjai, Y. Li, *Introduction to surface chemistry and catalysis*, John Wiley & Sons, 2010.
- [12] P. Atkins, J. de Paula, *Elements of physical chemistry*, Oxford University Press, USA, 2013.
- [13] J. Rouquerol, F. Rouquerol, P. Llewellyn, G. Maurin, K.S. Sing, *Adsorption by powders and porous solids: principles, methodology and applications*, Academic press, 2013.
- [14] D.H. Everett, G.D. Parfitt, K.S. Sing, R. Wilson, *Journal of Applied Chemistry and Biotechnology* 24 (1974) 199-219.
- [15] D. Everett, R. Haul, L. Moscou, R. Pierotti, J. Rouquerol, T. Siemieniowska, *Pure Appl. Chem* 57 (1985) 603.
- [16] P. Nellist, *Journal of Microscopy* 191 (1998) 109-110.
- [17] D.B. Williams, C.B. Carter, *Transmission Electron Microscopy: A Textbook for Materials Science*, Springer US, Boston, MA, 1996, pp. 3-17.
- [18] P.D. Nellist, S.J. Pennycook, *Advances in Imaging and Electron Physics* 113 (2000) 147-203.

- [19] J. Goldstein, D.E. Newbury, P. Echlin, D.C. Joy, A.D. Romig Jr, C.E. Lyman, C. Fiori, E. Lifshin, Scanning electron microscopy and X-ray microanalysis: a text for biologists, materials scientists, and geologists, Springer Science & Business Media, 2012.
- [20] P.D. Nellist, S.J. Pennycook, Scanning Transmission Electron Microscopy: Imaging and Analysis, Springer, 2011.
- [21] J. Clayden, W. Warren, N. Greeves, P. Wothers, Organic chemistry, Oxford University Press, 2001.
- [22] O. Kresnawahjuesa, R.J. Gorte, D. de Oliveira, L.Y. Lau, Catalysis Letters 82 (2002) 155-160.
- [23] D.J. Parrillo, A.T. Adamo, G.T. Kokotailo, R.J. Gorte, Applied Catalysis 67 (1990) 107-118.
- [24] J.G. Tittensor, R.J. Gorte, D.M. Chapman, Journal of Catalysis 138 (1992) 714-720.
- [25] M.P. Fuller, P.R. Griffiths, Analytical Chemistry 50 (1978) 1906-1910.
- [26] I. Chorkendorff, J.W. Niemantsverdriet, Concepts of modern catalysis and kinetics, John Wiley & Sons, 2006.

## ***Chapter 3***

### ***Characterisation of Heteropoly***

### ***Catalytic Materials***

### 3.1 Introduction

Heteropolyacids (HPAs) and their salts, often referred to as polyoxometalates as they are part of the family of mixed oxides [1], are unique solid acids, widely utilised as heterogeneous catalytic materials due to their highly tuneable properties, which facilitate their application for a broad spectrum of chemical transformations. Their synthesis arises from the condensation of oxoanions, and the final crystal structure depends on the number of condensed units, as depicted in **Figure 3.1**.

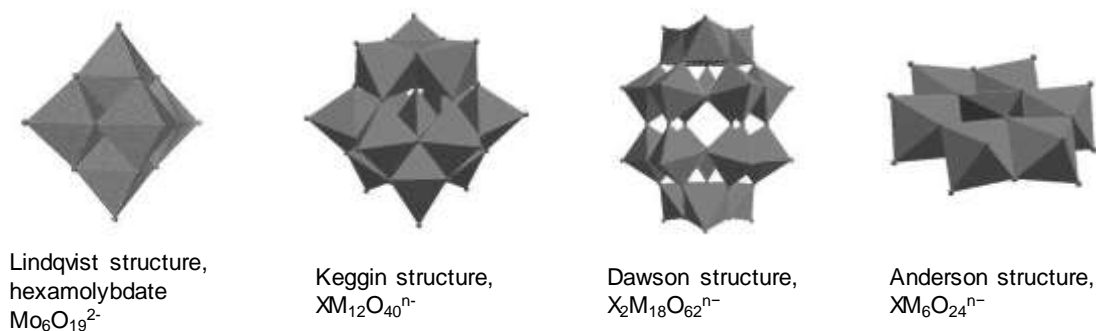


**Figure 3.1** – Representation of the most common HPAs architectures.

Keggin structured HPAs, with the general formula  $\text{H}_n(\text{MX}_{12}\text{O}_{40})^{n-}$ , have been studied, with both unsupported and supported variants. Silica support materials, fumed silica and high surface area mesoporous SBA-15 were utilised to optimise HPA dispersion and therefore proton availability, with the resulting positive effect expected to be beneficial in the catalytic conversion of gas and liquid substrates [2, 3]. The physiochemical properties of the catalytic materials have been evaluated through the utilisation of a wide range of characterisation techniques, which will facilitate the elucidation of structure relationships in subsequent catalytic screening chapters.

## 3.2 Results and discussion

### 3.2.1 Phosphotungstic acid based materials

The inherent properties of supported and unsupported phosphotungstic acid (HPW), on fumed silica and SBA-15, are reported to probe on the role of both support architecture and HPW loading.

#### 3.2.1.1 X-ray Fluorescence (XRF)

Elemental analysis of the supported materials, synthesised using the incipient wetness impregnation methodology, as described in **Chapter 2**, was carried out to determine

actual wt%. **Table 3.1** compares nominal with calculated HPW loadings, which were obtained from the stoichiometry of  $H_3PW_{12}O_{40}$  using the W wt% measured via XRF analysis. Data reveal that the calculated loadings are close to those desired (nominal), indicating that the synthetic protocol chosen is a reliable way to support HPW on Si-based materials. From here on, the physicochemical properties of catalytic materials will be evaluated to the bulk W mass loadings reported.

**Table 3.1** – XRF elemental analysis of HPW supported on fumed  $SiO_2$  and SBA-15 and corresponding unsupported material.

HPW/Fumed Silica			HPW/SBA-15		
Measured bulk W loading / wt%	Calculated HPW loading / wt%	Nominal HPW loading / wt%	Measured bulk W loading / wt%	Calculated HPW loading / wt%	Nominal HPW loading / wt%
2.2 ( $\pm 0.1$ )	2.9 ( $\pm 0.3$ )	5	3.2 ( $\pm 0.3$ )	4.3 ( $\pm 0.3$ )	5
6.1 ( $\pm 0.1$ )	8.2 ( $\pm 0.1$ )	10	9.0 ( $\pm 0.1$ )	12.1 ( $\pm 0.1$ )	10
6.2 ( $\pm 0.1$ )	8.3 ( $\pm 0.1$ )	15	11.9 ( $\pm 0.1$ )	16.0 ( $\pm 0.1$ )	15
11.7 ( $\pm 0.1$ )	15.7 ( $\pm 0.1$ )	20	16.9 ( $\pm 0.1$ )	22.8 ( $\pm 0.1$ )	20
15.5 ( $\pm 0.1$ )	20.9 ( $\pm 0.1$ )	30	19.9 ( $\pm 0.1$ )	26.8 ( $\pm 0.1$ )	30
34.9 ( $\pm 0.1$ )	47.1 ( $\pm 0.1$ )	40	25.4 ( $\pm 0.1$ )	34.2 ( $\pm 0.1$ )	40
37.6 ( $\pm 0.1$ )	50.7 ( $\pm 0.1$ )	50	38.2 ( $\pm 0.1$ )	51.6 ( $\pm 0.1$ )	50
59.6 ( $\pm 0.1$ )	80.4 ( $\pm 0.1$ )	75	55.7 ( $\pm 0.1$ )	75.2 ( $\pm 0.1$ )	75
74.0 ( $\pm 0.1$ )	100.0 ( $\pm 0.1$ )	100	74.0 ( $\pm 0.1$ )	100.0 ( $\pm 0.1$ )	100

### 3.2.1.2 Powder X-ray diffraction (XRD)

Low angle diffraction patterns of the parent SBA-15 support and HPW derivatives revealed the characteristic reflections of  $P6mm$  SBA-15 space group, over the  $2\theta$  range of  $0.8^\circ$ - $3^\circ$ , which are indexed as the  $d(100)$ ,  $d(110)$  and  $d(200)$  reflections, shown in **Figure 3.2**, confirming a highly ordered nature of the porous SBA-15 material and its preservation after impregnation with HPW. Unit cell calculations from the  $d(100)$  reflection using Bragg's law and pore spacing (see **Chapter 2, Equation 2.3** and **Figure 2.3**) were calculated for HPW/SBA-15 samples only. Fumed silica does not possess a long-range ordered pore structure and therefore does not exhibit reflections in the low angle region. As shown in **Table 3.2**, for HPWs supported on SBA-15, the mesopore architecture is unaffected with neither expansion nor contraction of the unit cell is observed as a function of W loading.

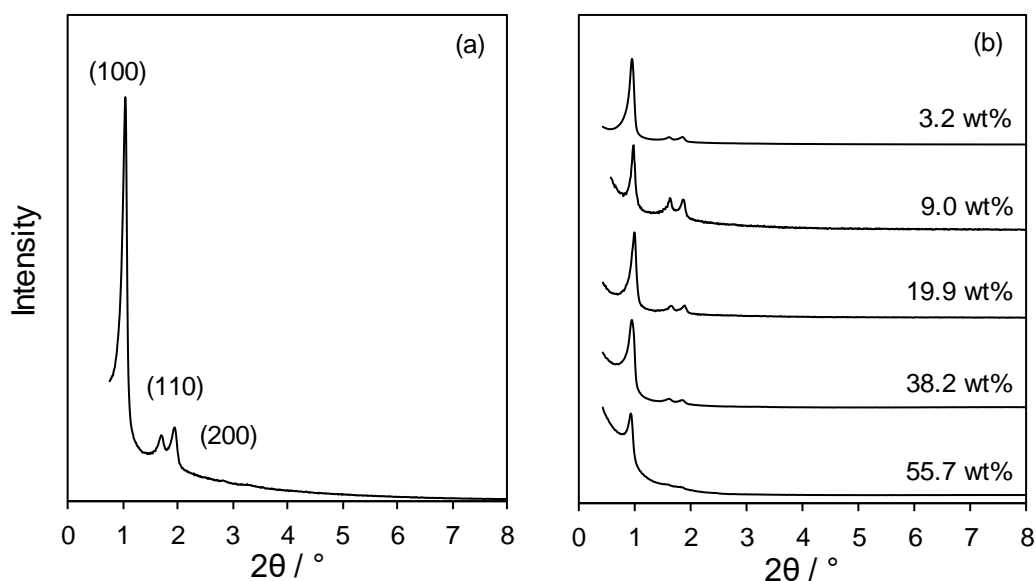


**Figure 3.2** – (a) Low angle powder XRD pattern of parent SBA-15 and (b) low angle powder XRD of HPW functionalised SBA-15.

**Table 3.2** – Unit cell parameter and corresponding pore spacings for HPW/SBA-15 samples.

HPW/SBA-15		
Bulk W loading / wt%	d(100) / nm	Pore spacing (a) / nm
SBA-15	8.5 ( $\pm 0.1$ )	9.9 ( $\pm 0.1$ )
3.2	8.6 ( $\pm 0.1$ )	9.9 ( $\pm 0.1$ )
9.0	8.6 ( $\pm 0.1$ )	10.0 ( $\pm 0.1$ )
19.9	8.6 ( $\pm 0.1$ )	10.1 ( $\pm 0.1$ )
38.2	8.7 ( $\pm 0.1$ )	10.0 ( $\pm 0.1$ )
55.7	8.7 ( $\pm 0.1$ )	10.1 ( $\pm 0.1$ )

**Figure 3.3** shows the wide angle XRD patterns of the two supports, fumed silica and SBA-15, the HPW functionalised materials, and the pattern of unsupported HPW. The bare supports reveal a single broad reflection peak within 22-23°, for both mesoporous SBA-15 and fumed silica, revealing the amorphous nature of these materials. The pattern of the unsupported HPW (74 wt% of bulk W) is in good agreement with the literature [4], which possesses a cubic structure, space group  $Pn3m$  (CCB), with a calculated unit cell of 12.1 Å which agrees with the literature reported value of 12 Å [5-7], evaluated from the most intense d(222) reflection peak at 25.4°, and all observed reflections can be index against the peaks of HPW, which is indicative of its high crystalline purity.

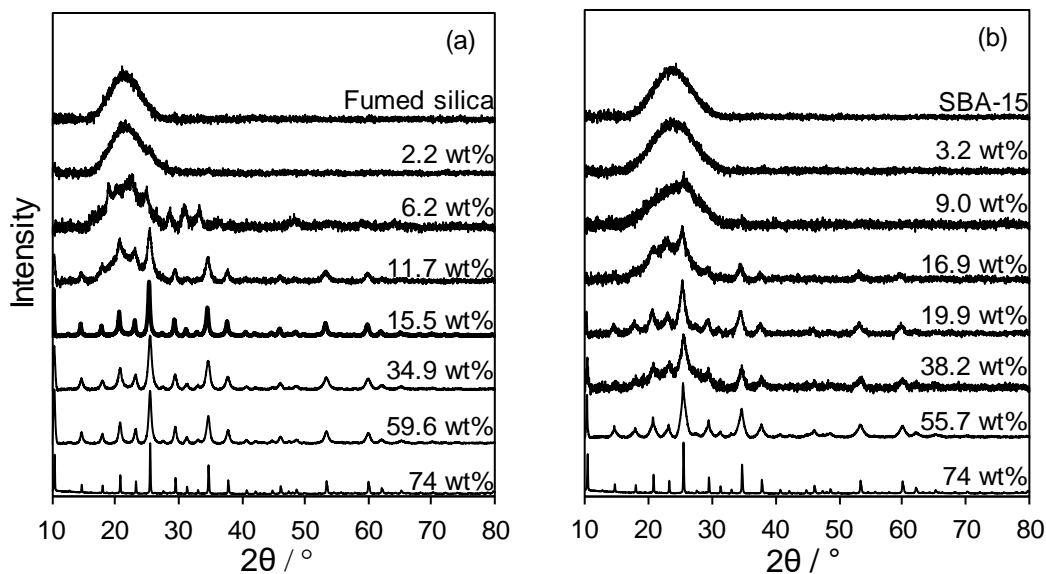


**Figure 3.3** – (a) Powder XRD patterns for fumed silica and HPW/fumed silica, and (b) SBA-15 and HPW/SBA-15 with pure HPW shown for reference.

As reported in **Figure 3.3**-(a), the HPW/fumed silica materials exhibit the characteristic reflections of phosphotungstic acid crystals at loading >6.2 wt%, with increasing reflection intensity with W loading. For the HPW/SBA-15 series (**Figure 3.3**-(b)), clear reflections appear at the higher loading of 16.9 wt%, again with increasing intensity with W wt%. This observation of reflections at higher loadings for the SBA-15 series, is attributed to increased dispersion of the Keggin units (K.U.), with smaller crystallites which are not XRD visible earlier in the series being size detection limits ~2-3 nm. Thus, the level of interaction between the K.U. and silica surface is greater on SBA-15 than on fumed silica, due to its porosity and therefore intrinsic high surface area, which enhances dispersion and inhibit HPW aggregation (responsible of the formation of bigger clusters). In addition, all HPW supported samples display comparable diffraction patterns, with no evidence of unit cell growth or contraction, from the absence of peak shift, with constant unit cells of 12.1 Å. Particle size, see **Table 3.3**, were evaluated using the Scherrer equation (**Chapter 2, Equation 2.5**), using the most intense reflections; in both series, the averaged crystallite size increases as a function of loading. As discussed in **Chapter 1**, the solid-state architecture of heteropoly compounds can be described hierarchically, with *primary*, *secondary* and *tertiary substructures*. The single Keggin polyanion, the *primary structure*, is ca. 0.8 nm [8]; the HPW coordinated to protons and water molecules represents the *secondary structure* ca. 1.2 nm, and finally the *tertiary structure* considers bigger agglomerates of nonporous crystallites ~10 nm [1]. Additional 5-8 nm particles can be associated to medium size agglomerates, which fall in a *sub-tertiary structure*. Particle size results show that tertiary and sub-tertiary structured HPW are XRD visible

because above the detection limitation of the technique, with nanoparticles sized 9-11 nm, formed on SBA-15 only at high loading (>16.9 wt%), while on fumed silica, the particles range in size between 9.2 and 18.3 nm, from 6.2 wt%.

**Table 3.3** – Particle size dependence on W loading for fumed silica and SBA-15 series.

HPW/Fumed Silica		HPW/SBA-15	
Bulk W loading / wt%	Particle size / nm	Bulk W loading / wt%	Particle size / nm
2.2	-	3.2	-
6.1	9.2 (±0.2)	4.3	-
6.2	9.4 (±0.2)	9	6.8 (±0.2)
11.7	9.5 (±0.2)	16.9	7.9 (±0.2)
15.5	11.6 (±0.2)	19.9	8.8 (±0.2)
34.9	14.3 (±0.2)	38.2	9.7 (±0.2)
59.6	18.3(±0.2)	55.7	10.2 (±0.2)

Unsupported  $H_3PW_{12}O_{40}$ =48.3 nm

*In-situ* wide angle XRD of the unsupported HPW was conducted to elucidate the intrinsic thermal stability, and results are shown in **Figure 3.4**. XRD patterns were collected over the temperatures range of 25 to 600 °C with 50 °C intervals, thermal stability was ensured through a 60-minute delay prior to data collection. The hexahydrate phosphotungstic acid structure is stable between 50-100 °C; at temperature >100 °C and up to 200 °C, the characteristic diffraction peaks shift to high 2θ values, d(222) reflection shift by 0.75, due to the removal of crystalline water which induces a shrinkage of the cubic *Pn3m* structure with the unit cell decreasing to 1.16 Å. The thermal transformation of the K.U. structure is induced at 250 °C with the removal of hydrogens and oxygen atoms from the polyoxometalate; from this temperature, the diffraction patterns reflect a mixture of defective species and intact HPW clusters. Finally, at 600 °C, full decomposition of the structure occurs, leading to the characteristic peaks related to monoclinic  $WO_3$ . **Figure 3.5** shows particle size dependence with temperature, with unsupported HPW crystallite sintering from 50 and 200 °C. As temperature increases further to 350 °C, the formation of defective Keggin units is observed, which eludes to the loss of structural water, with HPW crystallites size decreasing drastically from 60 to 21 nm (data obtained from reflection d(222) between 25.6-26.3 °) and defective species of ~19 nm (calculated at 24.8°). As temperature increases again, defective species remain constant in size before phase transformation of the structure to  $WO_3$  at 600 °C which have a crystallites size of 29.4 nm.

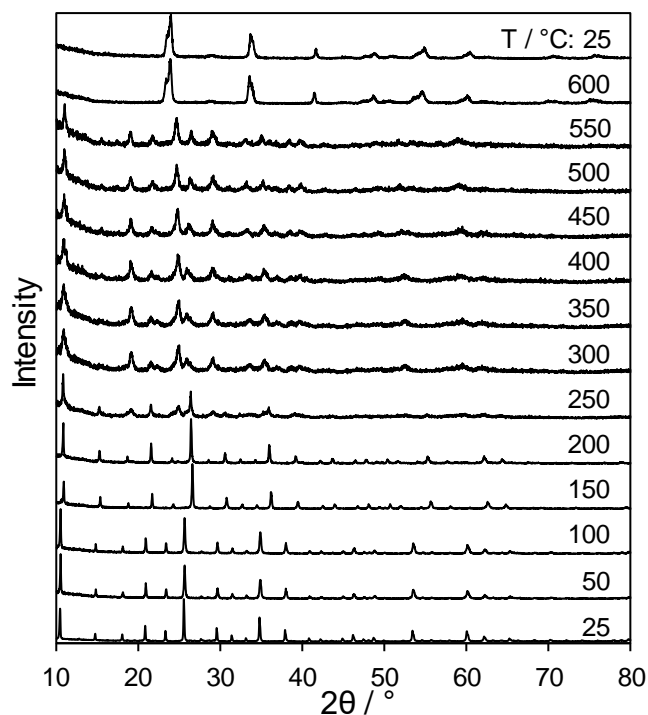


**Figure 3.4** – *In-situ* XRD pattern of the unsupported HPW collected from 25 to 600 °C (10 °C min<sup>-1</sup>) under N<sub>2</sub> flow (10 mL min<sup>-1</sup>).

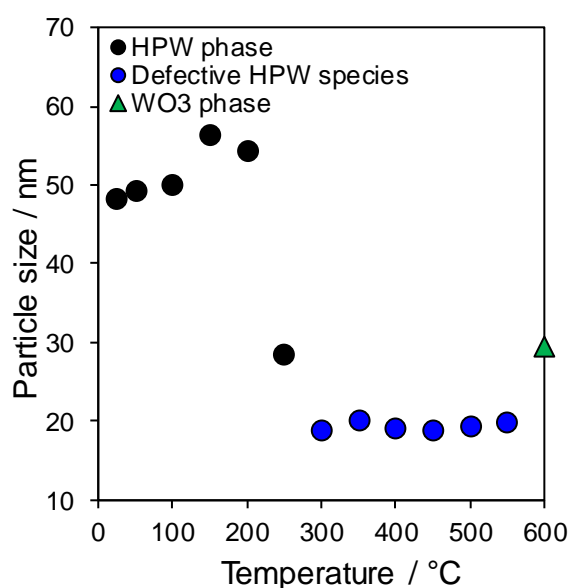


**Figure 3.5** – Effect of temperature on particle sizes from *in-situ* study.

### 3.2.1.3 Nitrogen porosimetry

N<sub>2</sub> adsorption analysis was carried out to evaluate surface areas, pore diameters and volumes. **Figure 3.6** shows the adsorption isotherms of the bare supports, fumed silica (a) and SBA-15 (b); fumed silica displays type II isotherm typical of a non-porous or microporous material, whereas SBA-15 displays the characteristic type IV isotherm

which is indicative of a mesoporous materials [9]. The  $N_2$  adsorption and desorption branches are due to the architecture of the silica-based material, where at low relative pressure values, the adsorption curve exhibits a *rounded knee* shape, which indicates, initially, the monolayer formation and, as it follows, the multilayer formation in the low inflection region. At increasing pressure, mesopore filling occurs in the case of type IV isotherms, and capillary condensation is apparent (gas-liquid transition); this effect is accompanied by hysteresis for pore diameters greater than  $\sim 4$  nm, due to difference between the adsorption and desorption process. Hysteresis loop manifests different forms due to different pore shape and interconnections, here the ordered mesoporous materials, SBA-15, have uniform cylindrical pores, which exhibit H1 hysteresis type.

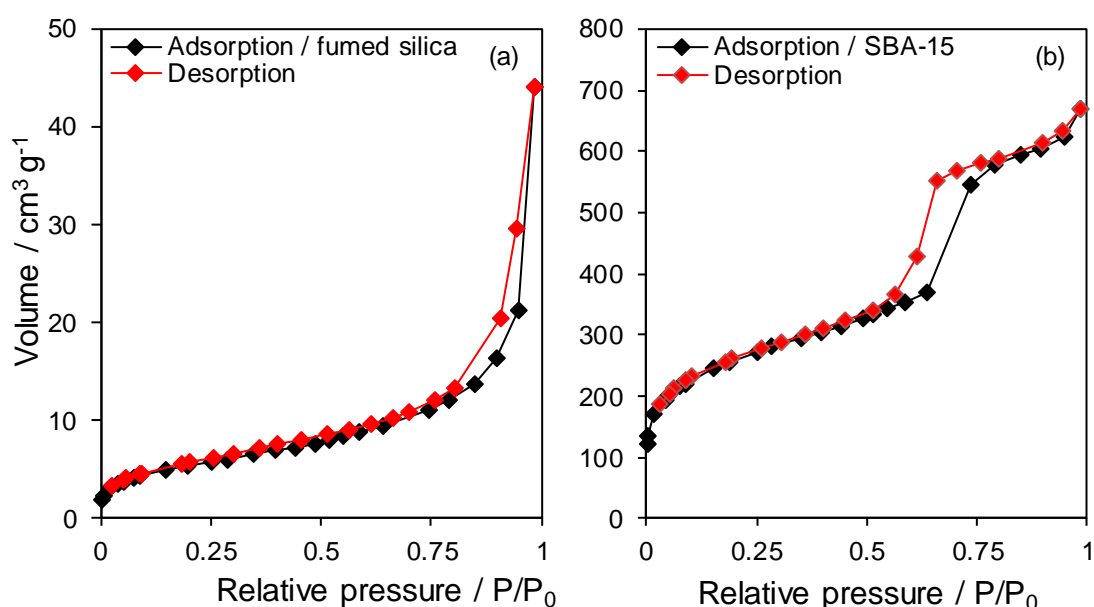


**Figure 3.6** – Isotherms with adsorption and desorption branches for both supports, fumed silica (a) and SBA-15 (b).

The textural properties of both supports are retained after HPW wet impregnation, as shown in **Figure 3.7**, with HPW/fumed silica series displaying the characteristic type II isotherms, as observed for the undoped support, whereas HPW/SBA-15 series the type IV of the parent SBA-15. In both series, increasing W loading results in a decrease in the volume of  $N_2$  adsorbed/desorbed relative to their parent supports suggesting a decrease of surface area mainly due to the presence of HPW species, which display negligible specific surface area values.

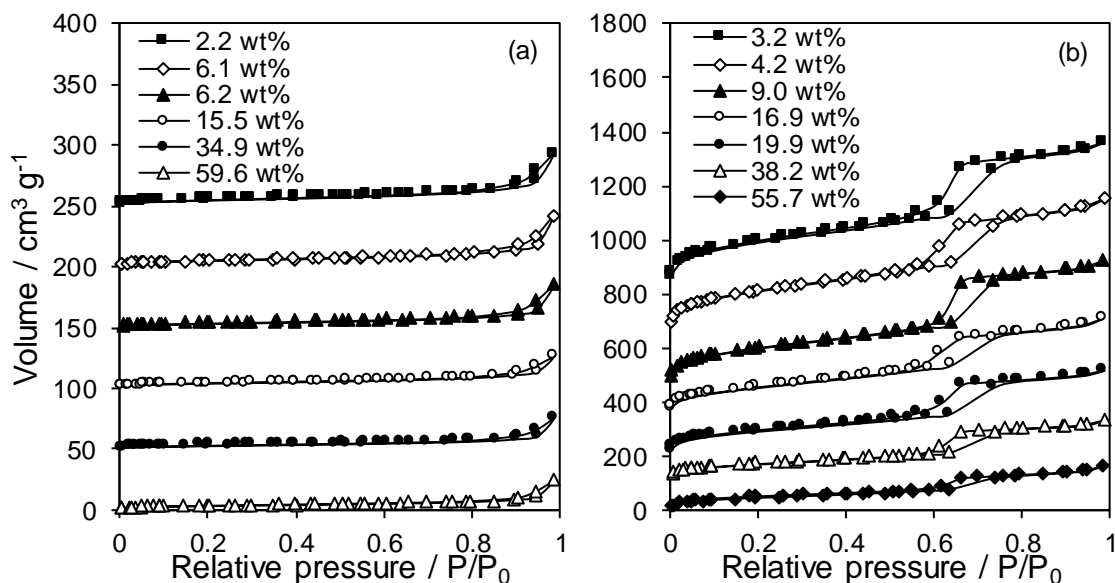


**Figure 3.7** – Isotherms of adsorption and desorption for supported materials at different W wt% HPW/fumed silica offset by  $50 \text{ cm}^3 \text{ g}^{-1}$  (a), and HPW/SBA-15 offset by  $150 \text{ cm}^3 \text{ g}^{-1}$  (b).

**Figure 3.8** shows (a) BET and (b) micropore surface areas (calculated via t-plot method) normalised to silica mass, in order to mitigate for inherent distortions at high loading of W wt%. HPW/fumed silica BET values exhibit an increasing surface area increasing the W wt%, suggesting that the three-dimensional HPW crystallites are located on the external surface of the support. Materials microporosity revealed that an initial drop of micropores area, within the range 0-15.5 wt%, to further increase to higher values indicating that the enhancement of surface area is due to the formation of *intercrystalline* micropores between adjacent HPW agglomerates. In contrast, the HPW/SBA-15 series exhibit an initial BET drop of  $140 \text{ m}^2 \text{ g}_{\text{SiO}_2}^{-1}$  compared to the parent material within the range of 0-9 wt%, which is attributed to filling or blocking of the complementary microporosity in SBA-15 [10-13], as confirmed also via t-plot method which shows the same drop over the same W range. Further increases in W wt%, results in both BET and micropore areas values plateauing, suggesting that only negligible mesopore blockage occurs up to the highest W loading, where the BET value is reduced by  $\sim 33\%$  (dropping from  $756$  to  $507 \text{ m}^2 \text{ g}_{\text{SiO}_2}^{-1}$ ), while micropores surface area remain constant at  $200 \text{ m}^2 \text{ g}_{\text{SiO}_2}^{-1}$ ; thus, suggesting mesopore blockage.

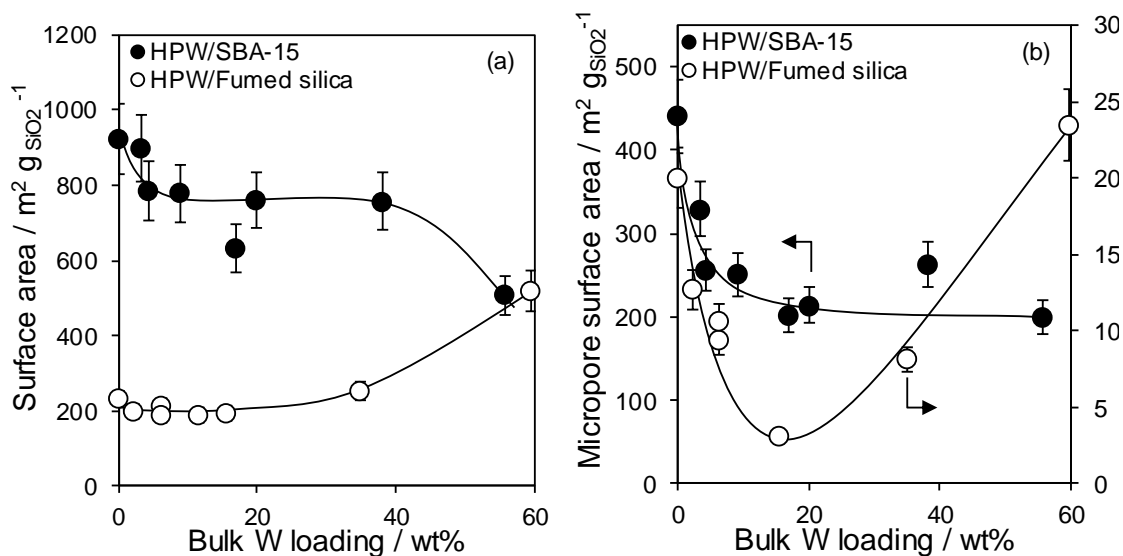


**Figure 3.8** – Surface area values of HPW/fumed silica and HPW/SBA-15 ( $\text{N}_2$  BET) (a); micropore surface area (on first and second y-axis) HPW/Fumed silica and HPW/SBA-15 ( $\text{N}_2$  t-plot) (b).

Detailed inspection of BJH pore size distribution plots, **Figure 3.9**-(a), further confirm that there are no changes in the average pore size with W loadings. **Figure 3.9**-(b) shows total pore volume obtained at  $0.975 P/P_0$  and mesopore BJH diameter obtained on the desorption branch isotherm of HPW/SBA-15 samples. The former mirrors the BET results, showing an initial drop followed by a plateau and a second decrease at the highest W wt% loading, whereas the latter remains unchanged  $\sim 5.8$  nm across the entire series. Results suggest that mesopores blockage occurs only at the highest loading showing a dramatic decrease in pore volume, while pore volume losses at lower loadings is due to micropores filling/blockage. Thus, the BJH diameter and pore volumes demonstrate that the HPW units are highly dispersed within the mesopores of SBA-15.

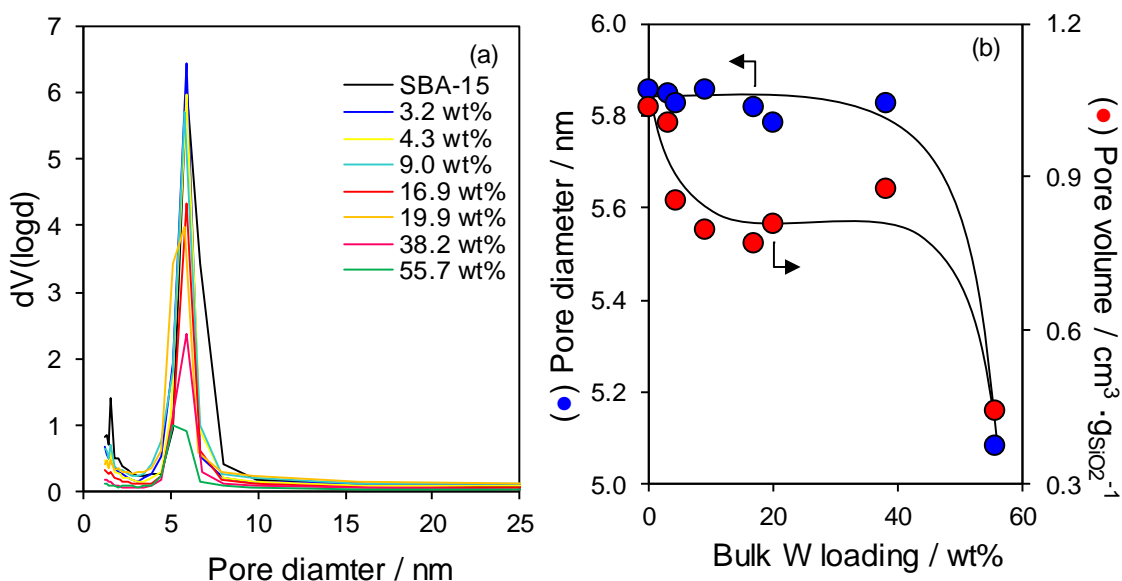


**Figure 3.9** – BJH pores size distributions of HPW/SBA-15 (a); and pore diameter and pore volume of HPW/SBA-15 as function of W loading (b).

In addition, as shown in **Equation 3.1**, the theoretical HPW surface coverage over the supports was calculated, where each Keggin units possess a cross section area of  $1.44 \text{ nm}^2$ , and are in a hexagonal closed packed arrangement [8, 14, 15].

$$\theta = \text{Area}_{\text{KU}} \cdot \frac{N_A \cdot \omega_{\text{HPW}}}{\text{MW}_{\text{HPW}}} \cdot \frac{1}{\text{SA}_{\text{support}}}$$

**Equation 3.1** – where  $\text{SA}_{\text{support}}$  is the BET measured surface area per gram of support,  $N_A$  is the Avogadro number, and  $\omega_{\text{HPW}}$  is the mass fraction.

**Figure 3.10** reports surface coverage ( $\theta$ ) values for HPW supported on SBA-15 and fumed silica, at different W wt% loading. The uniform HPW dispersion is confirmed by the increase of surface coverage on both supports, which is noticeably lower on SBA-15 due to its architecture, highlighting a greater dispersion of the K.U.

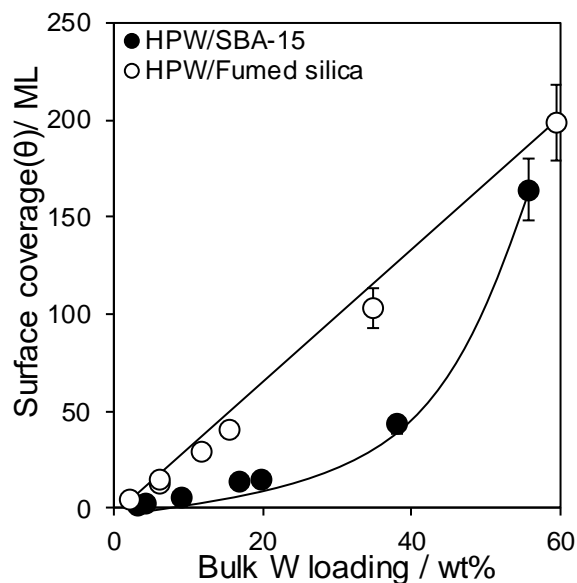


**Figure 3.10** – Surface coverage dependence of silica supported HPW.

#### 3.2.1.4 Scanning transmission electron microscopy (STEM)

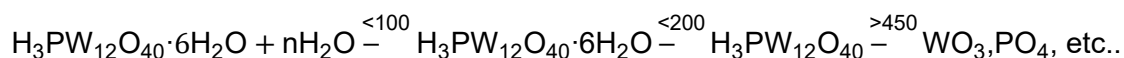
STEM micrographs allow visualisation of the HPW phase on the two support architectures, showing results in agreement with previous discussed techniques. SBA-15 facilitates higher HPW dispersions, with a preferential two-dimensional growth, relative to the lower surface area fumed silica support. HPW deposited on fumed silica exhibit larger particle sizes compared to HPW/SBA-15, in agreement with the reduced dispersions observed by wide angle XRD. For fumed silica series, **Figure 3.11**-(a) shows the presence of nanoclusters on the surface of the non-porous support at 2.2 wt% W, with sizes spanning 1-3 nm which reflect 1-2 K.U.. An increase in loading to 15.5 wt%, **Figure 3.11**-(b and c), results in the formation of a considerable degree of HPW agglomerates of 10-20 nm, which agree with the size evaluated from wide angle XRD patterns via the Scherrer equation. In contrast HPW/SBA-15 STEM images (**Figure 3.11**-(d-f)) shows discrete K.U., uniformly dispersed on the parent support with HPW diameters in agreement with literature values of 1.2 nm [8]. At both low and high HPW loadings, 3.2 and 55.7 wt%, we observed incorporation of the clusters within the mesopore channels of SBA-15, as illustrated in the EDX line scan profiles which are reported as W to Si ratio as function of distance (spatial resolution being 0.5 nm). For the 55.7 wt% HPW/SBA-15 sample, the identification of the single units was not possible with mesopores channels fully decorated (**Figure 3.11**-(c)).



**Figure 3.11** – STEM dark-field images of (a) 2.2 wt% HPW/fumed silica, (b) 15.5 wt% HPW/fumed silica, (c) 59.6 wt% HPW/fumed silica; (c and d) 3.2 wt% HPW/SBA-15, (e) 55.7 wt% HPW/SBA-15. Insets show corresponding EDX atomic ratio lines profiles.

### 3.2.1.5 Thermogravimetric analysis (TGA)

The thermal stability of unsupported HPW and silica supported variants were evaluated by thermogravimetric analyses under N<sub>2</sub> (60 mL min<sup>-1</sup>). **Scheme 3.1** shows the thermo-decomposition of HPW, with three discrete transformation occurring [2, 16, 17].



**Scheme 3.1** – Proposed thermo-decomposition process of phosphotungstic acid under N<sub>2</sub> flow [18].

In **Figure 3.12**, decomposition steps are reported as sample mass loss (%) plotted against temperature for unsupported HPW, both supported series, on fumed silica and SBA-15, and undoped supports.

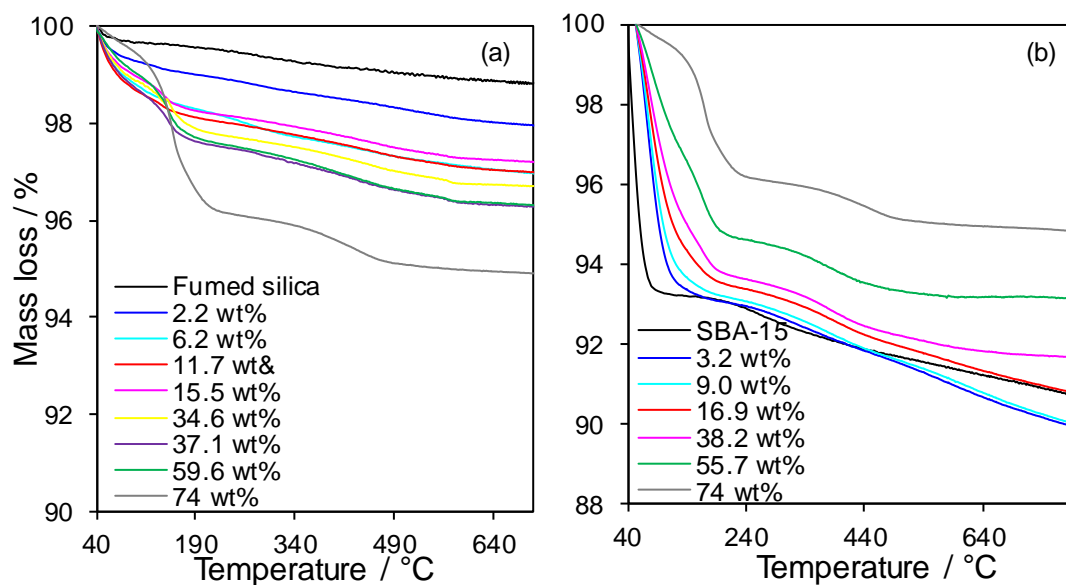


**Figure 3.12** – Thermal analysis expressed as % mass loss as function of temperature on HPW/fumed silica series (a) and HPW/SBA-15 (b).

The first mass loss, at  $< 100$  °C, is related to physisorbed water weakly bonded on the surface, which for pure HPW is only minor, whereas in the case of the supported systems a significant increase in mass loss is observed over the same temperature range. This is attributed to physisorbed water on the support, which is also visible to the same degree in the parent fumed silica and SBA-15. The two series exhibit different amount of physisorbed water desorbed due to the hydrophobicity of each support and the support surface areas. For bare fumed silica and SBA-15 (reported in the graph as 0 wt% of W loading), 0.5% and 6.5% of mass loss were measured respectively between 40 and 110 °C, suggesting that on the amorphous silica higher hydrophobicity is observed compared to mesostructured SBA-15 [19]. The better adsorption of water is correlated not only to higher values of SBA-15 surface area, but also to its greater amount of hydroxyl groups on the surface [20]. To further confirm the higher hydrophilic character of SBA-15, silanol density ( $\equiv\text{Si-OH}$ ) was estimated on both supports, calculating the mass loss between 250 - 800 °C due to dihydroxylation of the surface followed by water desorption [21]. Calculation revealed that mesoporous SBA-15 possesses almost 4 times the density of surface silanols of fumed silica, being  $2.8 \text{ mmol g}^{-1}$  against  $0.7 \text{ mmol g}^{-1}$  respectively.

As reported in **Figure 3.13**-(a), for HPW/fumed silica mass loss results (taken within 40 and 110 °C) evidence that across the series the amount of weakly bonded water molecules is almost constant  $\sim 1.5\%$ , with values comparable to pure HPW. In the contrary, HPW/SBA-15 show higher mass loss values similar to their parent support,  $\sim 6.5\%$ , which plateaus within 3.2 and 38.2 wt%, while it decreases at the highest loading.

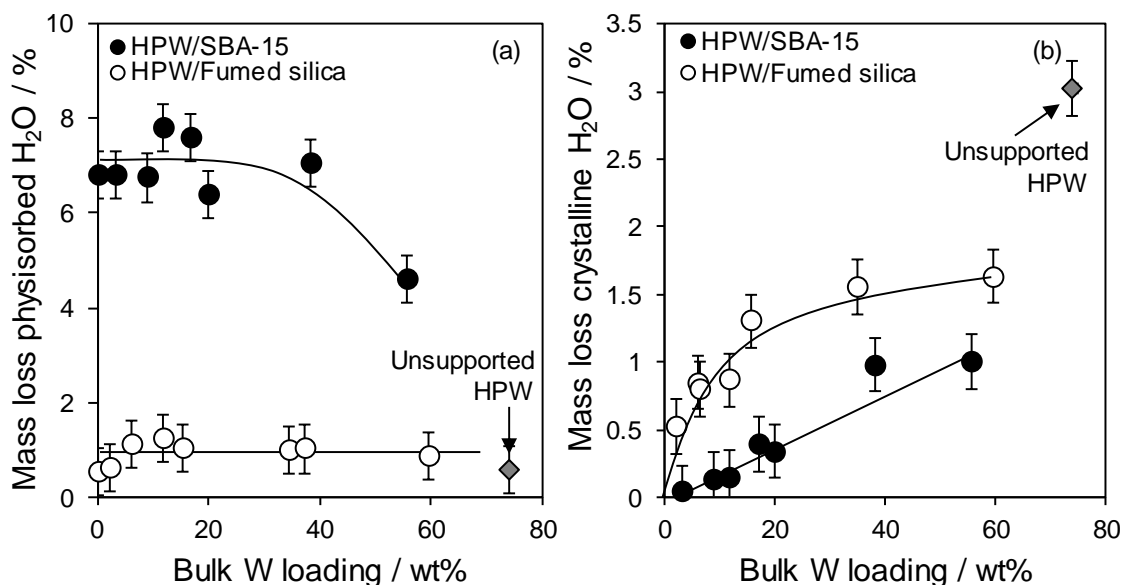


**Figure 3.13** – Physisorbed water (a) and crystalline water (b) mass loss for unsupported HPW and supported HPW on fumed silica and SBA-15.

The second loss, around 200 °C, reflect desorption of the crystalline water, which is due to entrapment of polar molecules, e.g. water, between the Keggin units of bulk HPW agglomerates and nanoclusters [22]. **Figure 3.13**-(b) reports mass loss % related to the desorption of crystalline water for each sample, between 120-240 °C, which indicates the level of aggregation of K.U.: the higher is the water mass loss, the higher will be the aggregation. For pure HPW, the amount of crystalline water measured revealed the  $H_3PW_{12}O_{40} \cdot 6H_2O$  stoichiometry as also observed in the literature [6, 23]. For supported species, HPW/fumed silica series shows a fast increase of water mass loss within 2.2-15.5 wt% to further plateauing at ~ 1.5 % at higher loadings, indicating highly dispersed K.U. at low W loadings (<20 wt%), and two-dimensional arrays at  $W > 20$  wt%. In contrast, SBA-15 supported HPW exhibits a single linear trend as a function of W loading, due to the presence of only highly dispersed species.

For supported species, differential profiles were calculated from the mass loss trends and plotted in **Figure 3.14**, wherein the two regions highlighted in blue and yellow indicate desorption of physisorbed water and crystalline water respectively. Differential profiles were chosen as a better method to evaluate the consistency of desorption temperatures. For HPW on fumed silica, mass losses related to crystalline water are clearly visible within the same temperature range of unsupported HPW; across this series, excluding the lowest loading, 2.2 wt%, the mass losses are greater increasing the W wt%. For samples supported on SBA-15, this feature grows progressively slower with HPW loading, suggesting that isolated highly dispersed K.U. trap significantly less

water molecules; while for larger agglomerates, at loading  $\geq 38.2$  wt%, a distinct peak is observed. Profiles related to crystalline water desorption for the two series suggest that on fumed silica, the formation of larger agglomerates occurs at lower loadings, in agreement with XRD and STEM analysis, and hence the amount of trapped water is greater. The final broad peak, observed across both series, is related to the gradual decomposition of the HPW structure, which starts at 300 °C [24], into tungsten trioxide.

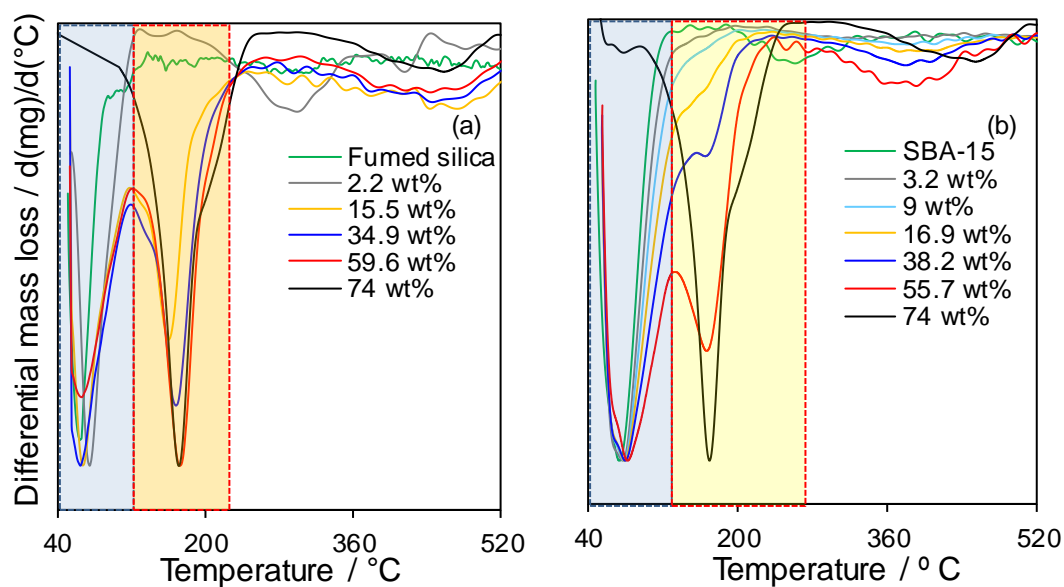


**Figure 3.14** – Differential thermal analysis of supported HPW as a function of loading, HPW/fumed silica (a) and HPW/SBA-15 (b).

### 3.2.1.6 n-Propylamine chemisorption and temperature programmed desorption (TPD)

Acid site density and strength were probed by n-propylamine TPD, monitored by Mass Spectrometry (MS), a widely used technique due to its simplicity in both experimental set up and data processing [25]. Alkyl-amines chemisorb at the acidic proton site of the solid sample, forming the alkyl-ammonium ion, subsequent desorption, at elevated temperature, can proceed via two routes; first through decomposition to propene and ammonia or second without reaction in which the amine desorbs. Via TPD-MS, the desorption of ammonia, propene and unreacted n-propylamine from the respective fragmentation channels of 17, 41 and 30 m/z (unique fragments for the 3 species), are monitored. Acid site strength is evaluated from the temperature at which reactive desorption (decomposition) occurs, i.e. the temperature at which ammonia and propene are simultaneously detected. Increasing acid strength exhibits propene and ammonia desorption at decreasing temperature, i.e. more reactive sites. **Figure 3.15** reports the data for supported HPWs, with pure HPW shown for comparison. Pure HPW exhibits a

first peak at 264 °C, which is associated to the strongest acid sites, and a second peak at ~400 °C, which is related to medium and weak strength acid sites, with observed lines shapes in agreement with literature [26]. Physisorbed species were not detected, being apparent at lower temperatures, ~120 °C, as reported in other studies [27, 28]. For supported materials, HPW on fumed silica shows similar behaviour with similar lines shapes, displaying the two peaks in the same temperature range but less intense. In contrast, on HPW/SBA-15 catalysts, the first propene desorption occurs at 245 °C, which appears at 30 °C lower than for unsupported HPW. The second peak, at ~400 °C, is apparent in all supported materials, suggesting that medium/weak acid sites are unaffected by the supporting of HPW.

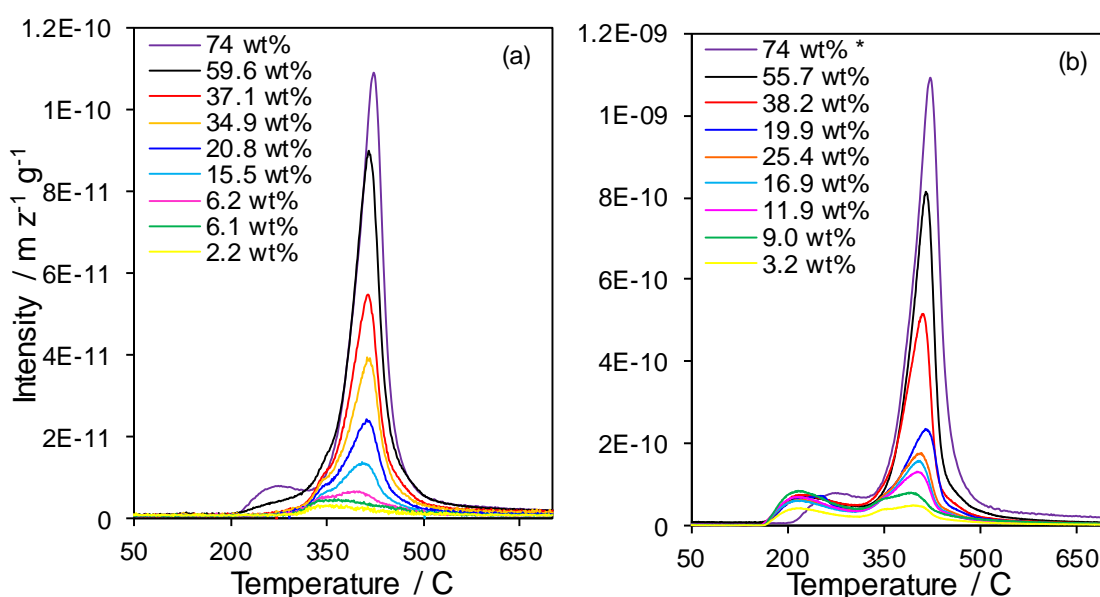


**Figure 3.15** – n-propylamine TPD relative intensities of m/z normalised per g of sample for supported HPW on fumed silica (a) and on SBA-15 (b). \*Signal multiplied for 10.

Total acid site densities were obtained over the temperature range of propene desorption, by calculating the moles of propene desorbed, with acid site to propene stoichiometry of 1:1. The acid site loading results,

**Table 3.4**, show that for W loading  $\leq 20$  wt%, both series possess similar values, suggesting that the alkyl amine finds equal numbers of reactive protons both in highly dispersed Keggin units on SBA-15 and in nano-clustered of HPW on fumed silica. At higher loadings,  $>20$  wt%, acid densities of HPW/SBA-15 are greater than those from the HPW/fumed silica series, which suggest acid site accessibility to the amine is hindered by larger crystallites.

**Table 3.4** – n-Propylamine measured acid sites densities of supported HPW.

HPW/Fumed silica		HPW/SBA-15	
Bulk W loading / wt%	Acid loading / mmol g <sup>-1</sup>	Bulk W loading / wt%	Acid loading / mmol g <sup>-1</sup>
2.2	0.19 (±0.01)	3.2	0.16 (±0.01)
6.2	0.19 (±0.01)	9	0.17 (±0.01)
6.1	0.20 (±0.01)	11.9	0.17 (±0.01)
11.7	0.25 (±0.02)	16.9	0.23 (±0.02)
15.5	0.26 (±0.02)	19.9	0.34 (±0.03)
34.9	0.38 (±0.03)	25.4	0.51 (±0.04)
37.6	0.42 (±0.03)	38.2	0.79 (±0.05)
59.6	0.49 (±0.03)	55.7	0.92 (±0.06)

Unsupported H<sub>3</sub>PW<sub>12</sub>O<sub>40</sub>=0.79 (±0.05) mmol g<sup>-1</sup>

To shed insight on the nature of acid sites, desorption profiles were deconvoluted in three different peaks, associated to strong, medium and weak acid sites. Low temperature reaction of propylamine with the 3 free protons of intact K.U. define the nature of strong acid sites, whereas medium and weak acid sites are related to partially decomposed HPA species, such as H<sub>2</sub>PW<sub>12</sub>O<sub>39.5</sub><sup>-1</sup> and HPW<sub>12</sub>O<sub>39</sub><sup>-2</sup>, and reaction occurs at higher temperatures. Deconvolution fitting was conducted with Casa XPS software, and Gaussian-Lorentzian line shape GL(30) (70% Gaussian and 30% Lorentzian) was used to fit all peaks. **Figure 3.16** displays two example fittings of the MS fragment 41 m/z obtained from similar W wt% samples on fumed silica and SBA-15. For both materials, profiles deconvolution reveals three peaks, which are related to reactively formed propene and its desorption from strong, medium and weak acid sites. Again, HPW/fumed silica catalyst shows that the majority of propene desorbed comes from weak and medium acid sites, whereas the contribution from the strong sites is little; in contrast, HPW/SBA-15 possesses a higher number of strong acid sites displaying a clear propene desorption profile.

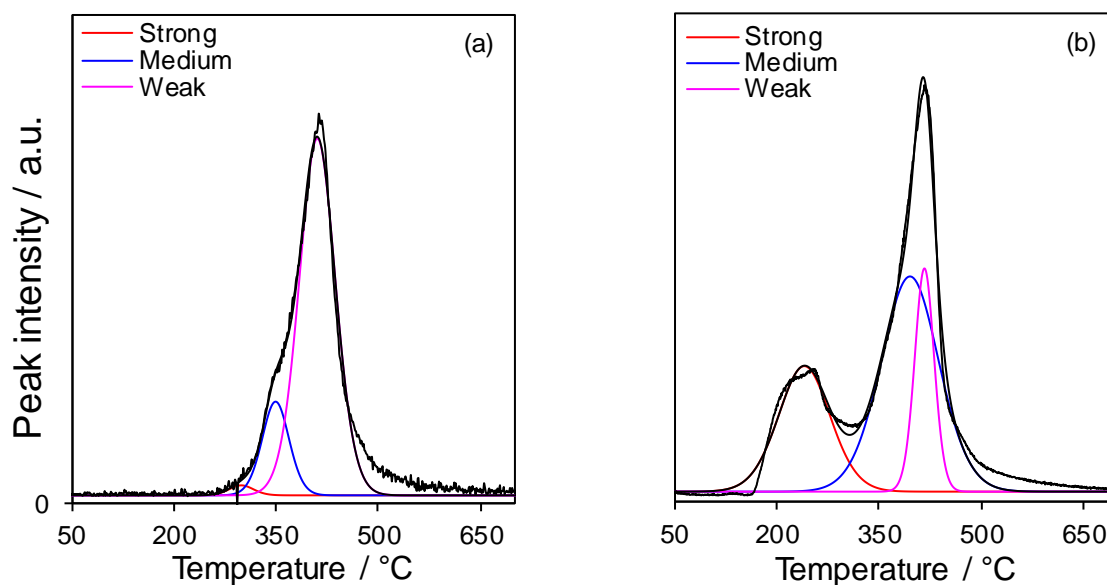
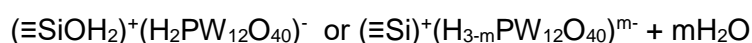


**Figure 3.16** – Fitting example of mass normalised 41 m/z MS channel from n-propylamine TPD-MS for 15.5 wt% W on fumed silica (a), and 16.9 wt% W on SBA-15 (b).

The strong, medium and weak acid site loadings, evaluated from deconvolution peak areas, are reported in **Figure 3.17** as function of bulk W loading for both supports. Fumed silica samples, apart from the lowest loading, display the majority of acid sites being of weak nature character, with an almost constant value of  $0.38 \text{ mmol g}^{-1}$ , followed by medium strength sites, with only a small contribution of strong acid sites. This indicates that tertiary HPW structures (with a certain level of aggregation) possess similar acidic properties. HPW supported on SBA-15, (**Figure 3.17**- (b)) displays a strong dependence on the W loading, witnessing a volcano trend of strong acid site, peaked at 38.2 wt%, in concomitance with the rise of weak and medium acid character as W wt% increases. In the case of SBA-15 systems, acid sites possess more of the strong character compared to fumed silica, thus more intact HPW structure with three acid protons. It is worth mentioning that in discrete heteropolyanion protons are both interacting with the support, to allow the attachment, and directly bonded to the terminal [29, 30] or to bridging [22, 31] oxygen atoms, with the true position of debate. HPW interaction with the support occurs in two different ways, either with direct hydrogen bond with one or more silanol at the surface, or via dehydration:



Attempts to discern between the two species have proven to be inconclusive and still under debate. It is suggested that during the anchoring of HPW species, dehydrated

silanol are more likely to be formed on fumed silica, whereas protonated species on SBA-15, being the protonated silanols still able to react. The hypothesis would therefore explain why on fumed silica although strong acid sites are of the same strength (being at the same temperature), are less in quantity. To further investigate on the nature of acid sites of the two series, ammonia titration and TPD analysis were undertaken.

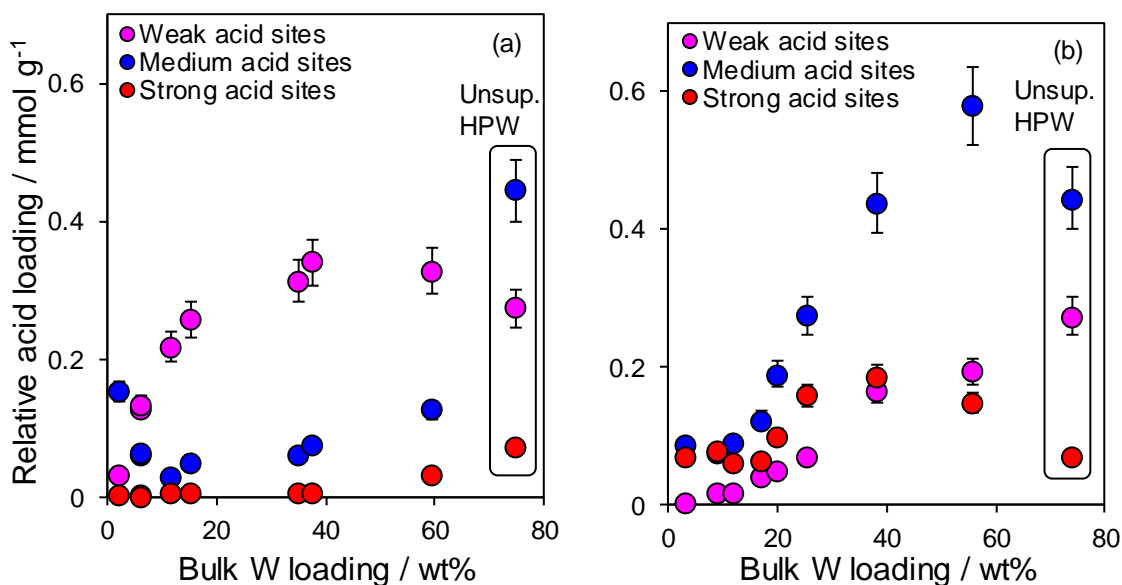


**Figure 3.17** – Relative acid loading for strong, medium and weak sites based on the relative peak area % (obtained from profile deconvolution) and the total acid loading as function of W wt% on both supports, fumed silica (a) and SBA-15 (b).

### 3.2.1.7 NH<sub>3</sub> titration and Temperature programmed desorption (TPD)

Ammonia TPD was carried out to further evaluate solid acidity of HPWs samples, with the results reported in **Figure 3.18**. These revealed three distinctive desorption peaks at ~ 200, 450 and 610 °C, being more clearly visible in the inset, which show the profile of the unsupported HPW. As with propylamine, each desorption peak relates to a different adsorption site, but as the desorption is not-reactive i.e. ammonia adsorbs and desorbed, desorption temperature is proportional to acid site strength. The first peak, at ~ 200 °C, is attributed to ammonia coordinated with protons of partially hydrated HPW units, its position remains constant across both series revealing no discernible differences in the strength of the weakest acid sites. At higher temperatures, the Keggin units are dehydrated and partially decomposed, and the peak at 450 °C is due to the coordination of ammonia to the last charge-balancing protons of heteropolyanion, in agreement with the result described in the thermogravimetric analysis [22, 32, 33]. The final desorption peak, at ~600 °C, is attributed to ammonia adsorbed with defective

polyoxometallates which possesses the strongest ammonia chemisorption sites [2, 7, 24, 29, 34].

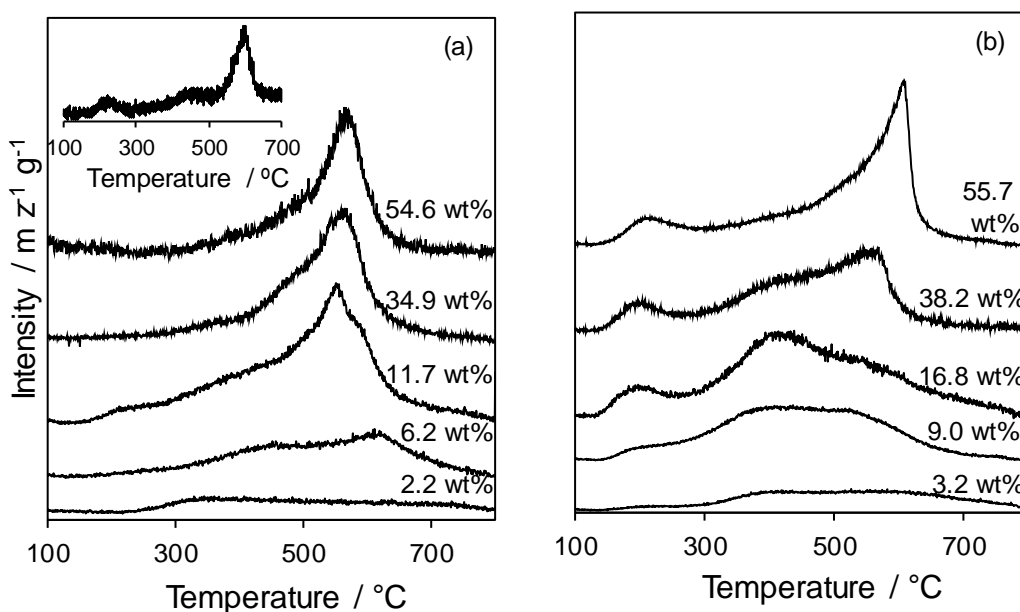


**Figure 3.18** – Stacked NH<sub>3</sub> TPD data of HPW/fumed silica (a) and HPW/SBA-15 (b). Inset, TPD profile obtained for unsupported HPW.

**Table 3.5** reveals acid site densities of both series, evaluated by ammonia titration, with HPW/fumed silica possessing lower acid site densities compared to HPW/SBA-15. Even at the lowest loadings, 2.2 and 3.2 wt% of bulk W on fumed silica and SBA-15 respectively, the difference in acid loading is doubled.

**Table 3.5** – NH<sub>3</sub>-TPD measures acid site densities of supported HPW.

HPW/Fumed silica		HPW/SBA-15	
Bulk W loading/wt%	Acid loading / mmol g <sup>-1</sup>	Bulk W loading/wt%	Acid loading / mmol g <sup>-1</sup>
2.2	0.06 (± 0.02)	3.2	0.15 (± 0.01)
6.2	0.16 (± 0.02)	3.6	0.23 (± 0.02)
6.1	0.16 (± 0.02)	9	0.24 (± 0.02)
11.7	0.19(± 0.02)	16.9	0.27 (± 0.03)
15.5	0.20 (± 0.02)	19.9	0.29 (± 0.03)
34.9	0.20 (± 0.02)	38.2	0.30 (± 0.03)
59.6	0.26 (± 0.03)	55.7	0.54 (± 0.05)

Unsupported H<sub>3</sub>PW<sub>12</sub>O<sub>40</sub>=1 mmol g<sup>-1</sup>

As for n-propylamine analysis, ammonia desorption profiles were deconvoluted in three different peaks, and fitting was conducted with Casa XPS software, and Gaussian-

Lorentzian line shape GL(30) (70% Gaussian and 30% Lorentzian) was used to fit all peaks. **Figure 3.19** displays two example fittings of ammonia desorption profile obtained by MS analysis (fragment 17 m/z) and obtained from similar W wt% samples on fumed silica and SBA-15. In both cases, profile deconvolution reveals the three peaks related to the distinct adsorption sites.

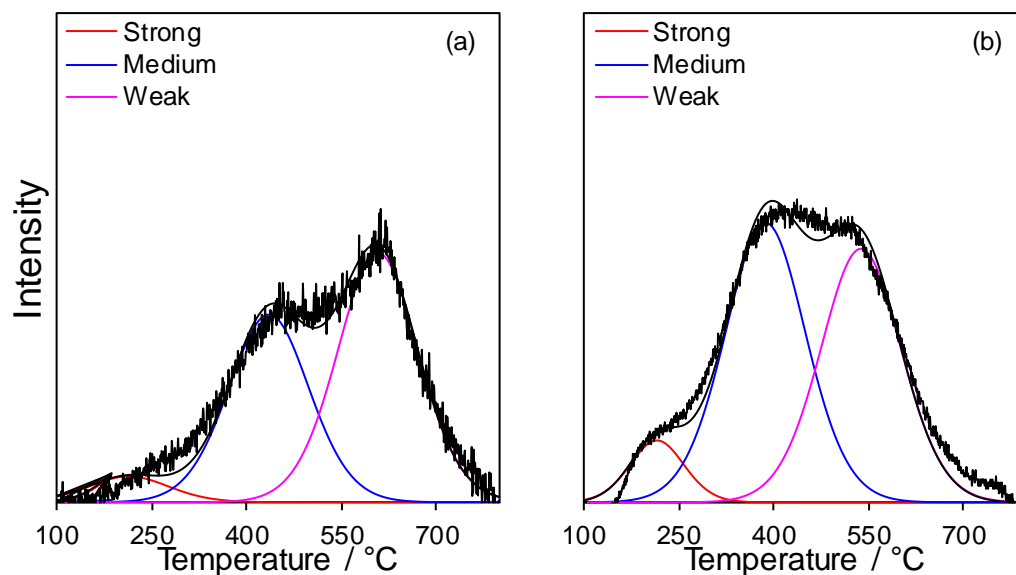


**Figure 3.19** – Fitting example of mass normalised 17 m/z MS channel from ammonia titration and TPD for 6.2 wt% W on fumed silica (a), and 9.0 wt% W on SBA-15 (b).

The weak, medium and strong acid site loading, evaluated from deconvolution peak areas, is reported in **Figure 3.20** as function of bulk W loading for both supports. HPW/fumed silica series exhibit an increase in medium acid sites loading with the W wt%, while the weak and strong remain almost constant across the series. In contrast, HPW/SBA-15 series show a linear increase of relative acid loading up to 38.2 wt% for all the adsorption sites (weak, medium and strong), accompanied to plateauing profiles at further loading. Comparison between ammonia titration and TPD and n-propylamine reveals similar acid loadings for the two supported HPW series, indicating a good correlation between the two techniques. Comparison of desorption temperatures from strong, medium and weak acid sites is more complicated. On one side ammonia TPD gives interesting information about the strength of interaction/adsorption between the small probe molecule and surface of solid materials; while on the other hand, n-propylamine TPD gives a narrower indication of the catalytic acid sites of catalysts [35].

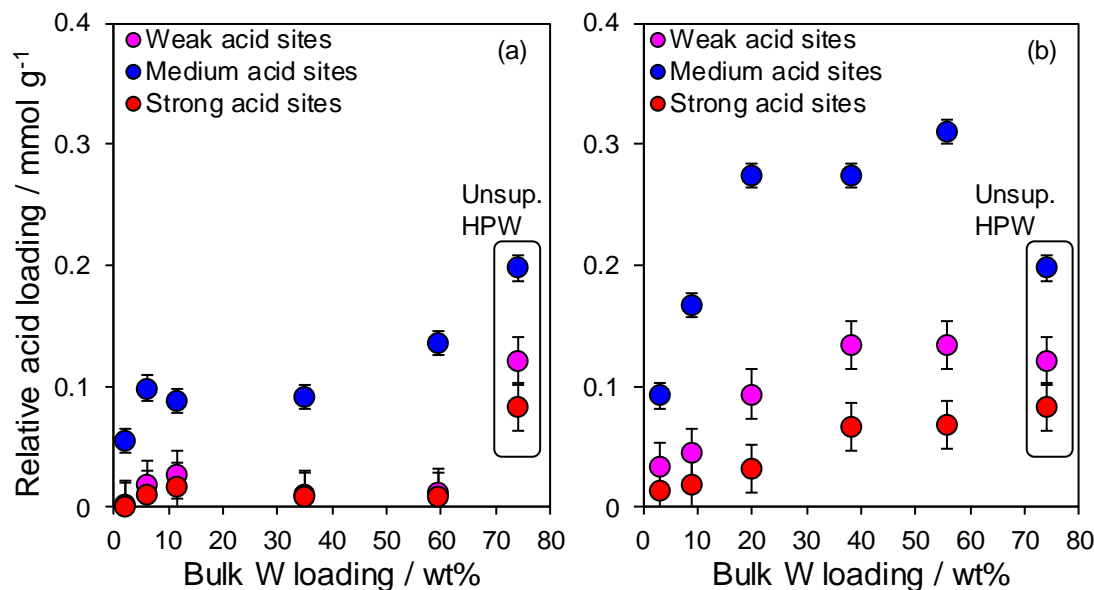


**Figure 3.20** – Relative acid loading for strong, medium and weak sites based on the relative peak area % (obtained from profile deconvolution) and the total acid loading as function of W wt% on both supports, fumed silica (a) and SBA-15 (b).

### 3.2.1.8 Diffuse reflection infrared Fourier transform spectroscopy (DRIFTS)

DRIFTS was initially carried out on the two parent support silicas to evaluate differences in surface silanol densities, which represent anchoring sites for the attachment of HPW and thus influencing the resulting agglomeration. **Figure 3.21**-(a) is in agreement with our TGA findings about the different silanols density of the two supports, with SBA-15 exhibiting OH stretches of isolated, vicinal and germinal OH groups being four time greater than those for fumed silica, with results comparable to the literature [19]. The evolution of isolated hydroxyl density as a function of bulk W loading for the two series is shown in **Figure 3.21**-(b). Surface OH groups, responsible for anchoring the HPW active phase, allow elucidation into the preferred aggregation model, monolayer or multilayer phases. Across both series, OH intensity is inversely proportional to HPW loading, exhibiting elimination of the isolated OH stretch for bulk W >35 wt%, for both series, indicating that above this loading the multilayer growth is the only possible. The higher OH intensities accompanied to higher surface area available, reflects a greater capacity for monolayer growth. In agreement with TGA and XRD analysis, at W loadings <35 wt%, the plot shows that on fumed silica, HPW preference is for the formation multilayers, whereas on SBA-15 results in monolayer growth of HPW.

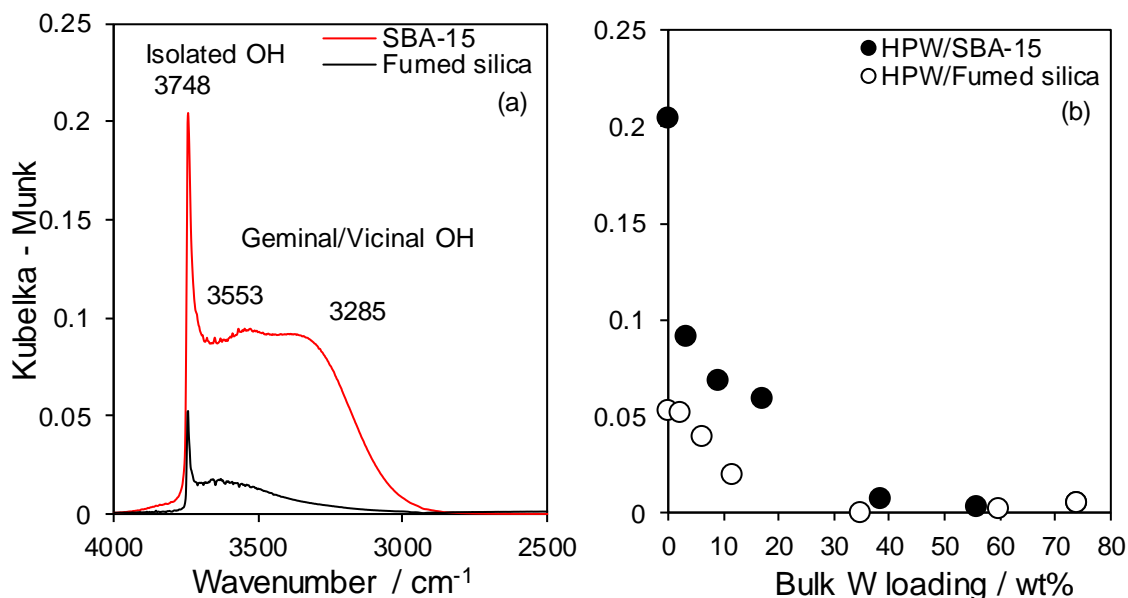


**Figure 3.21** – DRIFT spectra of SBA-15 and fumed silica, and assignment of silanol group function to vibrational signal (a); isolated OH K-M intensities as function of bulk W loading for HPW supported on fumed silica and SBA-15 [36] (b).

Furthermore, DRIFTS analysis was employed to examine the Keggin unit's structural integrity and potential effect of impregnation on both supports. IR spectral peaks of P-O, and W-O of HPW are observed in the region of 1150-700  $\text{cm}^{-1}$  wavenumbers [31, 37], as reported in **Figure 3.22**, with the upper loadings on both supports clearly exhibiting these features signifying retention of the HPW phase. At low loadings, the asymmetric P-O stretching and the internal stretching mode O-W-O are masked by the silanol vibrations, which are clearly visible at 1100 and 800  $\text{cm}^{-1}$  in the parent supports. Due to this loss in resolution between the heteropolyacid feature and those from the support. Raman spectroscopy was conducted to further prove the authenticity of the  $\text{H}_3\text{PW}_{12}\text{O}_{40}$  structure, results are reported in the following section.

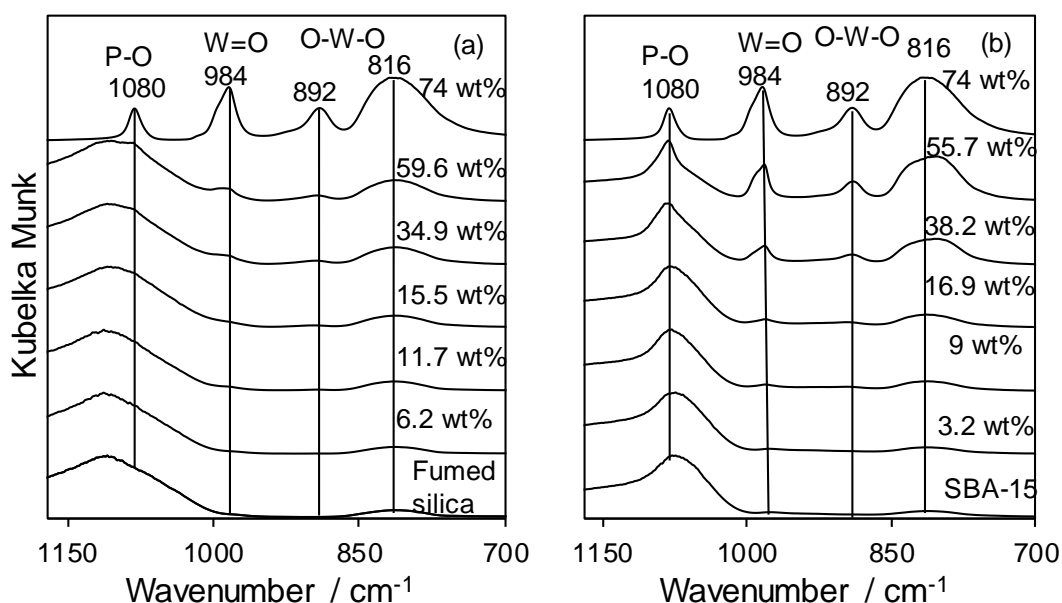


**Figure 3.22** – Stacked DRIFT spectra of supported HPW on fumed silica (a), and SBA-15 (b) as function of W bulk wt%, pure HPW and supports are reported for comparison.

*In situ* DRIFTS of the unsupported HPW was carried out to further investigate the thermo-decomposition steps of the Keggin unit, with an aim of studying how the structure decays. In **Figure 3.23**-(a), the vibrational bands of W-O, W-O-W and P-O stretches, over the the region 600-1200  $\text{cm}^{-1}$  wavenumbers, are shown as a function of temperature from 120 to 600 °C. Bridging vibrations, W-O-W, were discriminated as bridging core ( $W_{bc}$ ) and bridging edge ( $W_{be}$ ), the former referring to O atoms which interact with the central P atom; the latter refers to O atoms residing at the edge of the Keggin unit as the external surface. **Figure 3.23**-(b) reports Kubelka-Munk intensity of W=O and W- $O_{bc}$ -W as function of temperature; W=O terminal vibration (984  $\text{cm}^{-1}$ ) decreases as the temperature increases. The W- $O_{bc}$ -W vibration of core atoms varies following three different steps: starting at 120 up to 250 °C, shows a steady decrease of K-M intensity (in the same range was observed the dehydration of the HPW structure by XRD and TGA); a dramatic drop between 250 and 400 °C may reveal that the removal of the structural water begins with the extraction of the bridging oxygens which are more unstable, and destroying therefore the HPW structure; the final step, between 400 and 600 °C, shows the complete breakdown of the structure and partial disappearance of W- $O_{bc}$ -W. The ratio between the two stretching reveals the structure stability as function of temperature, indicating that the integrity of the HPW architecture is preserved when the the ratio W-O-W to W=O is stable (120-250 °C), while it drops dramatically mainly due to the decomposition of the W-O-W group.

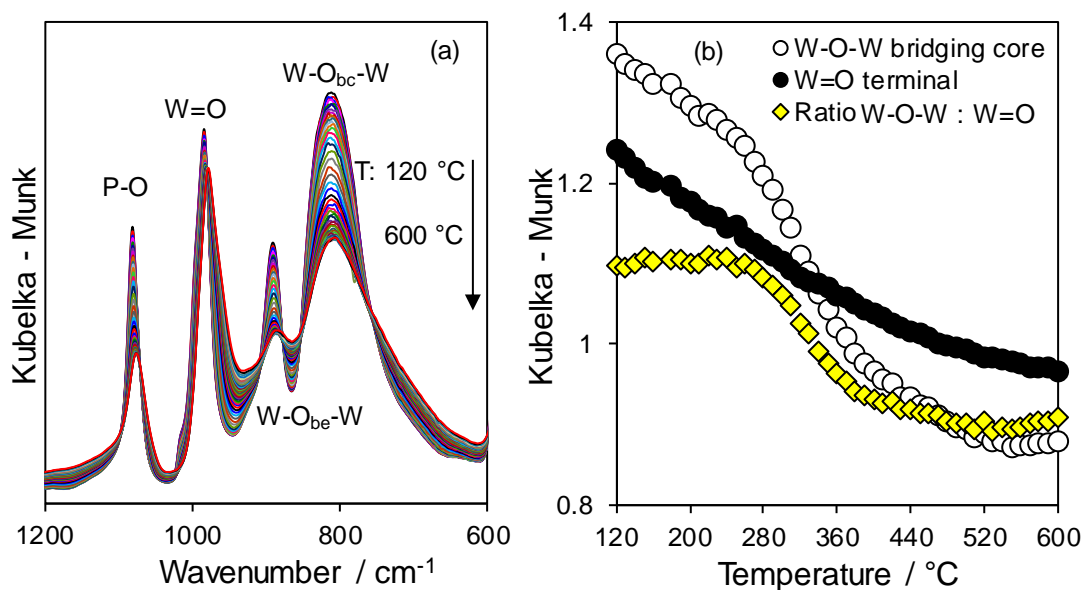


**Figure 3.23** – DRIFTS spectra of unsupported HPW collected from 120 to 600 °C (a); and dependence of Kubelka-Munk intensities on temperature indicating thermal stability of HPW units (b).

### 3.2.1.9 Raman spectroscopy

Raman spectroscopy was employed to further confirm the HPW structure of the two supports, and thus strengthen the conclusion drawn from XRD and DRIFT analysis. **Figure 3.24** reveals the Raman spectra of the bare SBA-15 support, with fumed silica the same shifts, and commercial WO<sub>3</sub>, a potential species from HPW decomposition. Both silicias exhibit Raman shifts at 976, 802, 607, and 487 cm<sup>-1</sup>, in agreement with the literature values [38], with a strong background signal due to fluorescence interference. The Raman shift at 976 cm<sup>-1</sup> is related to surface silanols Si-OH, whereas shifts at 800 cm<sup>-1</sup> are related to the Si-O-Si linkage and at 607 and 487 cm<sup>-1</sup> to three and four-membered siloxanes [39, 40]. WO<sub>3</sub> Raman spectra displays intense shifts at 805, 715, referred to  $\nu(W-O_b-W)$ , and at 270 cm<sup>-1</sup> related to  $\delta(W-O_b-W)$ , again as reported in literature [41].

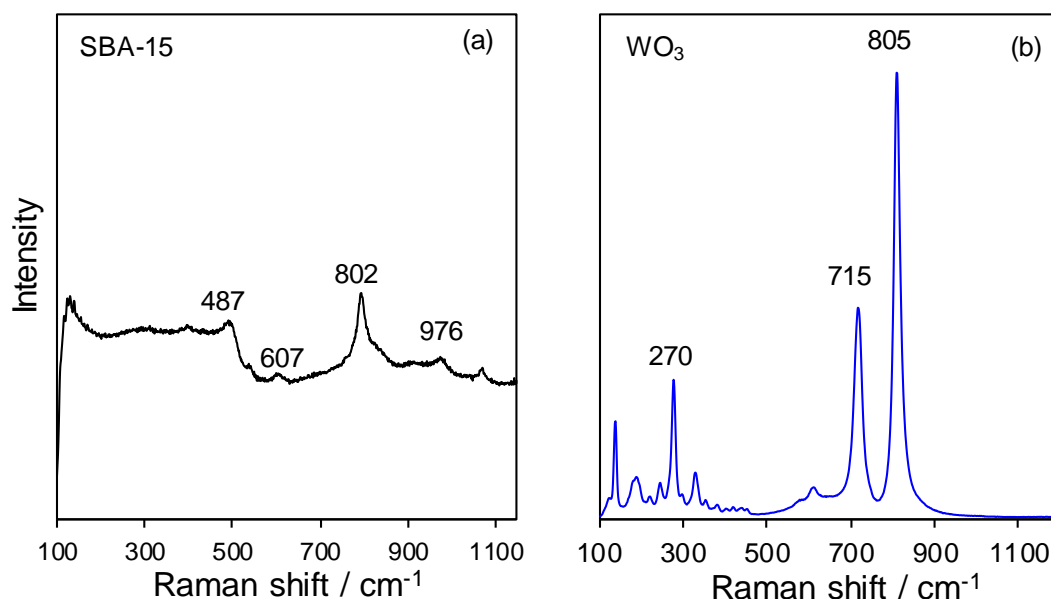


**Figure 3.24** – Raman spectra of mesoporous SBA-15 (a) and commercial WO<sub>3</sub> (b).

**Figure 3.25** reports the Raman spectra of the supported HPW samples; all samples possess the characteristics bands related to H<sub>3</sub>PW<sub>12</sub>O<sub>40</sub> in the “cage-like” Keggin arrangement, revealing no segregation has occurred during impregnation. HPW/SBA-15 materials display an increasing peak intensity with HPW loading. Along the series, for loading ≤16.9 wt%, vibrations have broad peaks and strong background signal due to support interference. The main shifts observed are at 1010, 990, 935, 890, 525 and 225 cm<sup>-1</sup> are assigned to  $\nu_s(W-O_t)$ ,  $\nu_{as}(W-O_t)$ ,  $\nu(P-O_a)$ ,  $\nu_{as}(W-O_b-W)$ ,  $\nu_s(W-O_{bc}-W)$ ,  $\nu_s(W-O_{be}-W)$  respectively. The various types of oxygen are distinguished as *b*, *bc*, *be* and *t*, where O<sub>b</sub> is the bridging atom between two W metals, O<sub>bc</sub> is internal bridging atom (core), whereas O<sub>be</sub> is the bridging edge oxygen atom, and O<sub>t</sub> is a terminal oxygen as W=O [42]. These stretches are in good agreement with those reported [43], and are similar to those of the bulk HPW shown in **Figure 3.24**. The same features are observed for samples on fumed silica with increasing peak intensities with increasing the W loading. Background interference is only appreciable for the lowest loadings, 2.2 wt%HPW/fumed silica and 3.2 wt% HPW/SBA-15, but even so the feature of HPW are still observed, and at loadings above 11.7 wt% this interference is not observed.

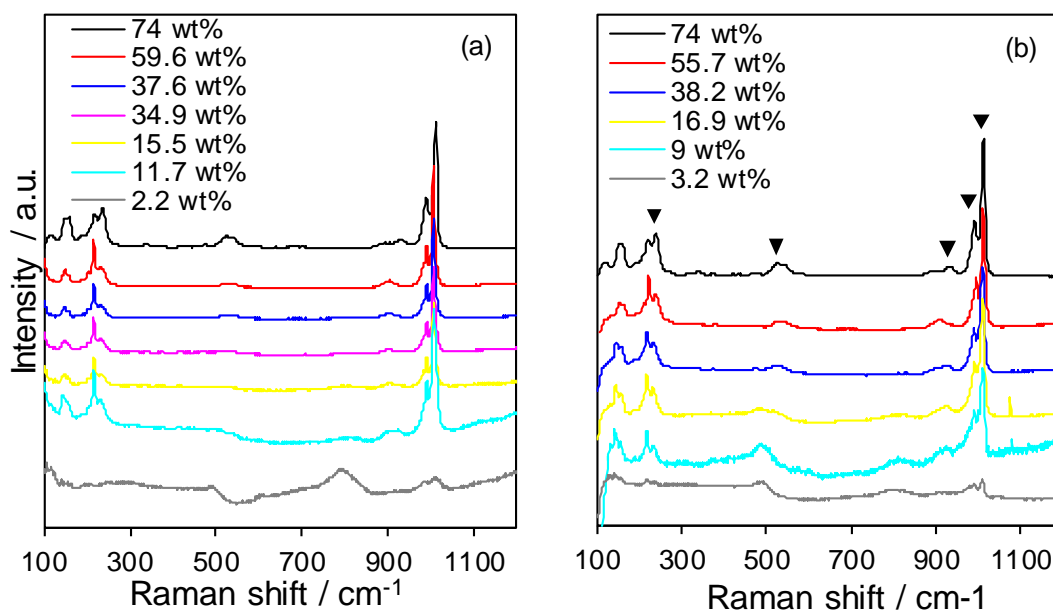


**Figure 3.25** – Stacked Raman spectra of HPW/Fumed silica (a); and HPW/SBA-15 (b). Labelled peaks (▼) are referred to unsupported HPW features.

Closer inspection of the major HPW peaks at  $1010\text{ cm}^{-1}$ , shown in **Figure 3.26**, which is related to terminal W-O symmetric vibration, are shifted to higher energies in both series, with  $\Delta\nu \sim 20\text{ cm}^{-1}$  and  $10\text{ cm}^{-1}$  for HPW on fumed silica and SBA-15 respectively. In the literature, shifts of the same band are associated either for HPW treated thermally, in which the heat leads to structural defects and increases the band shift [43], or when HPW coordinates with a different counter-cation than H, and interferes with the W=O<sub>t</sub> vibration [44, 45]. In our case, however, both cases are to be excluded, meaning that the  $\Delta\nu$  might be related to a defect in the structure, which changes the W-O<sub>t</sub> vibrational mode and hence its position. HPW species on fumed silica display a greater effect, and therefore can be described as being more defective compared to the samples on SBA-15, which suggests that a degree of the Keggin units are not fully intact, although the level of this is negligible due to the absence of peaks related to WO<sub>3</sub> (at 805, 715 and 270 cm<sup>-1</sup> [41]).

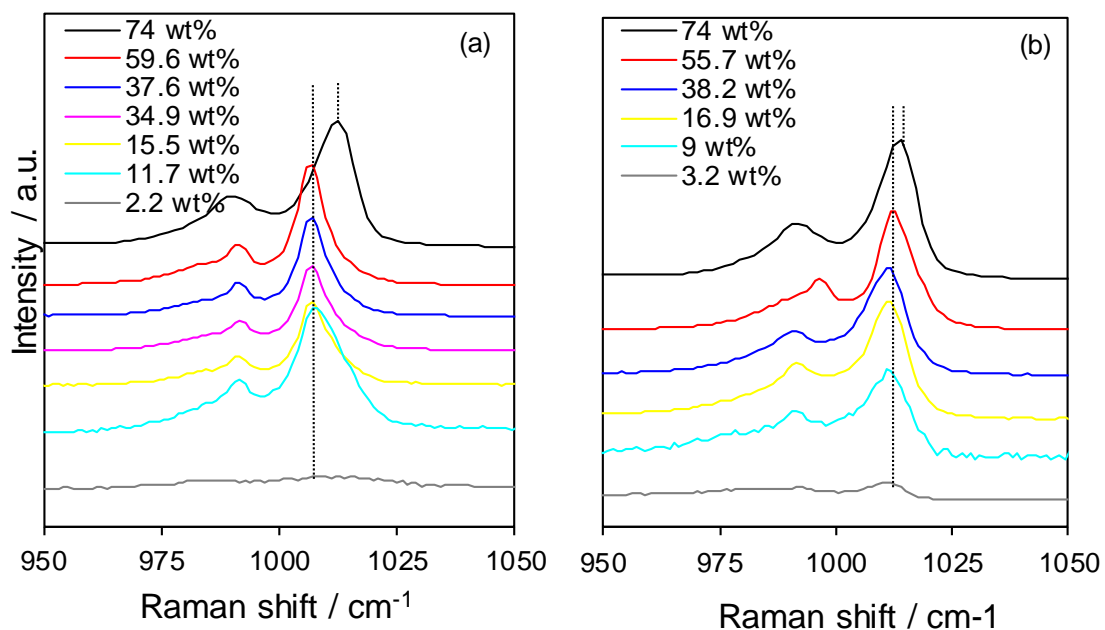


**Figure 3.26** – Stacked Raman spectra with dotted line indicating relative peak position, for HPW on fumed silica (a) and SBA-15 (b).

### 3.2.1.10 X-ray photoelectron spectroscopy (XPS)

XPS was conducted on the supported HPW series, with the W 4f signal of major interest, shown in **Figure 3.27** and **Figure 3.28**. The spectra for all samples can be deconvoluted into two distinct chemical species; the first W 4f<sub>7/2</sub> peak at 36.1 eV, and a spin-orbit splitting of 2.15 eV, is associated to the bulk W in the (VI) oxidation state, with the second W 4f<sub>7/2</sub> peak, associated to perturbed W species on the surface which are interacting either with the surface silanols or perturbed by vicinal HPW species [46-48], is observed at 34.5 eV.

HPW/fumed silica XPS spectra are reported in **Figure 3.27**, where unsupported HPW was plotted for comparison. Supported materials show same binding energies related to bulk W doublet of their parent at 36.1 eV; the additional doublet of interfacial W shifted of 1.6 eV towards lower binding energies exhibits same spin-orbit splitting of 2.15 eV. As reported in **Figure 3.27**-(b) across the series is observed the decreasing of interface species relative to the bulk, with increasing W loading. At low W loadings (<20 wt%), the ratio interfacial:bulk W species is almost constant at ~0.5 [49], at higher loadings, the value drops to ~0.3 and is due to the formation of big agglomerates, as also confirmed by XRD and STEM analysis. Surface W quantification indicates that when 59.6 wt% of bulk W (measured from XRF) is loaded on the support, only ~10.5 wt% is actually

detected from XPS, indicating the fast 3-D growth of HPW clusters on fumed silica (from bulk W >6.1 wt%) as confirmed from XRD, TGA, STEM and DRIFTS.

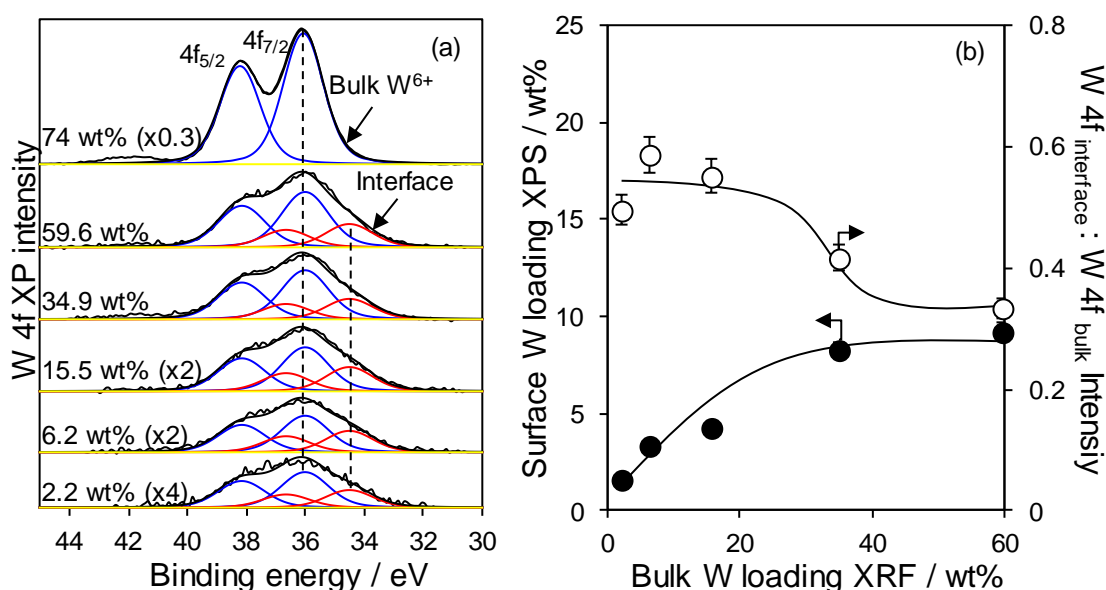


**Figure 3.27** – Background subtracted W 4f XP spectra of HPW/fumed silica series (a); and ratio of integrated signal of interfacial to bulk W 4f species across the loading on SBA-15, and correlation between surface and bulk W wt% loadings(b).

Similarly, on **Figure 3.28**-(a) HPW/SBA-15 exhibit equal binding energies and spin-orbit splitting of the two W species, bulk and interfacial, observed on fumed silica. Again, the ratio between relative intensities of W 4f surface and bulk species (**Figure 3.28**-(b)) decreases as bulk loading increases, suggesting that the interfacial W doublet is attenuated by with the formation of bigger particles, as observed previously. At the sub-monolayer coverage, between 3.2 and 16.9 wt%, species are widely dispersed on the surface and K.U. exhibit a trimodal coordination mode [46], which can lead to highly perturbed W=O<sub>t</sub> species. For loadings ≥38.2%, agglomeration is favoured, in agreement with the results from TGA, STEM and XRD.

Across both series, the level of perturbed W atoms may be higher than expected which could be due to the interaction of W with surface OH, due to the surface sensitivity of the techniques, or alternatively due to defective HPW that is too small to be detectable via other techniques including XRD and DRIFTS, but which are still able to perturb the neighbouring W and are indicated in the Raman analysis which shows a  $\Delta\nu$  for the most intense band, which is related to terminal W-O vibrations.

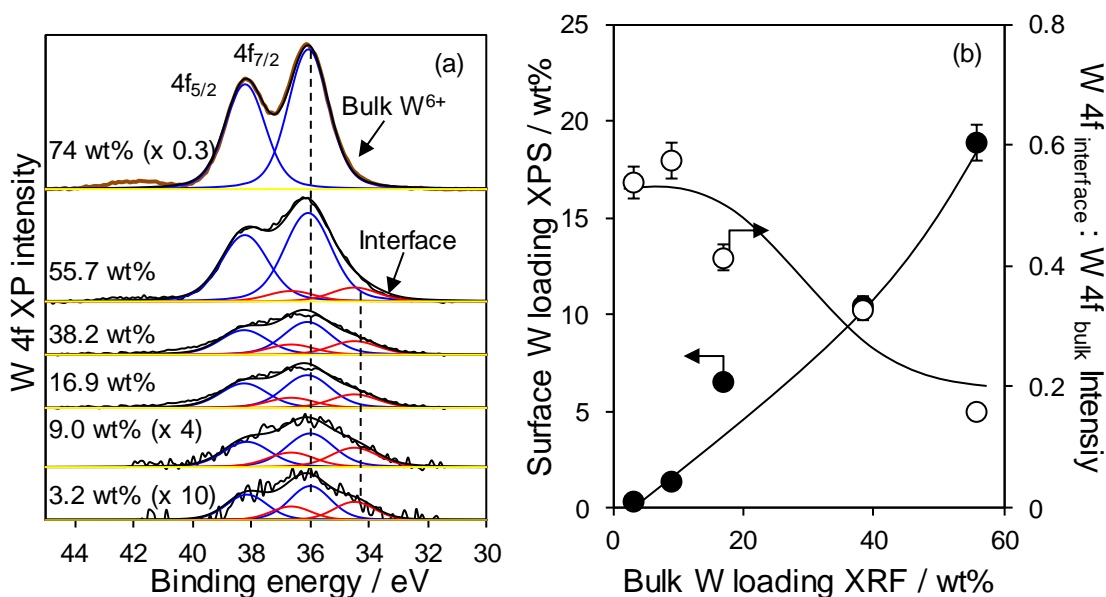


**Figure 3.28** – Background subtracted W 4f XP spectra of HPW/SBA-15 series (a); and ratio of integrated signal of interfacial to bulk W 4f species across the loading on SBA-15, and correlation between surface and bulk W wt% loadings (b).

### 3.2.2 Silicotungstic and phosphomolybdic acid based materials

Silicotungstic and phosphomolybdic acids (HSiW and HPMo respectively), Keggin type heteropolyacids, have been studied in order to investigate the influence of the central atom and heteroatoms on physiochemical properties and subsequent catalytic activity. The two alternative heteropolyacids, HSiW and HPMo, were deposited onto SBA-15, chosen due to its greater capacity towards higher dispersion of the HPAs units. Herein, the physiochemical properties of HSiW and HPMo on SBA-15 are reported, as elucidated by a wide array of characterisation techniques.

#### 3.2.2.1 X-ray Fluorescence (XRF)

SBA-15 supported HSiW and HPMo were synthesised utilising the same incipient wet impregnation method as for the HPW series. XRF elemental analysis was carried out to determine the actual wt% of bulk W and Mo, and prove the efficiency of our protocol. **Table 3.6** compares nominal with actual loadings, where each value is affected by standard error as reported by the instrument.

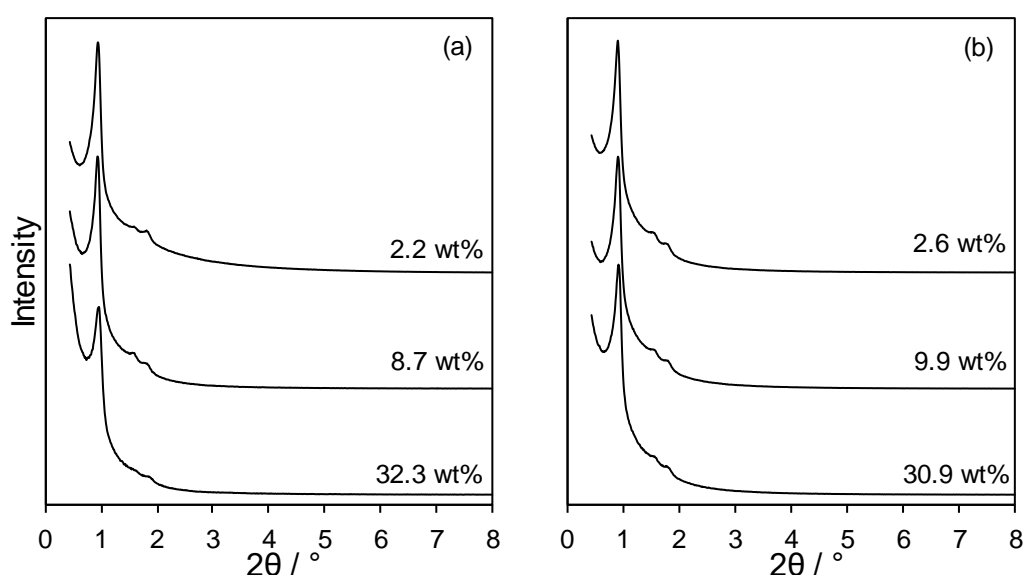
**Table 3.6** – XRF elemental analysis data of synthesised materials.

HPMo/SBA-15			HSiW/SBA-15		
Measured bulk Mo loading / wt%	Calculated HPMo loading / wt%	Nominal HPMo loading / wt%	Measured bulk W loading / wt%	Calculated HSiW loading / wt%	Nominal HSiW loading / wt%
2.2 ( $\pm 0.3$ )	3.4 ( $\pm 0.3$ )	5	2.6 ( $\pm 0.3$ )	3.5 ( $\pm 0.3$ )	5
8.7 ( $\pm 0.1$ )	13.8( $\pm 0.1$ )	15	9.9 ( $\pm 0.1$ )	13.3 ( $\pm 0.1$ )	15
32.3 ( $\pm 0.1$ )	51.3( $\pm 0.1$ )	50	30.9 ( $\pm 0.1$ )	41.7( $\pm 0.1$ )	50

### 3.2.2.2 Powder X-ray diffraction (XRD)

XRD analysis allowed the structural integrity of the mesoporous support, and any influence of the impregnation protocol, to be evaluated, and furthermore, allowed for the degree of aggregation, as a function of loading, of HSiW and HPMo on the SBA-15 support to be studied.

Low angle powder XRD analysis on both HPMo and HSiW on SBA-15 (**Figure 3.29**) confirm the retainment of the SBA-15 *P6mm* space group after impregnation as observed in (**Figure 3.2**-(a)). The three d(100), d(110) and d(200) reflections were observed over the  $2\theta$  range of  $0.8^\circ$ - $3^\circ$ , and indicate a mesoporous structure. For both series, unit cell calculations from the d(100) reflection was calculated and reported in **Table 3.7**. As observed for the HPW/SBA-15 series, the value is independent on the W wt% with no changes in unit cell and thus pore spacing observed.

**Figure 3.29** – Low angle powder XRD pattern of HPMo/SBA-15 (a) and HSiW/SBA-15 (b).

**Table 3.7** – Unit cell parameters and corresponding pore spacings for supported HPMo and HSiW on SBA-15.

Bulk Metal loading / wt%		d(100) / nm	Pore spacing (a) / nm
SBA-15	0	8.5	9.9
HPMo	2.2	9.0	10.3
	8.7	9.0	10.3
	32.3	8.9	10.2
HSiW	2.6	8.7	10.0
	9.9	8.7	10.1
	30.9	8.9	10.2

Wide angle XRD analyses for the two supported series and those for the unsupported HPMo and HSiW, which shown for comparison, are reported in **Figure 3.30**. Diffraction patterns of unsupported HPMo in **Figure 3.30**-(a), 63 wt% of bulk Mo loading, displays a triclinic structures of  $H_3PMo_{12}O_{40} \cdot 13H_2O$  with most intense peaks at  $26.2^\circ$  and  $27.7^\circ$ , and *a*, *b* and *c* unit cell parameter of 14.54, 14.79 and 13.65 Å respectively [50-52]. The unsupported HSiW XRD pattern in **Figure 3.30**-(b), 76.6 wt% of bulk W loading, displays the typical peaks of HSiW Keggin structure at  $10.9^\circ$ ,  $25.5^\circ$ ,  $34.7^\circ$ , which is in agreement with the literature [53-55]. For HSiW, the resulting pattern indicates a highly hydrated HSiW in an orthorhombic unit structure, with cell parameters *a*, *b*, *c* as 20.83, 13.09 and 18.87 Å respectively, in the final formula of  $H_4SiW_{12}O_{40} \cdot 24H_2O$  [53]. The HSiW structure becomes cubic after controlled removal of water in the hexahydrate arrangement. For supported HPAs, in both series, at metal loadings  $\leq 9\%$ , only the broad peak of SBA-15 at  $23.2^\circ$  is visible, revealing well dispersed HPAs structures over the support. Broad peaks of the characteristic patterns of parents are observed for 32.3 wt% and 30.9 wt% of heteroatom loading (W or Mo) of HPMo/SBA-15 and HSiW/SBA-15 respectively.

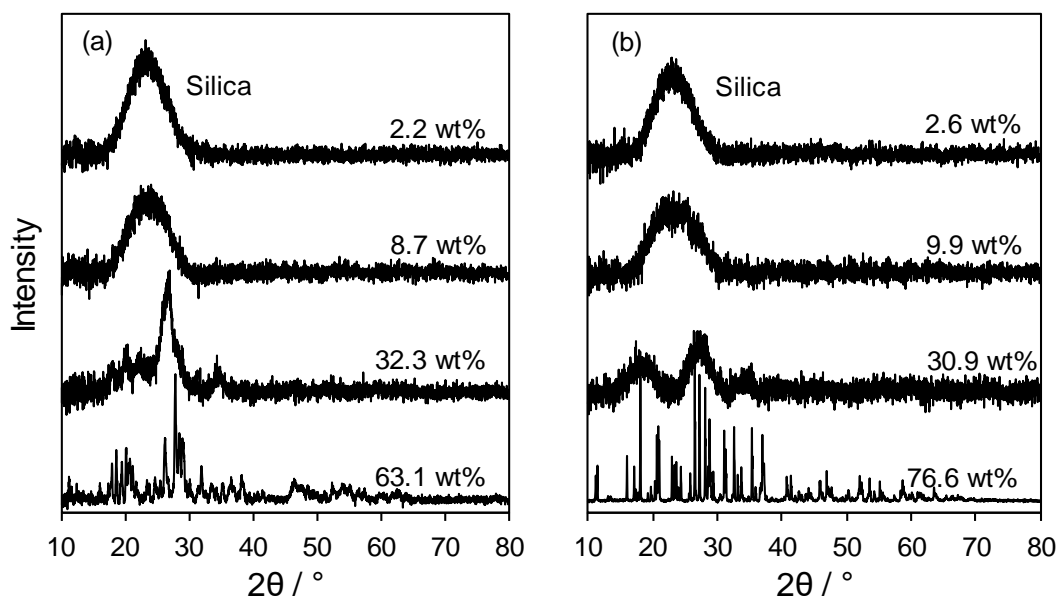


**Figure 3.30** – Wide angle XRD patterns for (a) HPMo/SBA-15, and (b) HSiW/SBA-15 as function of metal loading. Unsupported HPAs are added as reference.

Particle size results (**Table 3.8**) show that at low loading (5-8 wt%) HSiW/SBA-15 samples exhibit only discrete K.U., being HSiW peaks not detectable; at higher metal loading, 30.9 wt%, nano-clusters of ~4 K.U. are observed. Similar features are detected for HPMo/SBA-15 materials, where only at 32.2 wt% Mo loading are observed agglomerates of 7/8 K.U. suggesting that agglomeration is slightly higher compared to their counterpart HSiW.

**Table 3.8** – Particle size dependence of Mo and W loading on SBA-15.

HPMo/SBA-15		HSiW/SBA-15	
Bulk Mo loading / wt%	Particle size / nm	Bulk W loading / wt%	Particle size / nm
5	-	5	-
8.7	-	8	-
32.2	6.8 ( $\pm 0.2$ )	30.9	3.2 ( $\pm 0.2$ )
Unsupported $H_3PMo_{12}O_{40}$ =42.6 nm		Unsupported $H_4SiW_{12}O_{40}$ =101.4nm	

### 3.2.2.3 Nitrogen porosimetry

$N_2$  porosimetry was carried out to evaluate surface area, pore diameter and volume, for comparison with those textural properties of parent SBA-15 support material, shown in **Figure 3.6** and **Figure 3.9**. **Figure 3.31** reveal characteristic type IV isotherms for both series, HPMo/SBA-15(a) and HSiW/SBA-15 (b), which are typical of mesoporous

materials with both exhibiting type H1 hysteresis loops due to the mesopore diameters of SBA-15 and confirm the parent architecture is maintained [56].

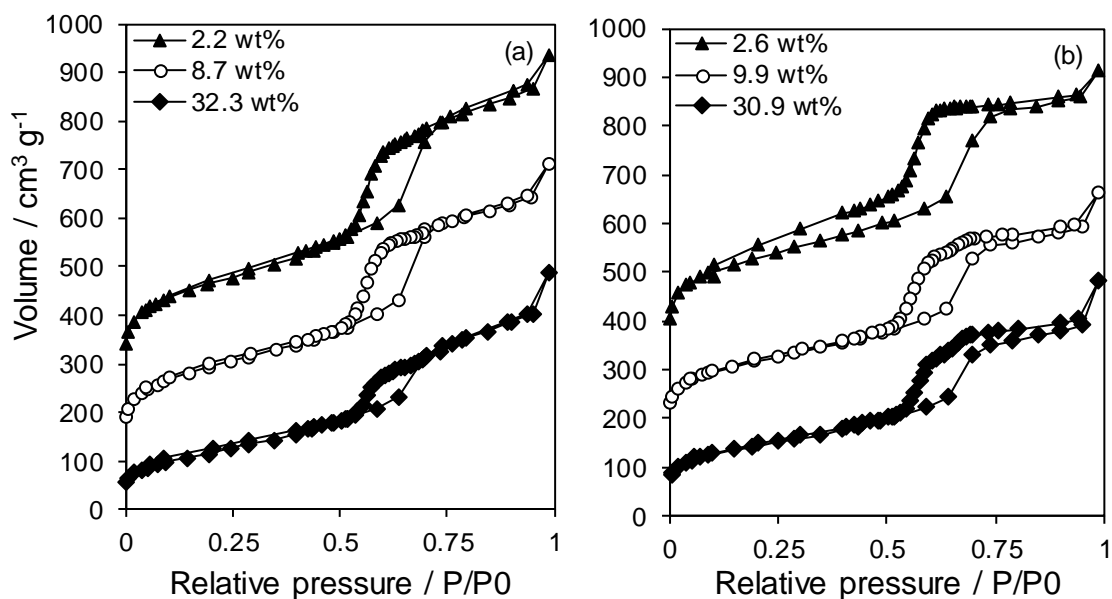


**Figure 3.31** – Stacked isotherms of nitrogen adsorption and desorption for SBA-15 supported HPAs at different metal wt%; HPMo/SBA-15 (offset of  $100 \text{ cm}^3 \text{ g}^{-1}$ ) (a) and HSiW/SBA-15 (offset of  $150 \text{ cm}^3 \text{ g}^{-1}$ ) (b).

The textural properties of HSiW and HPMo supported materials are reported in **Table 3.9**, where BET measurements and total pore volume were normalised per mass of silica. As for HPW/SBA-15, supported HPMo and HSiW show lower BET values compared to their parent SBA-15. Across both series, increasing the metal loading, surface areas exhibit almost constant values at  $\sim 850 \text{ m}^2 \text{ g}^{-1} \text{ SiO}_2$ . Micropore surface area calculated via  $\text{N}_2$  t-plot method showed diminishing values as both Mo and W wt% increases, suggesting micropores filling during silica impregnation. For the two series, pore volume values decrease constantly from  $1.04 \text{ cm}^3 \text{ g}^{-1}$  of the parent material to  $0.59$  and  $0.63 \text{ cm}^3 \text{ g}^{-1}$  obtained for  $32.3 \text{ wt}\%$  HPMo/SBA-15 and  $30.9 \text{ wt}\%$  HSiW/SBA-15 respectively.

Pore diameter measurements witnesses a small decrease for high loading samples, suggesting that HPAs Keggin units are dispersed over the surface of SBA-15, and have a narrow pore size distribution, as confirmed in **Figure 3.32**. It can be deduced that independently from the type of HPAs used, the high surface area of SBA-15 and its pore dimensions are highly suitable to disperse Keggin structures within the range of  $0\text{-}38 \text{ wt}\%$ .

**Table 3.9** – Textural properties of HPMo and HSiW on SBA-15 across the metal loading, wt%.

Sample/ SBA-15	Bulk metal loading / wt%	Pore diameter <sup>(a)</sup> / nm	Pore volume <sup>(b)</sup> / cm <sup>3</sup> g <sub>SiO<sub>2</sub></sub> <sup>-1</sup>	Surface area <sup>(c)</sup> / m <sup>2</sup> g <sup>-1</sup> SiO <sub>2</sub>	Micropore surface area <sup>(d)</sup> / m <sup>2</sup> g <sup>-1</sup> SiO <sub>2</sub>
SBA-15	0	5.86	1.04	923	441 (± 44)
HPMo	2.2	5.37	0.97	799 (± 79)	106 (± 10)
	8.7	5.36	0.91	804 (± 80)	137 (± 14)
	32.3	5.36	0.93	859 (± 86)	0 (± 10)
HSiW	2.6	5.36	0.89	849 (± 85)	302 (± 30)
	9.9	5.26	0.74	801 (± 80)	167.8 (± 17)
	30.9	5.50	0.85	870 (± 87)	163.3 (± 16)

<sup>(a)</sup>BJH desorption branch of isotherm, <sup>(b)</sup>Total pore volume recorded at 0.975 P/P<sub>0</sub>, <sup>(c)</sup>N<sub>2</sub> BET, <sup>(d)</sup>N<sub>2</sub> t-plot

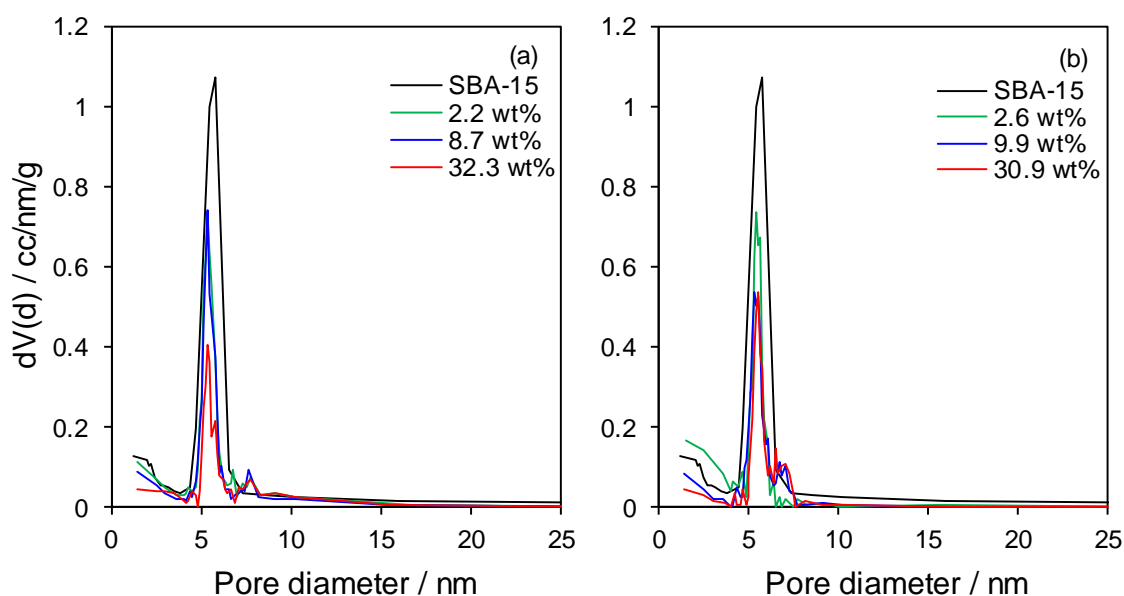


**Figure 3.32** – BJH pore size distribution for HPMo/SBA-15 series (a), and HSiW/SBA-15 series (b).

### 3.2.2.4 Thermogravimetric analysis (TGA)

The thermal stability of HSiW and HPMo supported on SBA-15 was evaluated by TGA, and is shown alongside the unsupported materials for comparison in **Figure 3.33**. As with the HPW, both HPMo and HSiW decompose following defined steps; first the loss of physisorbed water (<100 °C), second the loss of crystalline water trapped within HPA clusters that define the hydration stoichiometry (110-200 °C), and third the decomposition of the Keggin structure. Differential mass loss calculation was carried out to highlight each decomposition step, and results are reported in **Figure 3.34**.

The first desorption process is related to physisorbed water and is present in all SBA-15 supported samples (highlighted in blue). The desorption of crystalline water (highlighted in yellow) for unsupported HPMo, where crystalline water desorption was observed at 100 °C [6], is equal to 7.1% of weight loss and suggesting  $\text{H}_3\text{PMo}_{12}\text{O}_{40}\cdot 8\text{H}_2\text{O}$  stoichiometry, whereas for HSiW this occurs at 180 °C [57, 58], and corresponds to a 14.2% weight loss from the bulk, and is equivalent to ~23.6 of water molecules. In the case of HPMo, the water stoichiometry is lower than the amount determined by XRD (13  $\text{H}_2\text{O}$ ), which given its relatively lower temperature of adsorption can be attributed to the difference in temperature that the two techniques are conducted at, 25 °C for XRD whereas TGA starts at 50 °C under constant gas flow. In contrast, the TGA determined water of crystallinity for HSiW, with significantly higher desorption temperature, is in excellent agreement with XRD confirming the  $\text{H}_4\text{SiW}_{12}\text{O}_{40}\cdot 24\text{H}_2\text{O}$  stoichiometry.

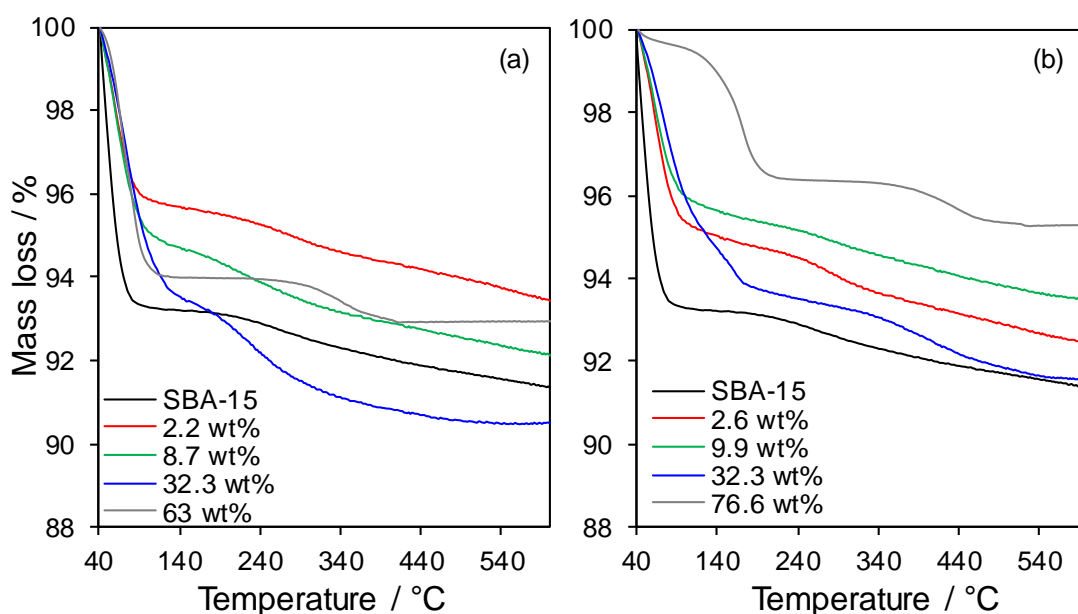


**Figure 3.33** – Thermal analysis expressed as % mass loss as function of temperature on HPMo/SBA-15 series (a) and HSiW/SBA-15 (b).

For the two supported series, the desorption of water of crystallinity is only visible at loading >10 wt%, as at low loadings, the highly dispersed Keggin units result in reduction in the degree of crystalline water present. The final evolution is the decomposition of the heteropolyacids, and witnesses the loss of *constitutional water* which for HPMo and HSiW starts at 240 and 300 °C respectively, and is completed at 450 °C for both series [23, 52].

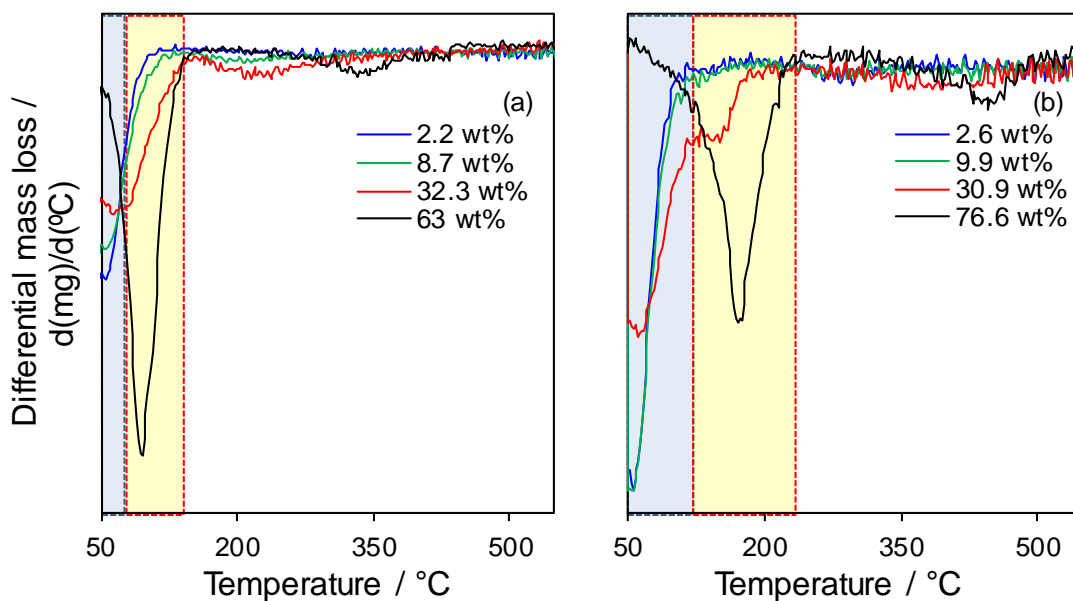


**Figure 3.34** – Thermogravimetric analysis of SBA-15 supported materials, HPMo (a) and HSiW (b).

### 3.2.2.5 n-Propylamine chemisorption and temperature programmed desorption (TPD)

The acidity of the solid catalysts, HSiW and HPMo on SBA-15, were investigated by n-propylamine chemisorption and TPD. From the HPW analysis (**Figure 3.15**), strong acidity was observed at 264 °C, with two further acid sites with medium and weak acidity, due to propene desorption being apparent at 340 and 414 °C respectively. **Figure 3.35-**(a) shows propene desorption from unsupported HPMo starting at 290 °C and finishing at 550 °C, with the HPMo supported on SBA-15 revealing the same trend, which can be attributed to common acidity, same acid strength, and confirming that the acid properties were unaffected by impregnation. **Table 3.10** reports the measured acid densities for supported and unsupported HPMo; with each evaluated from the corresponding mass loss with appropriate background correction using the untreated catalyst. Acid site density is proportional to bulk Mo loading, reaching the maximum of 1.32 mmol g<sup>-1</sup> for pure HPMo. The unsupported HSiW and supported on SBA-15 (**Figure 3.35-**(b)), display propene desorption in the range 200-530 °C. As reported in **Table 3.10**, acid site densities of HSiW series are comparable to those of the HPMo series, which increases as function of loading and reach a maximum of 1.16 mmol g<sup>-1</sup> for the unsupported HSiW, which agrees with the literature value [55].

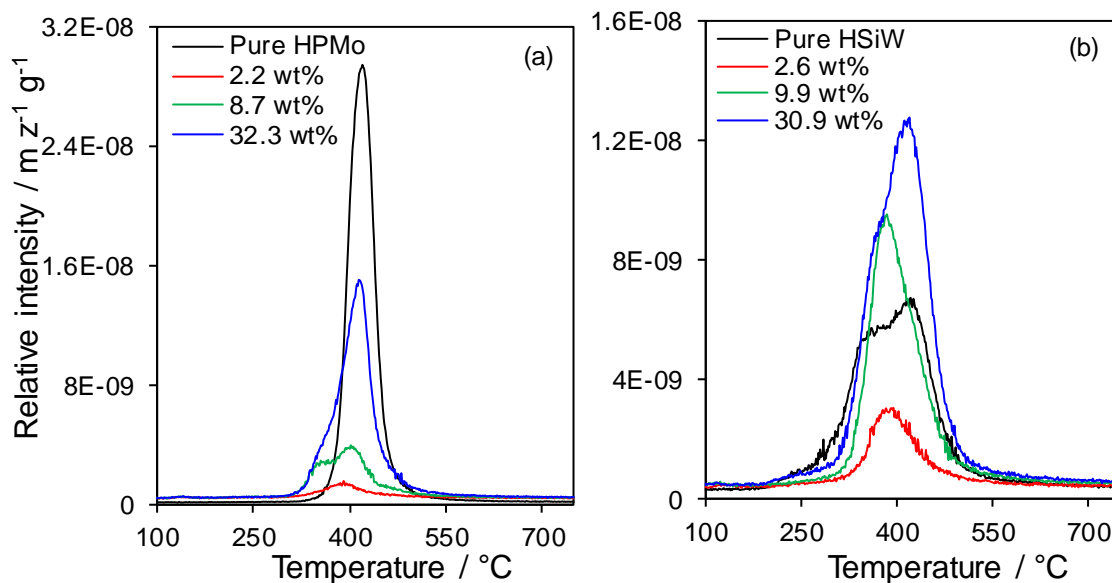


**Figure 3.35** – n-Propylamine TPD relative intensities of m/z normalised per g of sample for SBA-15 supported HPA over the metal wt% series; HPMo/SBA-15 (a) and HSiW/SBA-15 (b).

**Table 3.10** – n-Propylamine measured acid sites densities of SBA-15 supported HPMo and HSiW.

HPMo/SBA-15		HSiW/SBA-15	
Bulk Mo loading / wt%	Acid loading / mmol g <sup>-1</sup>	Bulk W loading / wt%	Acid loading / mmol g <sup>-1</sup>
5	0.09	5	0.08
8.7	0.27	8.0	0.23
50	0.60	50	0.54

Unsupported H<sub>3</sub>PMo<sub>12</sub>O<sub>40</sub>=1.32 mmol g<sup>-1</sup>    Unsupported H<sub>4</sub>SiW<sub>12</sub>O<sub>40</sub>=1.16 mmol g<sup>-1</sup>

To evaluate the degree of strong, medium and weak acid sites, deconvolution of the MS propene spectra was conducted. **Figure 3.36** shows a fitting example on both series, where signals have been deconvoluted in weak, medium and strong acid sites, as previously done for the HPW series, which showed peaks at 264, 367 and 407 °C. HPMo based materials desorbed propene at 310, 380 and 410 °C indicating that the Mo based materials are the weakest solid acids of the HPAs investigated, and that the replacement of W with Mo induces the greatest impact on the acidic strength [59]. The HSiW series showed slightly weaker acid strength compared to HPW, exhibiting the desorption of propene at higher temperatures for the strong acid site (at 285 °C) and lower desorption temperature 335 and 402 °C suggesting a stronger weak character compared to HPW.

The two materials differ especially for the medium type acid site, which changes of  $\Delta T = 30\text{ }^{\circ}\text{C}$ , and is related to the substitution of the central atom, P to Si [59].

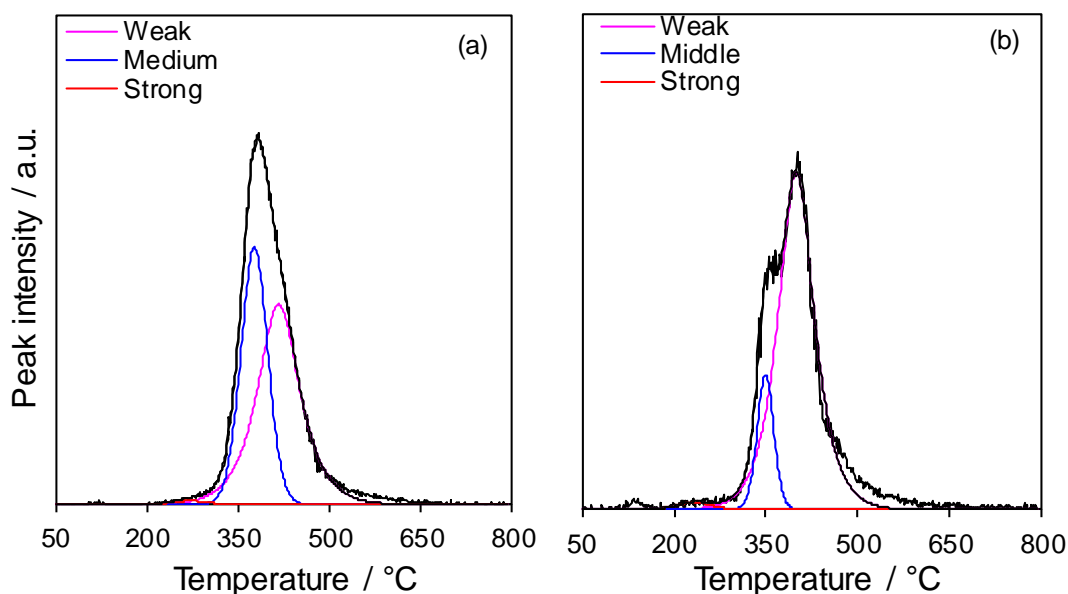


**Figure 3.36** – Fitting example of 41 m/z MS channel normalised for the g of solid sample, collected during n-propylamine chemisorption and TPD analysis, and obtained via Casa XPS software on and HPMo/SBA-15, bulk Mo 8.7 wt% (a), and HSiW/SBA-15, bulk W 9.9 wt% (b).

### 3.2.2.6 Diffuse reflection infrared Fourier transform spectroscopy (DRIFTS)

DRIFT measurements of the supported HPMo and HSiW, are reported in **Figure 3.37**, along with unsupported species and the parent SBA-15 support. For the HPMo/SBA-15 series, the same characteristic peaks of the unsupported HPMo are apparent, with intensity increasing as a function of loading. Reported literature values [45, 60-62], allow the following assignments; Mo-O-Mo asymmetric vibrations at  $870$  and  $790\text{ cm}^{-1}$  are related to the Mo stretching with bridging and core oxygen atoms, respectively; stretching of Mo=O are observed at  $963$  and P-O at  $1070\text{ cm}^{-1}$ , with Si-O-Si stretching observed for on the supported materials at  $1100\text{ cm}^{-1}$ , as seen previously for HPW on SBA-15. The unsupported HSiW, and deposited on SBA-15, exhibit vibrations that show a small shift in frequency relative to HPW counterparts, due to the different central atom, Si instead of P. Stretching at  $880$  and  $800\text{ cm}^{-1}$  are attributed to W-O-W vibrational modes interacting with bridging and internal oxygen atoms, whereas  $\nu$  at  $980\text{ cm}^{-1}$  are associated to W=O. For this type of series, two different Si-O signals are observed, one due to the support at  $1100\text{ cm}^{-1}$ , and a second due to Si being the central atom of the

Keggin structure, which is observed at  $930\text{ cm}^{-1}$  and in agreement with literature values [57, 63].

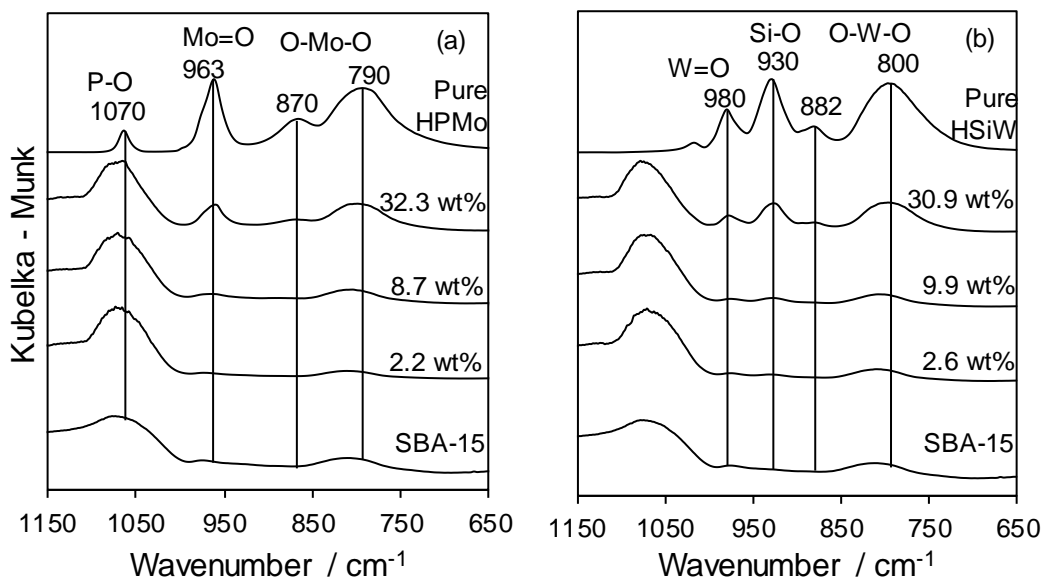


**Figure 3.37** – Stacked DRIFT spectra of HPMo/SBA-15 series (a), and HSiW/SBA-15 series (b), as function of metal loading wt%, pure HPAs and support are reported for comparison.

### 3.2.2.7 Raman spectroscopy

Raman spectroscopy was utilised to further confirm the retention of the Keggin structure after impregnation on SBA-15, and support the conclusion drawn from XRD and DRIFT analysis. **Figure 3.38** reports Raman shifts of unsupported HSiW and HPMo samples along with their supported species, revealing that for both series the heteropolyacid structure is retained after impregnation on the silica support and no formation of  $\text{MoO}_3$  and  $\text{WO}_3$  discernible. The spectra of unsupported HPMo is in agreement with the literature, showing shifts at 998, 975, 909, 630,  $251\text{ cm}^{-1}$  which correspond to  $\nu_s(\text{Mo-O}_t)$ ,  $\nu_{as}(\text{Mo-O}_t)$ ,  $\nu_{as}(\text{Mo-O}_{be}\text{-Mo})$ ,  $\nu_s(\text{Mo-O}_{be}\text{-o})$ ,  $\nu_s(\text{Mo-O}_{bc}\text{-Mo})$ , and  $\nu_s(\text{Mo-O}_a\text{-P})$ , respectively [61]. The supported species display the same features of their parent, with intensity proportional to loading, as observed before, and at low loading, bulk Mo 2.2 wt%, the signal suffers of background interference. HSiW supported series showed excellent agreement with the unsupported species, displaying peaks at 995, 972, 890, 500 related to  $\nu_s(\text{W-O}_t)$ ,  $\nu_{as}(\text{W-O}_t)$ ,  $\nu_{as}(\text{W-O-W})$ , [58, 64]. Again, no chemical shifts are observed suggesting the absence of defected species and further proving the integrity materials.

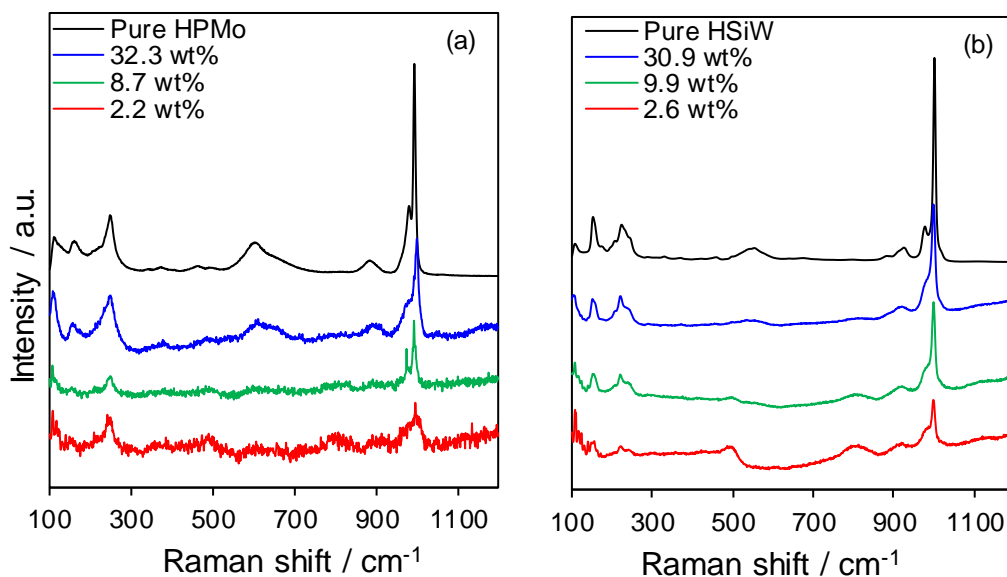


**Figure 3.38** – Stacked Raman spectra of HPMo/SBA-15 (a); and HSiW/SBA-15 (b).

### 3.2.2.8 XPS – X-ray photoelectron spectroscopy

XPS analysis were carried out on both series, HPMo/SBA-15 and HSiW/SBA-15, to investigate the surface character of the catalysts. As with the HPW supported on silica, we observe two metal M(VI) species, where M is either Mo or W, one representing unaffected metal atoms and the second due to perturbed species which arise from the interaction with neighbouring silanol groups or from defected species, although the latter was not apparent by alternative techniques such as Raman spectroscopy.

**Figure 3.39**-(a) reports the evolution of HPMo species on SBA-15, showing the Mo 3d<sub>5/2</sub> doublet at 232.90 eV characteristic of Mo(VI) species with a spin orbit digit of 3.15 eV [65, 66], accompanied with a second doublet at 231.17 eV related to perturbed species, possibly with a lower oxidation state, due to the linear dependence of Mo electronic state with the binding energy values [67]. Deconvolution allows the effect of loading on the ratio of bulk to perturbed to be determined, which is shown **Figure 3.39**-(b), where the ratio between interfacial to bulk Mo species decreases with loading. Additional studies were carried out to verify the dispersion of HPMo species on the silica support and to compare findings with the HPW/SBA-15 series. As reported in **Figure 3.39**-(b), the amount of surface Mo increases to a maximum of 7 wt%, which is significantly lower than the bulk loading of 32.3 wt% indicating an important degree of agglomeration of the Keggin units. At lower wt%, there is a good correlation between bulk and surface loadings, suggesting greater dispersion, with values comparable to those obtained with HPW/SBA-15.

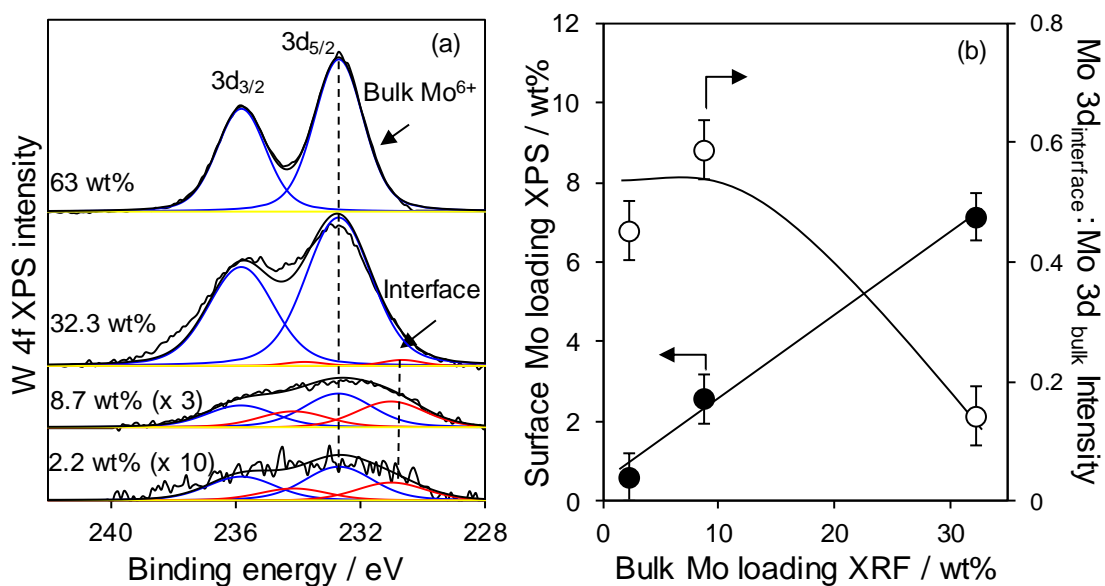


**Figure 3.39** – Background subtracted Mo 3d XP spectra of HPMo/SBA-15 series (a); and ratio of integrated signal of interfacial to bulk Mo 3d species across the loading on SBA-15, and correlation between superficial and bulk Mo wt% (b).

The evolution of HSiW species on SBA-15 is reported in **Figure 3.40**-(a), showing the W 4f  $_{7/2}$  doublet at 35.7 eV characteristic of W(VI) species with a spin orbit splitting of 2.15 eV; and a second doublet at 34.5 eV associated to the perturbed species. Compared to the HPW/SBA-15 series, there is a doublet shift of  $\sim 0.4$  eV, changing from P to Si as central atom, for only bulk species, meaning that for perturbed species of HPW and HSiW were observed at same eV. **Figure 3.40**-(b) show the surface loading as a function of bulk, and as with the HPMo series, at the highest loading there is a significant discrepancy which again is attributed to agglomeration of the Keggin unit, with at least 1/3 of the W at the support surface interface. The ratio of interface to bulk species is also reported, evaluated via spectra deconvolution, with the contribution from the perturbed (interface) species, relative to the bulk, decreasing with loading, down to 0.3 ratio, as observed also for previous supported series (HPW and HPMo).

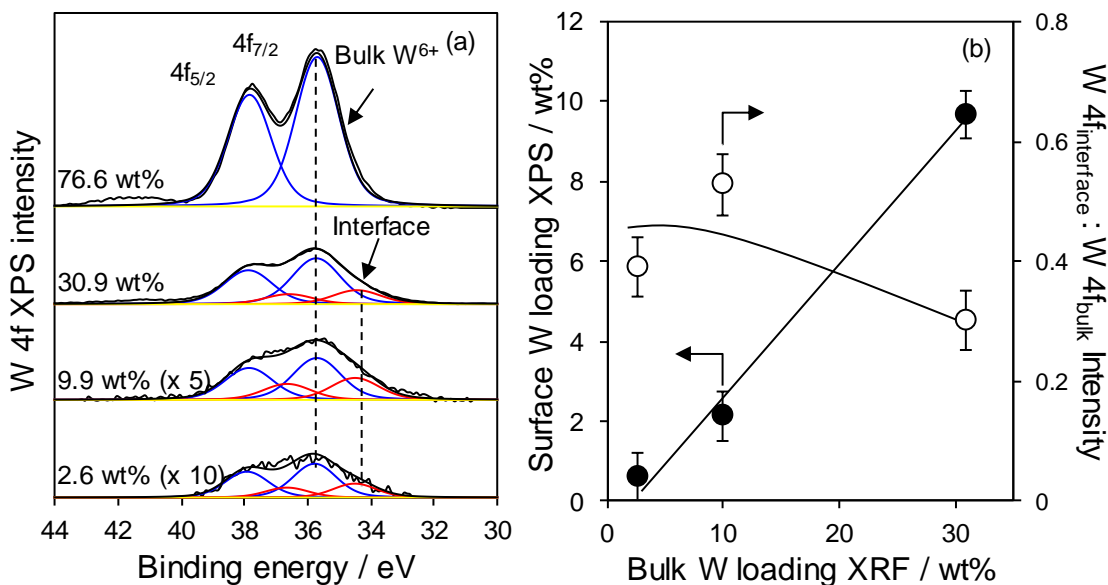


**Figure 3.40** – Background subtracted W 4f XP spectra of HSiW/SBA-15 series (a); and ratio of integrated signal of interfacial to bulk W 4f species across the loading on SBA-15, and correlation between superficial and bulk W wt% (b).

### 3.3 Conclusions

Two series of supported HPW, on fumed silica and SBA-15, have been prepared and fully characterised to probe the physicochemical nature of both the support materials and subsequent catalysts through the utilisation of a broad range of analytical techniques.

The structure of parent HPW was preserved over both supports; for fumed silica agglomeration was more prominent showing stronger diffraction peaks in XRD analysis even at low loadings and high crystalline water mass loss; whereas SBA-15 allowed highly dispersed Keggin units and/or low dimensional clusters, which entrapped less water. Solid acidity measurements proved that the acid strength was consistent for both series with unsupported HPW; on fumed silica proton density was lower compared to SBA-15 series.

Two additional series were synthesised and characterised, phosphomolibdic acid and silicotungstic acid supported on SBA-15 within 2-30 wt% of W/Mo, to investigate the effect of HPAs type on catalyst preparation and physicochemical properties.

Again, the retention of the Keggin HSiW and HPMo structure on SBA-15, was confirmed as for the HPW series, and support architecture guaranteed high dispersion of both

HPAs. HPMo showed the lowest decomposition temperatures suggesting that is the less thermally stable material, and acidity measurements revealed that, compared to HPW, HSiW and HPMo are weaker solid acid but have higher acid density.

### 3.4 References

- [1] M. Misono, *Heterogeneous Catalysis of Mixed Oxides: Perovskite and Heteropoly Catalysts*, Newnes, 2013.
- [2] I.V. Kozhevnikov, *Catalysis Reviews* 37 (1995) 311-352.
- [3] I.V. Kozhevnikov, *Chemical Reviews* 98 (1998) 171-198.
- [4] D.B. Taylor, J.B. McMonagle, J.B. Moffat, *Journal of colloid and interface science* 108 (1985) 278-284.
- [5] M.J. Janik, R.J. Davis, M. Neurock, *The Journal of Physical Chemistry B* 108 (2004) 12292-12300.
- [6] E.E.P. L. Marosi, J. Cifre, C. O. Arean, *Journal of Materials Chemistry* 10 (2000) 1949-1955.
- [7] L.C. Jozefowicz, H.G. Karge, E. Vasilyeva, J.B. Moffat, *Microporous Materials* 1 (1993) 313-322.
- [8] M.S. Kaba, I.K. Song, M.A. Barteau, *The Journal of Physical Chemistry B* 106 (2002) 2337-2342.
- [9] D.H. Everett, G.D. Parfitt, K.S. Sing, R. Wilson, *Journal of Applied Chemistry and Biotechnology* 24 (1974) 199-219.
- [10] A. Galarneau, H. Cambon, F. Di Renzo, F. Fajula, *Langmuir* 17 (2001) 8328-8335.
- [11] L. Vradman, L. Titelman, M. Herskowitz, *Microporous and Mesoporous Materials* 93 (2006) 313-317.
- [12] A. Galarneau, H. Cambon, F. Di Renzo, R. Ryoo, M. Choi, F. Fajula, *New Journal of Chemistry* 27 (2003) 73-79.
- [13] R. Ryoo, C.H. Ko, M. Kruk, V. Antochshuk, M. Jaroniec, *The Journal of Physical Chemistry B* 104 (2000) 11465-11471.
- [14] A.M. Alsalme, P.V. Wiper, Y.Z. Khimyak, E.F. Kozhevnikova, I.V. Kozhevnikov, *Journal of Catalysis* 276 (2010) 181-189.
- [15] T. Okuhara, N. Mizuno, M. Misono, in: W.O.H. D.D. Eley, G. Bruce (Eds.), *Advances in Catalysis*, Academic Press, 1996, pp. 113-252.
- [16] K. Narasimharao, D. Brown, A. Lee, A. Newman, P. Siril, S. Tavener, K. Wilson, *Journal of Catalysis* 248 (2007) 226-234.

- [17] M. Varga, B. Török, Á. Molnár, *Journal of Thermal Analysis and Calorimetry* 53 (1998) 207-215.
- [18] I.V. Kozhevnikov, *Journal of Molecular Catalysis A: Chemical* 262 (2007) 86-92.
- [19] L.J. Durndell, C.M.A. Parlett, N.S. Hondow, M.A. Isaacs, K. Wilson, A.F. Lee, *Scientific Reports* 5 (2015) 9425.
- [20] O. Isaienko, E. Borguet, *Langmuir* 29 (2013) 7885-7895.
- [21] L.T. Zhuravlev, *Colloids and Surfaces A: Physicochemical and Engineering Aspects* 173 (2000) 1-38.
- [22] B.B. Bardin, S.V. Bordawekar, M. Neurock, R.J. Davis, *The Journal of Physical Chemistry B* 102 (1998) 10817-10825.
- [23] A. Micek-Ilnicka, *Journal of Molecular Catalysis A: Chemical* 308 (2009) 1-14.
- [24] B.W.L. Southward, J.S. Vaughan, C.T. Oconnor, *Journal of Catalysis* 153 (1995) 293-303.
- [25] O. Kresnawahjuesa, R.J. Gorte, D. de Oliveira, L.Y. Lau, *Catalysis Letters* 82 (2002) 155-160.
- [26] J.E. Herrera, J.H. Kwak, J.Z. Hu, Y. Wang, C.H.F. Peden, *Top Catal* 49 (2008) 259.
- [27] D.J. Parrillo, A.T. Adamo, G.T. Kokotailo, R.J. Gorte, *Applied Catalysis* 67 (1990) 107-118.
- [28] A.I. Biaglow, D.J. Parrillo, G.T. Kokotailo, R.J. Gorte, *Journal of Catalysis* 148 (1994) 213-223.
- [29] J. Highfield, J. Moffat, *Journal of Catalysis* 88 (1984) 177-187.
- [30] I.V. Kozhevnikov, A. Sinnema, R.J.J. Jansen, H. van Bekkum, *Catalysis Letters* 27 (1994) 187-197.
- [31] K.Y. Lee, N. Mizuno, T. Okuhara, M. Misono, *Bulletin of the Chemical Society of Japan* 62 (1989) 1731-1739.
- [32] B.B. Bardin, R.J. Davis, *Applied Catalysis A: General* 200 (2000) 219-231.
- [33] B.B. Bardin, R.J. Davis, M. Neurock, *The Journal of Physical Chemistry B* 104 (2000) 3556-3562.
- [34] E. Lalik, A. Micek-Ilnicka, A. Groszek, A. Bielański, *Physical Chemistry Chemical Physics* 5 (2003) 3606-3609.
- [35] M.V. Juskelis, J.P. Slanga, T.G. Roberie, A.W. Peters, *Journal of Catalysis* 138 (1992) 391-394.
- [36] A.A. Christy, *Vibrational Spectroscopy* 54 (2010) 42-49.
- [37] C. Rocchiccioli-Deltcheff, M. Fournier, R. Franck, R. Thouvenot, *Inorganic Chemistry* 22 (1983) 207-216.

- [38] X. Gao, J. Fierro, I.E. Wachs, *Langmuir* 15 (1999) 3169-3178.
- [39] Z. Luan, E.M. Maes, P.A.W. van der Heide, D. Zhao, R.S. Czernuszewicz, L. Kevan, *Chemistry of Materials* 11 (1999) 3680-3686.
- [40] J.P. Thielemann, T. Ressler, A. Walter, G. Tzolova-Müller, C. Hess, *Applied Catalysis A: General* 399 (2011) 28-34.
- [41] E.I. Ross-Medgaarden, I.E. Wachs, *The Journal of Physical Chemistry C* 111 (2007) 15089-15099.
- [42] N. Legagneux, J.-M. Basset, A. Thomas, F. Lefebvre, A. Goguet, J. Sa, C. Hardacre, *Dalton Transactions* (2009) 2235-2240.
- [43] E. Grinival, X. Rozanska, A. Baudouin, E. Berrier, F.o. Delbecq, P. Sautet, J.-M. Basset, F. Lefebvre, *The Journal of Physical Chemistry C* 114 (2010) 19024-19034.
- [44] A. Popa, V. Sasca, E.E. Kiss, R. Marinkovic-Neducin, I. Holclajtner-Antunović, *Materials Research Bulletin* 46 (2011) 19-25.
- [45] C. Rocchiccioli-Deltcheff, M. Fournier, *Journal of the Chemical Society, Faraday Transactions* 87 (1991) 3913-3920.
- [46] A.D. Newman, D.R. Brown, P. Siril, A.F. Lee, K. Wilson, *Physical chemistry chemical physics : PCCP* 8 (2006) 2893-2902.
- [47] H. Chermette, G. Hollinger, P. Pertosa, *Chemical Physics Letters* 86 (1982) 170-175.
- [48] G. Hollinger, P. Pertosa, J.P. Doumerc, F.J. Himpsel, B. Reihl, *Physical Review B* 32 (1985) 1987-1991.
- [49] L. Frattini, M.A. Isaacs, C.M.A. Parlett, K. Wilson, G. Kyriakou, A.F. Lee, *Applied Catalysis B: Environmental* 200 (2017) 10-18.
- [50] H. Nair, J.T. Miller, E.A. Stach, C.D. Baertsch, *Journal of Catalysis* 270 (2010) 40-47.
- [51] M. Langpape, J.M.M. Millet, U.S. Ozkan, M. Boudeulle, *Journal of Catalysis* 181 (1999) 80-90.
- [52] M. Fournier, C. Feumi-Jantou, C. Rabia, G. Herve, S. Launay, *Journal of Materials Chemistry* 2 (1992) 971-978.
- [53] F.J. Berry, G.R. Derrick, M. Mortimer, *Polyhedron* 68 (2014) 17-22.
- [54] N. Narkhede, A. Patel, *RSC Advances* 4 (2014) 19294-19301.
- [55] A. Talebian-Kiakalaieh, N.A.S. Amin, *Catalysis Today* 256, Part 2 (2015) 315-324.
- [56] P. Van Der Voort, P. Ravikovitch, K. De Jong, M. Benjelloun, E. Van Bavel, A. Janssen, A. Neimark, B. Weckhuysen, E. Vansant, *The Journal of Physical Chemistry B* 106 (2002) 5873-5877.

- [57] B. Katryniok, S. Paul, M. Capron, V. Bellière-Baca, P. Rey, F. Dumeignil, *ChemSusChem* 5 (2012) 1298-1306.
- [58] L. Pesaresi, D.R. Brown, A.F. Lee, J.M. Montero, H. Williams, K. Wilson, *Applied Catalysis A: General* 360 (2009) 50-58.
- [59] M.N. Timofeeva, *Applied Catalysis A: General* 256 (2003) 19-35.
- [60] C. Rocchiccioli-Deltcheff, M. Fournier, R. Franck, R. Thouvenot, *Inorganic Chemistry* 22 (1983) 207-216.
- [61] C. Rocchiccioli-Deltcheff, A. Aouissi, S. Launay, M. Fournier, *Journal of Molecular Catalysis A: Chemical* 114 (1996) 331-342.
- [62] Y. Ding, B. Ma, Q. Gao, G. Li, L. Yan, J. Suo, *Journal of Molecular Catalysis A: Chemical* 230 (2005) 121-128.
- [63] T. Rajkumar, G. Ranga Rao, *Materials Chemistry and Physics* 112 (2008) 853-857.
- [64] H. Jin, X. Yi, X. Sun, B. Qiu, W. Fang, W. Weng, H. Wan, *Fuel* 89 (2010) 1953-1960.
- [65] X. Guo, D.-J. Guo, J.-S. Wang, X.-P. Qiu, L.-Q. Chen, W.-T. Zhu, *Journal of Electroanalytical Chemistry* 638 (2010) 167-172.
- [66] W. Swartz, D.M. Hercules, *Analytical Chemistry* 43 (1971) 1774-1779.
- [67] J.-G. Choi, L. Thompson, *Applied Surface Science* 93 (1996) 143-149.

## ***Chapter 4***

### ***$\alpha$ -Pinene isomerisation***

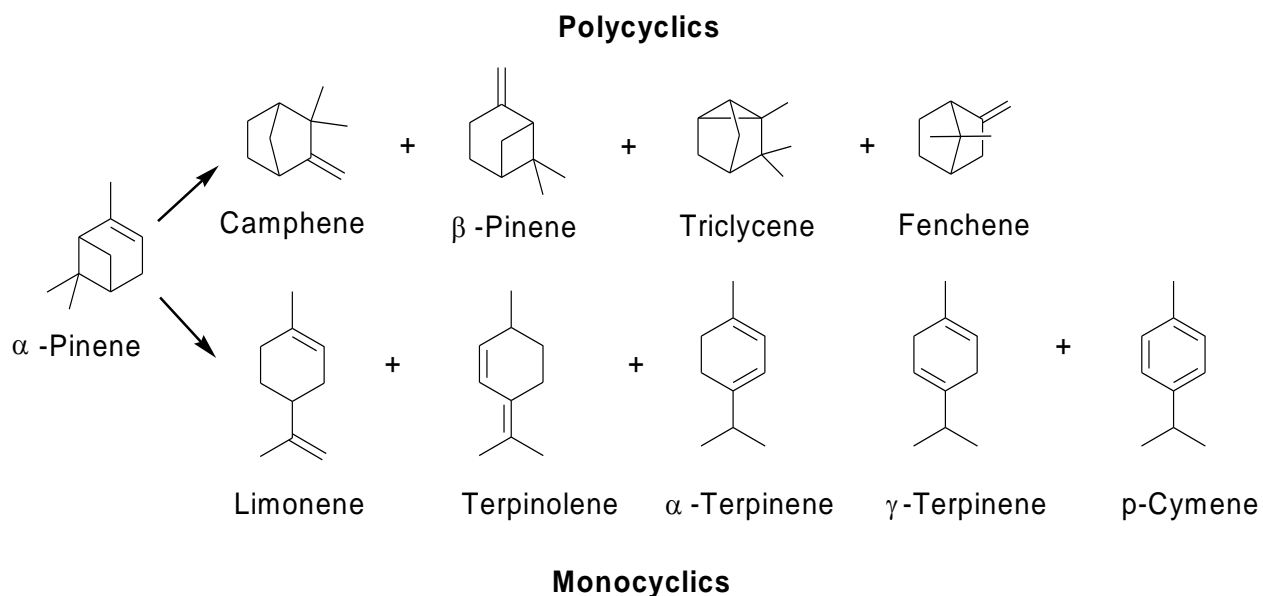
## 4.1 Introduction

As discussed in **Chapter 1**, turpentine is a valuable bio-resource for green building blocks, such as camphene, limonene and terpinenes [1].  $\alpha$ -Pinene is the major compound in its formulation, in addition to  $\beta$ -pinene and terpinolene, although the actual composition is strongly dependent on regional and seasonal variations.

The liquid phase isomerisation of  $\alpha$ -pinene has been widely investigated, and is often used as a test-reaction to study acidic properties of solid catalysts [2]. The reaction leads to the formation of numerous high-value products; including camphene, limonene, terpinolene,  $\beta$ -pinene,  $\alpha$ - and  $\gamma$ -terpinene, and p-cymene (**Scheme 4.1**). The resulting products distribution is strongly influenced by reaction conditions (gas/liquid phase, temperature and pressure) and the catalyst employed (homo/heterogeneous system). A number of heterogeneous catalysts are reported in the literature, alloys [3], clays [4, 5], zeolites [6-9], titania [10], sulfated zirconia [11-13] and heteropolyacids, both unsupported and supported on a range of different materials [2, 14-18]. Isomerisation leads predominately to the formation of monocyclic products (limonene, terpinenes, terpinolene etc.) and polycyclic products (camphene,  $\beta$ -pinene, fenchene and tricyclene); however, depending on the reaction conditions and the catalyst's properties (architecture, porosity, acid Brønsted/Lewis ratio) heavier products, formed via polymerisation/condensation of polyterpenoids, can also be produced.

Studies into the selectivity of the isomerisation pathway suggests that camphene production is favoured over catalysts possessing Brønsted acidity, with a clear production dependence on acid strength, and is to the detriment of the production of the monocyclic products [4, 8, 9, 19]. Camphene and tricyclene are independent from  $\alpha$ -pinene conversion while limonene, terpinenes and terpinolene, are highly dependent, due to consecutive secondary reaction [20-22]. The kinetic rate relative to  $\alpha$ -pinene consumption is of the first-order, with the activation energy, calculated by the Arrhenius equation equal to 80 kJ/mol [23, 24].

Herein,  $\alpha$ -pinene isomerisation activity was investigated as function of bulk W loading and support architecture at different reaction temperatures. The ratio, monocyclic to polycyclic products, was calculated to elucidate the dependence of camphene selectivity on catalysts acid strength, with a complimentary mechanism study conducted in order to elucidated the reaction network for the overall isomerisation process.



**Scheme 4.1** – Principal products of  $\alpha$ -pinene isomerisation.

## 4.2 Results and discussion

$\alpha$ -Pinene is a solventless reaction and conversion was calculated according to **Equation 4.1**:

$$\text{Conversion / \%} = \left( \frac{\text{mol}_{t=0} - \text{mol}_t}{\text{mol}_{t=0}} \right) \times 100$$

$$\text{Yield to product}_i \text{ / \%} = \left( \frac{\text{mol}_i}{\text{mol}_{t=0}} \right) \times 100$$

$$\text{Selectivity to product}_i \text{ / \%} = \left( \frac{\text{mol}_i}{\sum \text{mol}_{\text{product}}} \right) \times 100$$

**Equation 4.1** – Equation used to calculate ethanol conversion % and product selectivity.

where  $\text{mol}_{t=0}$  are the initial moles of  $\alpha$ -pinene;  $\text{mol}_t$  refers to the moles of  $\alpha$ -pinene at the sampling time (time 0, 5, 15, 30, 60, 120, 180, 240, 300, 360, 1440 min); and  $\text{mol}_i$  are the moles of product formed.

#### 4.2.1 Reaction profiles on supported HPW: support architecture effect

The  $\alpha$ -pinene isomerisation was initially investigated at varying stirring rates, from 500 to 700 rpm, in order to check for and overcome potential bulk mass-transfer limitations, resulting from diffusion from the bulk liquid to the support. The influence of agitation on the initial activity, over the 3.2 wt.% W/SBA-15 catalysts, is reported in **Figure 4.1**, with associated reaction profiles shown in **Appendix A, Figure 1**, and reveals an equal mass normalised initial rate of  $\sim 37 \text{ mmol h}^{-1} \text{ g}_{\text{cat}}^{-1}$ , indicative that, under these conditions, mixing is sufficient to eliminate external mass transport related problems, and therefore all further catalytic screening has been carried out using stirrer rate of 700 RPM.

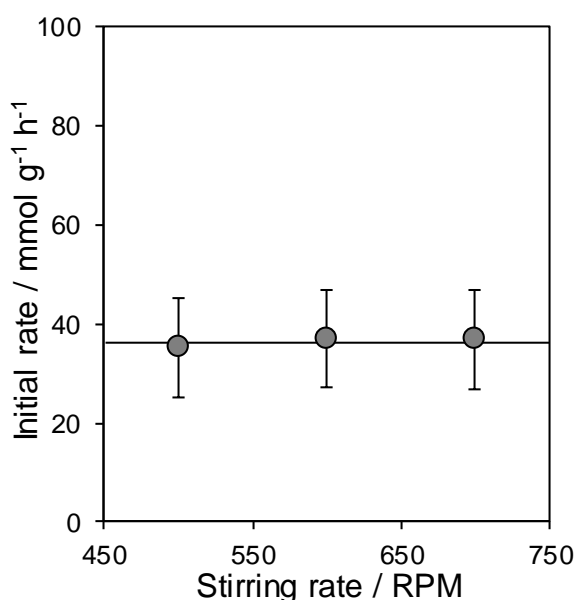


**Figure 4.1** – Influence of stirring rate on the  $\alpha$ -pinene normalised initial rate over 3.2 wt.% of HPW/SBA-15. Reaction conditions: 126 mmol of  $\alpha$ -pinene, 0.2 cm<sup>3</sup> of tetradecane (as an internal standard), 60 °C, 0.1 g of catalyst.

Having established an efficient mixing regime,  $\alpha$ -pinene isomerisation was investigated employing supported HPW on SBA-15 and on fumed silica. Reaction profiles at 60 °C as function of time and W bulk loadings over the two supports are reported in **Appendix A, Figure 2**, with the two parent supports shown to be inactive toward  $\alpha$ -pinene isomerisation under the mild reaction conditions utilised in the study herein. **Figure 4.2** shows an example reaction profile, for W 9 wt.% of HPW/SBA-15, with  $\alpha$ -pinene conversion and product yields reported as a function of time. The associated product yield clearly reveals that limonene and camphene are the two major products of the isomerisation reaction, and represent monocyclic and polycyclic product respectively.

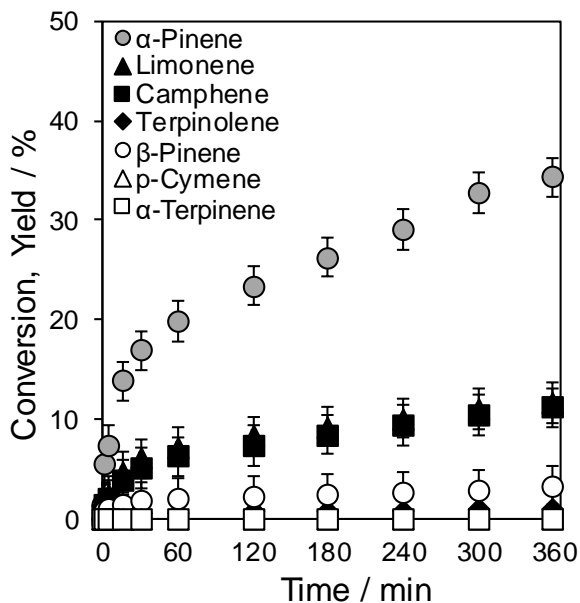


**Figure 4.2** –  $\alpha$ -Pinene isomerisation reaction profile for 9.0 wt% of bulk W on SBA-15. Reaction conditions: 126 mmol of  $\alpha$ -pinene, 0.2 cm<sup>3</sup> of tetradecane (STD), 60 °C, 0.1 g of catalyst, 700 rpm of stirring rate

As alluded to in **Chapter 3**, silica support architecture and W loading are a critical controlling factors on the dispersion of HPW. These parameters significantly influence the degree of active species, and thus the number of external surface protons that are readily accessible to apolar substrates that are incapable of diffusing into the HPW bulk [25].

The activity dependency of  $\alpha$ -pinene isomerisation as a function of support is reported in **Figure 4.3-(a)**, where unsupported HPW (74 wt% bulk W) values are added for comparison. The fumed silica supported series showed poor conversions <10% and low initial activities centred at 20 mmol h<sup>-1</sup> g<sub>cat</sub><sup>-1</sup>, being independent of HPW loading and comparable to the unsupported HPW. In comparison, the HPW/SBA-15 family revealed significantly enhanced conversions, with values reaching up to ~ 40%, with associated initial activities elevated to 121 mmol h<sup>-1</sup> g<sub>cat</sub><sup>-1</sup> for a W loading of 19.9 wt%, and with a strong volcano dependence on W loading. A dramatic loss in initial rate, for loading  $\geq 38.2$  wt% with values falling to ~56 mmol h<sup>-1</sup> g<sub>cat</sub><sup>-1</sup>, is attributed to the lower number of accessible protons which is directly related to HPW aggregation. The isolated and highly dispersed Keggin clusters (as observed for low loadings via STEM, **Chapter 3, Figure 3.11**) and low dimensional HPW arrays (confirmed via XRD and TGA), for loadings up to 19.9 wt%, allows for apolar liquids to access surface Brønsted sites, enhancing conversion and thus mass normalised activity. Three-dimensional HPW agglomerates, observed at higher W loadings

on SBA-15, results in a high degree of localisation of acid sites within the multi-layered structures, which, are inaccessible to the  $\alpha$ -pinene and thus correlates with the fall in catalytic activity. In comparison HPW on fumed silica, exhibits a drastically faster 3D growth rate, which is attributed to the fewer number of hydroxyl groups (than SBA-15), and thus a lower number of available site for catalysis relative to equivalent loadings on SBA-15 [26].

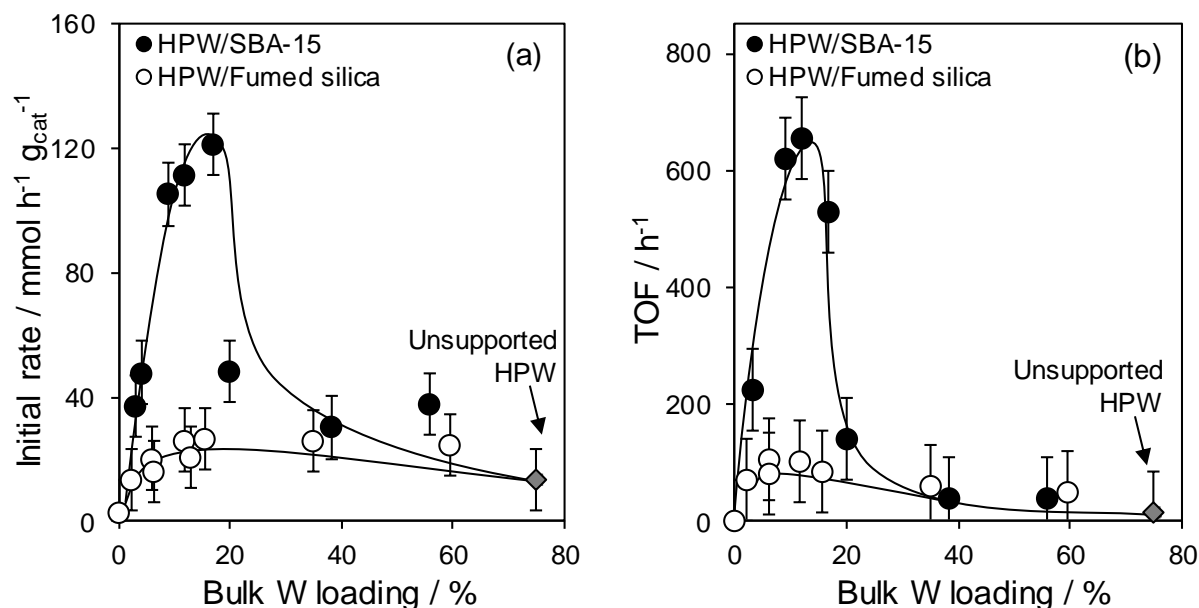


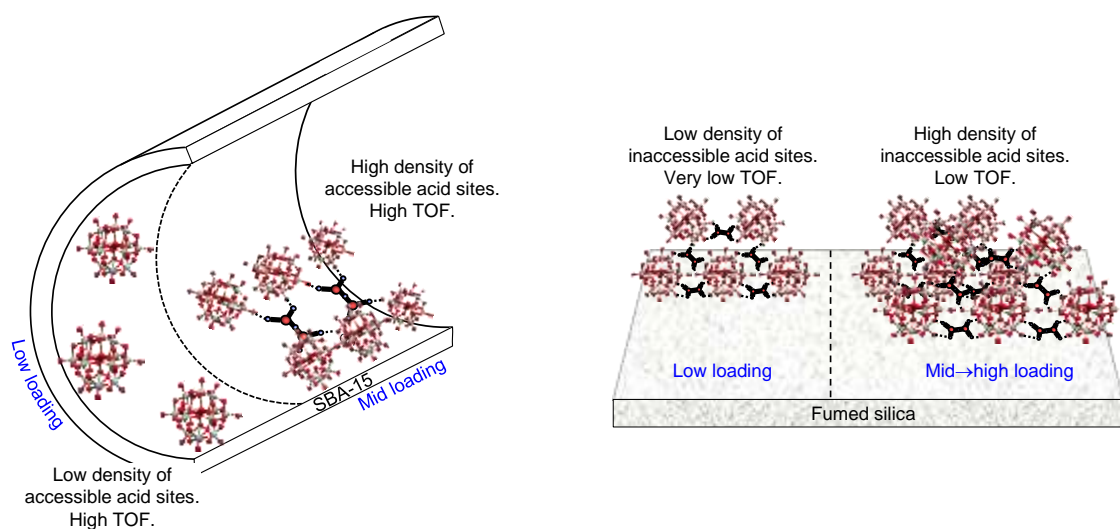
**Figure 4.3** – Effect of bulk W loading and silica supports on  $\alpha$ -pinene isomerisation activity (a) and turnover frequencies (b). Reaction conditions: 126 mmol of  $\alpha$ -pinene, 0.2 cm<sup>3</sup> of tetradecane (STD), 60 °C, 0.1 g of catalyst, 700 rpm of stirring rate.

Turnover frequencies values are reported on **Figure 4.3**-(b) as function of W loading and silica supports, and unsupported HPW (74 wt% of bulk W) performance is reported for comparison. Data were obtained dividing the  $\alpha$ -pinene catalytic activity by the number of specific acid site of each catalyst, measured via propylamine chemisorption and TPD. As described previously, the proton density of synthesised solid samples (mmol<sub>H+</sub> g<sub>cat</sub><sup>-1</sup>) increases almost linearly as the loading of bulk W increases, displaying higher values for the HPW/SBA-15, as confirmed also via ammonia titration. TOFs calculations mirror  $\alpha$ -pinene activity, and the strong dependence on the W loading over both supports. Fumed silica supported samples disclose a constant TOF of ~ 50 h<sup>-1</sup>, suggesting that big aggregates have poor acid accessibility with  $\alpha$ -pinene isomerisation confined on the external surface.

HPW/SBA-15 exhibit a formidable increase of TOF from 200 h<sup>-1</sup> to 600 h<sup>-1</sup> between 3.2 wt% and 16.9 wt% indicating that dispersed K.U. are less active compared to sub-monolayer small HPW

agglomerates, which own a higher proton mobility due to water molecules held within the secondary heteropolyacid structure. With the agglomeration of more than ~5-6 K.U., for W loadings >20 wt% on SBA-15, the number of accessible proton to non-polar  $\alpha$ -pinene decreases as the turnover frequencies drop to  $50 \text{ h}^{-1}$ , which are comparable with the unsupported HPW.

**Scheme 4.2** represents the observation with regard to the two supports and their influence on TOFs, depicting the dependence of a non-polar isomerisation reaction on the W loading and the 3D structure of HPW on both supports. A right balance between acidity and support porosity is required for optimal acid catalysed isomerisation of  $\alpha$ -pinene at small cluster of HPW, which are only generated at mid loadings on SBA-15 [2].



**Scheme 4.2** – Dependence of  $\alpha$ -pinene isomerisation reactivity on structure and loading of HPW supported on high surface area, mesoporous SBA-15 (left) and non-porous fumed silica (right).

Selectivity results are reported as ratio between mono and polycyclic products, in which each term is the sum of products selectivity of the same family (**Figure 4.4**). For the two catalyst families, ratios are independent from the mass loading of bulk W, being ~1.2 across the two catalysts series, with selectivity toward monocyclic products being ~55% and slightly higher than the polycyclic species ~45%. In comparison, unsupported HPW displays comparable results, with a mono/poly ratio ~1. Selectivity data are in agreement with Wu et al. investigation carried out on the isomerisation of  $\alpha$ -pinene employing thermally treated HPW on SBA-15, in which the selectivity was studied as function of T and catalyst amount [27]. Catalyst acid strength and reaction temperature are crucial factor to consider regarding product distributions [28], which are investigated herein.

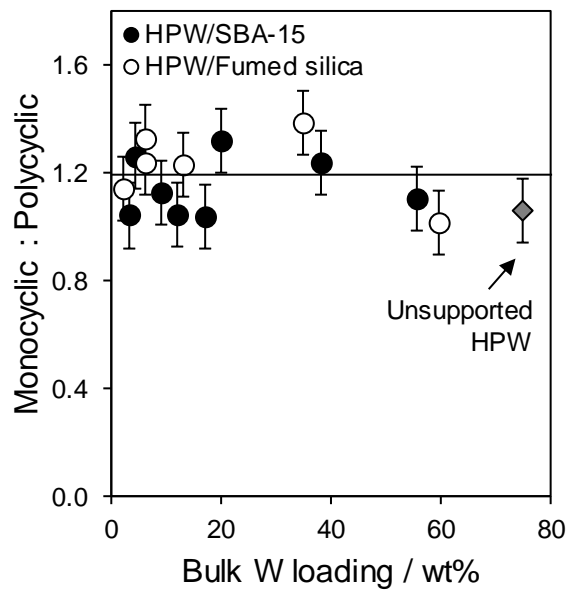


**Figure 4.4** – Product selectivity ratio as function of W wt% supported on SBA-15. Reaction conditions: 126 mmol of  $\alpha$ -pinene, 0.2 cm<sup>3</sup> of tetradecane (STD), 0.1 g of catalyst, at 60 °C, stirring rate 700 rpm (a). Dependence of monocyclic / polycyclic ratio to bulk W loading and silica supports (b).

#### 4.2.2 Reaction profiles on supported HPW: temperature effect

As reported in the literature,  $\alpha$ -pinene conversion and reaction temperature both play an important role in terms of selectivity toward camphene [20-22]. To study the effect of reaction conditions on the product distribution, i.e. the ratio mono to polycyclic products,  $\alpha$ -pinene isomerisation was carried out at 30 °C, employing 0.1 g of catalyst, 126 mmol of  $\alpha$ -pinene at 700 rpm of stirring rate. Reaction profiles at 30 °C as function of time and W bulk loadings over the two supports are reported in **Appendix A-Figure 3**.

**Figure 4.5** reports  $\alpha$ -pinene activity as a function of W loading on both supports, SBA-15 and fumed silica, where unsupported HPW (74 wt% of bulk W) performances are reported for comparison.  $\alpha$ -Pinene isomerisation was also performed in absence of catalyst to verify the authenticity of the catalytic process, which showed negligible conversion, with both silica supports also inert towards the isomerisation reaction. HPW/SBA-15 led to the best performances of  $\alpha$ -pinene conversions, reaching 3% when 16.9 wt% of bulk W was employed. At higher loadings, conversion halved to 1.5%, confirming that a non-polar substrate reacts with accessible active

sites localised on the external surface, which are greater in number in the sub-monolayer coverage <20 wt% of W/SBA-15. In contrast, fumed silica supported samples showed constant values of conversion within the range 0.75-0.9%, which are comparable with HPW. All samples showed reduced activities (**Figure 4.5**-(a)), with the highest values obtained when SBA-15 was used as support. As observed at 60 °C for HPW supported on SBA-15,  $\alpha$ -pinene isomerisation activity exhibits a clear dependence on mass loading, revealing a volcano plot as a function of loading across the W loading. In the range 3.2-16.9 wt% of W on SBA-15, the initial rate normalised for the mass of catalyst rises from 4.6 to 6.6 mmol h<sup>-1</sup> g<sub>cat</sub><sup>-1</sup>, reflecting an increase of acid density. For W loading >20 wt%, which display a continual increase of the number of acid sites, the normalised activity decreases due to the formation of larger agglomerates and reduced acid site accessibility. The catalysts that exhibited the best performance at 30 °C are most active also at 60 °C, confirming our previous findings. Fumed silica samples mirror conversions trend, with constant values (between 2.5 and 3 mmol h<sup>-1</sup> g<sub>cat</sub><sup>-1</sup>) even with the increase of the acid loading, with the presence of larger agglomerates across all loadings being detrimental to catalyst performance in the isomerisation reaction.

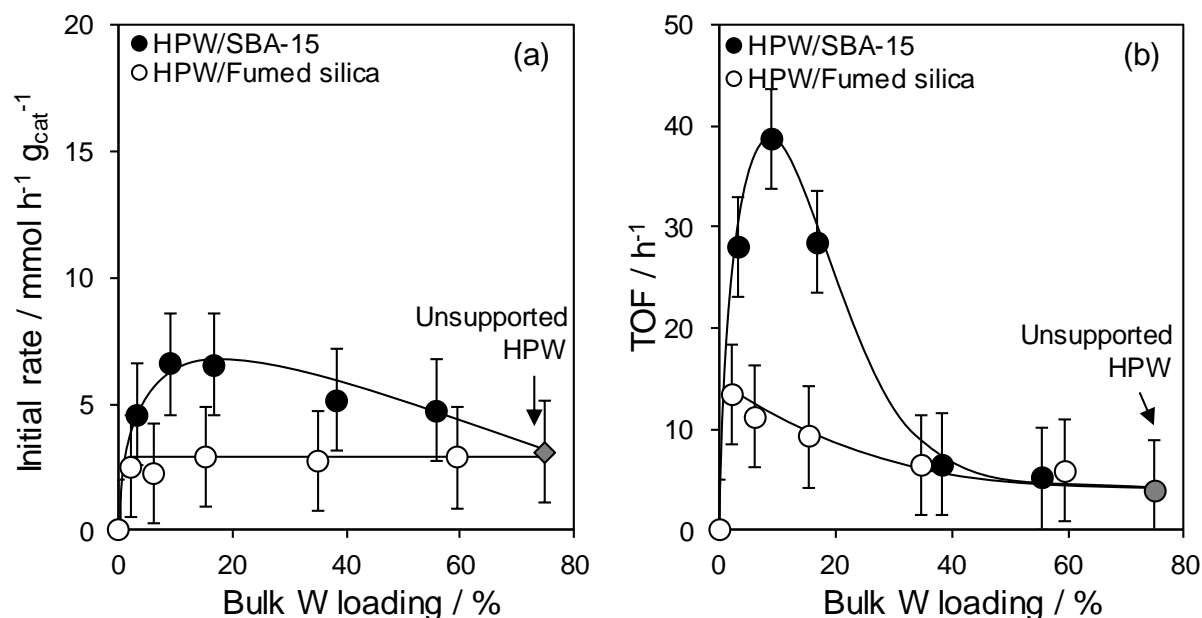


**Figure 4.5** – Effect of bulk W loading and silica supports on  $\alpha$ -pinene isomerisation activity (a) and turnover frequencies (b). Reaction conditions: 126 mmol of  $\alpha$ -pinene, 0.2 cm<sup>3</sup> of tetradecane (STD), 30 °C, 0.1 g of catalyst, 700 rpm of stirring rate.

TOF values, in **Figure 4.5**-(b), again reveal identical trends as observed at 60 °C, which reveal that proton accessibility of the non-polar substrate is a key role of isomerisation reaction, and thus

increasing total acid sites, being simply increasing HPW loading, is not the sole governing factor. Herein, highest turnover frequency (volcano trend maximum) is attained employing 9 wt% sample of HPW/SBA-15 and it is  $\sim 38 \text{ h}^{-1}$ ; 3.2 and 16.9 wt% samples reveal comparable TOF values being almost 20% lower compared to the maximum. At higher loadings, results display a strong decrease in TOF, losses of 84%, with TOFs values mirroring those of unsupported HPW. The effect of reduced temperature reveals a dramatic decrease in  $\alpha$ -pinene isomerisation activity, with turnover frequencies and catalytic activities decreasing by an order of magnitude.

Investigation into product distribution, under these milder reaction conditions, was evaluated from the ratio of monocyclic and polycyclic products, and is reported as function of loading (**Figure 4.6**).

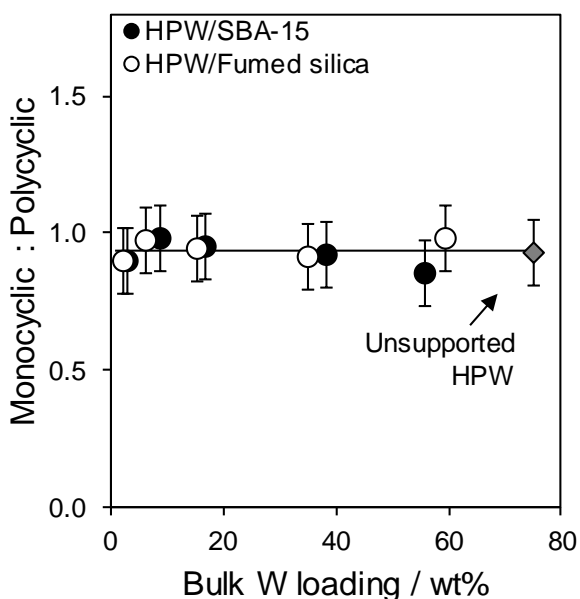


**Figure 4.6** – Dependence of monocyclic to polycyclic ratio to bulk W loading and silica supports.

Across both series, camphene and limonene were the only products of  $\alpha$ -pinene isomerisation, revealing that secondary products are strongly inhibited by the lower reaction temperature. As reported in the literature, limonene is more reactive than camphene and can be further transformed to terpinolene and terpinenes as the temperature or conversion increases [22-24, 29]. Additionally, Brønsted acid sites facilitate limonene conversion increasing the reaction rate of secondary products [2-4]. Theoretical calculation of the formation energy of the reaction intermediates to camphene and limonene revealed that camphene is more favourable at lower temperature [30], which are in agreement with our findings. The monocyclic to polycyclic ratio decreases to values lower than 1 indicating a higher formation of polycyclic products.

### 4.2.3 Selectivity dependence on acid strength

From the initial investigations, it is concluded that highly dispersed HPW Keggin units play a critical role in the  $\alpha$ -pinene isomerisation reaction, with SBA-15 being a superior support due to enhanced accessibility of the heteropolyacid surface to non-polar substrate, with W loadings between 10-20 wt% having the highest number of available protons.

To evaluate the role of acid strength on  $\alpha$ -pinene isomerisation, the selectivity of camphene was investigated by employing the heterogeneous solid acids, phosphomolybdic acid (HPMo) and silicotungstic acid (HSiW), both supported on SBA-15, which exhibit the same Keggin structure of HPW. A loading of ~9 wt% of the heteroatom was chosen as the counterpart HPW on SBA-15 showed optimal performances at both 30 and 60 °C. Synthesised materials, HSiW/SBA-15 and HPMo/SBA-15, were fully characterised in their physical and chemical properties, as reported in **Chapter 3**, with acid strength order being HPW>HSiW>HPMo, evaluated from n-propylamine and ammonia TPD, which is in agreement with the literature [31-36]. In addition, surface area measurements, pore diameter and pore volume suggested that textural properties of supported HPAs have comparable values, BET surface areas (normalised for the mass of silica support) span 750-800 m<sup>2</sup> g<sub>SiO<sub>2</sub></sub><sup>-1</sup>, pore diameter and volumes of 5.8 nm and 0.67-0.8 respectively, suggesting highly dispersed K.U. The absence of powder XRD peaks further supports the presence of discrete nano-clusters (<2 nm).

$\alpha$ -Pinene isomerisation was screened at 60 °C, employing HSiW/SBA-15 and HPMo/SBA-15, with heteroatom loading in the range of 8-9 wt%, and results compared with the counterpart HPW/SBA-15. Products yields for HPMo/SBA-15 and HSiW/SBA-15 are reported in **Appendix A, Figure 4**. Comparison of substrate conversions are reported in **Figure 4.7-(a)** in which HPW/SBA-15 reaches the highest values at 33%, followed by HPMo and HSiW, with 27% and 22% respectively. In all cases, the  $\alpha$ -pinene conversion rises rapidly in the first hour of reaction, and slowly reaches a plateau; additionally, colour change of catalysts, from white to brown, indicates some deposition of carbonaceous products on the catalytic material's surface.

TOFs are reported in **Figure 4.7-(b)** and mirror the close correlation between acid strength and reaction kinetics parameters. HPMo/SBA-15 exhibits lowest turnover frequencies at 275 h<sup>-1</sup>, value that rises to 315 h<sup>-1</sup> when HSiW/SBA-15 is employed, tripling finally to 600 h<sup>-1</sup> in the case of HPW/SBA-15. For equally dispersed heteropolyacids, with accessible protons and comparable values of acid site density, TOF differences are strictly related to the surface acidity. TOFs were

determined using total acid density, due to the presence of  $H_5O_2^+$  or  $H_3O^+$  species which facilitate the interanion migration of single protons, making unnecessary the discern between strong, medium and weak acid sites. As Uchida et al. reported in their study [37], in hydrated HPAs there are three types of proton migration; first is related to the  $H^+$  migration in the form of hydronium ion, which moves within large HPAs clusters; the second refers to interanion migration of isolated  $H^+$ , and the third is related to the hopping of single protons from one oxygen atom to another (eg. from  $O_t$  to  $O_b$  and vice versa) in the same heteropolyanion structure. In hydrated HPAs, the interanion migration is mediated by the water molecules, which allow to delocalise the acid protons conferring high mobility and easy protonation of the substrate [37]. The strong correlation between acidity and water molecules force us to consider the acid sites in its total value. It is also worth pointing out that the  $H^+$  motion is  $10^6$ - $10^3$  times faster than the organic transformation, and therefore the  $\alpha$ -pinene reaction is not proton diffusion limited [37].

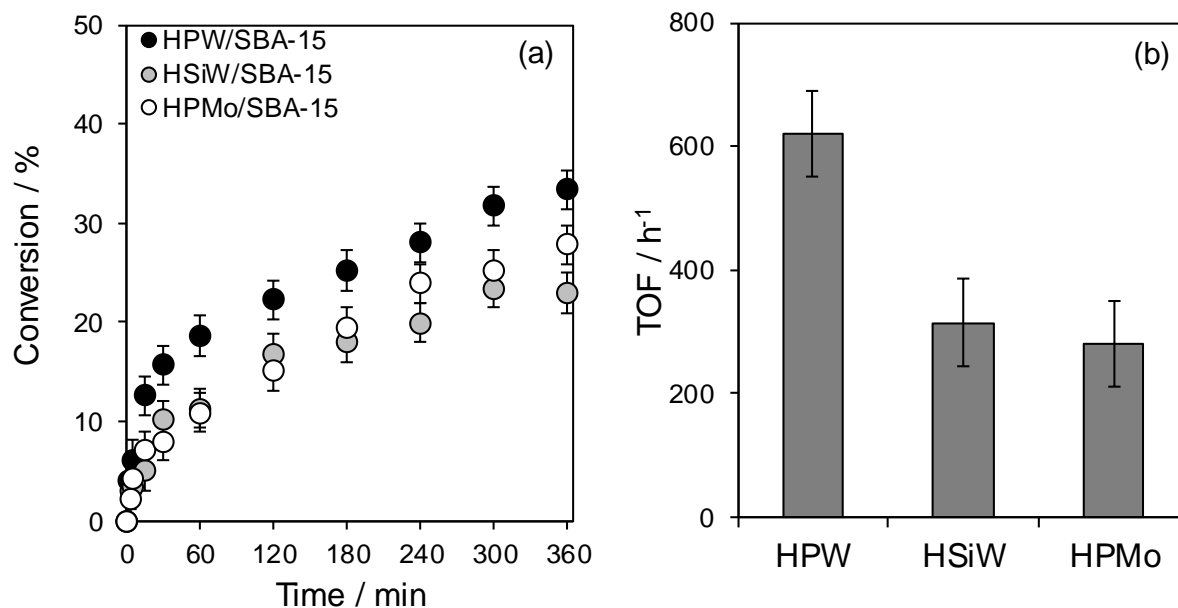


**Figure 4.7** –  $\alpha$ -Pinene isomerisation reaction profiles as function of time (min) depending on the heteropolyacid involved at 9 wt% of heteroatom supported on SBA-15 (a); and relative TOF (b). Reaction conditions: 126 mmol of  $\alpha$ -pinene, 0.2 cm<sup>3</sup> of tetradecane (STD), 0.1 g of catalyst, at 60 °C, stirring rate 700 rpm.

Dependence of selectivity toward polycyclic and monocyclic families on acid strength is reported in **Figure 4.8**, with camphene selectivity correlating to acid strength, and the weaker acid catalysts favouring limonene and its secondary products (monocyclics), with monocyclic to polycyclic ratio rising from 1.12 to 1.5 and finally to 1.7, when employing HPW, HSiW and HPMo respectively.

These findings suggest that stronger acids allow bicyclic rearrangements (leading to camphene), at the detriment of ring opening arrangements, responsible for limonene and its secondary derivative products family. **Scheme 4.3**, is generally accepted in the literature, reports the early steps of the  $\alpha$ -pinene isomerisation, which starts with the irreversible protonation of the substrate forming pinylicarbonium ion (1) [11, 22-24, 38, 39]. Further bicyclic rearrangements of compound (1) is believed to form camphene; whereas its ring opening leads to monocyclic products, such as limonene, terpinolene and  $\alpha/\gamma$ -terpinene. Results suggest that weak solid acid, as HPMo/SBA-15, facilitates the formation of the more thermodynamically stable structure, that being the single ring structures.

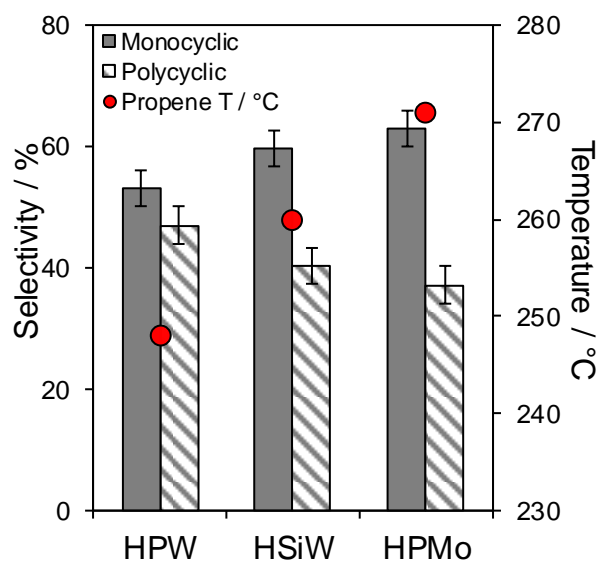
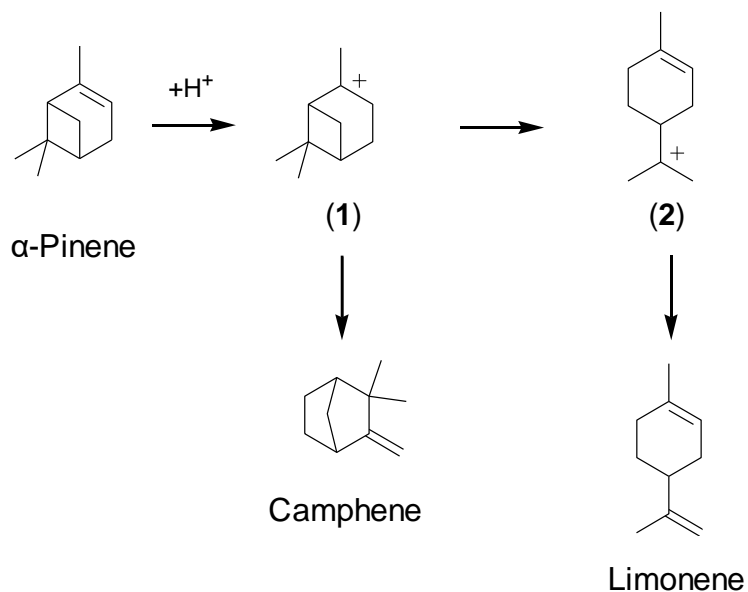


**Figure 4.8** – Correlation between selectivity towards the two product families (monocyclics / polycyclic) and acid strength measured via n-propylamine chemisorption and TPD of common 9 wt% W (or Mo) loading on SBA-15.



**Scheme 4.3** – Acid catalysed routes to polycyclic versus monocyclic products from  $\alpha$ -pinene.

#### 4.2.4 Mechanism study

To gain a complete understanding of the overall reaction mechanism, including secondary reactions of primary products, catalytic screening of all potential products was conducted.

In **Table 4.1**, the catalytic results for conversion (%) and product yields (%) after 6 hours of reaction. All reaction profiles are reported in **Appendix A, Figure 5**, for camphene, limonene, terpinolene,  $\alpha/\gamma$ -terpinene, p-cymene and  $\beta$ -pinene. Limonene conversion reached 5.1%, with product yields of terpinolene being 2.2%, and  $\alpha$  and  $\gamma$ -terpinene being 1.5% and 1.3% respectively, were formed after 6 h of reaction, clearly as secondary products of terpinolene (see **Appendix A, Figure 5**).

**Table 4.1** – Conversion and yields obtained after 6 h of reaction employing 0.1 g of catalyst (16 wt% W/SBA-15), 126 mmol of reagent, 0.2 cm<sup>3</sup> of tetradecane (STD), at 60 °C, stirring rate 700 rpm.

		$\alpha$ -Pinene	$\beta$ -Pinene	Limonene	Camphene	Terpinolene	p-Cymene	$\alpha$ -Terpinolene	$\gamma$ -Terpinolene	Fenchene
	Conversion / %	Yield / %								
Limonene	5.1	0.0	0.0	-	0.0	2.2	0.0	1.5	1.3	0.0
Camphene	11.0	0.0	0.0	0.0	-	0.0	0.0	0.0	0.0	0.0
Terpinolene	0.5	0.0	0.0	0.0	0.0	-	0.0	0.0	0.4	0.0
p-Cymene	1.0	0.0	0.0	0.0	0.0	0.0	-	0.0	0.0	0.0
$\alpha$ -Terpinene	5.2	0.0	0.0	4.1	0.0	0.3	0.0	-	0.0	0.0
$\gamma$ -Terpinene	6.3	0.0	0.0	0.0	0.0	1.5	0.0	3.8	-	0.0
$\beta$ -Pinene	97.0	0.0	-	25.0	32.0	10.1	0.0	5.0	3.4	2.4

Camphene's conversion reached 11% but only high retention time products (H RTP), attributed to dimers and trimers, were formed and not quantified because of the unknown composition of these species [40, 41]. The reaction with terpinolene resulted in very low conversion, only 0.5%, with the only product observed being  $\gamma$ -terpinene at 0.4% yield, whereas p-cymene's conversion attained 1% and no products observed.  $\alpha$ -Terpinene's conversion reached 5.2%, with yields of limonene and terpinolene being 4.1 % and 0.3% respectively, whereas carrying out reaction with  $\gamma$ -terpinene, which showed similar conversion of 6.3%, resulted in the formation of terpinolene, with a yield of only 1.5%, and  $\alpha$ -terpinene with a yield of 3.8%. Surprisingly, carrying out reaction with  $\beta$ -pinene almost full conversion was obtained, 97% after 6 h, leading limonene and camphene as major products, with 25% and 32% of yield respectively, followed by terpinolene (10%),  $\alpha$ -terpinene (5%) and  $\gamma$ -terpinene (3.4%) and finally fenchene (2.4%), obtained from isomerisation of camphene [42].

It is worth noticing that Nie et al. [38] carried out the isomerisation reaction using either  $\beta$  or  $\alpha$ -pinene or crude turpentine employing HPW supported on MCM-41 at different temperature and different HPW loading. The products distribution reported is similar to the present study, and they also observed similar superior conversion of  $\beta$ -pinene (75%) compared to  $\alpha$ -pinene (50%) at 90 °C reaction temperature, employing 0.4 g of 20 wt% of HPW loading. In the study, no further

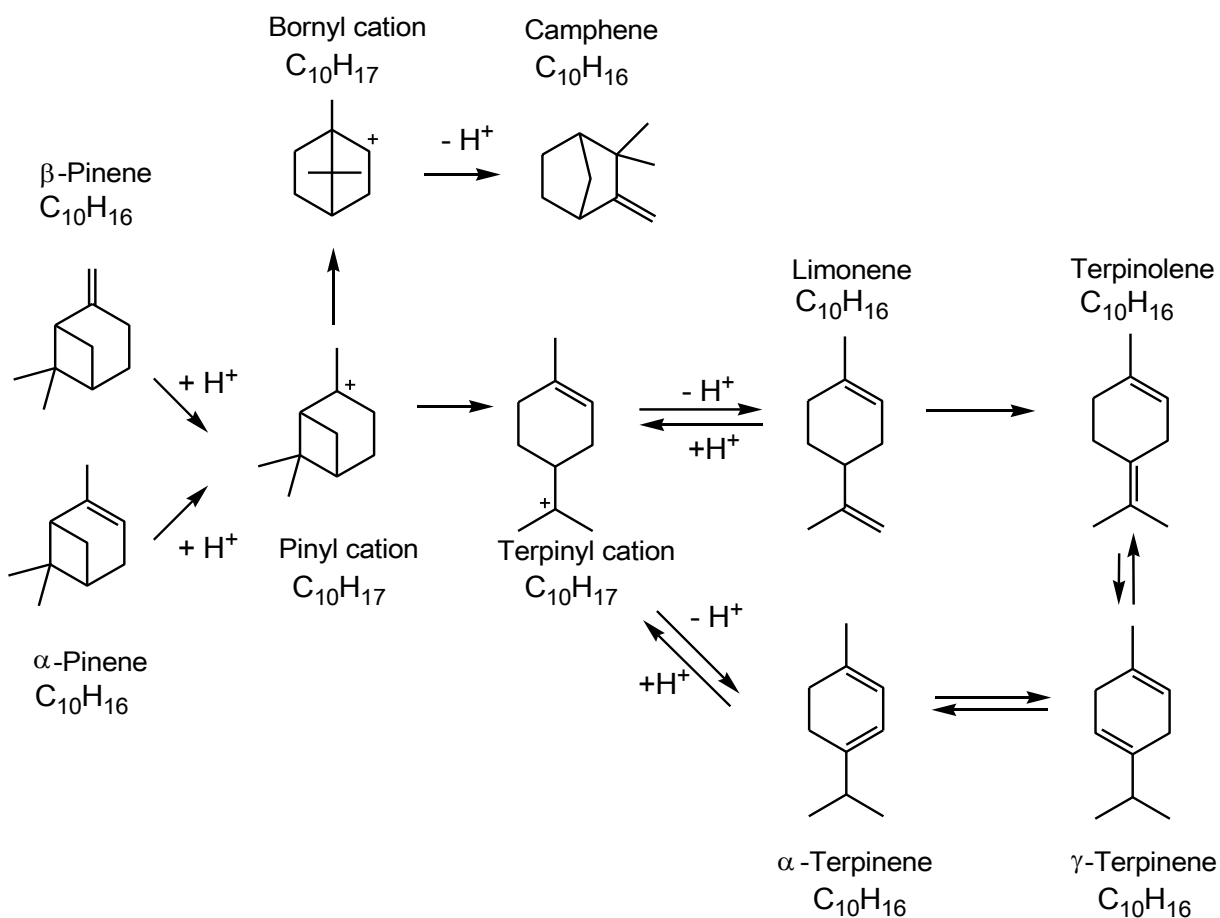
investigation was carried out to better understand the striking difference between the two isomers. However, it appears that protonation (forming the pinylicarbonium ion) of the exocyclic double bond of the  $\beta$ -pinene on the highly dispersed HPW units is easier/faster compared to the endocyclic C=C of the  $\alpha$ -isomer.

To confirm our results regarding the higher performance of the exocyclic protonation, the  $\beta$ -pinene isomerisation was carried out employing supported HSiW and HPMo on SBA-15 with bulk metal loading of 9 wt%. Catalytic results (**Appendix A, Figure 6-(a)**) show high conversion of the  $\beta$ -isomer, 100 % for HSiW/SBA-15 and 37% for the HPMo/SBA-15 and similar product distributions with camphene and limonene as major products, followed by terpinolene and terpinenes. Selectivity towards monocyclic and polycyclic products mirror the results obtained from isomerisation of the  $\alpha$ -pinene with supported HPAs, confirming that increasing the catalyst's acid strength favours polycyclic product formation (**Appendix A, Figure 6-(b)**).

Rocha et al. [43] also investigated the isomerisation reaction of  $\beta$ -pinene to the  $\alpha$ -isomer; theoretical calculations revealed high activation energies for the  $\beta \rightarrow \alpha$  isomerisation, and hence explains the absence of  $\alpha$ -pinene during  $\beta$ -isomerisation. It was also shown that the exocyclic  $\beta$ -pinene double bond coordinates with a transition metal centre, forming a  $\pi$ -allylic system which lowers the isomerisation energy barrier, enhancing pinene activity.

**Scheme 4.4** summarise our findings regarding the overall reaction network in which  $\alpha$ -pinene or  $\beta$ -pinene are protonated forming the pinylicarbonium ion, a precursor of both monocyclic and polycyclic species. Consequently, two types of reaction may occur; rearrangement with ring opening, leading to terpylicarbonium ion (monocyclic), or rearrangement without ring opening, forming bornylcarbonium ion (bicyclic) [23, 24, 44]. Limonene, terpinolene and terpinenes are products of the ring opening rearrangement, when the pinylic cation reacts to form terpylic cation. Isomerisation catalytic tests carried out starting from the products, suggested that limonene is the main product of the deprotonation of terpylic cation, and that terpinolene is mainly obtained from double bond migration from the limonene structure, as reported in the literature [24], and because at low conversions of  $\alpha$ -pinene, terpinolene is the second monocyclic compound after limonene.  $\alpha$  and  $\gamma$ -terpinenes are formed as secondary products, which occurs via the protonation of limonene or terpinolene [44], and are only observed after ~3 h of reaction. Rearrangements, without ring opening, lead to the formation of bi- and polycyclic compounds, principally from the bornylcarbonium ion. The latter, precursor of camphene, is believed to be formed via Wagner-Meerwein rearrangement of the pinylic cation as reported in **Appendix A, Scheme 1** [23, 24, 45].

Independently from the type of rearrangement reaction, neither camphene or limonene and its secondary products can be converted to  $\alpha/\beta$ -pinene [28].



**Scheme 4.4** – Proposed mechanism of the  $\alpha$ -pinene isomerisation reaction.

### 4.3 Conclusion

The isomerisation of  $\alpha$ -pinene is a solventless, non-polar, surface-type reaction for which catalyst activity and TOFs are strictly dependent on proton loading and accessibility. Findings revealed that SBA-15 allows superior HPW dispersion, relative to commercial low surface area fumed silica, facilitating a greater proton availability for a non-polar reagent unable to diffuse within the internal HPW cluster structures.

Reaction temperature is a critical factor in the isomerisation of alpha pinene, with significantly influence on camphene selectivity; lower temperatures favour camphene production, whereas higher temperatures result in higher conversion of  $\alpha$ -pinene and subsequent secondary reaction of limonene forming monocyclic secondary products.

HPA acid strength is also important, with camphene (and polycyclic products) selectivity increases with the increase of acid strength, whereas limonene and monocyclic are preferentially formed over weaker Brønsted acid.

Mechanism studies allowed the elucidation of the overall reaction network, and revealed the higher activity of  $\beta$ -pinene isomerisation which further confirmed the direct correlation between polycyclic selectivity and acid strength.

#### 4.4 Reference

- [1] A. Corma, S. Iborra, A. Velty, *Chemical Reviews* 107 (2007) 2411-2502.
- [2] B. Atalay, G. Gündüz, *Chemical Engineering Journal* 168 (2011) 1311-1318.
- [3] V. Wystrach, L. Barnum, M. Garber, *Journal of the American Chemical Society* 79 (1957) 5786-5790.
- [4] N. Beşün, F. Özkan, G. Gündüz, *Applied Catalysis A: General* 224 (2002) 285-297.
- [5] S. Findik, G. Gündüz, *J Amer Oil Chem Soc* 74 (1997) 1145-1151.
- [6] K. Hensen, C. Mahaim, W.F. Hölderich, *Applied Catalysis A: General* 149 (1997) 311-329.
- [7] A. Severino, A. Esculcas, J. Rocha, J. Vital, L.S. Lobo, *Applied Catalysis A: General* 142 (1996) 255-278.
- [8] G. Gündüz, R. Dimitrova, S. Yilmaz, L. Dimitrov, M. Spassova, *Journal of Molecular Catalysis A: Chemical* 225 (2005) 253-258.
- [9] G. Gündüz, R. Dimitrova, S. Yilmaz, L. Dimitrov, *Applied Catalysis A: General* 282 (2005) 61-65.
- [10] A. Severino, J. Vital, L.S. Lobo, *Studies in Surface Science and Catalysis*, Elsevier, 1993, pp. 685-692.
- [11] N.P. Comelli, Esther; Ponzi, Marta, *J Amer Oil Chem Soc* 82 (2005) 531-535.
- [12] M.A. Ecomier, A.F. Lee, K. Wilson, *Microporous and Mesoporous Materials* 80 (2005) 301-310.
- [13] M.A. Ecomier, K. Wilson, A.F. Lee, *Journal of Catalysis* 215 (2003) 57-65.
- [14] G. Kamalakar, K. Komura, Y. Sugi, *Applied Catalysis A: General* 310 (2006) 155-163.
- [15] L. Grzona, O. Masini, N. Comelli, E. Ponzi, M. Ponzi, *Reaction Kinetics and Catalysis Letters* 84 (2005) 199-204.

- [16] A.M. Alsahme, P.V. Wiper, Y.Z. Khimyak, E.F. Kozhevnikova, I.V. Kozhevnikov, *Journal of Catalysis* 276 (2010) 181-189.
- [17] A. Alsahme, E.F. Kozhevnikova, I.V. Kozhevnikov, *Applied Catalysis A: General* 390 (2010) 219-224.
- [18] O. Masini, L. Grzona, N. Comelli, E. Ponzi, M. Ponzi, *Journal of the Chilean Chemical Society* 48 (2003) 101-104.
- [19] N.A. Comelli, L.M. Grzona, O. Masini, E.N. Ponzi, M.I. Ponzi, *Journal of the Chilean Chemical Society* 49 (2004) 245-250.
- [20] O. Akpolat, G. Gündüz, F. Ozkan, N. Beşün, *Applied Catalysis A: General* 265 (2004) 11-22.
- [21] C.M. López, F. J. Machado, K. Rodríguez, B. Méndez, M. Hasegawa, S. Pekerar, *Applied Catalysis A: General* 173 (1998) 75-85.
- [22] F. Özkan, G. Gündüz, O. Akpolat, N. Beşün, D.Y. Murzin, *Chemical Engineering Journal* 91 (2003) 257-269.
- [23] A.I. Allahverdiev, S. Irandoust, D. Yu. Murzin, *Journal of Catalysis* 185 (1999) 352-362.
- [24] A.I. Allahverdiev, S. Irandoust, B. Andersson, D.Y. Murzin, *Applied Catalysis A: General* 198 (2000) 197-206.
- [25] N. Mizuno, M. Misono, *Chemical Reviews* 98 (1998) 199-217.
- [26] A.D. Newman, A.F. Lee, K. Wilson, N.A. Young, *Catalysis Letters* 102 (2005) 45-50.
- [27] C.H. Wu, H.Q. Liu, C.F. Zhuang, G.B. Du, Study on Mesoporous PW/SBA-15 for Isomerization of  $\alpha$ -Pinene, *Applied Mechanics and Materials*, Trans Tech Publ, 2014, pp. 134-137.
- [28] M. Golets, S. Ajaikumar, J.-P. Mikkola, *Chemical Reviews* 115 (2015) 3141-3169.
- [29] T. Yamamoto, T. Tanaka, T. Funabiki, S. Yoshida, *The Journal of Physical Chemistry B* 102 (1998) 5830-5839.
- [30] N. Flores-Holguín, A. Aguilar-Elguézabal, L.-M. Rodríguez-Valdez, D. Glossman-Mitnik, *Chemical Physics Letters* 546 (2012) 168-170.
- [31] M.N. Timofeeva, *Applied Catalysis A: General* 256 (2003) 19-35.
- [32] Y. Izumi, R. Hasebe, K. Urabe, *Journal of Catalysis* 84 (1983) 402-409.
- [33] J. Highfield, J. Moffat, *Journal of Catalysis* 88 (1984) 177-187.
- [34] L.C. Jozefowicz, H.G. Karge, E. Vasilyeva, J.B. Moffat, *Microporous Materials* 1 (1993) 313-322.

- [35] E. Lalik, A. Micek-Ilnicka, A. Groszek, A. Bielański, *Physical Chemistry Chemical Physics* 5 (2003) 3606-3609.
- [36] B.B. Bardin, R.J. Davis, M. Neurock, *The Journal of Physical Chemistry B* 104 (2000) 3556-3562.
- [37] S. Uchida, K. Inumaru, M. Misono, *The Journal of Physical Chemistry B* 104 (2000) 8108-8115.
- [38] G. Nie, J.-J. Zou, R. Feng, X. Zhang, L. Wang, *Catalysis Today* 234 (2014) 271-277.
- [39] M. Golets, S. Ajaikumar, M. Mohln, J. Wärnå, S. Rakesh, J.P. Mikkola, *Journal of Catalysis* 307 (2013) 305-315.
- [40] H.A. Meylemans, R.L. Quintana, B.G. Harvey, *Fuel* 97 (2012) 560-568.
- [41] J.J. Zou, N. Chang, X. Zhang, L. Wang, *ChemCatChem* 4 (2012) 1289-1297.
- [42] O.I. Yarovaya, D.V. Korchagina, Y.V. Gatilov, V.A. Barkhash, *Russian Journal of Organic Chemistry* 38 (2002) 810-822.
- [43] W.R. Rocha, H.M.S. Milagre, W.B. De Almeida, *Journal of Molecular Structure: THEOCHEM* 544 (2001) 213-220.
- [44] G.L.K. Hunter, W.B. Brogden, *The Journal of Organic Chemistry* 28 (1963) 1679-1682.
- [45] N. Flores-Holguín, A. Aguilar-Elguézabal, L.M. Rodríguez-Valdez, D. Glossman-Mitnik, *Journal of Molecular Structure* 854 (2008) 81-88.

## ***Chapter 5***

### ***Ethanol Dehydration***

## 5.1 Introduction

As previously described in **Chapter 2**, the dehydration of bio-ethanol is a challenging reaction to produce 'green ethylene' which has been studied since 1987 by Saito et al. using heteropolyacids as solid acid catalysts [1]. The literature agrees with ethylene and diethyl ether as the major products of ethanol dehydration, with the stoichiometric reactions, and associated enthalpy of formation, reported in **Equation 5.1**.



**Equation 5.1** – Products formed by the direct dehydration of ethanol, with relative formation enthalpies at 25 °C [2].

Reaction (1) displays the path to obtain ethylene, showing that is an endothermic process, which requires only one ethanol molecule, and is favoured over the temperature range 200-350 °C. Above this temperature, the catalytic decomposition of ethylene occurs forming undesirable secondary products. In contrast, reaction (2), leading to ether formation, is exothermic, requires two ethanol molecules and is favoured at lower temperatures. Several studies [1-8] have been carried out to identify the reaction pathways, and to determine if ethylene is a primary or secondary product.

The reaction proceeds under Brønsted acid conditions, with a great number of catalysts having been studied in an attempt to elucidate the reaction mechanism, which include  $\gamma$ -alumina and microporous aluminophosphates [9, 10], H-mordenites, H-beta and H-ZSM5 [2, 11-13], activated carbon [14], different metal oxides [15], and heteropolyacids [3, 16-19]. Saito et al.'s study [1] was one of the first to employ heteropolyacids as solid acid catalysts, pointing out on the role of the *pseudoliquid* phase on product yields, suggesting that it serves as reservoir of physisorbed ethanol molecules. The latter supposedly facilitating the formation of the undesired ether, which arises from the reaction between a chemisorbed and a physisorbed species, whereas ethylene is formed from the unimolecular decomposition of ethanol. Bokade et al. [16] studied the diluted ethanol (80% m/m) dehydration activity on phosphotungstic acid (HPW), its Na salt (NaPW) and phosphomolybdic acid (HPMo) supported on montmorillonite at different wt%. The best performances were obtained using the 30 wt% supported HPW to enhance the surface area, obtaining 74% of conversion and high ethylene yields. In the study, the use of diluted ethanol was chosen over anhydrous ethanol as a more realistic feedstock choice [16]. Cesium salts of HPMo and cerium, copper and nickel

salts of HPW have also been studied, showing greater selective catalysts for ethylene at low temperatures compared to their acids, leading, however, to the formation of acetaldehyde as a secondary product [3, 20].

## 5.2 Results and discussion

Ethanol conversion was calculated according to **Equation 5.2**, where  $\text{mol}_{Rt=0}$  are the initial moles before the feed stream passes through the reactor, and  $\text{mol}_{Rt}$  are referred to the moles of ethanol detected with the GC at time  $t$  of reaction on stream. Selectivity values were also calculated, with the equation reported below, where  $\text{mol}_P$  is referred to the moles produced of product, and  $v_P$  is the related stoichiometric coefficient and  $\text{mol}_R$  are the moles of reagent (ethanol converted).

$$\text{Conversion} / \% = \left( \frac{\text{mol}_{Rt=0} - \text{mol}_{Rt}}{\text{mol}_{Rt=0}} \right) \times 100$$

$$\text{Selectivity} / \% = \left( \frac{v_R \cdot \text{mol}_P}{v_P \cdot \text{mol}_{Rt}} \right) \times 100$$

**Equation 5.2** – Equation used to calculate ethanol conversion % and products selectivity.

In the current chapter, products are reported as space time yield (**Equation 5.3**) which measures the amount of product formed  $g_i$  per unit of time (h) and volume of catalyst (L) at the outlet.

$$\text{Space time yield (STY)} / \frac{\text{g}}{\text{L} \cdot \text{h}} = \frac{\text{mol}_{Pt}}{\text{h}} \times \frac{\text{MW}}{V_{\text{catalyst}}}$$

**Equation 5.3** – Space time yield equation where  $\text{mol}_{Pt}$  are the moles of ethylene or diethyl ether formed per unit of time, MW is the molecular weight of the compound of interest, and  $V_{\text{catalyst}}$  is the volume of the fixed bed reactor.

Reaction was performed under ethanol liquid flow rate,  $L = 0.0034 \text{ mol min}^{-1}$ ,  $\text{N}_2$  flow  $G = 50 \text{ cm}^3 \text{ min}^{-1}$  (25 °C), with a volumetric flow of the mixture calculated at the inlet (100 °C) of  $173 \text{ cm}^3 \text{ min}^{-1}$ . Space time was calculated based on the volume of catalyst  $V = 5 \text{ cm}^3$  per unit of volumetric flow of the stream. Repeated runs of ethanol dehydration were carried out to evaluate the error of each kinetic value.

## 5.2.1 Reaction profiles on unsupported HPA

### 5.2.1.1 Unsupported HPW

The dehydration of ethanol was initially investigated using unsupported HPW to study conversion dependence as a function of the mass of catalyst employed, which also allowed to define a protocol in which the intrinsic kinetics of reaction were not affected by mass-transport limitations (bulk diffusion). The influence of HPW mass (g) on activity was investigated using very mild conditions, 150 °C, to avoid any possible thermal degradation effect, with the total volume of the catalytic bed kept constant (5 cm<sup>3</sup>) by using a physical mixture of 50,100 and 150 g of HPW with quartz chips.

Ethanol conversion values and products space time yields are reported in **Appendix B-Figure 1-2-3**.

As confirmed in **Figure 5.1**, steady state rates of ethanol dehydration normalised for the mass of W were independent from the amount of catalyst used, exhibiting constant values at approximately 380 mmol h<sup>-1</sup> g<sub>W</sub><sup>-1</sup>.

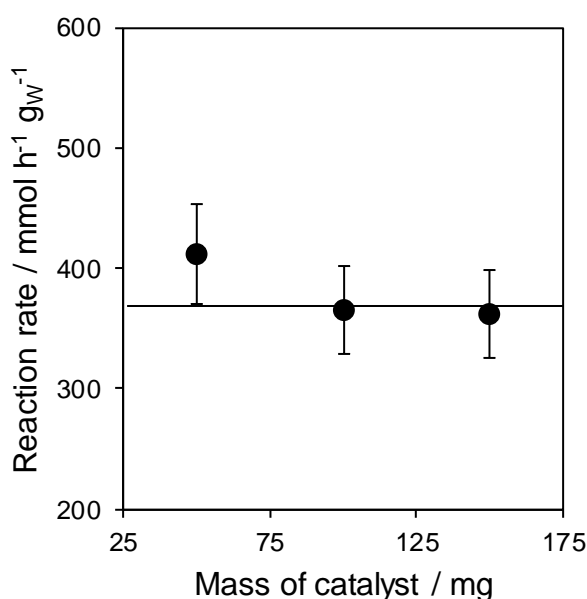


**Figure 5.1** – Influence of the mass catalyst on ethanol dehydration at 150 °C. Values were averaged after 90 min on stream.

Having established that substrate activity is independent on mass of catalyst used, ethanol dehydration was investigated as function of temperature, over the range of 150-275 °C, with the mass of catalyst being 50, 100 or 150 mg. **Figure 5.2** shows two examples of reaction profiles of ethanol conversion and products space time yields (sty), as function of time, at high and low temperature, employing 100 mg of catalyst.

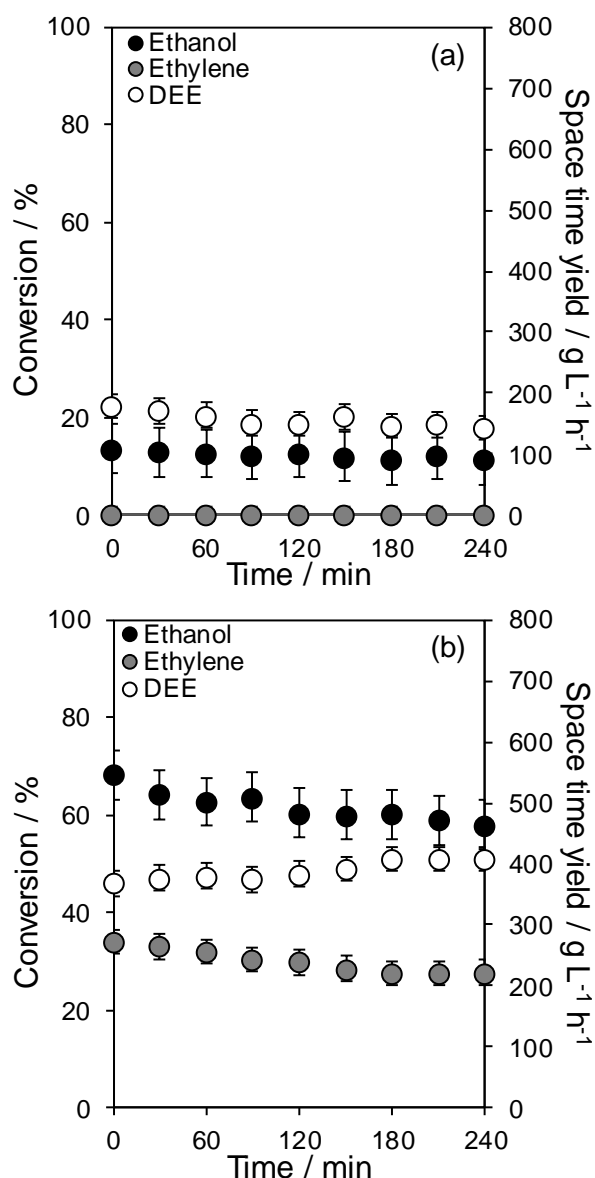


**Figure 5.2** – Ethanol dehydration reaction profiles carried out with unsupported HPW at different temperatures: 150 °C (a) and 275 °C (b). Reaction conditions: 100 mg catalyst,  $V_{\text{catalyst}} = 5 \text{ cm}^3$ ,  $L_{\text{Ethanol}} = 0.0034 \text{ mol min}^{-1}$ ,  $G_{\text{N}_2} = 50 \text{ cm}^3 \text{ min}^{-1}$  at 150 and 275 °C.

All reaction profiles for studies between 150 and 225 °C showed a constant ethanol conversion independently from the amount of catalyst; while a 7% loss in ethanol conversion was observed at 250 and 275 °C, suggesting some sort of deactivation process. This can be due to either site blocking for strong chemisorption of carbon species (poisoning), or thermal degradation of the active phase [21, 22]. Potential causes of catalyst deactivation will be investigated more in detail herein. To reduce the effect of catalyst deactivation on our measurements, all kinetic values were evaluated at 30 minutes of reaction. Ethanol conversion as a function of increasing temperature is shown in **Figure 5.3**-(a), where nearly a linear increase of conversion is observed as

function of temperature within 180-225 °C, as also reported by Varisli et al. [19]. For the three series, highest performance was observed at 275 °C, for which 67.3% of ethanol was converted employing 150 mg of catalyst, followed by 62.8 and 36.2% obtained with 100 and 50 mg respectively. Selectivity values were also investigated; results suggest that ethylene production increases with the temperature and is independent from the mass of HPW used (**Figure 5.3-(b)**), in agreement with the literature [19].

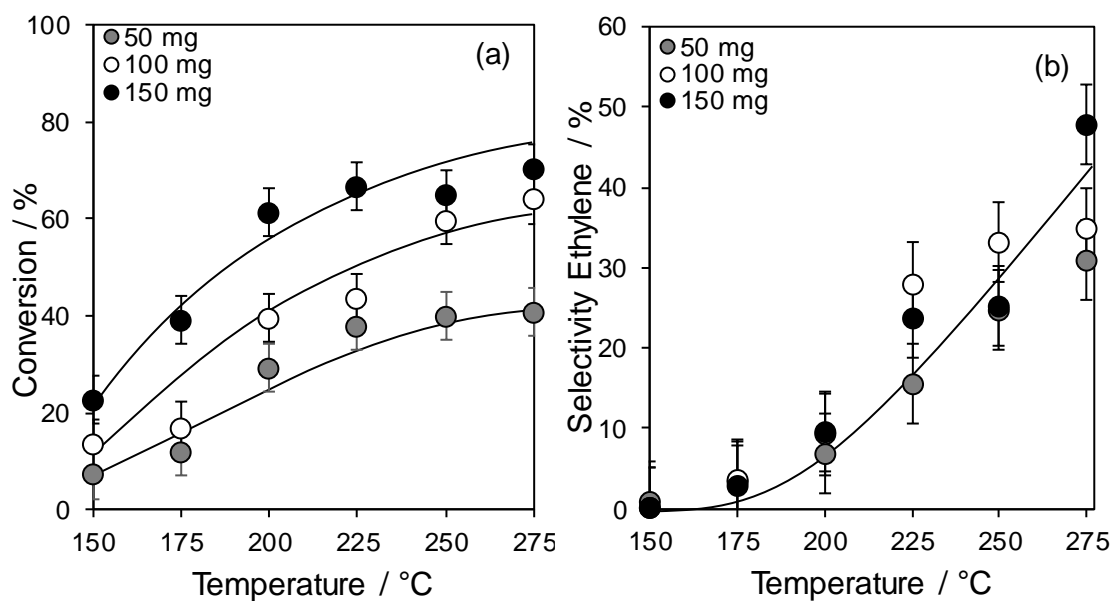


**Figure 5.3** – Influence of catalyst mass to volume ratio on ethanol conversion as function of temperature (a), and influence of temperature on ethylene selectivity (b). Reaction conditions: 50,100,150 mg catalyst,  $V_{\text{catalyst}} = 5 \text{ cm}^3$ ,  $L_{\text{Ethanol}} = 0.0034 \text{ mol min}^{-1}$ ,  $G_{\text{N}_2} = 50 \text{ cm}^3 \text{ min}^{-1}$  at 150, 175, 200, 225, 250 and 275 °C.

Apparent activation energy of the HPW catalyst for ethanol dehydration was calculated using the Arrhenius equation [23] for the three different amounts of catalyst (50, 100, 150 mg) within 150-275 °C. **Figure 5.4** shows results obtained employing 100 mg of HPW, which gives an  $E_a = 27 \text{ kJ mol}^{-1}$ . Comparable  $E_a$  results are also obtained employing 50 and 150 mg of unsupported HPW, revealing no correlation with the catalyst mass, and confirming the absence of mass transfer limitations under the reaction conditions used. Additionally, the  $E_a$  value is in good agreement with the literature ( $43 \text{ kJ mol}^{-1}$ ) for a comparable temperature range [16].

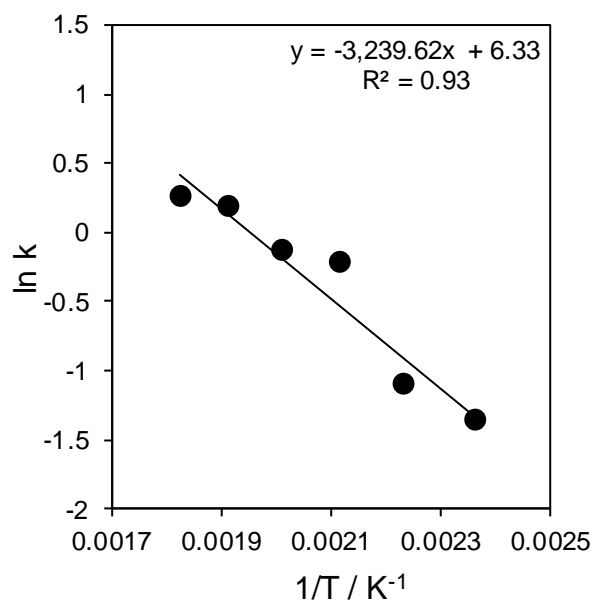


**Figure 5.4** – Arrhenius  $E_a$  for ethanol dehydration reaction carried out on unsupported HPW.

#### 5.2.1.2 Unsupported HSiW and HPMo

Ethanol dehydration was additionally carried out employing 100 mg of unsupported silicotungstic acid (HSiW) and phosphomolybdic acid (HPMo) to investigate dehydration kinetics and selectivity dependence on the nature of the heteropolyacid involved. **Figure 5.5** reports ethanol conversion and products space time yield profiles for both unsupported HSiW and HPMo at 225 °C. The plot reveals that HSiW seems to be more active than HPMo; but both catalysts suffer from ~ 15% decrease in ethanol conversion, and in the order of 50% loss in space time yields towards the products. It is hypothesised that the lower thermal stability (compared to HPW), affects onstream stability, which in turn leads to a in decreased activity and ethanol conversion (as confirmed by TGA analysis, **Chapter 3, Figure 3.26**).

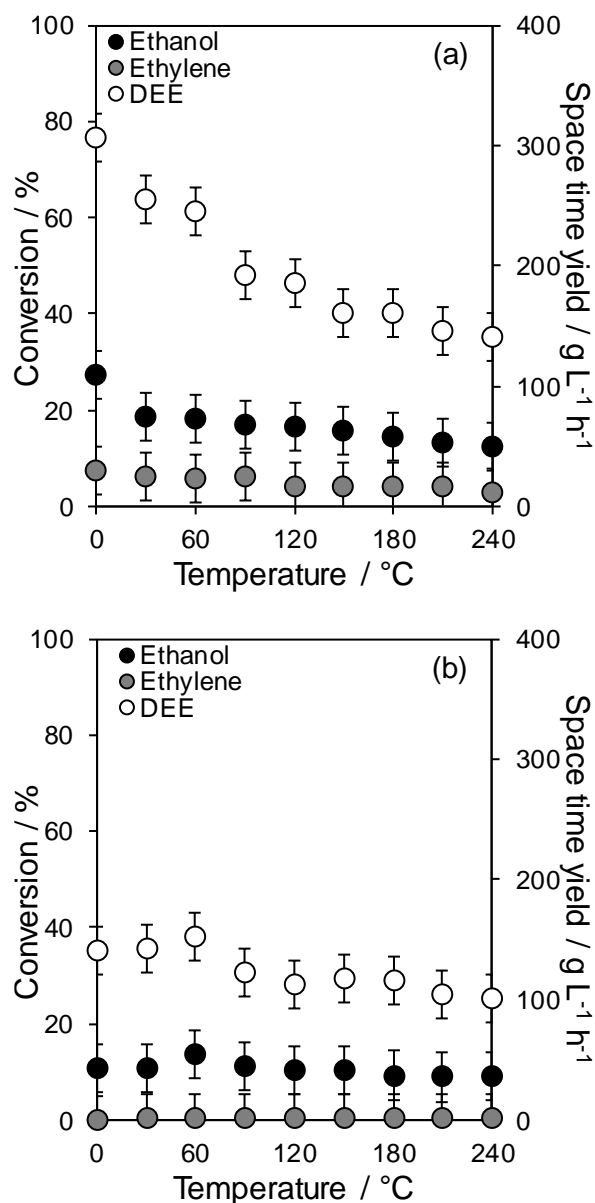


**Figure 5.5** – Ethanol dehydration reaction profile carried out with unsupported HSiW (a) and unsupported HPMo (b). Reaction conditions: 100 mg catalyst,  $V_{\text{catalyst}} = 5 \text{ cm}^3$ ,  $L_{\text{Ethanol}} = 0.0034 \text{ mol min}^{-1}$ ,  $G_{\text{N}_2} = 50 \text{ cm}^3 \text{ min}^{-1}$  at 225 °C.

**Figure 5.6** compares the results of the three unsupported HPAs, revealing that HPW displays the greatest performance for both ethanol conversion and ethylene selectivity. When HPW is employed at 225 °C, 43% conversion was obtained, while HSiW and HPMo reached 20% and 11% respectively. Selectivity toward ethylene follows the same trend across the different heteropolyacid species, indicating that both conversion and selectivity are related to difference in acid strength, in which strong acid sites increase dehydration reactions.

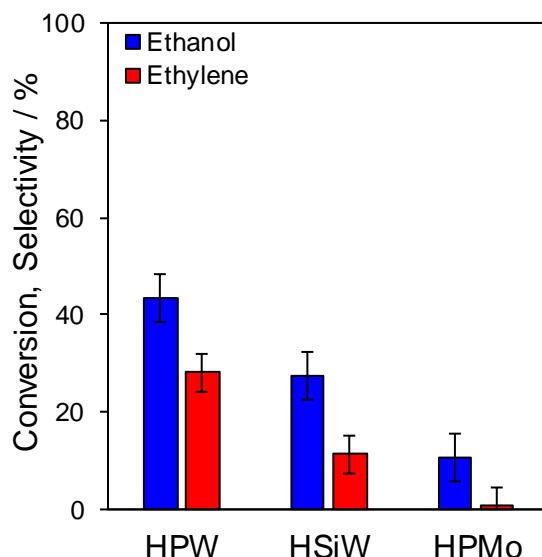


**Figure 5.6** – Ethanol conversion and ethylene selectivity depending on the heteropolyacid used. Reaction conditions: 100 mg catalyst,  $V_{\text{catalyst}} = 5 \text{ cm}^3$ ,  $L_{\text{Ethanol}} = 0.0034 \text{ mol min}^{-1}$ ,  $G_{\text{N}_2} = 50 \text{ cm}^3 \text{ min}^{-1}$  at 225 °C.

Turnover frequencies and selectivity values as a function of catalyst acid strength is shown in **Figure 5.7**, with acid strength evaluated by n-propylamine TPD described in **Chapter 3**. Unsupported HPW possess the strongest acidity, as observed from the desorption of propene at 264 °C; unsupported HSiW and HPMo revealed a weaker acidity with propene desorption at 280 and 310 °C respectively. The acid strength order observed for the three unsupported heteropolyacids,  $\text{HPW} > \text{HSiW} > \text{HPMo}$ , is in agreement with the literature [24-30], and strongly relates with ethylene selectivity and TOFs. Propylamine analysis also revealed that the  $\text{H}^+$  density on these materials follows the inverse order,  $\text{HPMo} > \text{HSiW} > \text{HPW}$ , indicating that neither ethylene selectivity nor TOFs are influenced by the acid site loading. Variations due to proton accessibility were not considered because all the considered unsupported HPAs display similar low surface area and crystallite size as reported in **Chapter 3**. The influence of proton accessibility will be studied later employing the supported HPA species.

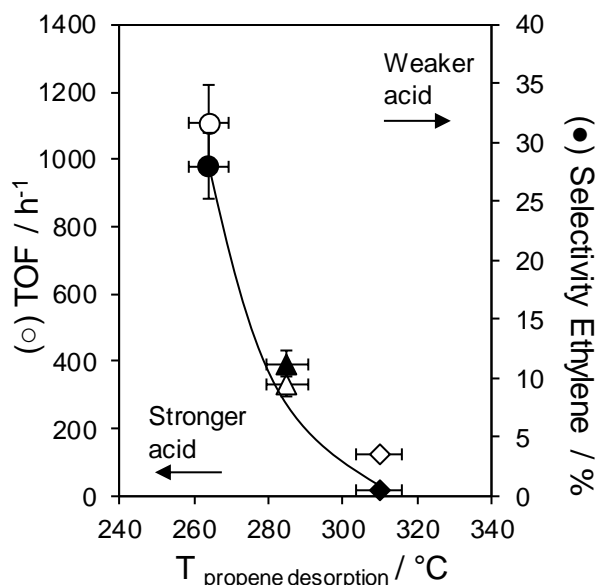


**Figure 5.7** – Ethylene selectivity dependence on the proton density and acid strength, determined via n-propylamine TPD of unsupported heteropolyacid, HPW (●), HSiW (▲) and HPMo (◆). Reaction conditions: 100 mg catalyst,  $V_{\text{catalyst}} = 5 \text{ cm}^3$ ,  $L_{\text{Ethanol}} = 0.0034 \text{ mol min}^{-1}$ ,  $G_{\text{N}_2} = 50 \text{ cm}^3 \text{ min}^{-1}$  at 225 °C.

Additional tests were carried out to study the influence of temperature on catalytic conversion of ethanol using HSiW and HPMo, at 175 and 250 °C. HSiW and HPMo reaction profiles of ethanol conversion and space time yields at three different temperatures and as a function of time are reported in **Appendix B** in **Figure 4** and **5**. In both series, at all temperatures, a reduction of 10% in ethanol conversion is observed over the 4 h of reaction, as well as products space time yields. Results suggested that catalyst undergoes through deactivation. **Figure 5.8** reports conversion and selectivity values take at 30 minutes to minimise the influence of deactivation. For unsupported HSiW (a), ethylene selectivity increases significantly with the temperature, starting from 5% at 175 °C and reaching 20% at 250 °C. A comparable trend is also observed when employing 100 mg of HPMo, in which 4.2% ethylene selectivity is obtained at the highest temperatures. In contrast to the HPW system, for both series ethanol conversion decreases with temperature, indicative that HSiW and HPMo are more susceptible to thermal deactivation [22].

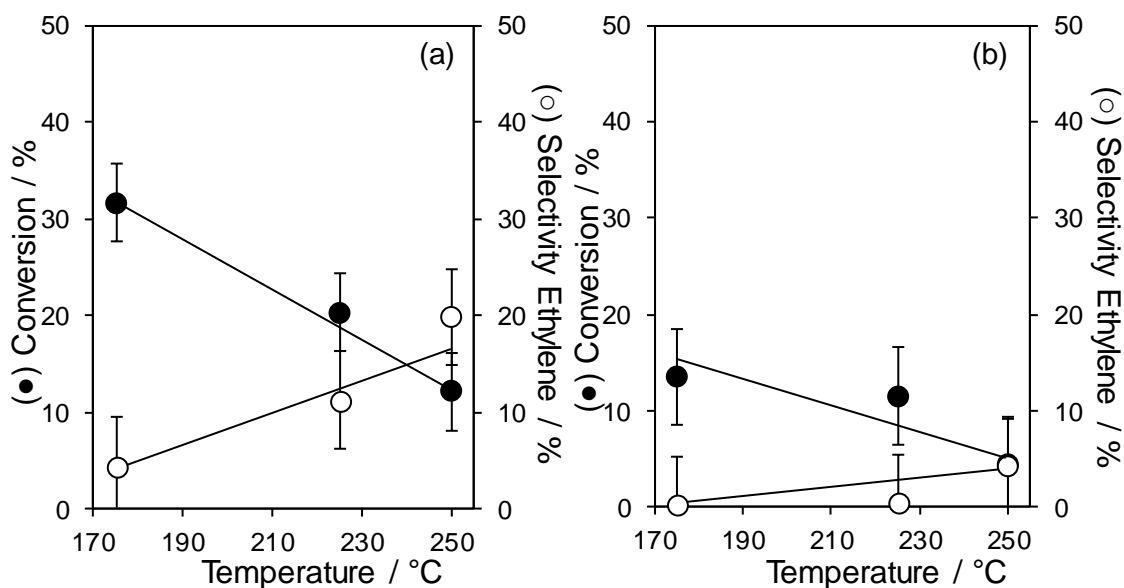


**Figure 5.8** – Ethanol dehydration dependence on reaction temperature employing unsupported HSiW (a) and HPMo (b). Reaction conditions: 100 mg catalyst,  $V_{\text{catalyst}} = 5 \text{ cm}^3$ ,  $L_{\text{Ethanol}} = 0.0034 \text{ mol min}^{-1}$ ,  $G_{\text{N}_2} = 50 \text{ cm}^3 \text{ min}^{-1}$  at 175, 225 and 250 °C.

## 5.2.2 Reaction profiles on supported HPAs

### 5.2.2.1 Supported HPW: the influence of support architecture

The effect of proton accessibility on the reaction kinetics was investigated by depositing HPW on two silica supports with different architecture, commercial non-porous fumed silica and well-ordered mesoporous SBA-15, previously synthesised and characterised in **Chapter 3**. Blank reactions, using 100 mg of both bare supports, were also conducted at 150, 200 and 250 °C showing negligible contribution in ethanol conversion.

Catalyst screening was conducted at 225 °C employing 100 mg of supported catalyst, to probe differences in conversion and selectivity as a function of bulk W loadings over the two support materials. Reaction profiles are reported in **Figure 5.9**, where for all the samples, ethanol conversion is constant as function of time, with a slight 5% decrease only observed at higher loadings, behaviour also observed for ethylene space time yields. **Appendix B-Figure 6** reports diethyl ether space time yields obtained for the two series. Ethylene and DEE were the major products with mass balance above 85%. Coke deposition and negligible formation of  $\text{CO}_2$  as well as butylene isomers, as detected from GC analysis, make up the unaccounted mass.

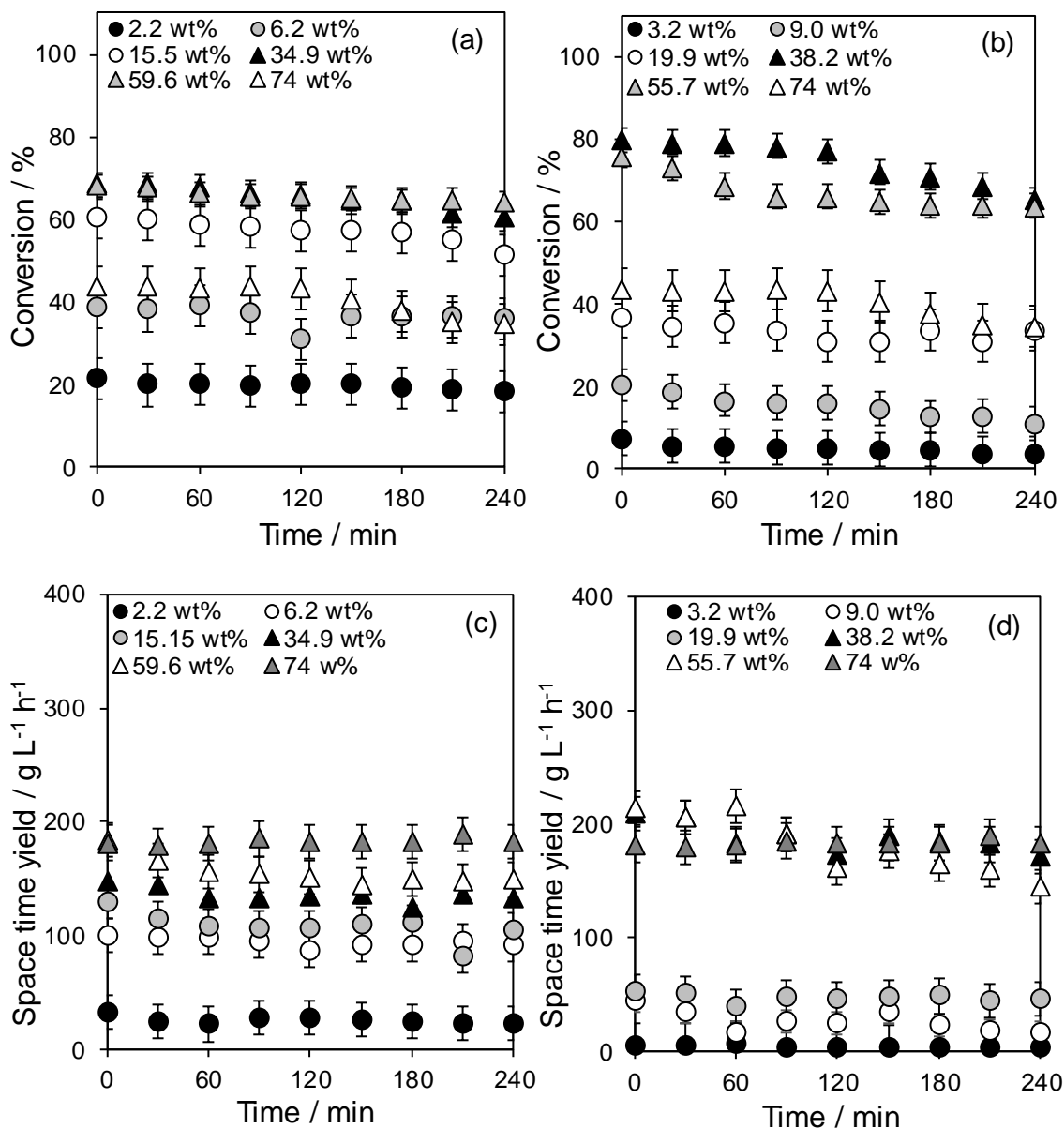


**Figure 5.9** – Ethanol conversion and ethylene space time yields as function of time at 225 °C, employing HPW/Fumed silica (a, c), and HPW/SBA-15 (b, d). Reaction conditions: 100 mg catalyst,  $V_{\text{catalyst}} = 5 \text{ cm}^3$ ,  $L_{\text{Ethanol}} = 0.0034 \text{ mol min}^{-1}$ ,  $G_{\text{N}_2} = 50 \text{ cm}^3 \text{ min}^{-1}$  at 225 °C.

**Figure 5.10** summarises the conversion of ethanol as a function of W loading, with reported conversion values taken at 30 min of reaction to minimise the influence of deactivation on-stream. HPW supported on fumed silica reach rapidly a plateau for W loading  $\geq 15.5 \text{ wt}\%$  at approximately 62% of ethanol conversion. In comparison, HPW catalysts on SBA-15 exhibit a more linear trend within the loadings 3.2 and 38.2 wt%, for which the maximum of conversion (79%) is observed. At higher loadings, as observed for the fumed silica series, conversion values plateau, indicating that the two series

behave similarly at these wt%. The striking difference between the two series appears in the low loading region, where performances are greater over HPW deposited on fumed silica. This would suggest that structural differences in the HPW aggregation impart the controlling factor, for which the conversion is independent on the amount of HPW used.

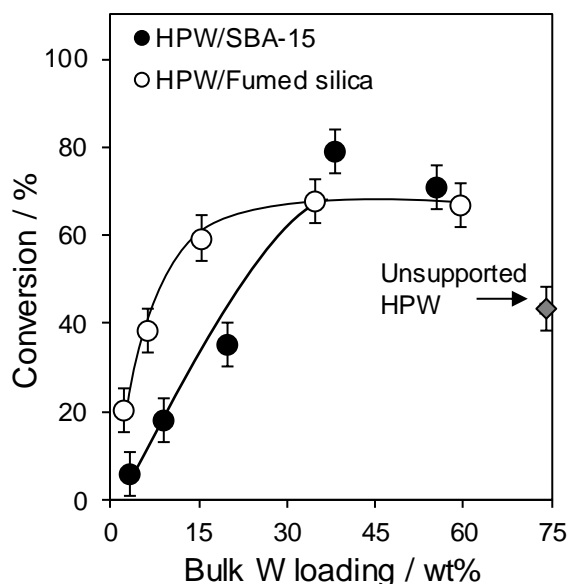


**Figure 5.10** – Influence of bulk W loading on the conversion of ethanol for the two series, HPW/SBA-15 and HPW/Fumed silica. Reaction conditions: 100 mg catalyst,  $V_{\text{catalyst}} = 5 \text{ cm}^3$ ,  $L_{\text{Ethanol}} = 0.0034 \text{ mol min}^{-1}$ ,  $G_{\text{N}_2} = 50 \text{ cm}^3 \text{ min}^{-1}$  at 225 °C.

Selectivity data evaluated at iso-conversion values (within the range 25-50%) reveals that support architecture have no influence on product selectivity (see **Figure 5.11**), with constant DEE and ethylene selectivity of 78% and 19% respectively, these being consistent with bulk HPW. The plot indicates a common reaction mechanism across both supported and unsupported bulk HPW, revealing that the intrinsic chemistry of the unsupported HPW is retained after impregnation.

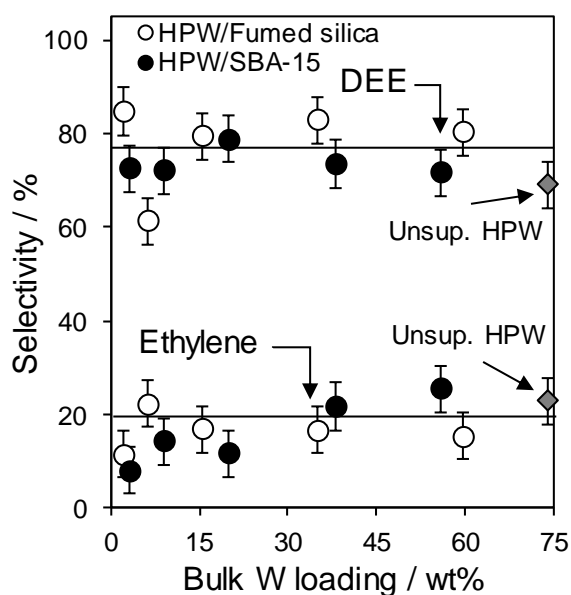


**Figure 5.11** – Influence of W loading on the selectivity towards diethyl ether (DEE) and ethylene for the two series, HPW/SBA-15 and HPW/Fumed silica. Reaction conditions: 100 mg catalyst,  $V_{\text{catalyst}} = 5 \text{ cm}^3$ ,  $L_{\text{Ethanol}} = 0.0034 \text{ mol min}^{-1}$ ,  $G_{\text{N}_2} = 50 \text{ cm}^3 \text{ min}^{-1}$  at 225 °C.

Reaction rates normalised to the mass of W are shown in **Figure 5.12**. An inverse correlation between activity and bulk loading emerges for HPW on fumed silica, with catalysts with HPW loadings between 2.2-15.5 wt% exhibiting the highest activities, reaching 20000  $\text{mmol h}^{-1} \text{ g}_W^{-1}$  for the lowest wt%. At higher loadings,  $\geq 34.9 \text{ wt}\%$ , activity decreases and plateaus at a value comparable to the unsupported HPW (74 wt%). The dehydration rates over the SBA-15 series show lower values than the fumed silica counterparts, being around 5000  $\text{mmol h}^{-1} \text{ g}_W^{-1}$  for the 3.2 wt% loading, and mirroring the fumed silica series at higher loadings ( $> 38.2 \text{ wt}\%$ ). The activity dependence on HPW loading confirms the critical role that the physiochemical properties of the deposited active site plays, and suggesting that the most active system is the one that shows an optimal aggregation level rather than a more dispersed systems (as for the alpha pinene).

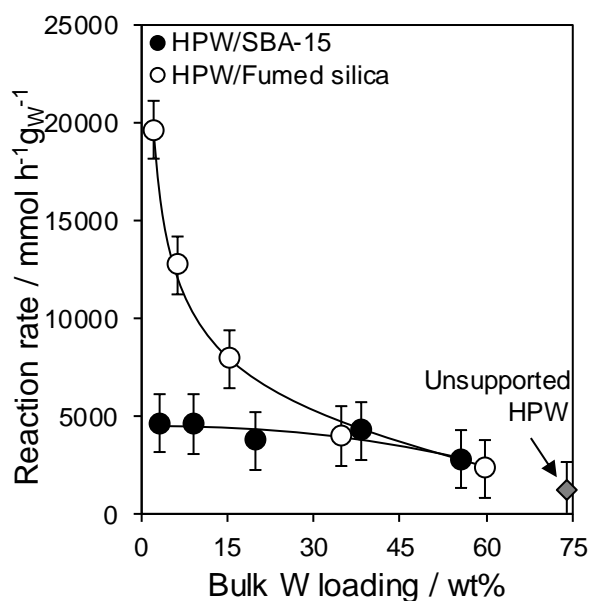


**Figure 5.12** – Dependence of ethanol dehydration activity on bulk W loading and silica support. Reaction conditions: 100 mg catalyst,  $V_{\text{catalyst}} = 5 \text{ cm}^3$ ,  $L_{\text{Ethanol}} = 0.0034 \text{ mol min}^{-1}$ ,  $G_{\text{N}_2} = 50 \text{ cm}^3 \text{ min}^{-1}$  at 225 °C.

To better understand why HPW on fumed silica is more active than comparable loadings on SBA-15, turnover frequencies were calculated based on the total acid density measured via n-propylamine chemisorption. The method was chosen over ammonia titration analysis as the probe molecule n-propylamine is closer in molecular size to ethanol, with values of 5.4 and 1.6 for n-propylamine and ammonia respectively, relative to 4.0 Å for ethanol (calculation made using Chem3D software).

Turnover frequencies were investigated as function of bulk W loading for the two supports to highlight the effect of support architecture on catalyst activity. Results obtained for the two series are reported on **Figure 5.13**, showing again that, at comparable bulk W loadings, catalysts supported on fumed silica are far more active than on SBA-15. HPW on fumed silica display a volcano-like trend as function of W wt%, reaching  $\sim 4766 \text{ h}^{-1}$  for 15.5 wt% catalysts, to further decrease to  $3000 \text{ h}^{-1}$  at higher loadings. On the other hand, TOF calculated for SBA-15 supported catalysts reveal almost constant values at  $\sim 2000 \text{ h}^{-1}$ , with TOF value more comparable with the unsupported HPW, as already observed by Haber et al. [31].

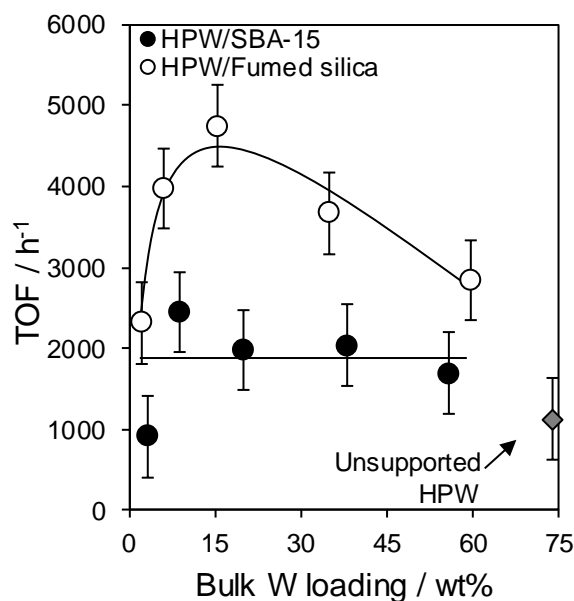


**Figure 5.13** – Turnover frequencies for ethanol dehydration as function of bulk W loading for HPW/SBA-15 and HPW/Fumed silica. Reaction conditions: 100 mg catalyst,  $V_{\text{catalyst}} = 5 \text{ cm}^3$ ,  $L_{\text{Ethanol}} = 0.0034 \text{ mol min}^{-1}$ ,  $G_{\text{N}_2} = 50 \text{ cm}^3 \text{ min}^{-1}$  at 225 °C.

As extensively described in **Chapter 1**, one of the unique characteristics of heteropolyacids is the ability to carry out bulk-type catalysis in the presence of polar reactant, in the so-called *pseudoliquid* phase, as well as an excellent proton mobility, both within the K.U. and within K.U. clusters [31-34]. When HPW are supported on silica, part of the protons is directly bounded with the surface and thus do not participate as catalytically active sites, while the other part is free, easily accessible and therefore able to take part in the catalytic active site turnover. Increasing the loading of HPW results in the genesis of bigger agglomerates, which are structurally similar to the unsupported species, where proton density is significant, resulting in the presence of a greater degree of so-called *crystalline* water. This crystalline water, trapped between adjacent K.U., is responsible of the further adsorption and subsequent reaction of ethanol within the bulk HPW structure, and serves as reservoir for ethanol, whilst also facilitating proton mobility. In order to evaluate whether the amount of crystalline water is a governing factor, the dependence of TOF on this physiochemical property, determined from the mass loss measured via thermogravimetric analysis (see **Chapter 3, Fig 3.13**), is shown in **Figure 5.14**. The plot reveals a striking linear correlation that is independent of support architecture, indicating the critical role that water of crystallinity plays in the catalytic activity towards the polar ethanol reactant forming more of the so called *pseudoliquid* phase in which higher levels of  $\text{H}_3\text{O}^+$  and  $\text{H}_5\text{O}_2^+$  are present.

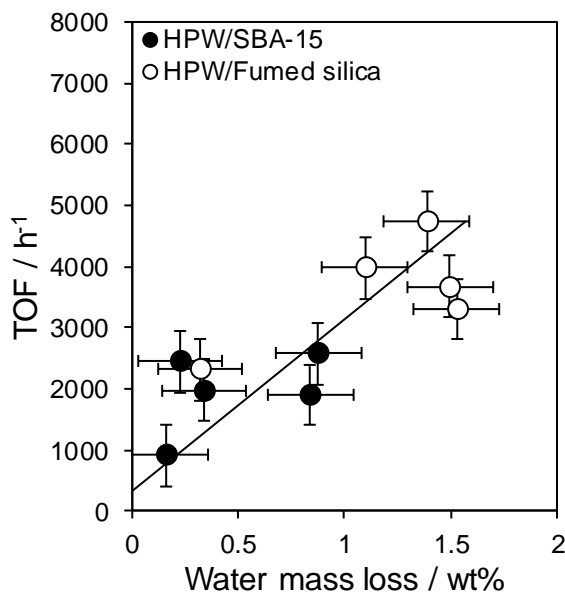


**Figure 5.14** – Correlation between ethanol dehydration TOFs and water mass loss measured for unsupported and supported HPW on fumed silica and SBA-15. Reaction conditions: 100 mg catalyst,  $V_{\text{catalyst}} = 5 \text{ cm}^3$ ,  $L_{\text{Ethanol}} = 0.0034 \text{ mol min}^{-1}$ ,  $G_{\text{N}_2} = 50 \text{ cm}^3 \text{ min}^{-1}$  at 225 °C.

### 5.2.2.2 Supported HPW: recycling the catalyst

The on-stream lifetime and recyclability of a catalyst are critical factors when designing a material for industrial application. To evaluate the recyclability of these systems, the W 38.2 wt% on SBA-15 was assessed for 3 consecutive reactions, at 225 °C, between each run the reactor was slowly cooled under inert gas ( $\text{N}_2$ ) with no catalyst reactivation process implemented.

**Figure 5.15**-(a) shows the reaction profiles for the three consecutive runs. Ethanol conversion diminishes with each run, losing 50% of the initial value by the 3<sup>rd</sup> cycle. During each cycle, conversion values remain constant values over time, indicating that during the reaction the HPW is stable and is not effected by any sort of deactivation, with ethylene space time yield values for the three runs constant and thus supporting this conclusion, as reported in **Figure 5.15**-(b, c). Selectivity towards ethylene was also evaluated for each run (see **Figure 5.15**-(d)) which is reported with conversion at 30 minutes. The plot clearly reveals that, although the catalyst loses 23% and 35% of its activity, after the 1<sup>st</sup> and 2<sup>nd</sup> run, selectivity is unaffected, suggesting only a loss in the total number of active sites arose from poisoning and/or a physiochemical change to an inactive phase.

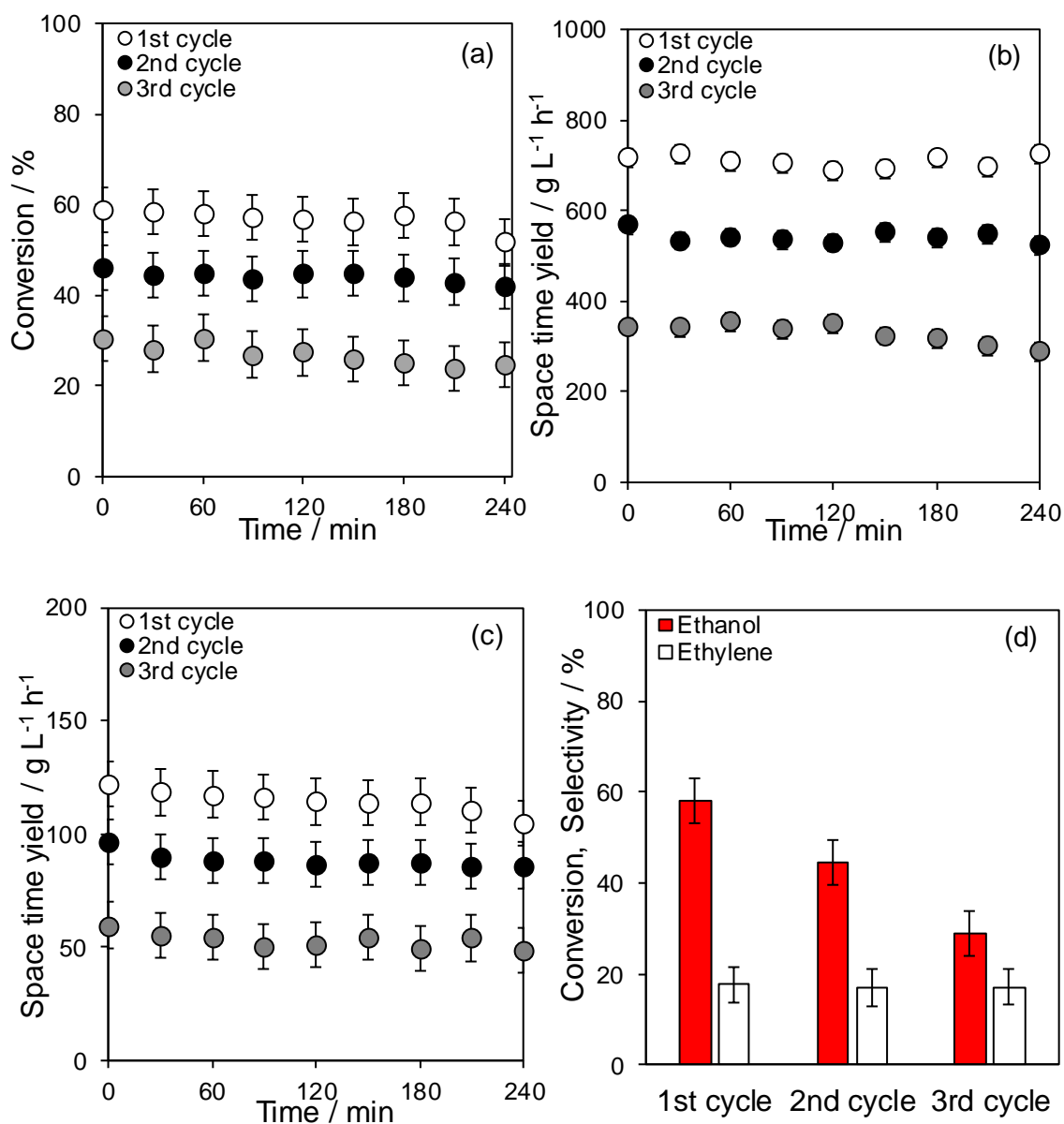


**Figure 5.15** – Reaction profiles for fresh and recycled 38.2 wt% of bulk W loaded on SBA-15: ethanol conversion (a), diethyl ether (b) and ethylene (c) space time yield, and comparison of conversion and ethylene selectivity after each run (d). Reaction conditions: 50 mg catalyst,  $V_{\text{catalyst}} = 5 \text{ cm}^3$ ,  $L_{\text{Ethanol}} = 0.0034 \text{ mol min}^{-1}$ ,  $G_{\text{N}_2} = 50 \text{ cm}^3 \text{ min}^{-1}$  at  $225 \text{ }^\circ\text{C}$ .

According to literature and from the previous characterisation (TGA, XRD and DRIFTS), hydrated HPW lose the so-called crystalline water at approximately  $200 \text{ }^\circ\text{C}$ , with dehydrated structures stable up to  $300 \text{ }^\circ\text{C}$ , and only at higher temperatures dehydroxylation takes place. During the reaction (at  $225 \text{ }^\circ\text{C}$ ), besides ethylene and diethyl ether, water is also formed, as a beneficial by-product, which is rapidly absorbed by the HPW and in turn partially rehydrates the structure. In addition, hydrogen bonded ethanol molecules have also been shown to play the same role as water in stabilising

the HPW structure [33]. Janik et al. 2003 [35] studied the reversibility of the dehydration process on phosphotungstic acid, proving by FTIR that samples, previously pre-treated at 200 °C and exposed to water vapour, are easily re-hydrated, evidenced by the reappearance of bending vibration of the six water molecules of the hydrated HPW structure at 1716 cm<sup>-1</sup> wavenumber. The rehydration, however, is irreversible if the HPA is heated to 300 °C and above, when the dehydroxylation takes place. Under the recycle condition implemented, upon completion of the reaction, the catalytic bed was cooled under a flow of inert gas before the next cycle, potentially removing all the weakly bonded molecules, both protonated water and ethanol, and thus increasing the anhydrous character of the HPW structure. This hypothesis is further supported by the reserches of Furuta et al. [36], who showed that the presence of water vapours is crucial to stabilise both the primary and secondary structure of the Keggin units, and Micek-Ilnicka et al. [37] who found that the addition of water to the reactant stream can positively influence the physicochemical properties of the HPW Keggin unit slowing the dehydration process, and hence keeping the structure hydrated, more stable and less prone to deactivation.

To test this hypothesis, the role of water on catalyst stability and reaction kinetics was investigated, recyclability tests were carried out using ethanol spiked with a known amount of water. Two different water concentrations, 2.9 mol L<sup>-1</sup> (~5% vol/vol) and 6.2 mol L<sup>-1</sup> (~10% vol/vol), were chosen, with the former molarity being akin to the azeotropic mixture, and the latter similar to the water concentration present in bioethanol, which is used as fuel blends [38] and widely produced. The tests carried out using the water concentration of 2.9 mol L<sup>-1</sup> are reported in **Figure 5.16**, where reaction profiles of fresh and recycled 38.2 wt% HPW/SBA-15 catalyst are plotted as function of time. **Figure 5.16-(a)** reveals that constant values of ethanol conversion are observed during the 4 h or reaction, as witnessed for anhydrous ethanol feedstock and further confirming that there is no thermal deactivation of materials at 225 °C. In comparison with the anhydrous test, for the first cycle, the presence of water slightly lowers ethanol conversion, as both compounds, ethanol and water, competitively adsorbed on the catalyst surface. Interestingly, after the 3<sup>rd</sup> cycle, only 13% of the initial conversion is lost (going from ~56% to 43%), compared to 35% previously, clearly indicating that water helps to maintain the hydrated catalyst structure. Additionally, products space time yields are constant during the 4 hours of reaction with only a slightly decrease after each cycle (**Figure 5.16-(b, c)**), and change in selectivity is observed (**Figure 5.16-(d)**), displaying constant values with both fresh and spent catalyst

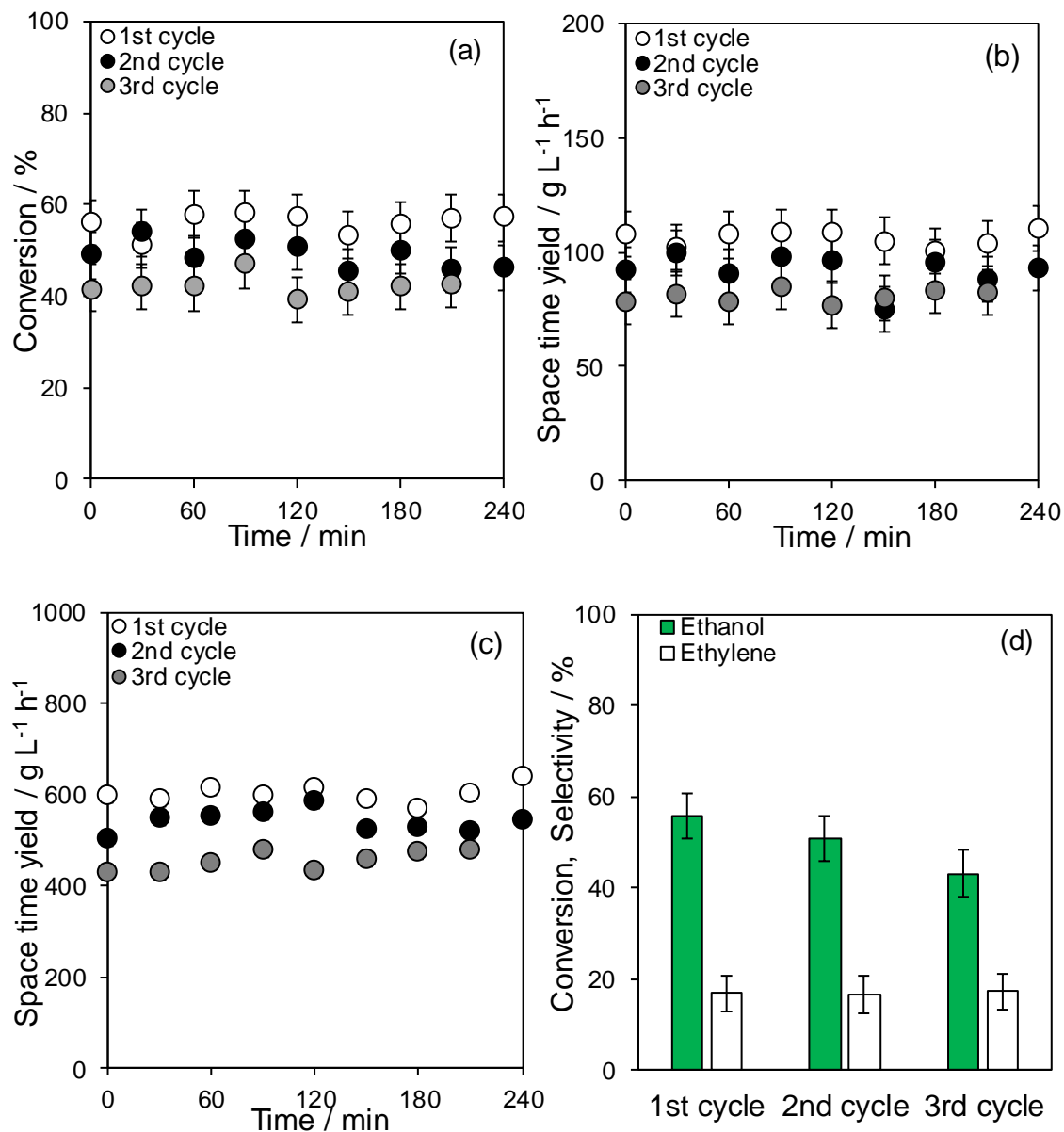


**Figure 5.16** – Reaction profiles for fresh and recycled 38.2 wt% of bulk W loaded on SBA-15, employing a 2.9 M solution of water in ethanol as feed: ethanol conversion (a), and ethylene (b) and diethyl ether (c) space time yield, and comparison of conversion and ethylene selectivity after each run (d). Reaction conditions: 50 mg catalyst,  $V_{\text{catalyst}} = 5 \text{ cm}^3$ ,  $L_{\text{Ethanol}} = 0.0033 \text{ mol min}^{-1}$ ,  $L_{\text{H}_2\text{O}} = 0.0004 \text{ mol min}^{-1}$ ,  $G_{\text{N}_2} = 50 \text{ cm}^3 \text{ min}^{-1}$  at 225 °C.

The tests carried out on using water concentrations of  $6.2 \text{ mol L}^{-1}$  as the reaction stream, as reported in **Figure 5.17**, where reaction profiles of fresh and recycled 38.2 wt% HPW/SBA-15 catalyst are plotted as function of time. **Figure 5.17**-(a) displays constant values of ethanol conversion during the 4 h or reaction, as observed in both previous tests. In comparison, although the increase in the amount of water further lessened the conversion to 48%, the value remains constant for each cycle, suggesting preservation

of the HPW primary structure. Product space time yields are also constant over the 4 hours of reaction (**Figure 5.17**-(b, c)), as is product selectivity (**Figure 5.17**-(d)) which again agree excellently with the previous studies.

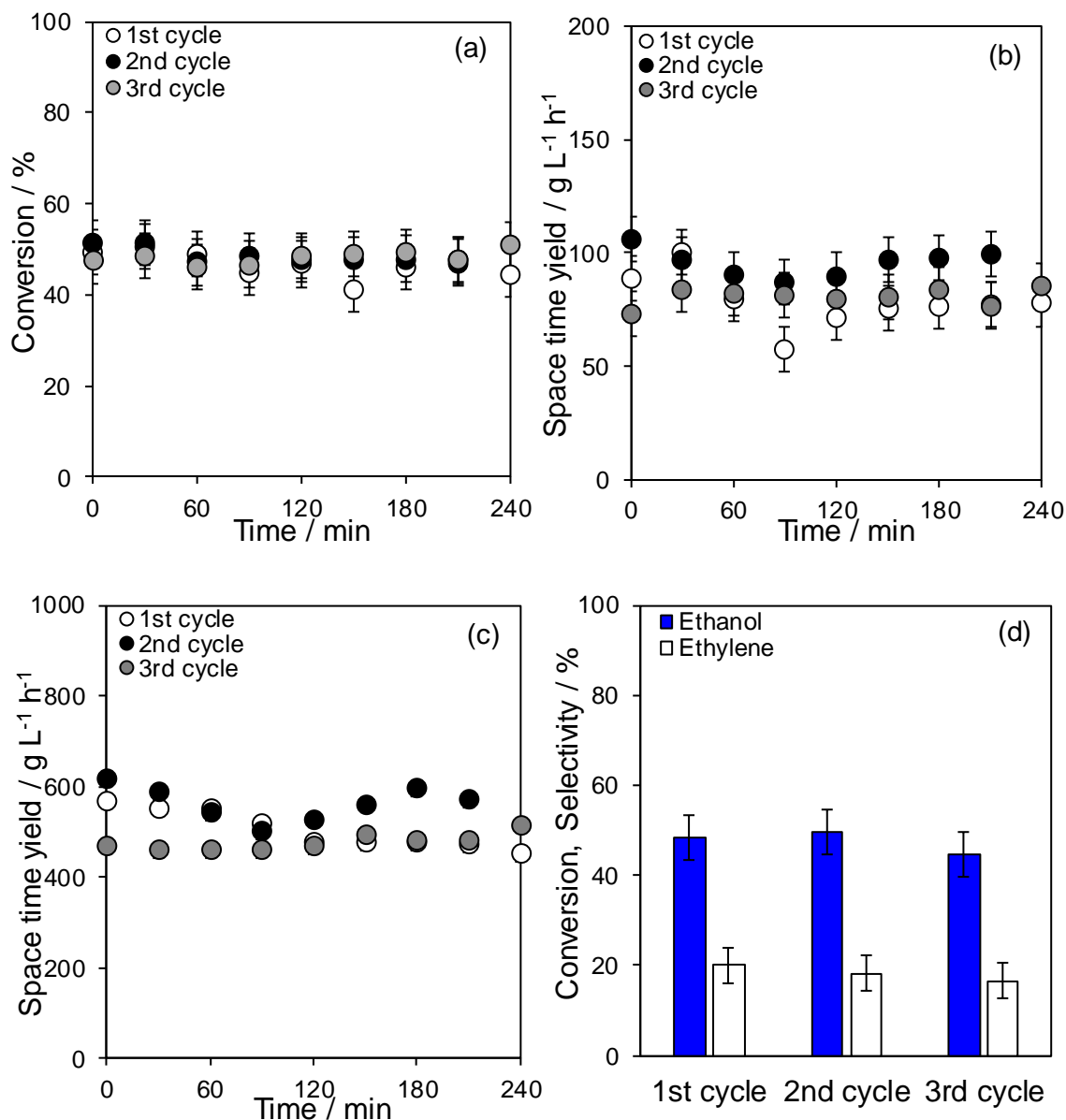


**Figure 5.17** – Reaction profiles for fresh and recycled 38.2 wt% of bulk W loaded on SBA-15, employing a 6.2 M solution of water in ethanol as feed: ethanol conversion (a), and ethylene (b) and diethyl ether (c) space time yield, and comparison of conversion and ethylene selectivity after each run (d). Reaction conditions: 50 mg catalyst,  $V_{\text{catalyst}} = 5 \text{ cm}^3$ ,  $L_{\text{Ethanol}} = 0.0032 \text{ mol min}^{-1}$ ,  $L_{\text{H}_2\text{O}} = 0.0009 \text{ mol min}^{-1}$ ,  $G_{\text{N}_2} = 50 \text{ cm}^3 \text{ min}^{-1}$  at 225 °C.

The influence of water content on ethanol conversion and ethylene selectivity is reported in **Figure 5.18**, wherein data are compared based on the first reaction point of the steady state. **Figure 5.18**-(a) compares conversions between all recycling tests indicating that

in the absence of water after each run there is a dramatic drop in conversion, which is attributed to a loss in activity from the partial collapse of the Keggin structure. The addition of water helps to mitigate the loss of conversion, as it is believed to aid the rehydration and stabilisation of the catalytic structure, with this effect proportional to water concentration. **Figure 5.18**-(b) reports the selectivity values for all the recycling tests, revealing that selectivity is independent to the amount of water present in the feed-stream, which is indicative of water only stabilising the active phase and not inducing the formation of a different catalytically active species.

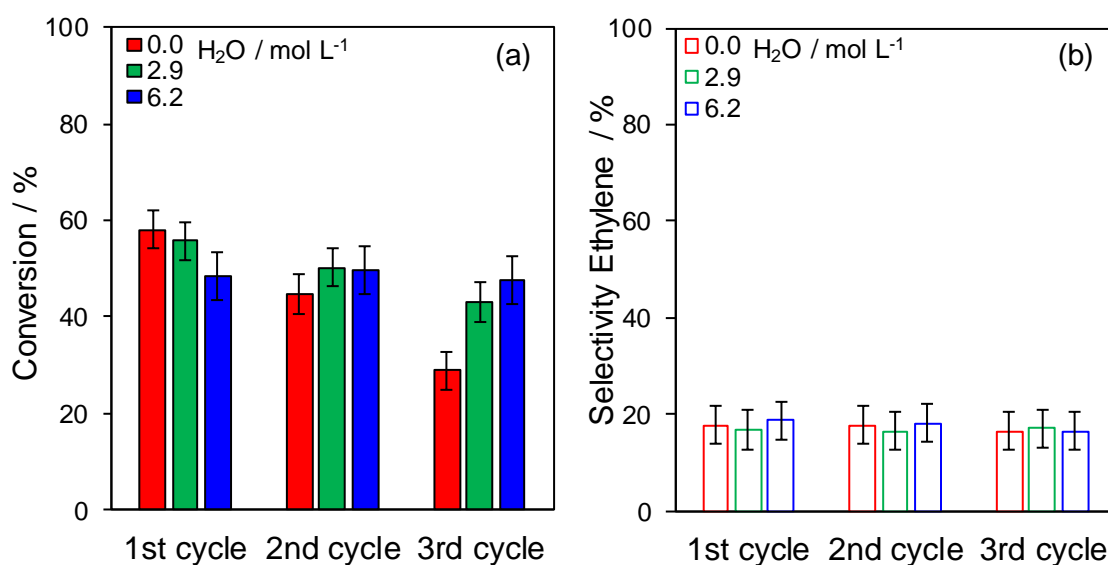


**Figure 5.18** – Comparison between conversion (a) and ethylene selectivity (b) after each run for anydrous ethanol (0 mol L<sup>-1</sup>), 2.9 and 6.2 mol L<sup>-1</sup> of hydrous ethanol. Reaction conditions: 50 mg catalyst,  $V_{\text{catalyst}} = 5 \text{ cm}^3$ ,  $L_{\text{Ethanol}} = 0.0034, 0.0033, 0.0032 \text{ mol min}^{-1}$ ,  $L_{\text{H}_2\text{O}} = 0, 0.0004, 0.0009 \text{ mol min}^{-1}$ ,  $G_{\text{N}_2} = 50 \text{ cm}^3 \text{ min}^{-1}$  at 225 °C.

**Figure 5.19** displays the retainment of catalytic activity after the three cycles independently from the conversion obtained, wherein catalyst longevity is linearly proportional to the concentration of water. Hence, only by employing the solution with a water concentration of 6.2 mol L<sup>-1</sup> can the full catalytic active sites be retained after recycling, and it suggests any further increases in water will have no beneficial impact on active phase stability but would likely result in further decreases in ethanol conversion from increased competitive absorption.

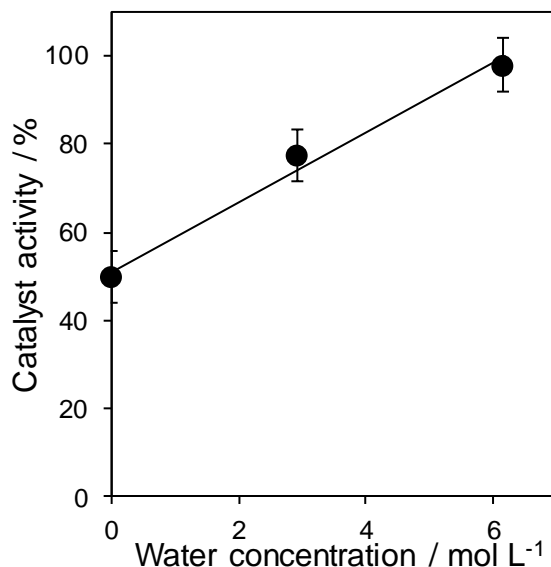


**Figure 5.19** – Influence of water content on the retainment of catalyst activity after three consecutive cycles. Reaction conditions: 50 mg catalyst,  $V_{\text{catalyst}} = 5 \text{ cm}^3$ ,  $L_{\text{Ethanol}} = 0.0034, 0.0033, 0.0032 \text{ mol min}^{-1}$ ,  $L_{\text{H}_2\text{O}} = 0, 0.0004, 0.0009 \text{ mol min}^{-1}$ ,  $G_{\text{N}_2} = 50 \text{ cm}^3 \text{ min}^{-1}$  at 225 °C.

### 5.2.2.3 Supported HPW: the influence of temperature

The influence of temperature on selectivity and catalyst deactivation was investigated carrying out the reaction with HPW/SBA-15, using the 38.2 wt% W loading as it exhibits the highest conversion of ethanol at 225 °C, due to its optimal balance between dispersion (STEM), particle size (XRD) and degree of crystalline water (TGA).

The resulting selectivity, determined for conversion values between 50-95 %, are reported in **Figure 5.20**, with each the average over the first 30 mins of reaction. We observed that ethylene selectivity is proportional to reaction temperature, at the expense of DEE, which is in agreement with previous studies [2, 16, 18, 19, 31]. DEE selectivity dramatically decreased to 20%, from an initial value of 70%, as temperature rises from 225 °C to 275 °C, with ethylene selectivity rising to 60% from an initial 16%. As temperatures increases further the selectivity plateaus, at values of 70% for ethylene and DEE at 15 %. The unaccounted remaining products comprise carbonaceous species; CO<sub>2</sub> and butylene isomers, which were observed in the GC/GCMS but only present in trace amounts, and ethoxy groups strongly chemisorbed to the Brønsted acid

sites, which are formed instantaneously on the catalyst surface, with their density inversely dependent on temperature [10].

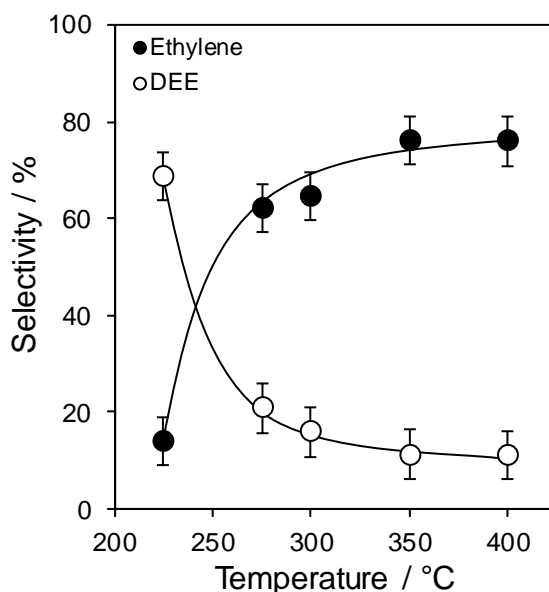


**Figure 5.20** – Influence of temperature on selectivity toward ethylene and diethyl ether, for 38.2 wt% of bulk W loaded on SBA-15. Reaction conditions: 50 mg catalyst,  $V_{\text{catalyst}} = 5 \text{ cm}^3$ ,  $L_{\text{Ethanol}} = 0.0034 \text{ mol min}^{-1}$ ,  $G_{\text{N}_2} = 50 \text{ cm}^3 \text{ min}^{-1}$  at 225, 275, 300, 350 and 400 °C.

The overall reaction mechanism in ethanol dehydration is one of contention and an area still under investigation [39]. From literature, in addition to the main products, acetaldehyde [9, 15, 40], short-chain hydrocarbon, as butylenes [41] and light gases [42], are also formed depending on the catalyst used. The degree of formation of these side products is typically very low, and therefore the overall mechanism commonly only considers the main two products, which can be obtained via parallel reactions [43], a series of sequential reactions, or both as an interconnected framework [5, 44]. Saito et al. [1] suggested that on heteropolyacids ethylene formation occurs via unimolecular decomposition of chemisorbed ethanol species while diethyl ether is obtained via condensation between a chemisorbed protonated species and physisorbed ethanol molecule. Takahara et al. [11] studied the catalytic activity of zeolites and silica-alumina with different % of Brønsted acid sites on ethanol dehydration, suggesting that strong Brønsted solid acid are responsible of the formation of ethylene. Varisli et al. [19] studied the reaction employing unsupported HPW, HSiW and HPMo, reporting results that are in agreement with those present herein, and put forward a mechanism that proceeds via parallel reactions, which is applied to the subsequent discussion.

In parallel to the critical role that temperature impacts on reaction selectivity, it simultaneously leads to a diminishing loss in ethanol conversion with time on stream and

increasing discrepancies in mass balances. The effect of temperature on conversion is reported in **Figure 5.21**, where ethanol dehydration catalytic tests were carried out within the range of 225-400 °C. For reaction temperature  $\leq 300$  °C, conversion values are constant, with only a modest  $\sim 5\%$  decrease drop over a 4 h reaction period, and optimal conversion levels are observed and 275 and 300 °C. As reaction temperature is increased to 350 °C and then further to 400 °C a dramatic drop in conversion with time on stream is observed, being indicative of catalyst deactivation.

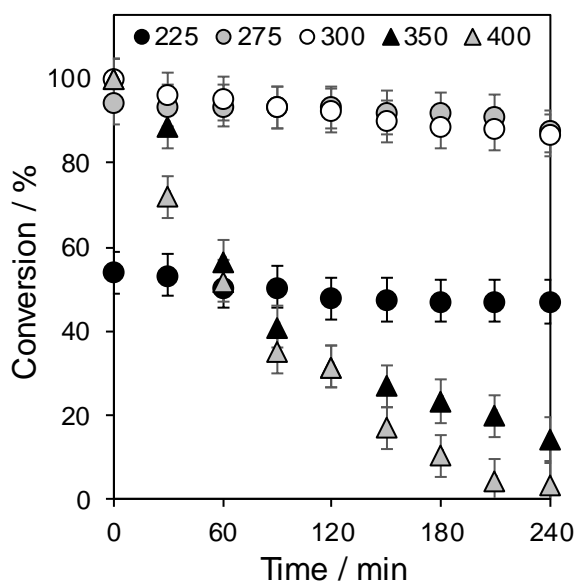


**Figure 5.21** – Influence of temperature on ethanol conversion for 38.2 wt% of bulk W loaded on SBA-15. Reaction conditions: 50 mg catalyst,  $V_{\text{catalyst}} = 5 \text{ cm}^3$ ,  $L_{\text{Ethanol}} = 0.0034 \text{ mol min}^{-1}$ ,  $G_{\text{N}_2} = 50 \text{ cm}^3 \text{ min}^{-1}$  at 225, 275, 300, 350 and 400 °C.

In **Figure 5.22**, space time yields of diethyl ether and ethylene are reported as a function of time. Interestingly, the plot reveals that of the two major products only ethylene is affected by the observed catalyst deactivation, displaying a significant decrease over the four hours of reaction for all the temperatures used, except for 225 °C, whereas the space time yield for DEE is influenced solely by temperature and not time, that is it remains reasonably constant of the duration of the reaction.

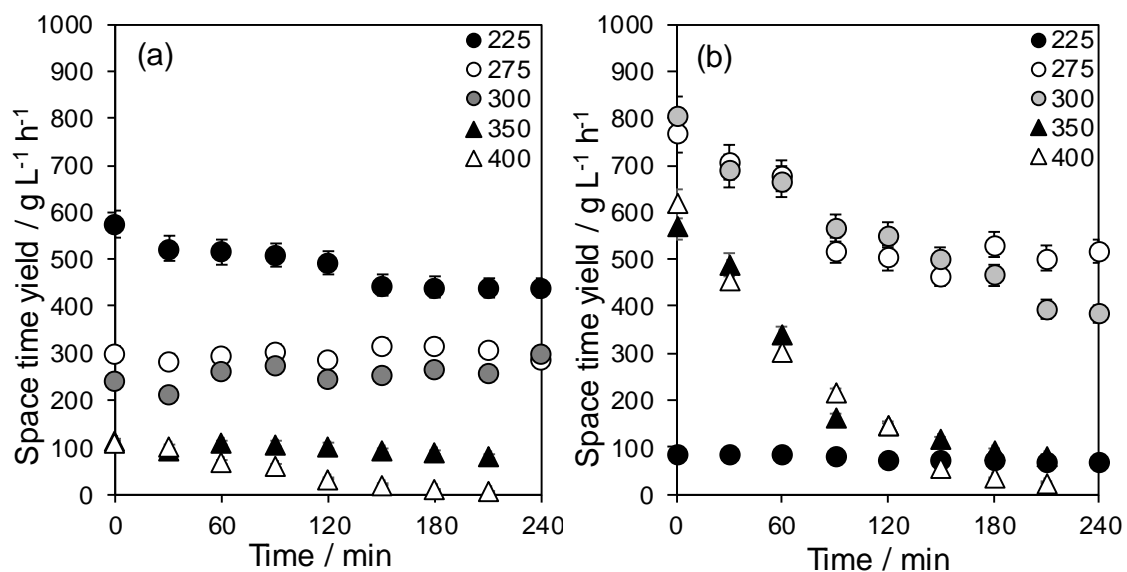


**Figure 5.22** – Temperature influence on ethylene and DEE space time yields employing 50 mg 38.2 wt% HPW/SBA-15 as function of time: diethyl ether space time yield (a) and ethylene space time yield (b). Reaction conditions: 50 mg catalyst,  $V_{\text{catalyst}} = 5 \text{ cm}^3$ ,  $L_{\text{Ethanol}} = 0.0034 \text{ mol min}^{-1}$ ,  $G_{\text{N}_2} = 50 \text{ cm}^3 \text{ min}^{-1}$  at 225, 275, 300, 350 and 400 °C.

In order to shed insight into the catalyst life time during the dehydration of ethanol, gradients of reaction rate vs time were calculated and plotted as function of temperature. Ethanol reaction rate normalised for amount of W over time at different temperatures, are reported in **Figure 5.23**-(a), while deactivation rate data are reported in **Figure 5.23**-(b), revealing a strong dependency to temperature. For reactions carried out at  $T \leq 300$  °C the dehydration activity reduces only slightly  $\sim 1000 \text{ mmol h}^{-1}$  (in the order of 10% of the initial value) after 1 h of reaction, while for higher temperatures, at 350 and 400 °C, the activity is almost halved.

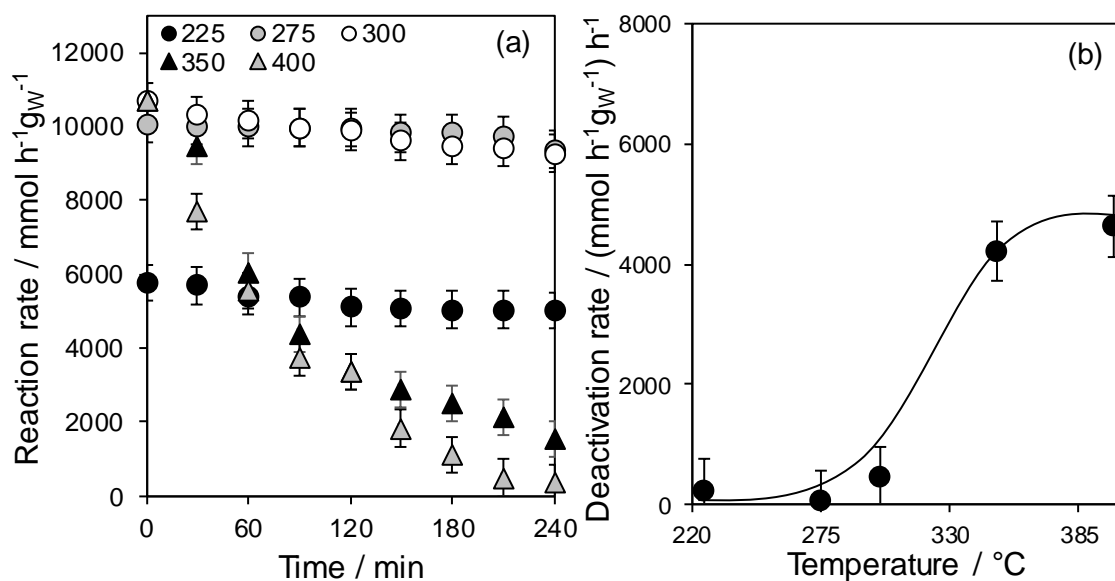


**Figure 5.23** – Influence of temperature on ethanol activity (a), and catalyst deactivation rate (b). Reaction conditions: 50 mg catalyst,  $V_{\text{catalyst}} = 5 \text{ cm}^3$ ,  $L_{\text{Ethanol}} = 0.0034 \text{ mol min}^{-1}$ ,  $G_{\text{N}_2} = 50 \text{ cm}^3 \text{ min}^{-1}$  at 225, 275, 300, 350 and 400 °C.

Upon completion of 4 hour on stream, at 350 and 400 °C, it was observed that the catalyst displayed significant colour change, from pure white for the fresh material to black. From previous literature studies this can be attributed to either thermal decomposition of the active species, also observed post TGA analysis, or deposition of heavy organic, often aromatic compounds, or a combination of the two. Aromatics are suggested being formed via cyclo-polymerisation of adsorbed ethylene on strong acid sites, as reported in the literature when employing HZMS-5 zeolite at 400 °C [39, 41]. Formation of heavy compounds is also related to a drop with time onstream of ethylene space time yields and losses in mass balance which increase with temperature, being at 350 °C of only 75%, and at 400 °C of 60%.

CHNS analysis accompanied with temperature programmed oxidation analysis (TPO) were utilised to evaluate the level of carbon deposition and to deduce different possible carbon species that have been deposited on the catalyst surface.

The C wt% results measured via CHNS on spent catalyst are shown in **Figure 5.24**-(a), which reveals an exponential correlation between carbonaceous species formed on the surface and reaction temperature, suggesting that at elevated temperatures (at 350 °C and above), the heat can initiate ethylene chain growth/or aromatisation reaction. Mass normalised  $\text{CO}_2$  desorption profiles are reported in **Figure 5.24**-(b), and correlate strongly with CHNS analysis, mirroring the increase of carbonaceous species with the increase of  $\text{CO}_2$  desorption peaks intensity. The two major peaks, at 485 and 530 °C,

are attributed to high aliphatic oligomers and polyaromatics respectively, referred to as also hard coke [45]. The shoulder observed at 380 °C, for spent catalysts at 350 and 400 °C, is associated to lower molecular weight ethylene oligomers.

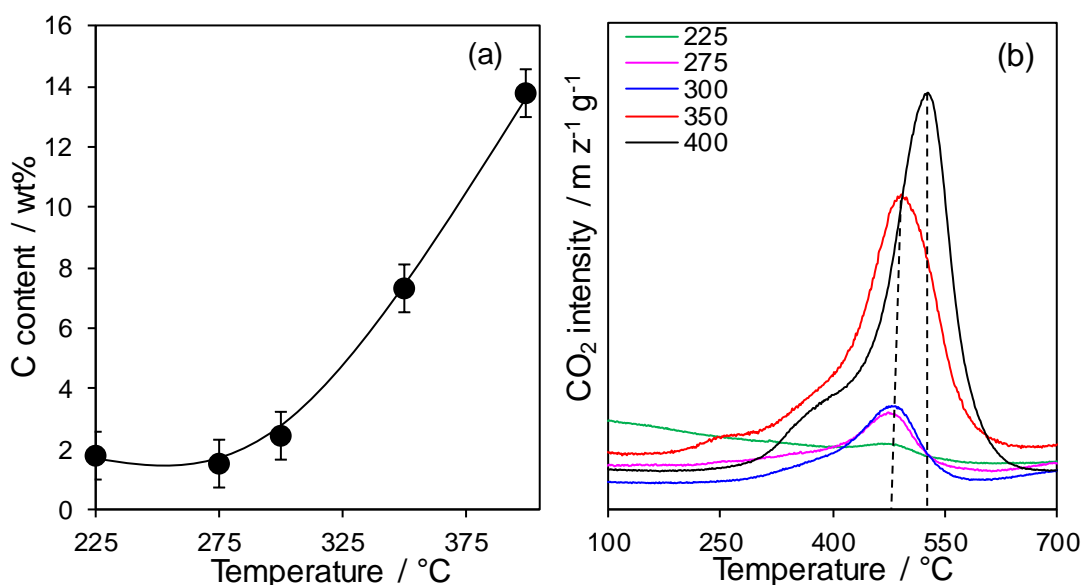


**Figure 5.24** – CHNS elemental analysis (a) and TPO (b) obtained on spent catalyst (38.2 wt% HPW/SBA-15) at different reaction temperatures. Reaction conditions: 50 mg catalyst,  $V_{\text{catalyst}} = 5 \text{ cm}^3$ ,  $L_{\text{Ethanol}} = 0.0034 \text{ mol min}^{-1}$ ,  $G_{\text{N}_2} = 50 \text{ cm}^3 \text{ min}^{-1}$ .

To further investigate the catalyst's deactivation process, wide angle XRD was conducted on the spent 38.2 wt% HPW/SBA-15 catalysts for the different reaction temperatures (**Figure 5.25-(a)**). XRD pattern of each catalyst displayed diffraction peaks related to HPW and  $\text{WO}_3$ , which represent the active and deactivated phase of the catalytic material, respectively. Furthermore, information on the dominant crystalline phases, HPW or  $\text{WO}_3$ , were determined for each sample (see **Figure 5.25-(b)**).

As expected, HPW is the dominant phase in the fresh catalyst (97%); after reaction at 225 and 275 °C, 76% of HPW crystalline phase is still present, whilst characteristic  $\text{WO}_3$  diffraction peaks rise. Increasing the reaction temperature, further results into a flip of the dominant phase, with  $\text{WO}_3$  present at 56.4 % and 72.4 % for 350 and 400 °C respectively. The preservation, albeit partial, of the HPW phase, even at the upper most temperature, explains the activity for the 38.2 wt% HPW on SBA-15 across all temperature studied. These observation being consistent with the thermal decomposition of the HPW structure, due to the loss of structural oxygen atoms, as water molecules, which initiates at ~300 °C (as shown in TGA analysis, **Chapter 3, Figure 3.12**) with the break-down of the W-O<sub>b</sub>-W chemical bond (as shown in DRIFT analysis, **Chapter 3, Figure 3.23**), which has also been reported in the literature [22].

To confirm the inactivity of  $\text{WO}_3$  towards ethanol dehydration, in particular at the highest temperatures, ethanol dehydration was screened at 400 °C, employing 100 mg of commercial  $\text{WO}_3$ , revealing 4.8% of ethanol conversion, which was comparable with the non-catalytic ethanol conversion measured at 350 °C (5.7%).

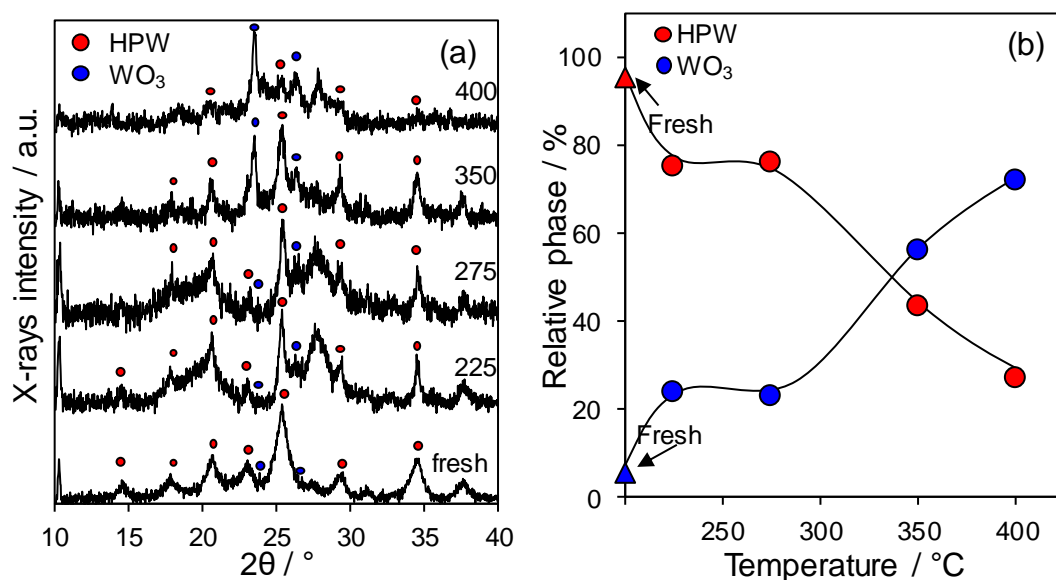


**Figure 5.25** – XRD pattern of fresh and spent catalyst at different reaction temperatures (a); HPW and  $\text{WO}_3$  phase % calculated for each catalyst.

The catalyst's recyclability studied proved that water is important to maintain the hydration and thus stability of HPA Keggin structure. Furthermore, water is reported to have also the ability to diminish catalyst deactivation due to coke deposition. Kozhevnikov et al [45] studied the effect of water on coke formation over HPAs, revealing that adding water to the reactant stream decreases the rate of coke formation during propene polymerisation, suggesting that water and other polar solvents facilitate the desorption of coke precursors from the catalyst, thus, preventing its formation. In addition, Rossetti et al. [13] found that also on BEA-based catalyst, water helps limiting the coke, in the detriment of ethanol conversion.

To further investigate on the role of water in the catalytic system, ethanol dehydration reaction was carried out at 350 and 400 °C, employing 50 mg of the sample 38.2 wt% of the HPW/SBA-15 series as catalyst, using the solution 6.2 mol L<sup>-1</sup>, 10% (vol / vol), of water in ethanol, as this previously proved to lead to the best performances in term of HPW stability. As reported in **Figure 5.26**, ethanol conversion decreased in the presence of water, which competes with the alcohol for the adsorption on the surface. Conversion, dropped from 95% to 56% and 65% for reaction carried out at 350 and 400 °C, respectively. During the reaction, ethanol conversion does not remain constant but decreases, although to a lesser extent as evidenced by the smaller gradient compared

to previous experiments, hence the deactivation effect is reduced. Space time yields for diethyl ether are constant, while, as observed previously, ethylene values gradually decrease throughout the reaction time.

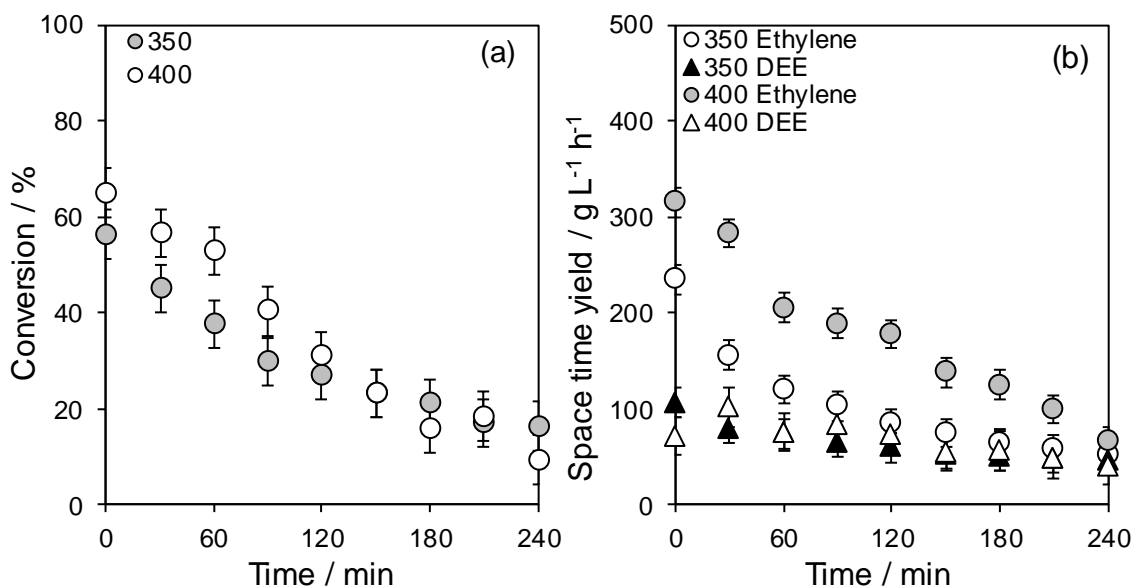


**Figure 5.26** – Ethanol dehydration carried out with water as co-feed, using 38.2 wt% of HPW/SBA-15 as catalyst; ethanol conversion (a), and space time yields of ethylene and DEE (b). Reaction conditions: 50 mg catalyst,  $V_{\text{catalyst}} = 5 \text{ cm}^3$ ,  $L_{\text{Ethanol}} = 0.0034 \text{ mol min}^{-1}$ ,  $G_{\text{N}_2} = 50 \text{ cm}^3 \text{ min}^{-1}$  at 350 and 400 °C.

The new values of deactivation in rates carrying out the reaction at 350 and 400 °C, are reported in **Figure 5.27**, showing that important improvements were achieved through introducing water into the feed. The extent of deactivation was reduced by 55% compared to previous calculation at 350 °C, 1895 ( $\text{mmol h}^{-1} \text{ g}^{-1}$ )  $\text{h}^{-1}$ , whereas at 400 °C, the deactivation, 2466 ( $\text{mmol h}^{-1} \text{ g}^{-1}$ )  $\text{h}^{-1}$ , is 46% smaller compared to the experiment carried out using an anhydrous ethanol stream. Further proving the critical role that water plays on maintaining the HPW structure hydrated and active.

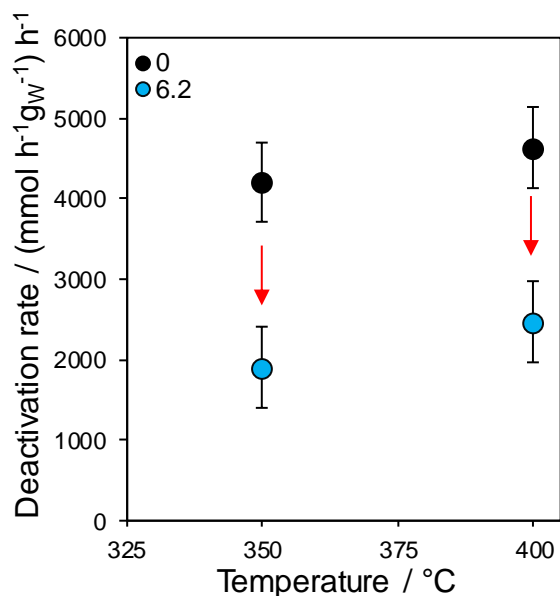


**Figure 5.27** – Catalyst deactivation rate employing a solution 6.2 M of water in ethanol (10% vol/vol). Reaction conditions: 50 mg catalyst,  $V_{\text{catalyst}} = 5 \text{ cm}^3$ ,  $L_{\text{Ethanol}} = 0.0034 \text{ mol min}^{-1}$ ,  $G_{\text{N}_2} = 50 \text{ cm}^3 \text{ min}^{-1}$  at 350 and 400 °C.

The apparent activation energy of ethanol dehydration (in anhydrous conditions) for supported HPW was calculated using the Arrhenius equation [23], shown in **Figure 5.28**. The temperatures studied were decreased from 225-400 °C to 150-275 °C to reduce deactivation of the HPW structure arising from thermal decomposition. A calculated activation energy of 46 kJ mol<sup>-1</sup> for the 9.0 wt% HPW/SBA-15 catalyst concurs with previous values obtained for unsupported HPW (27 kJ mol<sup>-1</sup>), and also agrees with the literature value [16].

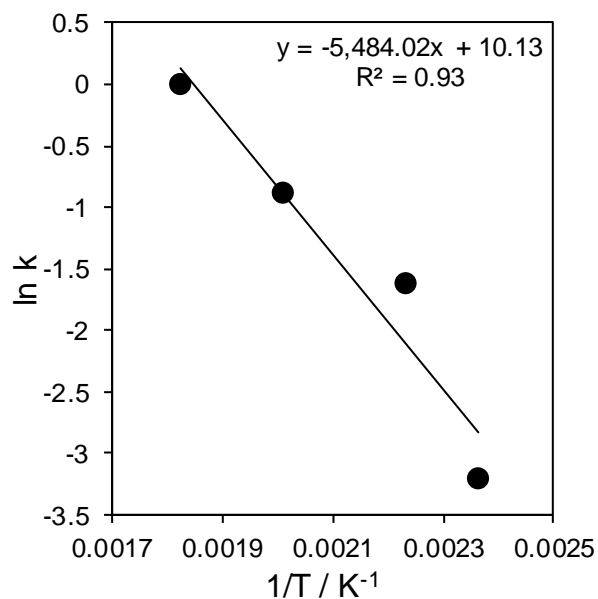


**Figure 5.28** – Arrhenius  $E_a$  for ethanol dehydration reaction over W loading 9.0 wt% on SBA-15. Reaction conditions: 100 mg catalyst,  $V_{\text{catalyst}} = 5 \text{ cm}^3$ ,  $L_{\text{Ethanol}} = 0.0034 \text{ mol min}^{-1}$ ,  $G_{\text{N}_2} = 50 \text{ cm}^3 \text{ min}^{-1}$  at 150, 175, 225 and 275 °C

#### 5.2.2.4 Supported HSiW and HPMo

The influence of the nature of supported heteropolyacid on the ethanol dehydration reaction was evaluated at 225 °C, employing common loadings of HSiW, 30.9 wt%, and HPMo, 32,3 wt%, on SBA-15 with the results compared to the ones obtained for 38.2 wt% of HPW/SBA-15. The metal loading at approximately 35 wt% was chosen as they display optimal dispersion of small HSiW and HPMo nano clusters, of ~ 4-8 K.U. akin to the HPW system. **Figure 5.29** reports the ethanol conversion, and ethylene space time yields as function of time. Data referred to diethyl ether are in **Appendix B-Figure 10**.

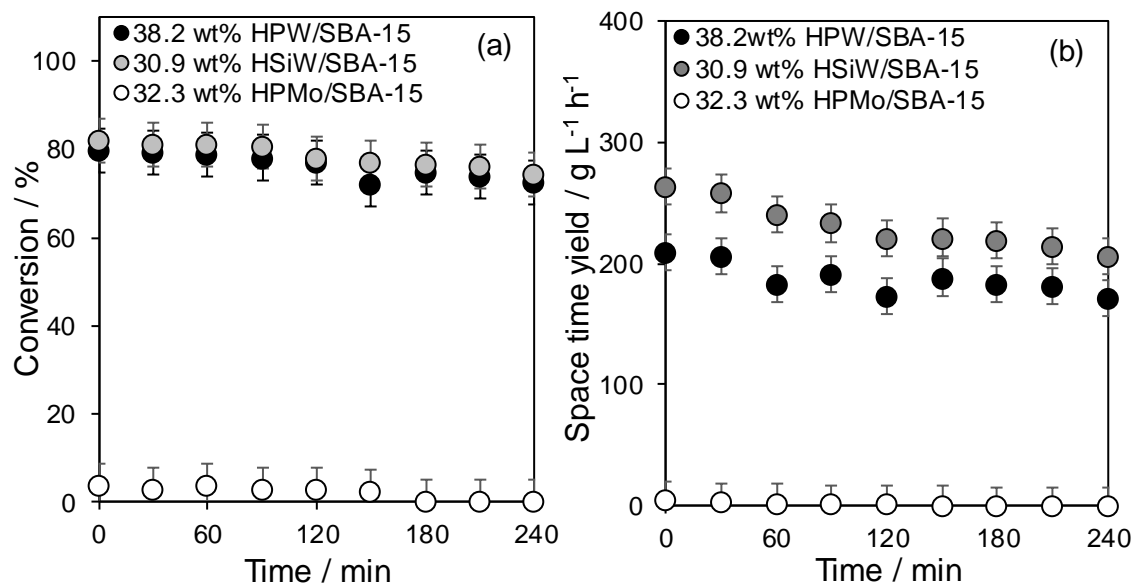


**Figure 5.29** – Ethanol dehydration kinetic parameters attained at 225 °C, employing SBA-15 supported HPAs as function of time: conversion (a) and ethylene space time yield (b). Reaction conditions: 100 mg catalyst,  $V_{\text{catalyst}} = 5 \text{ cm}^3$ ,  $L_{\text{Ethanol}} = 0.0034 \text{ mol min}^{-1}$ ,  $G_{\text{N}_2} = 50 \text{ cm}^3 \text{ min}^{-1}$  at 225 °C.

Interestingly, the supported species exhibited better results compared to the bulk HPW, HSiW and HPMo, with W-based materials, phosphotungstic and silicotungstic acid, showed greater performances compared to the Mo-based catalyst. Ethanol conversions are steady during the 4 hours of reaction, reaching 80% for both HPW and HSiW, while only 5% for HPMo. Constant values as function time were also recorded for ethylene and diethyl ether space time yields, revealing that HSiW has the highest activity toward the unsaturated hydrocarbon.

**Figure 5.30** displays the dependence of ethylene selectivity and TOF as function of acid strength, as reported previously for unsupported HPAs. W-based materials (HPW and HSiW) possess similar selectivity (~25%) and similar turnover frequencies, while for HPMo/SBA-15 ethylene selectivity is halved and TOF dropped by two orders of magnitude compared to its counterparts. Remarkably, comparing results with the unsupported system: HPW on SBA-15 behaves just like the bulk with equal values of both TOF and ethylene selectivity; whereas SBA-15 supported HSiW is greatly enhance with ethylene selectivity more than doubled (from 11% to 26%) and TOFs elevated by an order of magnitude from 330 to 2500 h<sup>-1</sup>. Likewise, HPMo when supported, exhibits higher performances with ethylene selectivity growing from 1% to 7% and TOFs from 120 to 285 h<sup>-1</sup>. Through comparison of the W-based and Mo-based heteropolyacid materials, it is clear that acid strength plays a crucial role in selectivity and activity; whilst comparison of the W-based materials, which possess similar acid strength, the slight

improvement in performance of the HSiW could result from the different amounts of crystalline water, being 4.1 % for HPW/SBA-15 against 5.8% for HSiW/SBA-15.

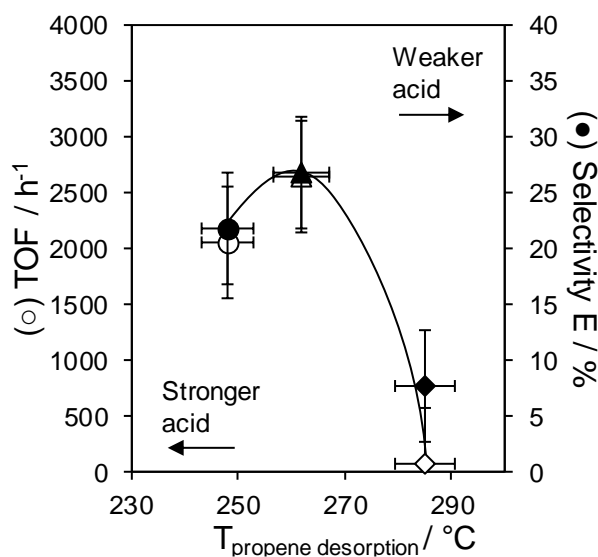


**Figure 5.30** – Ethylene selectivity and TOFs dependence on acid strength of SBA-15 supported heteropolyacid, 38.2 wt% HPW/SBA-15 (●), 30.9 wt% HSiW/SBA-15 (▲) and 32.3 wt% HPMo/SBA-15 (◆). Reaction conditions: 100 mg catalyst,  $V_{\text{catalyst}} = 5 \text{ cm}^3$ ,  $L_{\text{Ethanol}} = 0.0034 \text{ mol min}^{-1}$ ,  $G_{\text{N}_2} = 50 \text{ cm}^3 \text{ min}^{-1}$  at 225 °C.

### 5.3 Conclusions

Ethanol dehydration reactions were initially investigated over unsupported HPAs, proving that the most active and selective catalysts towards ethylene is HPW which is the most thermally stable materials and the strongest acid, as concluded in **Chapter 3**.

Supported HPW on silica based materials, as fumed silica or SBA-15, exhibit greater ethanol conversion but impart no effect on ethylene selectivity. Support architecture influences the degree of HPW aggregation and therefore the amount of crystalline water, which together effect catalyst activity and TOF.

High recyclability of supported HPW is only feasible if the HPW structure remain hydrated after each cycle, which can be achieved by co-feeding water in the ethanol stream which also inhibits coke formation.

For HPAs on SBA-15, as witnessed for the unsupported equivalent materials, selectivity and TOFs are highly influenced by the type of the heteropolyacid involved, with both

HSiW and HPW on SBA-15 behave similarly whilst HPMo/SBA-15 exhibits considerable lowest performance due to its weak acid strength.

## 5.4 References

- [1] Y. Saito, H. Niiyama, *Journal of Catalysis* 106 (1987) 329-336.
- [2] T.K. Phung, G. Busca, *Chemical Engineering Journal* 272 (2015) 92-101.
- [3] A. Popa, V. Sasca, *Reaction Kinetics, Mechanisms and Catalysis* (2017) 1-16.
- [4] J.F. DeWilde, H. Chiang, D.A. Hickman, C.R. Ho, A. Bhan, *ACS Catalysis* 3 (2013) 798-807.
- [5] C.B. Phillips, R. Datta, *Industrial & engineering chemistry research* 36 (1997) 4466-4475.
- [6] M. Kang, J.F. DeWilde, A. Bhan, *ACS Catalysis* 5 (2015) 602-612.
- [7] S. Roy, G. Mpourmpakis, D.-Y. Hong, D.G. Vlachos, A. Bhan, R.J. Gorte, *ACS Catalysis* 2 (2012) 1846-1853.
- [8] T. Okuhara, T. Arai, T. Ichiki, K.Y. Lee, M. Misono, *Journal of Molecular Catalysis* 55 (1989) 293-301.
- [9] Z. Fang, Y. Wang, D.A. Dixon, *The Journal of Physical Chemistry C* 119 (2015) 23413-23421.
- [10] M.E. Potter, S. Van Aswegen, E. Gibson, I.P. Silverwood, R. Raja, *Physical Chemistry Chemical Physics* (2016).
- [11] I. Takahara, M. Saito, M. Inaba, K. Murata, *Catalysis Letters* 105 (2005) 249-252.
- [12] A. Galadima, O. Muraza, *Journal of Industrial and Engineering Chemistry* 31 (2015) 1-14.
- [13] I. Rossetti, M. Compagnoni, E. Finocchio, G. Ramis, A. Di Michele, Y. Millot, S. Dzwigaj, *Applied Catalysis B: Environmental* 210 (2017) 407-420.
- [14] J. Bedia, R. Barrionuevo, J. Rodríguez-Mirasol, T. Cordero, *Applied Catalysis B: Environmental* 103 (2011) 302-310.
- [15] T.K. Phung, L. Proietti Hernández, G. Busca, *Applied Catalysis A: General* 489 (2015) 180-187.
- [16] V.V. Bokade, G.D. Yadav, *Applied Clay Science* 53 (2011) 263-271.
- [17] A. Popa, V. Sasca, O. Verdes, I. Holclajtner-Antunović, *Reaction Kinetics, Mechanisms and Catalysis* 115 (2015) 355-375.
- [18] A. Ciftci, D. Varisli, K. Cem Tokay, N. Aslı Sezgi, T. Dogu, *Chemical Engineering Journal* 207-208 (2012) 85-93.

- [19] D. Varisli, T. Dogu, G. Dogu, *Chemical Engineering Science* 62 (2007) 5349-5352.
- [20] W. Trakarnpruk, *Mendeleev Communications* 23 (2013) 168-170.
- [21] C.H. Bartholomew, *Applied Catalysis A: General* 212 (2001) 17-60.
- [22] M.J. Janik, B.B. Bardin, R.J. Davis, M. Neurock, *The Journal of Physical Chemistry B* 110 (2006) 4170-4178.
- [23] P. Atkins, J. De Paula, *Elements of physical chemistry*, Oxford University Press, USA, 2013.
- [24] M.N. Timofeeva, *Applied Catalysis A: General* 256 (2003) 19-35.
- [25] Y. Izumi, R. Hasebe, K. Urabe, *Journal of Catalysis* 84 (1983) 402-409.
- [26] B.B. Bardin, S.V. Bordawekar, M. Neurock, R.J. Davis, *The Journal of Physical Chemistry B* 102 (1998) 10817-10825.
- [27] J. Highfield, J. Moffat, *Journal of Catalysis* 88 (1984) 177-187.
- [28] S. Ganapathy, M. Fournier, J.F. Paul, L. Delevoye, M. Guelton, J.P. Amoureux, *Journal of the American Chemical Society* 124 (2002) 7821-7828.
- [29] L. Pesaresi, D.R. Brown, A.F. Lee, J.M. Montero, H. Williams, K. Wilson, *Applied Catalysis A: General* 360 (2009) 50-58.
- [30] I.V. Kozhevnikov, *Chemical Reviews* 98 (1998) 171-198.
- [31] J. Haber, K. Pamin, L. Matachowski, D. Mucha, *Applied Catalysis A: General* 256 (2003) 141-152.
- [32] K. Pamin, A. Kubacka, Z. Olejniczak, J. Haber, B. Sulikowski, *Applied Catalysis A: General* 194–195 (2000) 137-146.
- [33] A. Bielański, A. Lubańska, *Journal of Molecular Catalysis A: Chemical* 224 (2004) 179-187.
- [34] M. Misono, *Chemical communications* (2001) 1141-1152.
- [35] M.J. Janik, K.A. Campbell, B.B. Bardin, R.J. Davis, M. Neurock, *Applied Catalysis A: General* 256 (2003) 51-68.
- [36] F. Motonobu, S. Kanji, M. Makoto, Y. Yukio, *Chemistry Letters* 8 (1979) 31-34.
- [37] A. Micek-Ilnicka, *Journal of Molecular Catalysis A: Chemical* 308 (2009) 1-14.
- [38] R.C. Costa, J.R. Sodr e, *Fuel* 89 (2010) 287-293.
- [39] M. Zhang, Y. Yu, *Industrial & Engineering Chemistry Research* 52 (2013) 9505-9514.
- [40] M. D m k, M. T th, J. Rask , A. Erd helyi, *Applied Catalysis B: Environmental* 69 (2007) 262-272.

- [41] Z.S.B. Sousa, C.O. Veloso, C.A. Henriques, V. Teixeira da Silva, *Journal of Molecular Catalysis A: Chemical* 422 (2016) 266-274.
- [42] V.V. Galvita, G.L. Semin, V.D. Belyaev, V.A. Semikolenov, P. Tsiakaras, V.A. Sobyenin, *Applied Catalysis A: General* 220 (2001) 123-127.
- [43] W.S. Brey, K. Krieger, *Journal of the American Chemical Society* 71 (1949) 3637-3641.
- [44] K. Alexopoulos, M. John, K. Van der Borght, V. Galvita, M.-F. Reyniers, G.B. Marin, *Journal of Catalysis* 339 (2016) 173-185.
- [45] I.V. Kozhevnikov, S. Holmes, M. Siddiqui, *Applied Catalysis A: General* 214 (2001) 47-58.

# **Chapter 6**

## ***Conclusions***

## 6.1 Conclusions

The aim of this project was to investigate the chemistry of supported HPAs, focusing on the two supports; high surface area mesoporous SBA-15 and commercial low surface area fumed silica, and three different HPA; HPW, HSiW and HPMo, and evaluated for their catalytic potential relative to their bulk equivalents for  $\alpha$ -pinene isomerisation and ethanol dehydration.

### 6.1.1 Effect of type of support

The role of support surface area, elucidated by employing a high surface area mesoporous silica (SBA-15) to compare to a commercial lower surface area silica, was shown to have a positive influence on dispersion of the HPAs (see **Figure 6.1**). On fumed silica, HPAs agglomeration occurs to a significantly greater extent, leading to the formation of large 3-dimensional structures, as detected by XRD and STEM, which in turn result in a higher degree of crystalline water evaluated by TGA analysis. In contrast, on SBA-15, HPAs form isolated sites, at lower loadings, and 2-dimensional rafts as loading increases, as observed by STEM, and, as a consequence, exhibits significantly reduced levels of crystalline water across the series relative to the fumed silica counterparts. The superior HPAs dispersion witnessed for the SBA-15 series resulted in the desirable elevation of accessible acid density, confirmed through TPD studies utilising n-propylamine and ammonia, which further highlighted that the acid strength of the bulk HPA was retained after impregnation for both supports.

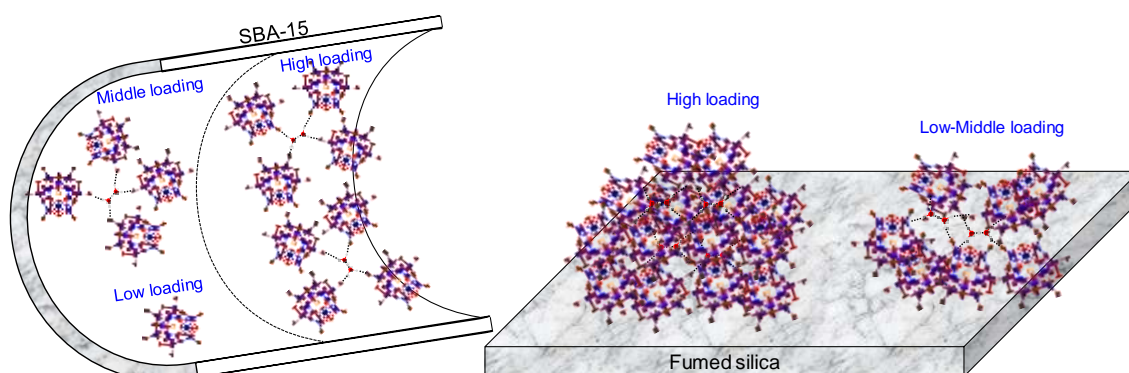


**Figure 6.1** – Dependence of Keggin units dispersion and/or agglomeration on loading and support architecture for HPW/SBA-15 series (left) and HPW/fumed silica series (right).

The catalytic activity of the two series towards the low temperature solventless  $\alpha$ -pinene isomerisation, a surface reaction wherein the rate is highly dependent on catalyst surface area and thus active sites accessibility [1], is shown in **Figure 6.2-(a)**. The optimal TOFs

were observed for the lower loadings of HPAs on SBA-15, due to their highly dispersed nature. Upon formation of larger 3D HPAs agglomerates, as seen across all loadings on fumed silica and at the highest loadings for SBA-15, TOFs dropped dramatically due to a high majority of protons being localised within the bulk HPA architecture, and thus are inaccessible to the apolar substrate. In contrast, the gas-phase dehydration of ethanol is a bulk-like reaction, wherein the small polar alcohol is able to diffuse within the HPAs clusters and react with the inner protons; therefore, high surface areas with externally accessible protons do not govern optimal catalytic performances. It was observed that the degree of crystalline water trapped between K.U. was the controlling factor on catalytic performance as revealed in **Figure 6.2**-(b). This governed both stability and activity, with it serving as a diffusion media and reservoir for ethanol molecules whilst simultaneously maintaining the HPAs structure hydrated, and therefore intact (as previously reported in the literature [2]). Therefore, supports and HPA loadings that enhance agglomeration, leads to higher TOFs for ethanol dehydration whereas supports and loading induce high dispersion are favourable for  $\alpha$ -pinene isomerisation.

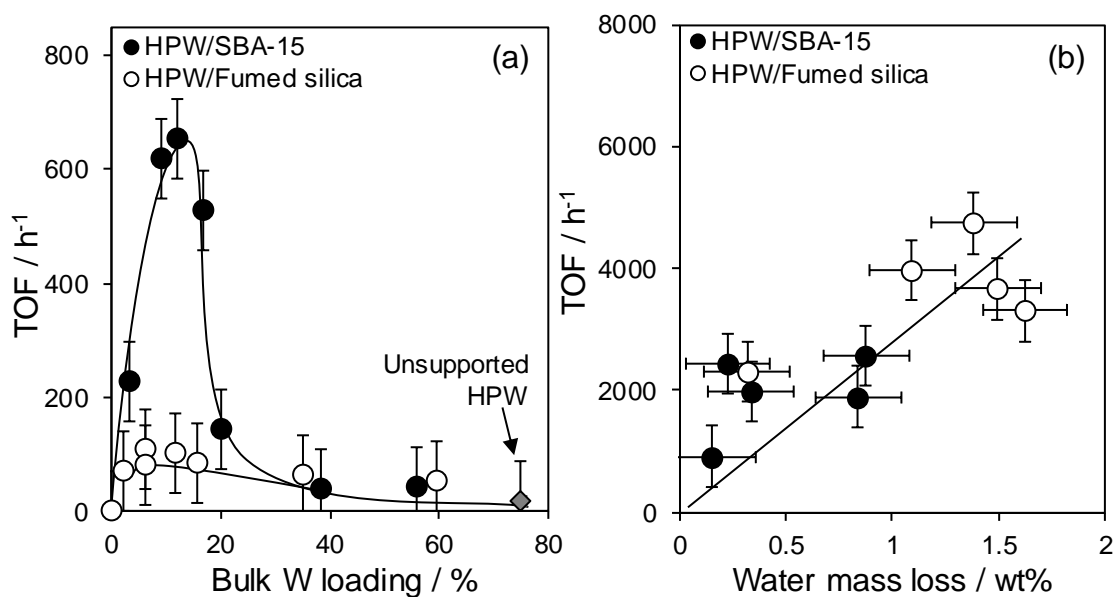


**Figure 6.2** – (a) TOFs for  $\alpha$ -pinene isomerisation reaction as a function of bulk W loadings and (b) ethanol dehydration TOFs as a function of water mass loss (trapped crystalline water).

### 6.1.2 Effect of HPA type

Three varieties of heteropolyacids; phosphotungstic acid (HPW), silicotungstic acid (HSiW) and phosphomolibdic acid (HPMo) both supported and unsupported were investigated. Although, all three HPAs species possess the same Keggin structure, their

physiochemical properties differ, a common order of HPW>HSiW>HPMo for both thermal stability and acid strength was observed, whereas HPA dispersions are comparable for all three.

$\alpha$ -Pinene isomerisation exhibited a variation in products distribution, which is attributed solely to changes in acid strength. Polycyclic compounds, such as camphene, were formed to a greater extent when HPW was employed, as reported in **Figure 6.3**-(a), being indicative that this pathway is favoured over strong Brønsted acid sites. Likewise, higher TOFs were also observed for HPW, which again arises due to its greater acid strength. The dehydration of ethanol also displays products distribution and TOFs that are dependent to the type of HPAs used, as reported in **Figure 6.3**-(b). In contrast to  $\alpha$ -pinene isomerisation, comparable results, TOFs and selectivity towards ethylene, were observed for the two W-based compounds, HPW and HSiW, which both greatly exceeded HPMo performances.

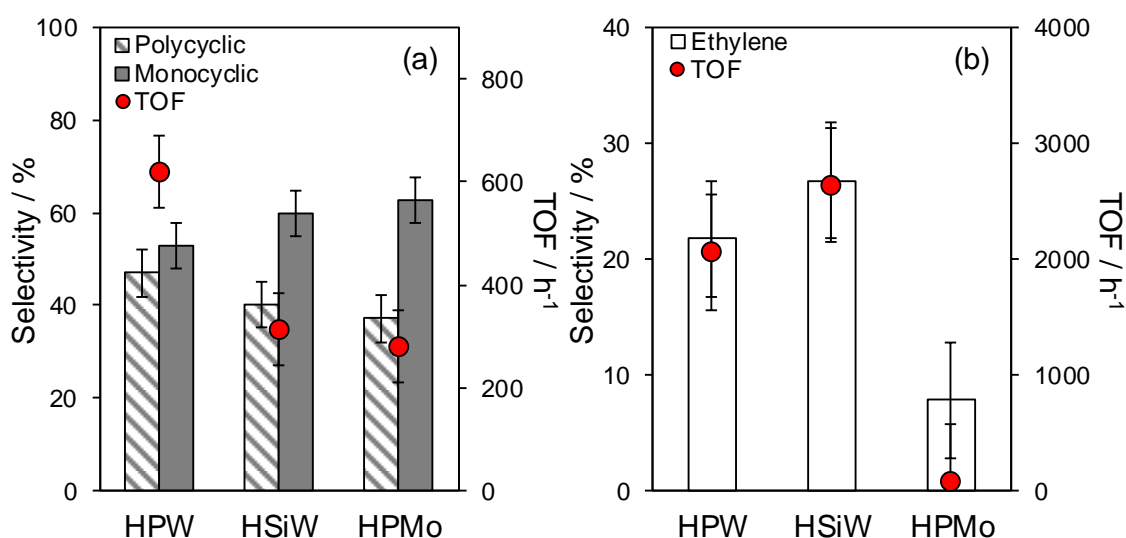


**Figure 6.3** – (a) Selectivity and TOFs for SBA-15 supported HPAs for  $\alpha$ -pinene isomerisation reaction over a common 9 wt% of W or Mo; and (b) ethanol dehydration TOFs and ethylene selectivity for 38 wt% of W, 31 wt% of W, and 32 wt% of Mo, of SBA-15 supported HPW, HSiW and HPMo respectively.

### 6.1.3 Cost analysis

Catalysts development at the bench and lab scale typically only considers catalysts optimisation, with little attention paid to the economic aspects of a large-scale production [3]. Herein, a brief study into the manufacturing costs to produce 1 kg of silica supported HPW has been carried out to evaluate the potential for their use in industrial production of bulk and fine chemicals. The prices for 500 g of HPW and fumed silica, and 1000 g of

commercial SBA-15 were taken from Sigma-Aldrich UK, whilst 2.5 L of methanol was from VWR Chemicals, with prices correct as of August 2017. The cost analysis of in-house synthesis of SBA-15 was evaluated using the optimal price from Sigma Aldrich.

Initial cost evaluations are made comparing commercial fumed silica and commercial SBA-15 against in-house synthesised SBA-15, and results are reported in **Table 6.1**. As would be expected, the non-porous fumed silica is the most economical support at only £ 137 per kg of solid material. In contrast, for the highly ordered high surface area mesoporous SBA-15s, both commercial and in-house produce, prices soar dramatically to between ~10-100 times higher than fumed silica. Unsurprisingly, the in-house synthesised SBA-15 is significantly more cost effective than the commercial one. The price reported for the in-house synthesised SBA-15 is based on a mass yield of 80 %.

**Table 6.1** – Costs evaluation for 1 kg of silica support.

	Price per kg / £ kg <sup>-1</sup>
Commercial Fumed silica	137
Commercial SBA-15	13548
Synthesised SBA-15*	1288

\*Based on 80% yield.

Catalyst cost evaluation was carried out on HPW supported on SBA-15 and fumed silica, calculating the cost of 1 kg of supported HPW on both siliceous materials, and normalising on the amount of product yield obtained after 6 h of reaction, i.e. camphene and ethylene, expressed in £ kg<sup>-1</sup>, see **Table 6.2**. The amount of substrate needed to produce 1 kg of product was also calculated, allowing the estimation of a total costs, although economical aspects regarding energy consumption for the catalyst preparation and reactions have not been included.

For  $\alpha$ -pinene isomerisation, as shown in **Table 6.2**, SBA-15 supported HPW materials are considerably more cost effective than both the unsupported species and deposited on fumed silica, with the higher cost of the SBA-15 catalysts more than offset by their superior catalytic performance resulting in lower total prices for camphene production. Within the SBA-15 series, the 9.0 wt% and the 13.0 wt% are the most active catalysts showing the highest TOFs and therefore possess the lowest total costs, with the 9.0 wt% being slightly more economic than the 13.0 wt%, with a difference of 55.2£ kg<sup>-1</sup>.

In the case of ethanol dehydration, the most economical catalysts for each series, 55.4 and 15.5 wt% for the SBA-15 and fumed silica families respectively, were compared to the unsupported HPW. The 15.5 wt% on fumed silica was the most active catalyst and

the most economical, with overall costs spanning 90.9 and 114.8 £ kg<sup>-1</sup>, following the order of 15.5 wt% HPW/fumed silica < Unsupported HPW < 55.4 wt% HPW/SBA-15.

This cost evaluation has further highlighted the advantage of supported HPA in both reactions, with SBA-15 superior in  $\alpha$ -pinene isomerisation whereas fumed silica is the preferred support choice in ethanol dehydration.

**Table 6.2** – Costs evaluation for 1 kg of supported HPW catalysts based on the amount of product formation.

Reaction / support	Bulk W loading /wt%	TOF / h <sup>-1</sup>	Cost for 1 kg of catalyst / £	<sup>a</sup> / mmol of product after 6 h	<sup>b</sup> / £ catalyst kg <sup>-1</sup> of product	Total cost / <sup>c</sup>
$\alpha$ -Pinene isomerisation / SBA-15	9.0	619.2	1263.5	14.7	63.0	2290.4
$\alpha$ -Pinene isomerisation / SBA-15	13.0	655.0	1232.6	14.3	62.9	2345.6
$\alpha$ -Pinene isomerisation / Fumed silica	59.6	50.7	408.4	4.4	67.4	7450.7
$\alpha$ -Pinene isomerisation / Unsupported	74.0	16.9	486	0.7	509.9	47456.3
Ethanol dehydration / SBA-15	55.4	1694	905.6	228.2	14.1	114.8
Ethanol dehydration / Fumed silica	15.5	4744	241.1	174.2	4.9	90.9
Ethanol dehydration / Unsupported	74.0	1125	486.0	194.1	8.9	108.2

<sup>a</sup>Attained using 100 mg of catalyst

<sup>b</sup>Cost of 1 kg of catalyst to obtain 1 kg of product

<sup>c</sup>Total cost to obtain 1 kg of product based on the cost of catalyst and substrate

## 6.2 References

- [1] M. Misono, Chemical communications (2001) 1141-1152.
- [2] A. Bielański, A. Lubańska, Journal of Molecular Catalysis A: Chemical 224 (2004) 179-187.
- [3] N. Pernicone, Catalysis Today 34 (1997) 535-547.

# ***Appendices***

## Appendix A – $\alpha$ -Pinene isomerisation

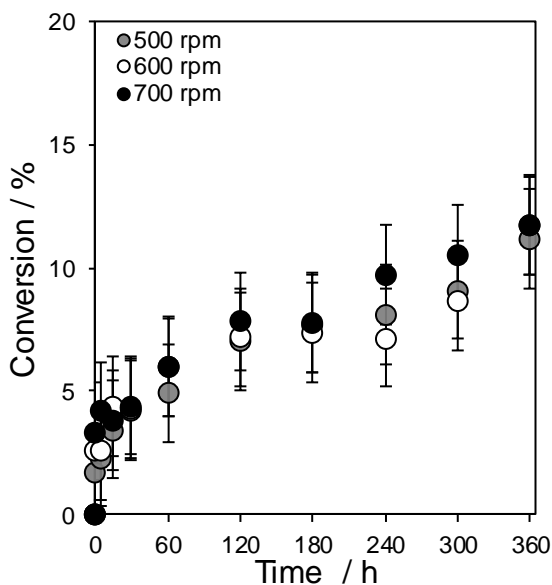


**Figure 1**– Reaction profiles of  $\alpha$ -pinene isomerisation as function of time employing bulk W 3.2 wt% on SBA-15. Reaction conditions: 126 mmol of  $\alpha$ -pinene, 0.2 cm<sup>3</sup> of tetradecane (STD), 0.1 g of catalyst, at 60 °C, stirring rate 500, 600 and 700 rpm.

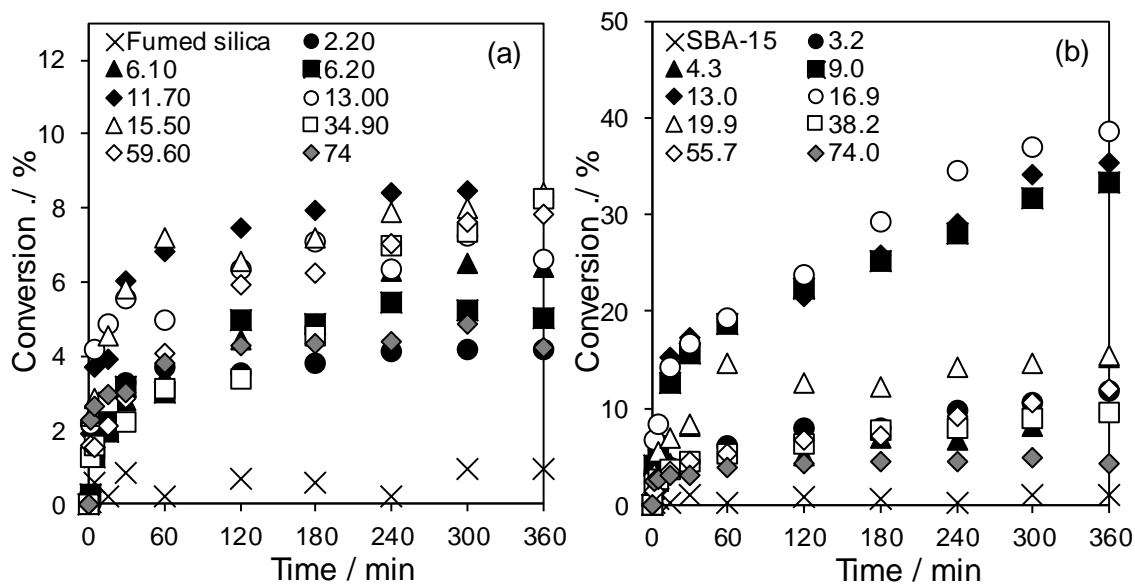


**Figure 2** – Reaction profiles of  $\alpha$ -pinene isomerisation as function of time and bulk W loadings over fumed silica (a), and SBA-15 (b). Reaction conditions: 126 mmol of  $\alpha$ -pinene, 0.2 cm<sup>3</sup> of tetradecane (STD), 0.1 g of catalyst, at 60 °C, stirring rate 700 rpm.

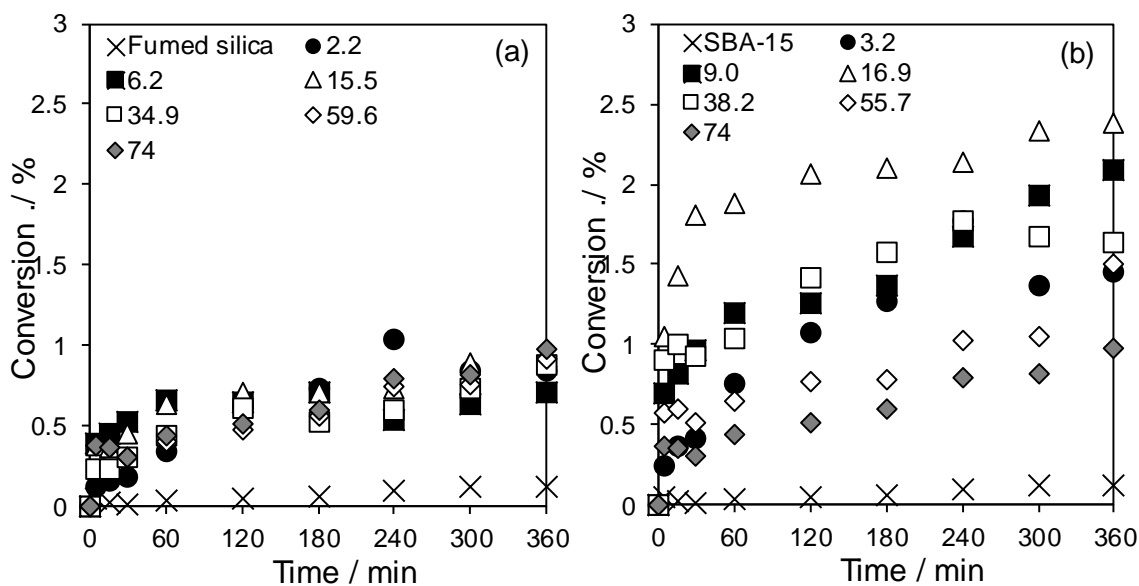


**Figure 3** – Reaction profiles of  $\alpha$ -pinene isomerisation as function of time and bulk W loadings over fumed silica (a), and SBA-15 (a). Reaction conditions: 126 mmol of  $\alpha$ -pinene, 0.2 cm<sup>3</sup> of tetradecane (STD), 0.1 g of catalyst, at 30 °C, stirring rate 700 rpm.

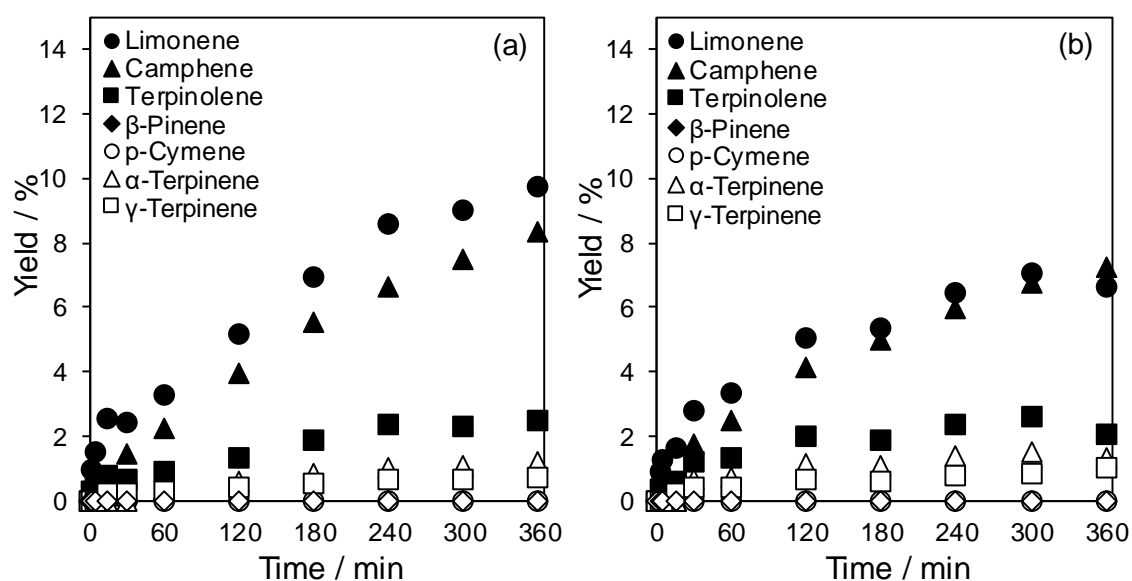


**Figure 4** – Reaction profiles of products yields of  $\alpha$ -pinene isomerisation as function of time for supported HPMo and HSiW on SBA-15 with 9 wt% of bulk metal loading. HPMo/SBA-15 (a), HSiW/SBA-15 (b). Reaction conditions: 126 mmol of  $\alpha$ -pinene, 0.2 cm<sup>3</sup> of tetradecane (STD), 0.1 g of catalyst, at 60 °C, stirring rate 700 rpm.

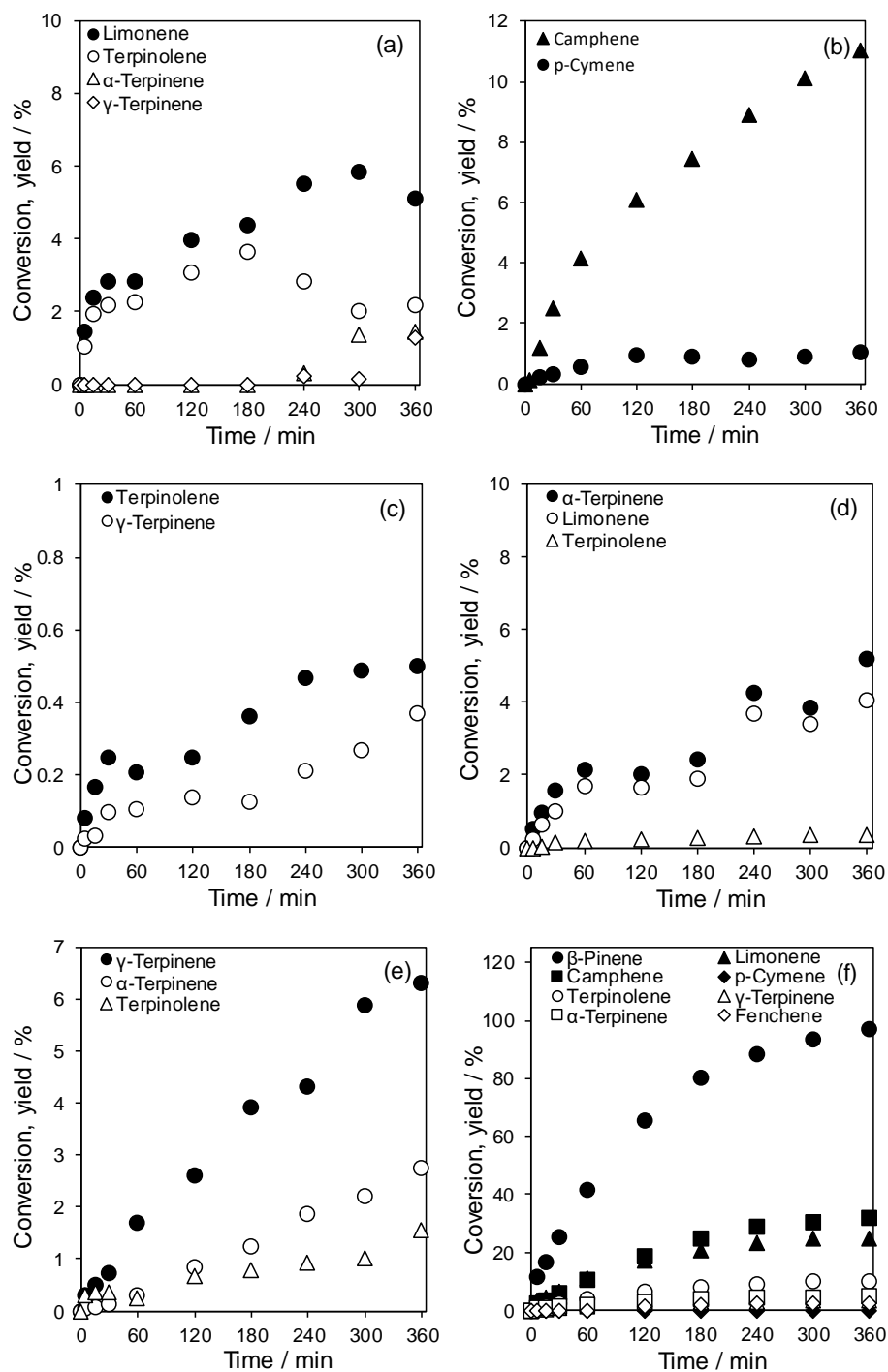


**Figure 5**– Reaction profiles of  $\alpha$ -pinene isomerisation products as function of time employing 9.0 wt% of bulk W on SBA-15;  $\gamma$ -Terpinene (a), Limonene (b), Terpinolene (c),  $\beta$ -Pinene (d),  $\alpha$ -Terpinene (e), Camphene and p-Cymene (f). Reaction conditions: 126 mmol of reagent, 0.2 cm<sup>3</sup> of tetradecane (STD), 0.1 g of catalyst, at 60 °C, stirring rate 700 rpm.

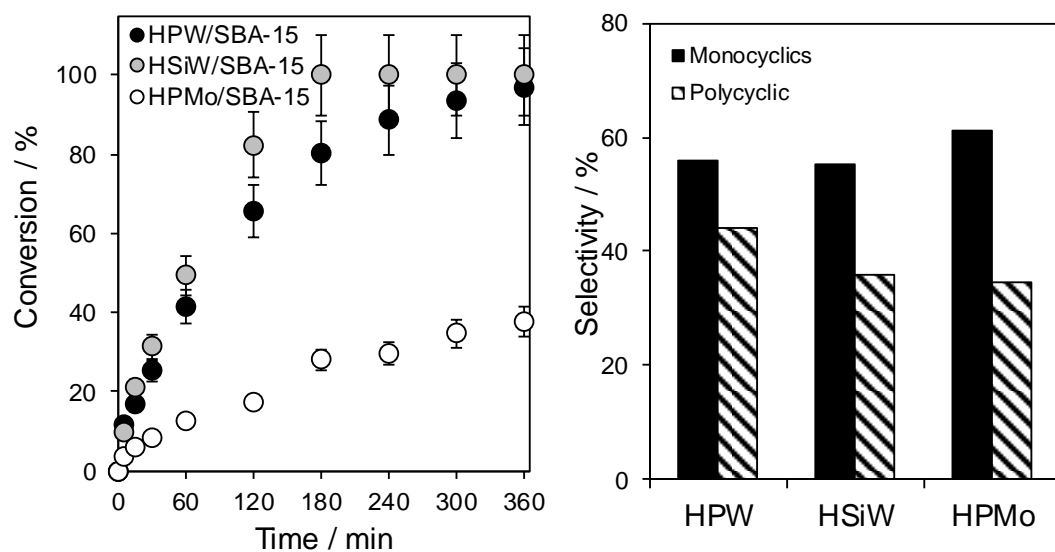
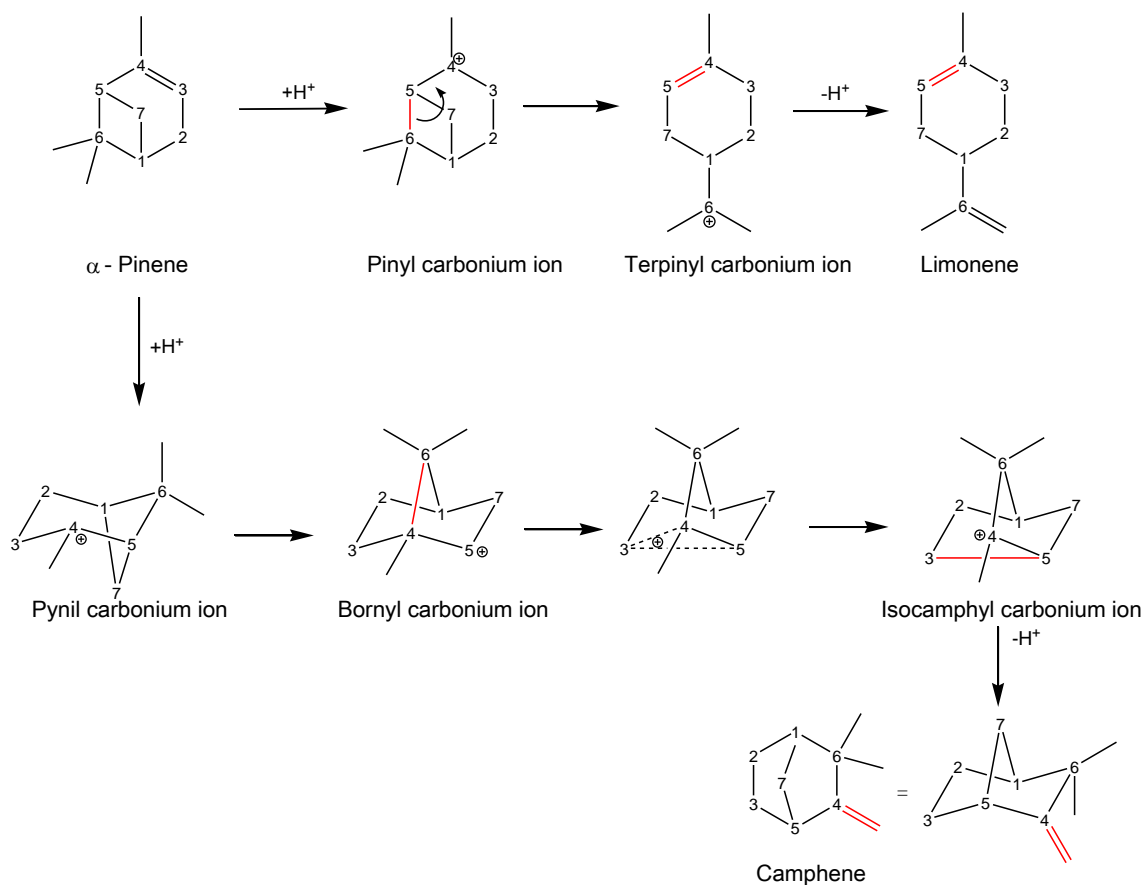


**Figure 6**– Reaction profiles of  $\beta$ -pinene isomerisation as function of time for supported HPAs on SBA-15 with 9 wt% of heteroatom. Reaction conditions: 126 mmol of  $\beta$ -pinene,  $0.2 \text{ cm}^3$  of tetradecane (STD), 0.1 g of catalyst, at  $60 \text{ }^\circ\text{C}$ , stirring rate 700 rpm.



**Scheme 1** – Reaction mechanism from isomerisation of  $\alpha$ -pinene to the main products limonene and camphene.

## Appendix B – Ethanol dehydration

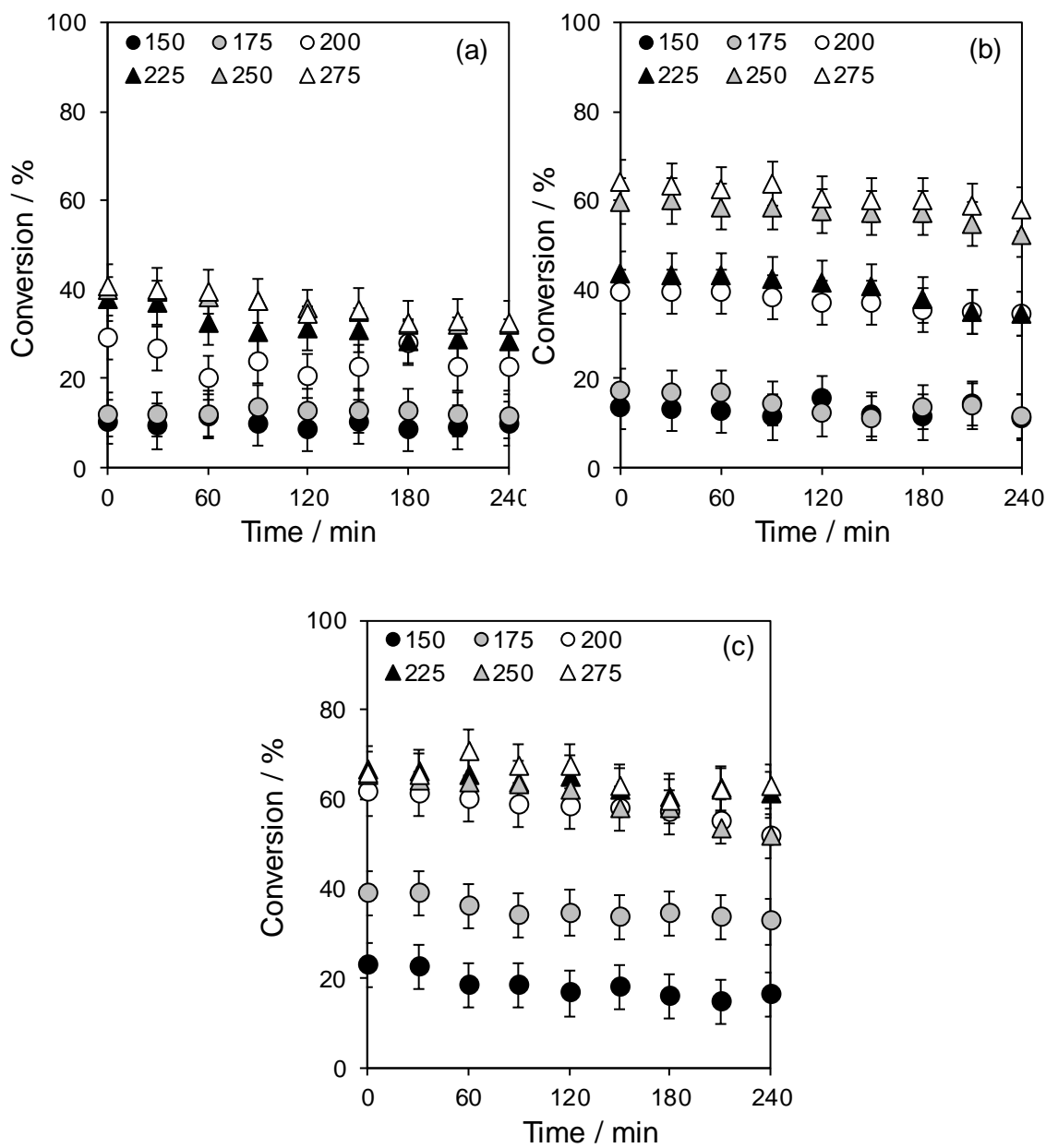


**Figure 7**– Ethanol conversion as function of time at different temperatures ranged, using as catalyst 50 (a), 100 (b) and 150 (c) of unsupported HPW. Reaction conditions: 50, 100, 150 mg catalyst,  $V_{\text{catalyst}} = 5 \text{ cm}^3$ ,  $L_{\text{Ethanol}} = 0.0034 \text{ mol min}^{-1}$ ,  $G_{\text{N}_2} = 50 \text{ cm}^3 \text{ min}^{-1}$  at 150, 175, 200, 225, 250, 275 °C.

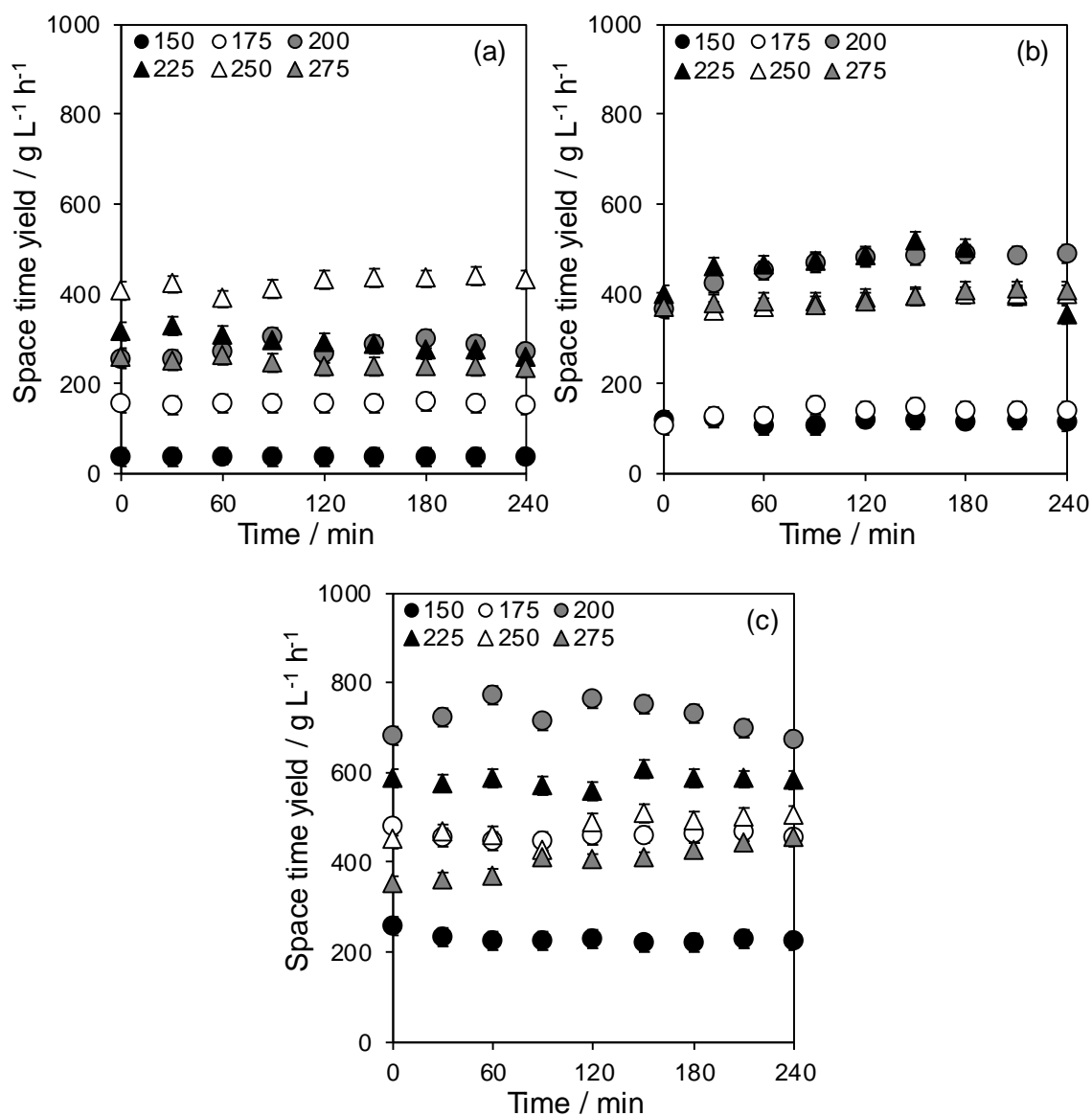


**Figure 8** – Diethyl ether space time yield as function of time at different temperatures, using as catalyst 50 (a), 100 (b) and 150 (c) of unsupported HPW. Reaction conditions: 50, 100, 150 mg catalyst,  $V_{\text{catalyst}} = 5 \text{ cm}^3$ ,  $L_{\text{Ethanol}} = 0.0034 \text{ mol min}^{-1}$ ,  $G_{\text{N}_2} = 50 \text{ cm}^3 \text{ min}^{-1}$  at 150, 175, 200, 225, 250, 275 °C.

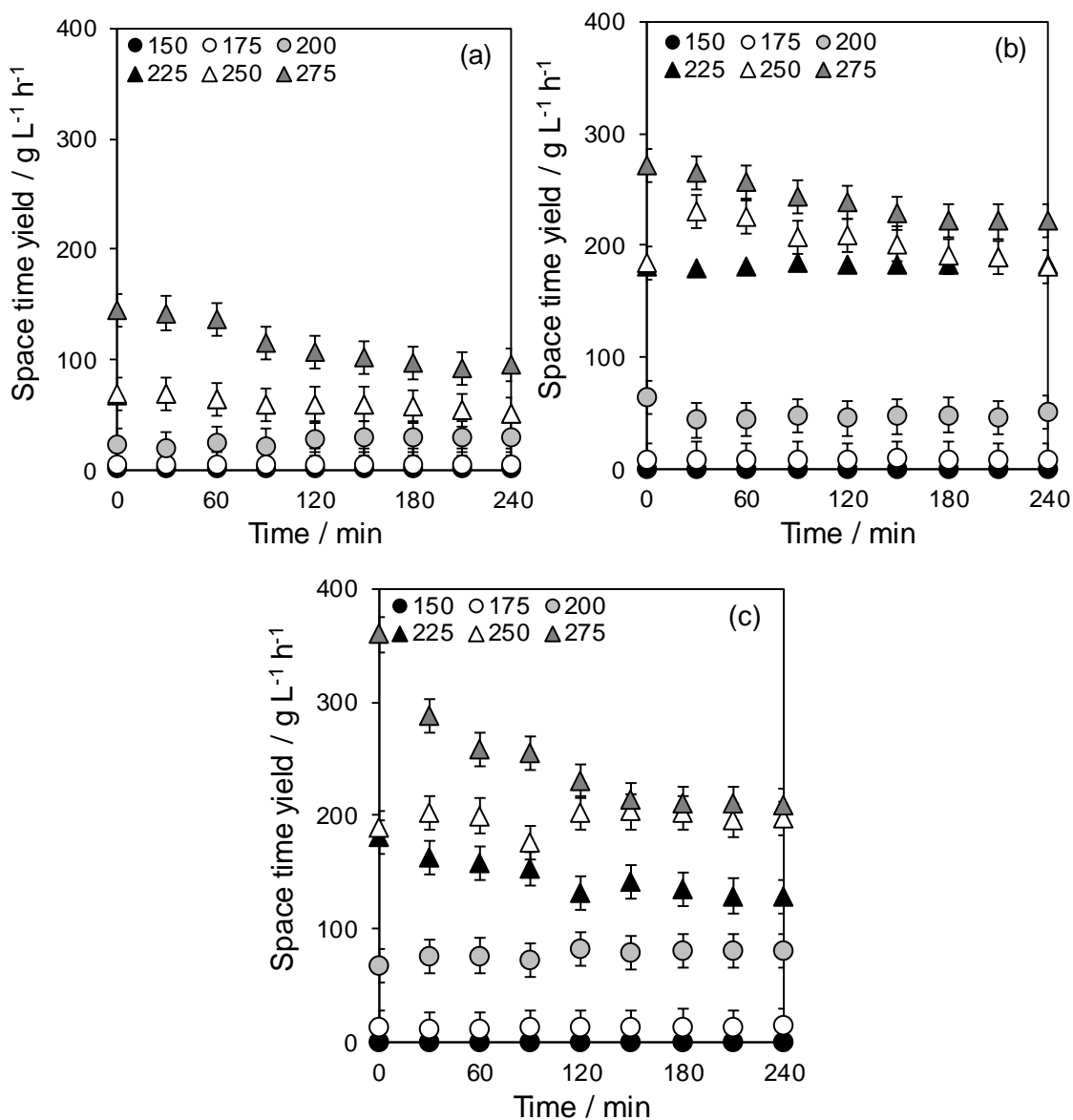


**Figure 9** – Ethylene space time yield as function of time at temperatures ranged 150-275 °C, using as catalyst 50 (a), 100 (b) and 150 (c) of unsupported HPW. Reaction conditions: 50, 100 and 150 mg catalyst,  $V_{\text{catalyst}} = 5 \text{ cm}^3$ ,  $L_{\text{Ethanol}} = 0.0034 \text{ mol min}^{-1}$ ,  $G_{\text{N}_2} = 50 \text{ cm}^3 \text{ min}^{-1}$  at 225 °C.

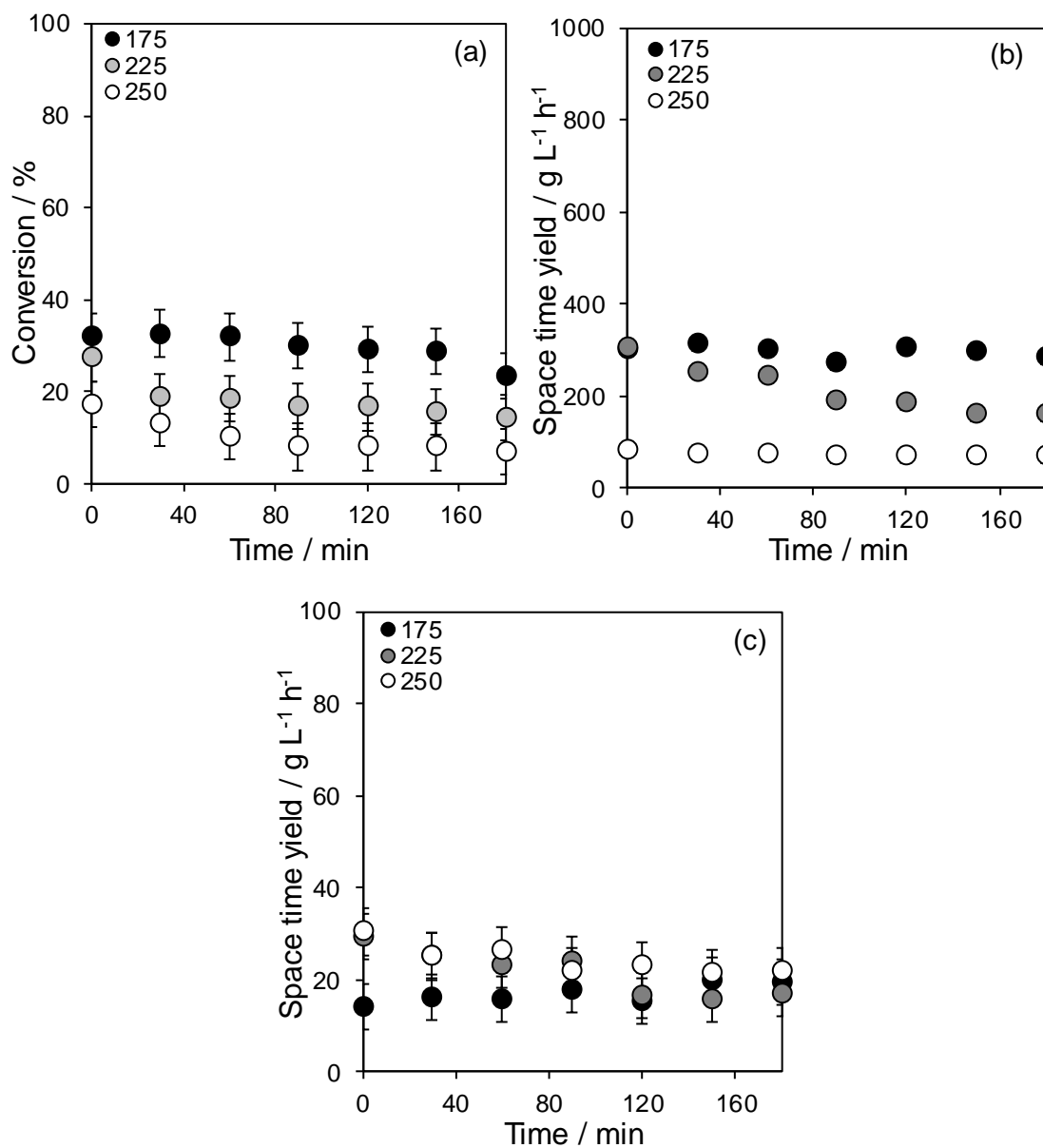


**Figure 10** – Ethanol dehydration reaction values obtained employing unsupported HSiW as function of time: conversion (a), diethyl ether space time yield (b) and ethylene space time yield (c). Reaction conditions: 100 mg catalyst,  $V_{\text{catalyst}} = 5 \text{ cm}^3$ ,  $L_{\text{Ethanol}} = 0.0034 \text{ mol min}^{-1}$ ,  $G_{\text{N}_2} = 50 \text{ cm}^3 \text{ min}^{-1}$  at 175, 225, 250 °C.

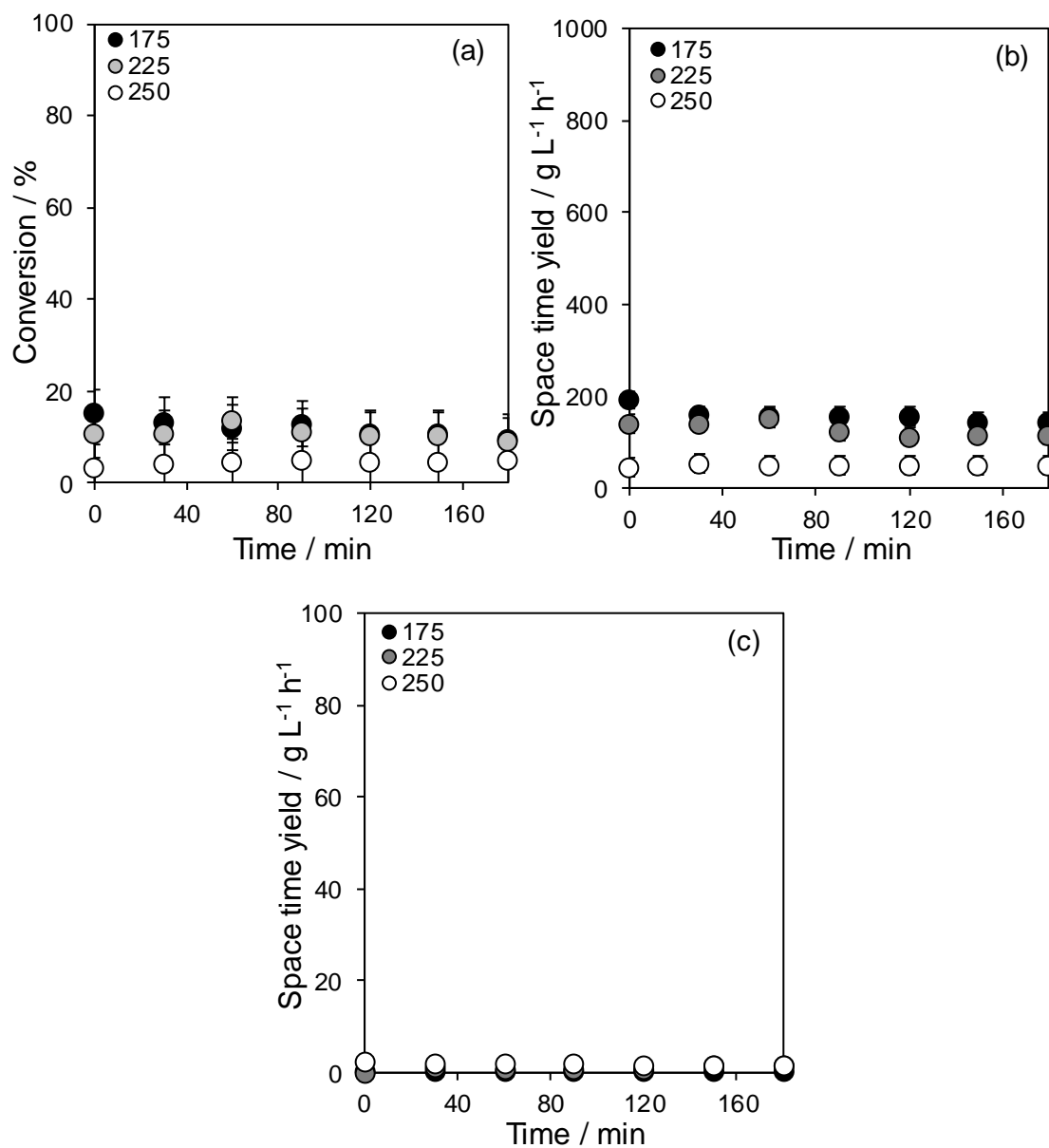


**Figure 11** – Ethanol dehydration reaction values obtained employing unsupported HSiW as function of time: conversion (a), diethyl ether space time yield (b) and ethylene space time yield (c). Reaction conditions: 100 mg catalyst,  $V_{\text{catalyst}} = 5 \text{ cm}^3$ ,  $L_{\text{Ethanol}} = 0.0034 \text{ mol min}^{-1}$ ,  $G_{\text{N}_2} = 50 \text{ cm}^3 \text{ min}^{-1}$  at 175, 225 and 250 °C.

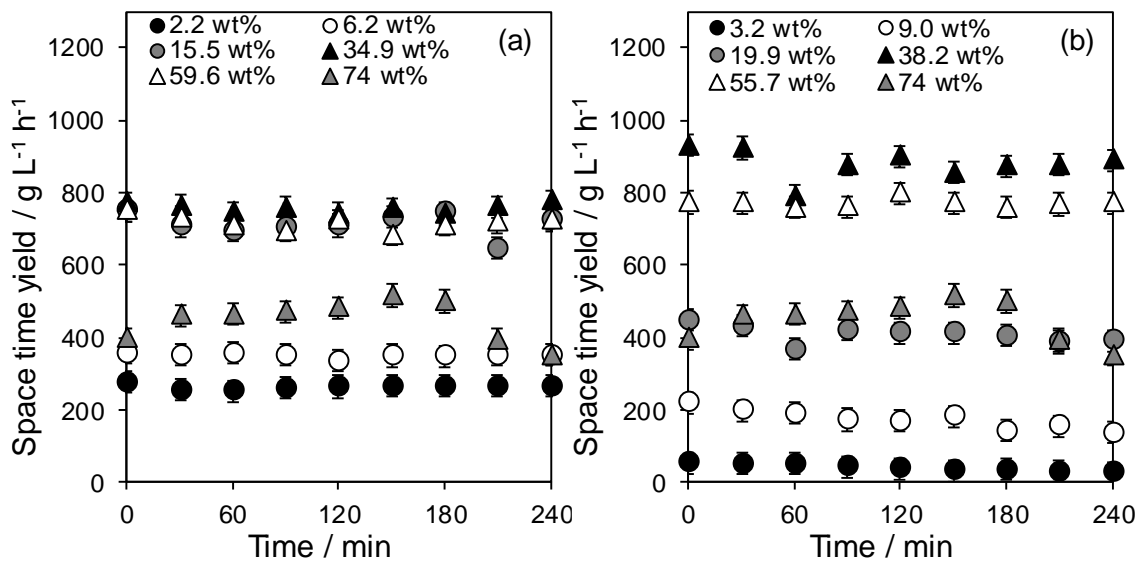


**Figure 12** – Diethyl ether space time yield as function of time at 225 °C, employing HPW/SBA-15(a), and HPW/Fumed silica. Reaction conditions: 100 mg catalyst,  $V_{\text{catalyst}} = 5 \text{ cm}^3$ ,  $L_{\text{Ethanol}} = 0.0034 \text{ mol min}^{-1}$ ,  $G_{\text{N}_2} = 50 \text{ cm}^3 \text{ min}^{-1}$  at 225 °C.

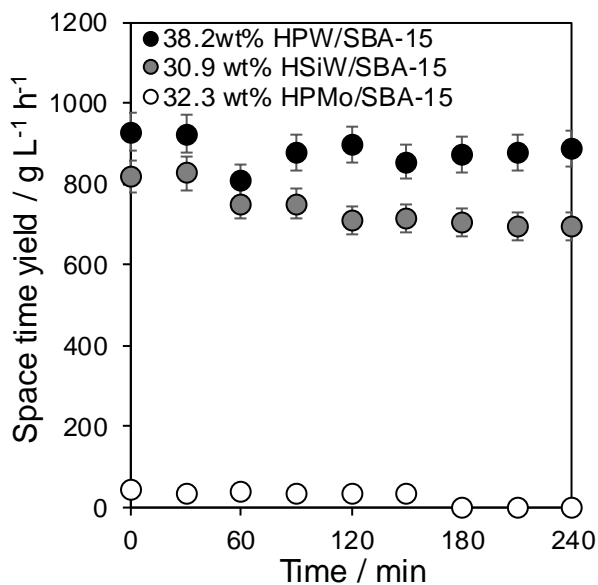


**Figure 13** – Diethyl ether space time yield attained at 225 °C, employing SBA-15 supported HPAs as function of time. Reaction conditions: 50 mg catalyst,  $V_{\text{catalyst}} = 5 \text{ cm}^3$ ,  $L_{\text{Ethanol}} = 0.0034 \text{ mol min}^{-1}$ ,  $G_{\text{N}_2} = 50 \text{ cm}^3 \text{ min}^{-1}$  at 225 °C.